Formation of $Cu(In,Ga)Se_2$ from solution processed sodium containing metal precursors

Ulrich Maximilian Berner

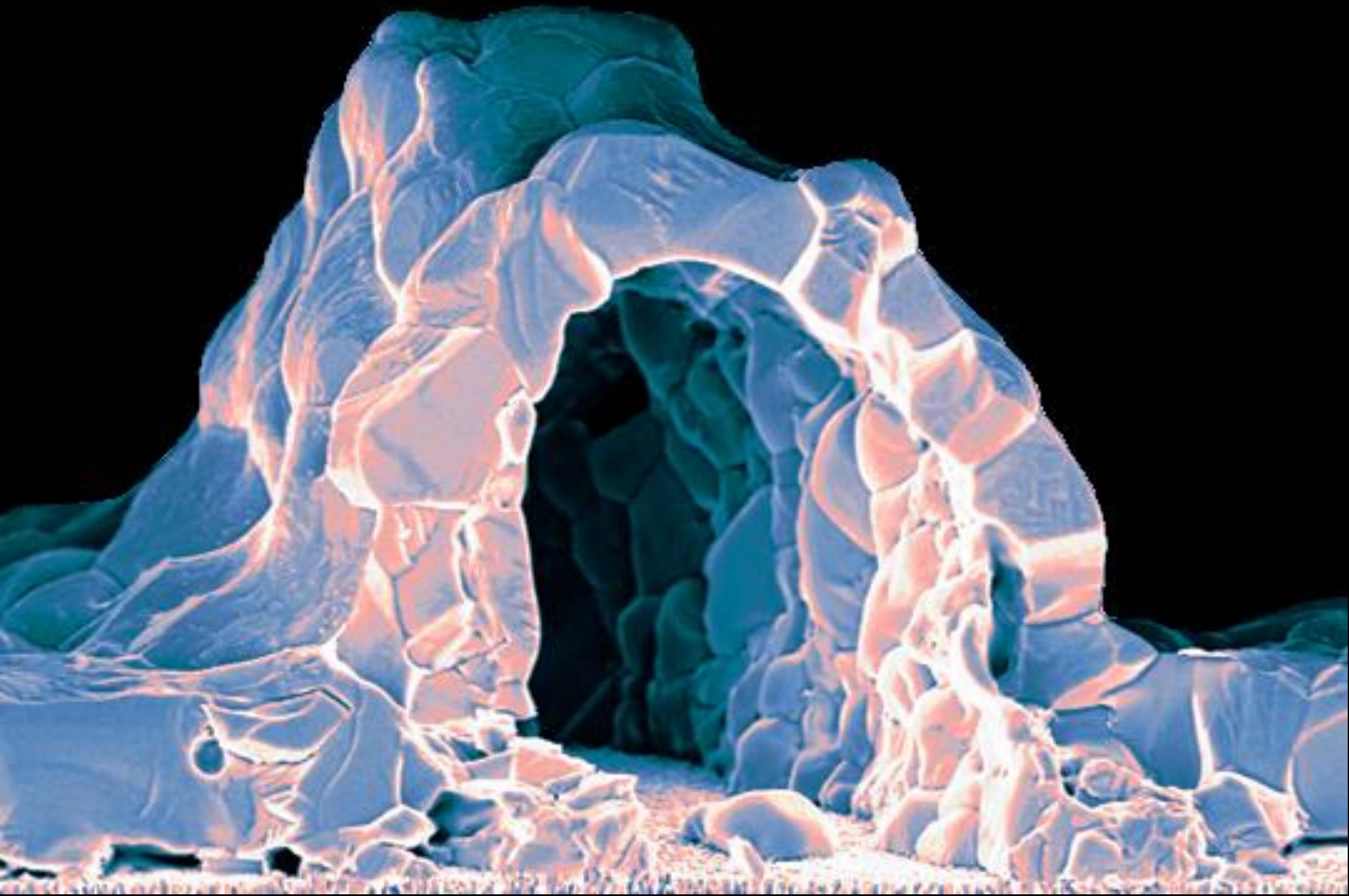

PhD-FSTC-2015-16
The Faculty of Sciences, Technology and Communication

DISSERTATION

Defense held on 17/04/2015 in Luxembourg
to obtain the degree of

DOCTEUR DE L'UNIVERSITÉ DU LUXEMBOURG EN CHIMIE

by
Ulrich Maximilian Berner
Born on 19 March 1985 in Stuttgart (Germany)

FORMATION OF $\mathrm{CU(IN,GA)SE_2}$ FROM SOLUTION PROCESSED SODIUM CONTAINING METAL PRECURSORS

Dissertation defense committee

Dr. Phillip DALE, dissertation supervisor
Professor, Université du Luxembourg

Dr. Jan LAGERWALL, chairman
Professor, Université du Luxembourg

Dr. Diego COLOMBARA, vice chairman
Université du Luxembourg

Dr. Zeger HENS
Professor, University of Ghent

Dr. Markus WIDENMEYER, industrial supervisor
Robert Bosch GmbH, Stuttgart

Table of content

Abstract

In this thesis a new chemical deposition process for the fabrication of Cu(In,Ga)Se_2 absorber layers applicable as absorber material in thin film solar cells is described. Within this work a power conversion efficiency of up to 13.3% (13.8% on active area) has been achieved which is among the highest reported values for non-vacuum based processes. The main part of this thesis is divided into 4 chapters describing the synthesis of the base materials and the ink (i), the individual process steps coating and drying together with the metal film formation (ii) as well as the selenization of the metal layer to chalcopyrites (iii). The last chapter investigates the influence of dissolved sodium salts (iv).

(i) Metal formates synthesized from their respective nitrates have been chosen as starting salts due to the high reduction potential of the anion and its clean decomposition. With the reasonably toxic solvents tetramethylguanidine and methanol an ink can be produced which is highly concentrated, chemically stable and cheap.

(ii) The coating and drying steps have been identified as crucial production processes to deposit homogeneous layers. In this context the solvent mixture has been shown to be responsible for unwanted material agglomerations close to the substrate boundaries. In order to minimize this effect a combined coating-drying device has been developed.

The formation of metallic layers has been studied in detail. It could be shown that the respective metal ions are getting reduced consecutively at elevated temperatures between 130 and 200°C. The morphology of the resulting layers is highly dependent on the process conditions and varies from thick and porous structures to incoherent particle agglomerations. In order to overcome this issue an ink additive has been identified to densify and homogenize the metallic layer. A mechanism is proposed based on the formation of an intermediate polynuclear metal organic structure.

(iii) The metallic layers could be selenized with elemental selenium in a tube oven to form dense chalcopyrites. By simulating the selenium evaporation a strong dependency of the final photovoltaic cell properties on the process temperature of the substrate layer getting in contact with evaporated selenium could be identified.

(iv) Several sodium salts conveniently added to the ink have been proven to be suitable as sodium source. Compared to diffusion from the glass substrate the immediate sodium availability resulted in significantly improved cell properties. Within the evaluated sodium salts large differences have been found for example regarding the layer morphology.

Chapter 1

Introduction

Photovoltaics describe the direct conversion of (sun) light to electricity. The benefits of this technology are obvious allowing power generation without a detour via heat or kinetic energy. With an abundant light source like the sun, photovoltaics have the potential to replace the prevailing limited fossil fuels like coal or gas in the near future. In this introductory chapter the pathway to the development of today's high efficiency devices is described briefly beginning with the discovery of the photoelectric effect. Subsequently, the focus is set on the chalcopyrite material system and its use as an absorber material for thin film solar cells. Finally, several production processes for these devices are introduced ranging from the well developed physical based methods to several upcoming alternatives including the chemical deposition.

1.1 Development in photovoltaics

Edmund Becquerel discovered the photoelectric effect in 1839. He observed a low potential difference when illuminating one of two identical platinum electrodes placed in a weak conducting solution. This observation could later be theoretically explained by Albert Einstein in 1905. In 1873 Willoughby Smith found photoconductivity in selenium. Based on this discovery Charles Fritts presented a working cell in 1883 consisting of a thin gold layer on pure selenium yielding an energy conversion efficiency of 1% [1]. Thus, for the following decades solar cell research primarily focused on selenium based devices. This changed with the introduction of the first silicon based devices developed in the Bell Telephone Laboratories in 1954 [2], [3]. The following success of this technology was mostly founded on the further development of the Czochalski method in the 1940s enabling the production of high purity silicon [4]. The breakthrough came with the satellite "Vanguard 1" launched in 1958 which was equipped with silicon solar cells having an energy output of less than one watt and a chemical battery. Contrary to all expectations the signals of the satellite could be received up to 1964. The upcoming research activities in the field of transistors gave the silicon photovoltaics another push due to the similar base materials and physical mechanisms. However, silicon is not the ideal material for a light conversion being an indirect semiconductor with a low absorption coefficient. Due to the mechanical properties of silicon the devices also require material thicknesses of around 200 μm with a high purity making the production process highly material and energy consuming.

Since the discovery of selenium as suitable semiconductor several alternative materials have been identified most of them having a direct band gap which allows a light absorption within a few micrometers. These technologies are therefore often summarized as thin film solar cells. One material in particular, the $CuInSe_2$ chalcopyrite was synthesized first by Hahn et al. in 1953 [5]. However, it took until 1974 to discover its use as a light absorber material with the first devices based on single crystals [6]. Polycrystalline layers exceeded 10% energy conversion efficiency in the early 80s with a co-evaporation process mostly developed at the Boeing Corporation [7]. The first commercially available modules were produced in 1998 by the Siemens Solar but did not succeed on the free market at that time. Today, the chalcopyrite based thin film technology holds the lab scale efficiency record within all thin film technologies with 21.7% [8].

1.2 $Cu(In,Ga)(Se,S)_2$ thin film technology

$Cu(In,Ga)(Se,S)_2$ based solar cells, often abbreviated as CIGSSe, are named after the elements forming the light absorbing layer: copper, indium and/or gallium as well as selenium and/or sulfur. In this thesis CIGS is used as abbreviation for the sulfur free material due to the focus on selenium. In the current section the CIGS technology is introduced beginning with the absorber layer material properties. Thereafter, the layer stack which is necessary for a working solar cell device is described and the optoelectronic properties are explained.

1.2.1 Material properties

The material CIGS including the ternary $CuInSe_2$ (CIS) and $CuGaSe_2$ (CGS) belongs to the I-III-VI_2 compounds and crystallizes in the typical tetragonal structure of chalcopyrites. This structure is derived from the zinc blend unit cell of II-VI materials. In chalcopyrites equal amounts of copper and indium/gallium atoms are alternatingly replacing the zinc positions leading to an isoelectronic substitution. More information about the lattice properties can be found elsewhere [9]. The chalcopyrite material is a semiconductor with a band gap that depends on the composition of the elements. Due to the full element miscibility of In and Ga, the range varies between 1.0-1.05 eV for $CuInSe_2$ (depending on the copper content) and 1.7 eV for $CuGaSe_2$ [10]. By including sulfur into the lattice, this range can be extended up to 2.4 eV [11]. The possibility to tailor the band gap is very useful and allows adjusting the absorber properties to the terrestrial solar spectrum. For this spectrum a theoretical conversion efficiency limit can be calculated as a function of the semiconductor's band gap which has been reported first by Shockley and Queisser [12], [13]. The limit has two optima for band gap energies of 1.15 eV and 1.35 eV corresponding to Ga/(Ga+In) or (Ga/III) ratios of about 0.25 and 0.65 in sulfur free absorbers.

1.2.2 Solar cell layer stack and band alignment

In the previous section the absorber material consisting of the CIGS chalcopyrites has been introduced. The primary function of this layer is the energy absorption of the sun's radiation by transferring electrons from the valence band to the conduction band resulting in an electron-hole pair. This absorption is only possible if the energy of the incoming photons is larger than the band gap of the semiconductor. The energy of the photons is dependent on the light's frequency and therefore wavelength and can be calculated as following:

$$E_{photon} = hf = h\frac{c}{\lambda}$$

f	frequency in 1/s
h	Planck constant (4.14×10^{-15} eV s)
λ	wavelength in m
c	speed of light (in a vacuum) in m/s

The resulting electron-hole pairs have a finite lifetime and recombine if they are not separated. Thus, additional functional layers are necessary to separate the generated charge carriers. Figure 1 shows a typical CIGS solar cell layer stack in the so-called substrate configuration which is typically used for high efficiency devices. On top of the absorber is an approximately 50 nm thin CdS layer coated by chemical bath deposition. This layer is an n-type semiconductor with a band gap of 2.4 eV and therefore transparent for most photons emitted from the sun. At the interface between CdS and the p-type CIGS a p-n-junction is forming. This junction is responsible for the charge separation which is further discussed below. A several hundred nanometer thick molybdenum back contact (BC) beneath the absorber is deposited on a soda lime glass (SLG) substrate by sputtering. The same deposition method is used for the front contact on top of the CdS layer consisting of a 50 nm thick intrinsic ZnO and an approximately 1 µm thick conducting aluminum doped ZnO layer (ZnO:Al). The current collection is improved by a grid usually made of nickel and aluminum (Ni:Al).

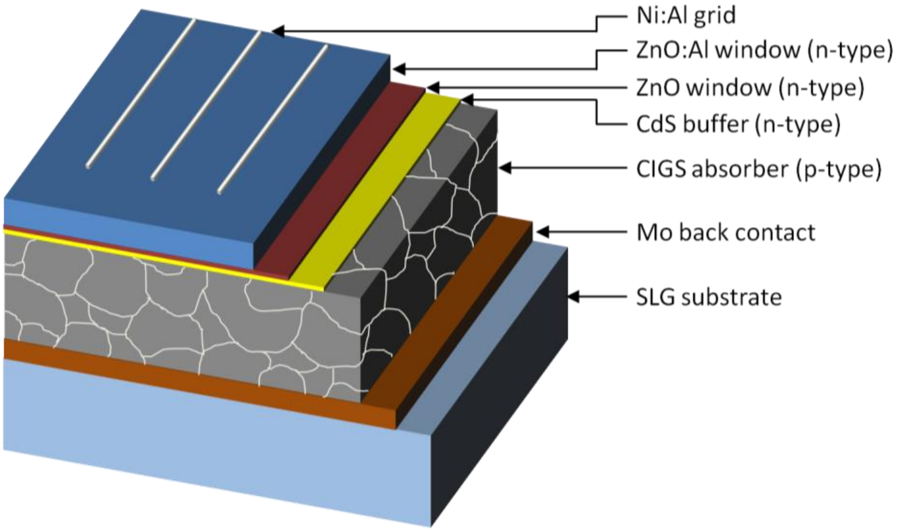

Figure 1: Schematical representation of a typical layer stack used for CIGS solar cells. Mo/CIGS/CdS/ZnO/ZnO:Al.

The band diagram of the described layer stack is shown in Figure 2. Here, the Fermi level is denoted as E_F and the valence band and the conduction band are abbreviated as E_V and E_C, respectively. The p-n junction between the p-type CIGS layer and the n-type CdS leads to a strong band bending. This band bending divides the absorber layer into a space charge region (SCR) and a quasi neutral region (QNR). The SCR is responsible for the separation of the photogenerated electron hole pairs due to the built in electric field. The shown band diagram also includes a back surface field (BSF) typically found in gallium containing chalcopyrites. Depending on the process conditions gallium often accumulates at the BC increasing the conduction band offset. This offset acts as a barrier for the electrons in the conduction band decreasing the chances of a BC recombination. On top of the absorber layer the two window layers ZnO and ZnO:Al are visible with a band gap of 3.3 eV which is transparent for almost all photons emitted from the sun. More information about the band alignment can be found in [14].

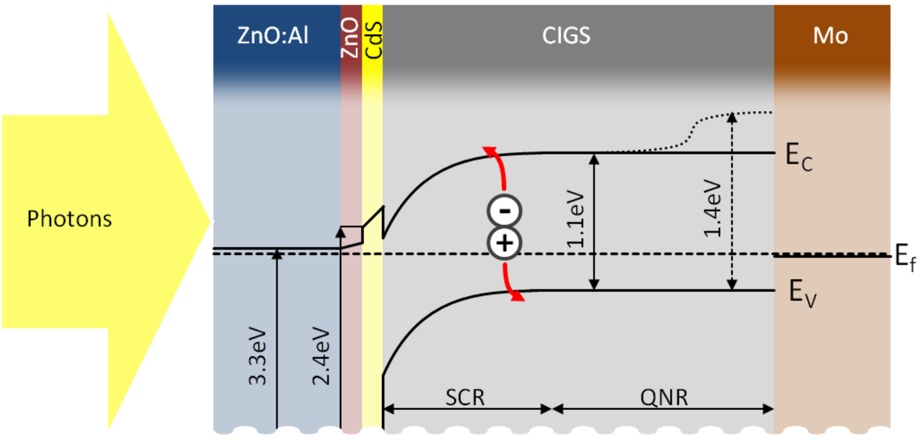

Figure 2: Band diagram of a Mo/CIGS/CdS/ZnO/ZnO:Al solar cell device layer stack. Photons arrive at the window layer and are mostly absorbed in the CIGS layer. Here the absorbed energy can transfer electrons from the valence band to the conduction band. The charge separation of the resulting electron-hole pair is achieved by the gradient in the electrochemical potential in the space charge region.

1.2.3 Electrical characterization

In this section the basics concerning the electrical characterization of solar cell devices are introduced. Without illumination (dark) solar cells show the typical characteristics of a diode. If an external voltage is applied the current density-voltage (j-V) characteristics can be described by the ideal-diode equation, an analytical solution found by Shockley [15].

$$j_{dark}(V) = j_0\left(e^{\frac{qV}{k_BT}} - 1\right)$$

j_{dark}	dark current
j_0	reverse saturation current
q	elementary charge (1.602176565 ×10^{-19} C)
V	voltage in V
k_B	Boltzmann constant (1.3806488 × 10^{-23} m^2kg/s^2K)
T	absolute temperature in K

Under illumination excess minority charge carriers are generated which either recombine or are separated by the electric field, thus, leading to a photo current j_{ph}. In this case the diode equation is superimposed to the following expression.

$$j_{light}(V) = j_0\left(e^{\frac{qV}{k_BT}} - 1\right) - j_{ph}$$

j_{ph}	photo current

The j-V curves of a solar cell with and without illumination are shown in Figure 3.

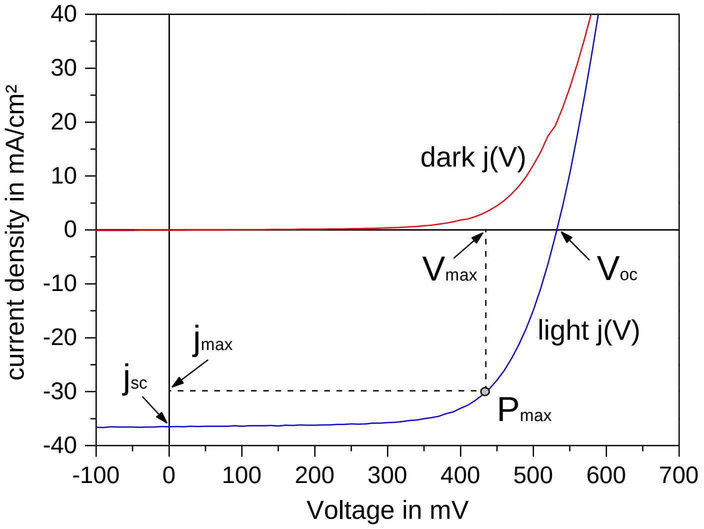

Figure 3: j-V characteristics of a typical solar cell with and without illumination.

The intersection of the light j-V curve with the y-axis is the short circuit current j_{sc} (at V=0) and with the x-axis the open circuit voltage V_{oc} (at j=0). The maximum power P_{max} is achieved at j_{max} and V_{max}. With these values the power conversion efficiency of the solar cell η can be calculated.

$$\eta = \frac{FF \cdot j_{sc} \cdot V_{oc}}{P_{ill}}$$

η	energy conversion efficiency
FF	fill factor
j_{sc}	short circuit current
V_{oc}	open circuit voltage

Here, P_{ill} is the power of the incident illumination and FF the fill factor. The fill factor describes the deviation between the two rectangular areas $(j_{sc} \cdot V_{oc})$ and $(j_{max} \cdot V_{max})$.

$$FF = \frac{j_{max} \cdot V_{max}}{j_{sc} \cdot V_{oc}}$$

j_{max}	current density at maximum power
V_{max}	voltage at maximum power

1.3 CIGS absorber layer processing

The industrial scale processing of CIGS absorbers today is dominated by physical vacuum based methods. However, due to the high energy consumption and the low material efficiency of these processes several new concepts are currently under investigation and various methods have already been published in the literature. Most of these approaches are based on deposition methods that don’t require any vacuum and are therefore usually summarized as vacuum-free methods. In this section the basics of the standard physical deposition methods are introduced as well as the vacuum free liquid film coating processes.

1.3.1 Vacuum based CIGS deposition methods

In general the vacuum based methods can be divided into two processes, sputtering and co-evaporation. Sputtering is a common physical vapor deposition method used for various materials to produce uniform thin films. In the case of CIGS it is possible to deposit all elements in one step from a quaternary target [16]. However, to achieve high efficiencies a different process is applied where only the metals are deposited by sputtering while the chalcogens are incorporated in a second step. Therefore, this process is often called the two-step process. The metal precursor is usually deposited in the form of several stacked layers of pure indium and a copper-gallium alloy [17]. The alloy is necessary because gallium cannot be sputtered separately. Ternary sputter targets are also possible containing all three elements [18]; yet, the achieved cell efficiencies with this approach so far are below those of the stacked metal layers. The transformation of the precursor to the chalcopyrite semiconductor is usually achieved by exposing the sputtered metal layer at elevated temperatures to liquid or gaseous chalcogenides. Regarding the gaseous chalcogen sources evaporated elemental Se or S as well as H_2Se or H_2S can be used.

Co-evaporation is a single step process where all elements are deposited simultaneously from separated sources. By heating the substrate during the deposition the chalcopyrite formation can be achieved instantaneously. Due to the direct control over the individual deposition rates, variable element depth profiles can be prepared. High efficiency cells have been processed from a so-called three stage process [19]. In the first stage a copper free $(In_{1-x}Ga_x)_2Se_3$ layer is deposited at low temperatures followed by a copper selenium layer at 540°C. This leads to the formation of a mobile CuSe phase that is believed to promote the growth of large grains. In the last stage the now copper rich layer is covered with indium and gallium up to the desired Cu/(In+Ga) ratio of 0.92.

With both physical deposition methods high efficiency solar cells have been processed. The current world record for CIGS solar cells of 21.7% has been achieved by co-evaporation [8] while the record for sputtered cells is following closely behind with 20.9% [20]. However, the necessary high vacuum conditions and the low material efficiency of these processes leave room for optimization.

1.3.2 Vacuum free liquid film coating

Vacuum free deposition technologies have inherent advantages over their vacuum based competitors [21]. Important factors are the significantly lower capital costs of the manufacturing equipment and the lower running costs for example by using roll-to-roll processing techniques allowing a higher throughput. Also important is the possibly high material utilization that can reach up to 100%. Concerning the ink deposition there are various non-vacuum based methods to deposit the absorber layers ranging from spray pyrolysis and electrodeposition to the liquid film coating. A comprehensive review has been published for example by Ebersbacher et al. [22]. In this section the focus is on the liquid film coating processes which can be divided into the particle based methods and the solution based methods.

1.3.2.1 Particle based approaches

The category “particle based coating” covers a large area of different approaches. More detailed information can be found in the numerous reviews [23]–[25]. The main characteristic of these approaches is that the inks contain nanoparticles which are dispersed in a liquid transfer compound. These nanoparticles have to be synthesized in a separate step. For the synthesis numerous methods have been published including hot injection [26], several solvothermal routes [25], [27]–[34], melt atomization [35], mechanical alloying and milling [36], [37], precipitation of hydroxides [38], salt-assisted ultrasonic spray pyrolysis [39] and several others. The synthesis method itself is rather unimportant for the cell processing; therefore it is more practical to categorize the approaches by the chemical state and composition of the final nanoparticles. The particles can vary from metal-oxides [38], [39], binary or ternary metals [30] to ternary or quaternary chalcopyrites [31], [32], [34].

Independently of the composition all nanoparticles have to fulfill several requirements. In solar cells dense absorber layers are particularly necessary to minimize the pathway of the separated charge carriers. In order to process a dense layer with a thickness in the range of several hundred nanometers to a few micrometers, the median diameter of the particles has to be in the sub-micron level. Small particles with similar diameters are particularly necessary when using mixtures of singular metal-oxides or (binary) metals. The reason for this is that agglomerations and different settling rates can lead to stoichiometry deviations between the precursor ink and the deposited layer [40]. This can ultimately result in a highly non-uniform elemental distribution.

Multi-component chalcopyrite nanoparticles containing all elements in the desired composition don't have this disadvantage and therefore give the best control of composition. However, in this approach the layer porosity can be a severe problem due to the absence of a sintering agent that could promote inter-particle sintering. Without an external force, the high melting point of the chalcopyrites, which is far above the working limit of standard substrates like glass, hinders a densification. Approaches to lower the melting point of a crystalline material by decreasing the median diameter of the nanoparticles to below 25 nm did not achieve the desired decrease in the melting point temperature [41]. Thus, usually an external fluxing agent is necessary. Guo et al. used a chalcogen exchange mechanism by annealing sulfide nanoparticles in a selenium atmosphere. This led to a volume expansion of 14.6% [42]. The addition of an excess of copper resulting in a mobile copper selenide phase also improved the sintering, but made an additional KCN etching step necessary [43].

In contrast, the chalcogen free metal precursors have the advantage of a volume expansion during the chalcopyrite formation. The incorporation of an equimolar amount of selenium and/or sulfur increases the volume of the metal layer by a factor of 2-3. Attempts with copper and indium powders struggled with oxidation issues especially with the fine indium particles that could afterwards not be selenized to $CuInSe_2$ [44]. Instead, binary CuIn nanoparticles are more stable to oxygen and the lower ductility of the alloy compared to elemental indium also improves the particle size distribution achieved by mechanical milling [45]. This is a significant advantage as Başol et al. could show that smaller nanoparticles can have beneficial influence on the solar cell performance [46]. However, typical binary metal nanoparticles are composed of copper-rich CuIn-phases due to a miscibility gap in the binary phase diagram. Thus, stoichiometric or indium-rich mixtures tend to segregate prior to the arrival of the chalcogens. Approaches to overcome this problem by mixing metal nanoparticles with elemental selenium in the ink led to the formation of chalcopyrites during the milling process [47]. As mentioned before, agglomerations of particles forming in the ink or during the coating process can increase the precursor porosity or result in material inhomogeneities. These issues raise additional challenges during the layer processing. In order to inhibit the formation of agglomerations the nanoparticles are usually dispersed in a liquid prior to the coating step. Either a charge or a steric stabilization is necessary to stabilize the particles. This can for example be achieved by using capping agents [30], [32] or the addition of dispersants [48].

Many ink deposition techniques are applicable to produce homogeneous wet films [24]. After the drying and/or decomposition of the transfer medium and the additives the following treatment depends on the nature of the nanoparticles. Metal oxides for example usually have to be reduced to their elemental form which can be achieved by a separate high temperature treatment in hydrogen. Another possibility is the use of hydrogen selenide or sulfide in the subsequent annealing step to exchange the oxygen with sulfur or selenium. High energy conversion efficiencies of 13.6% have been achieved with solar cells made from nanoparticles with an oxide route (0.08 cm^2 cell area) [38]. In contrast, pure metal precursors don't require this reduction step and can be reacted directly to the chalcopyrite phase in a chalcogen atmosphere. Precursor layers consisting of ternary or quaternary chalcopyrite nanoparticles already contain the chalcogens. Thus, these samples theoretically don't need a further chalcogen treatment for the chalcopyrite formation. However, annealing without selenium can lead to a partial loss of selenium [49] and/or indium as well as gallium [50] and can also deteriorates the absorber quality [51].

1.3.2.2 Solution based approaches

The category "solution based coating" summarizes all methods, where a particle free solution containing copper and at least one of the metals indium and gallium is obtained. In some particular cases also the chalcogens are present in the liquid phase. Because the used precursors for these inks are usually off-the-shelf chemicals, many of these approaches have significant advantages concerning the precursor preparation and purification compared to the particle based methods discussed in the previous section. The dissolution of the precursors also allows a precisely controlled composition. So far various approaches have been published that can be further divided into three subcategories. Functional layers have been processed either by dissolving metal salts, metal organic precursors or metal chalcogenides.

Metal salts

Metal salts are the most convenient precursors to produce an ink with. Many salts are readily available in high purities and can usually be dissolved in several solvents. However, in contrast to the particle based approaches where the liquids are mostly used as a transfer agent, the solvents in solutions play a key role. Their main purpose is the complexation of the metal salts to form a stable ink. Thus, properties like polarity, pH-value, solubility, reactivity and cost have to be considered. Additionally, appropriate values for the surface tension as well as the viscosity are crucial to prepare a thin and uniform liquid film.

After the deposition, the solvents have to evaporate or decompose completely without precipitating precursor salt crystals or cause other non-uniformities. For this reason solution based approaches often use binders to preserve the integrity of the layer by avoiding cracks and delamination during the solvent removal. Since the early publication of Kaelin et al. who used ethylcellulose as binding material yielding 6.7% efficiency solar cells [52], several other groups followed his example. The used binders usually consist of similar macromolecular structures like polyvinyl-acetate [53], polymethyl-methacrylate [54] or polypropylene-carbonate [55]. However, similar to the initial publication of Kaelin et al., many of these approaches suffer from a significant residual layer of carbon in the final device. One reported possibility to reduce the amount of carbon is to introduce an additional air annealing step after the film deposition. The idea behind this step is to decompose the binder molecules by an oxidation to gaseous products. However, the air annealing can be critical as it also oxidizes the precursor metals as well as the molybdenum back contact. Thus, this step usually makes a subsequent heat treatment in hydrogen or H_2S/H_2Se necessary. An example for this approach is the publication of Lee et al. who used an ink containing a macromolecular binder mixture [56]. The effect on their device performance is rather unsatisfying leading to efficiency values of around 4.5%.

Other approaches tried to limit the carbon residues by substituting the binder macromolecules with compounds that have a lower molar mass like ethylene glycol [57] or propylene glycol [58]. With the latter the carbon layer could be significantly reduced yielding cells with an efficiency of 8% [58]. Furthermore, this publication comprises another important variation regarding the precursor salts away from metal chlorides to acetates. Many approaches use metal chlorides due to the good availability, the high purity and the comparatively low cost. However, the chloride ion is believed to catalyze increase the oxidation of the widely used alcohol solvents, further increasing the carbon residues [58]. Chloride ions could also be measured in the layer after the selenization [59] which assumingly can negatively influence the properties the absorber layer. Tanaka et al. proposed a chloride ion induced reduction of the hole concentration eventually leading to an n-type conductivity [60].

Metal-organic precursors

Beside the metal salts, organ metallic structures can be used as precursor materials [61], [62]. Wangen et al. reported the synthesis of air stable precursors made of copper oxide and indium hydroxide with butyldithiocarbamic acid which are highly soluble in several organic solvents [62]. Due to the exclusive use of low molecular carbon containing compounds, a good decomposition behavior has been expected. The resulting layer consists of ternary $CuInS_2$ nanocrystals and could be densified to larger grains by a subsequent selenization similar to the particle based approach reported by Guo et al. [42] (see section 1.3.2.1). With this method a maximum conversion efficiency of 10.1 % has been achieved. However, the necessary precursor synthesis and purification as well as the comparatively low solubility which requires up to seven consecutive coating steps are major disadvantages.

Hydrazine route

The third route of the solution based approaches is named after the used solvent, hydrazine. Hydrazine has several unique properties. Firstly, in contrast to all solvents presented so far, hydrazine contains only nitrogen and hydrogen. Secondly, the molecules are coordinating very weakly and are sufficiently volatile to be removed completely after the liquid film deposition. The third and probably most important advantage is the dissolubility of metal chalcogenides in hydrazine described as a dimensional reduction with additional chalcogens [63]. It is explained by the disruption of the metal chalcogenides frameswork by small cationic species. This property allows an inclusion of all elements in the same solution and therefore reduces the typical two step process with gas phase selenization to a simple annealing.

With this approach the highest reported efficiencies of all solution based approaches could be achieved reaching up to 15.2% [63]. Nevertheless, this method has several severe disadvantages. The solvent hydrazine is highly toxic and explosive and therefore requires extensive precautions for the liquid film deposition and solvent decomposition. Additionally, the dissolution of the metal chalcogenides is very slow taking up to several days. The final precursor concentrations in the inks are also rather low making 4-12 consecutive coating steps necessary [63], [64].

1.3.3 Liquid film deposition

All direct liquid coating approaches described in the literature review require at least one coating step to deposit a uniform liquid layer on the chosen substrate. Concerning the possible types of substrates, solid (e.g. glass) or flexible (e.g. aluminum or polymer foil) materials are applicable. Due to the strong connection between the layer homogeneity on the cell performance, this step can be critical for the solar cell processing. Therefore, this section presents a short overview on the most important coating techniques focusing on the differences and advantages of the specific methods regarding their application for a CIG(S) precursor layer deposition.

When choosing the right deposition method, several important criteria for the final precursor layers have to be fulfilled which can be translated into two macroscopic film properties. Firstly, the layer has to fully cover the substrate without dewetting. Secondly, a uniform film thickness has to be achieved avoiding aggregations of ink. Regarding these properties, liquid film deposited layers for CIGS solar cells share the same requirements as films for organic solar cell applications. In contrast to CIGS, however, research in this field has advanced greatly due to the cheaper source materials and the easy implementation of flexible low temperature substrate materials. Thus, for a general overview and current research topics on liquid film coating the reader is also referred to a publication by Krebs et al. [65]. Coming back to CIGS, the vast majority of reports on inks are limited to lab scale coating techniques also showing the low degree of maturity of these processes. The only exception so far has been reported by the company Nanosolar that went bankrupt in 2013.

Several lab scale coating processes are suitable for fulfilling the mentioned requirements and have been used to process CIGS as well as the similar CZTS solar cells [66]. Figure 4 shows schematic illustrations of four applicable methods which are briefly introduced below and evaluated in terms of their usability.

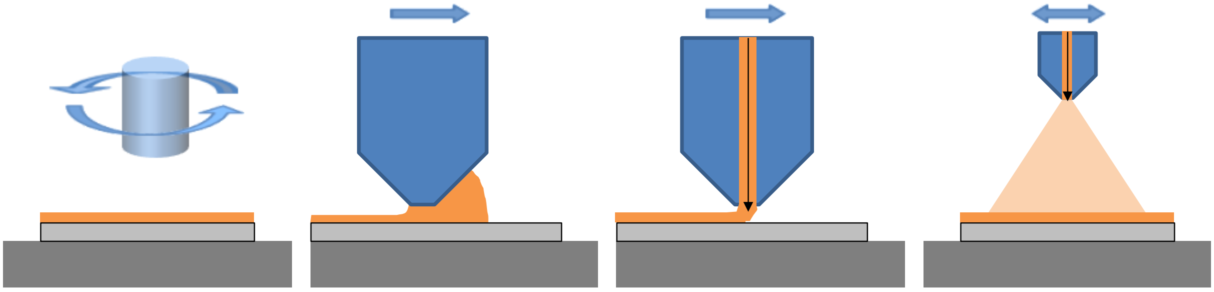

Figure 4: Schematic representations of four widely used coating techniques. From left to right: spin coating on a rotating table, blade coating, slot-die coating and spray coating.

The preferred coating process in the literature is spin coating (SPC). For this process the ink is casted on a symmetrical substrate placed in the center of a rotatable table. Due to the rotation a homogeneous and reproducible ink distribution on the surface can be achieved. However, the fast spin leads to a high material loss of up to 90% [67] resulting in the deposition of rather thin layers. For this reason, approaches using SPC usually have to carry out several consecutive coating steps to achieve the required film thickness. Other downsides are the required ink properties. SPC is dependent on inks with sufficiently high viscosities. A conclusive review on spin coating of polymer films with results that can mostly be transferred to CIG(S) inks can be found in the literature [68].

Blade coating (BLC) offers more process parameters to control the film thickness allowing a deposition of inks with a wider range of properties. For the film deposition the fluid is placed in front of the blade gap and is moved over the substrate. The material utilization of this process usually is very high reaching near unity [67]. Due to the exclusive use of this method in this thesis, a detailed evaluation of BLC can be found in section 3.1.1.

Slot die coating (SDC) is an extended version of BLC. In contrast to the latter, the liquid is applied on the surface through a precise slot with a defined volume flow. Thus, by moving the device over the surface, a liquid film is deposited with a constant film height only dependent on the applied volume flow of liquid and the coating speed which is why SDC is widely used in the industry to deposit high quality layers. Due to the comparably complex device design and the high volume of unused ink inside of the device, the applications for this method on a lab scale are limited.

Spray coating (SC) describes a method where the ink is pressed through a nozzle to nebulizer it to small droplets. In some cases a carrier gas or an electric field is applied to enhance the deposition. The advantages of SC lie in the possible coverage of rough surfaces or even non-planar substrates [69], [70]. However, the formation of flat layers can be challenging with this method [71]. SC can also be applied on heated surfaces with temperatures between 100 and 500°C to facilitate the formation of certain phases. In this case the process is called spray pyrolysis [72].

Guideline to the results

In the introductory part the most important non-vacuum based deposition methods for CIGS layers have been introduced. The solution based approach has been further investigated in this thesis leading to the development of a new process based on preliminary findings of Dr. Markus Widenmeyer. The results have been published in three papers [73]–[75].

In order to achieve the goal of producing working devices, a broad field of subjects had to be investigated leading to results in several interdisciplinary topics. To simplify the reading and to systematically cover all areas that are necessary to understand this process, the content has been divided into the five typical steps which are presented in this thesis in their process order. Figure 5 shows a schematic overview.

Chapter 2 covers the precursor choice and synthesis methodology followed by the ink formulation. Chapter 3 begins with a description of the applied liquid film deposition method. Subsequently, the formation of metallic layers is explained beginning with the solvent evaporation and metal ion reduction. A further section dealing with the densification of the metallic nanoparticles is included. Chapter 4 focuses on the selenization step necessary to transform the metal layer into a chalcopyrite semiconductor. The last chapter number 5 comprises the layer and cell characterizations as well as an investigation on the influence of sodium salts dissolved in the ink.

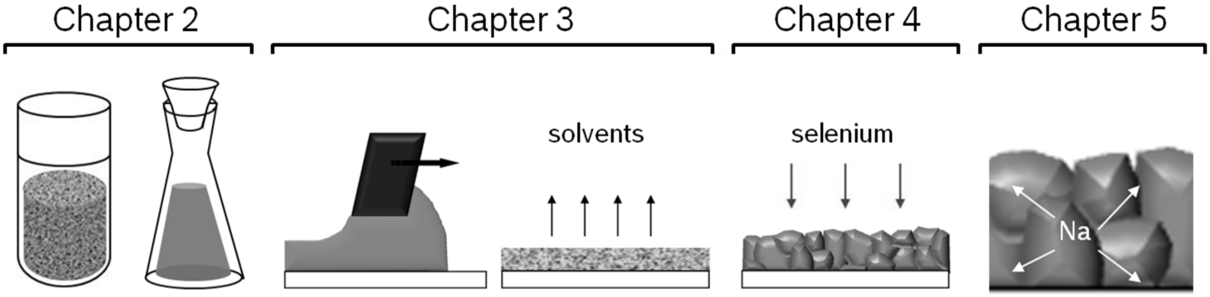

Figure 5: A schematic representation of the thesis structure based on the five process steps for the chemical processing of CIGS layers. Chapter 2: precursor synthesis and ink formulation. Chapter 3: liquid film deposition, solvent drying and metal film formation. Chapter 4: selenization. Chapter 5: absorber as well as device characterization and the effect of different sodium sources.

Chapter 2

From the metal salt to the ink

This chapter begins with an introduction justifying the chosen materials for this particular process. Following this, the synthesis for the selected metal salts is described. In this context, several possible base materials are introduced and their applicability is evaluated. The synthesized precursor salts are further characterized with a focus on their stability regarding degradation in air. Thereafter, the solvents are introduced as well as the ink formulation procedure.

2.1 Material choice

In solution based approaches the used compounds as well as the associated chemistry have a great influence on the properties of the intermediate layer and therefore determine the quality of the final absorber. Inappropriate material choices in this very first step can make the processing of efficient cells impossible as has been shown in the literature review in section 1.3.2.2. Thus, two types of approaches have been evaluated in detail and have been modified in order to develop this process. The first examples are the metal salt based approaches usually applying metal chlorides or nitrates dissolved with a binder material in an alcohol. After the solvent evaporation the salts precipitate in an organic binder matrix. Taken from these approaches is the use of cheap materials that are available in large scales. The main difference here is the idea to achieve a direct conversion of the metal ions to the respective metals. In this context an important requirement was to accomplish this without an energy-intensive additional reduction step (e.g. in hydrogen).

Thus, a chemical system has been searched containing a strong reducing agent. Previous experiments of Dr. Markus Widenmeyer and new findings during the development of this process identified formate salts as a suitable material fulfilling the requirements. It could also be shown that the salt anions decompose cleanly. The second type of processes used as antetype are the hydrazine approaches [76]. In their case a nitrogen-rich solvent is used that doesn't contain any carbon or oxygen atoms and which decomposes cleanly during the layer formation. Thus, when choosing the solvents and additives for this process, a focus was set on compounds with an expected clean evaporation and/or decomposition. In order to minimize the chances for the formation of a carbon layer, nitrogen rich compounds with isolated carbon atoms have been preferred. These nitrogen rich compounds are also often advantageous regarding their complex formation properties with metal salts allowing the formulation of concentrated inks. Contrary to the hydrazine approach, only non explosive materials have been considered which are either commercially available as well as cheap or can be easily synthesized. The last point is particularly important to keep the price advantage over the vacuum based processes.

2.2 Synthesis of metal formates

Due to the poor availability of metal formate salts at common chemical suppliers (only copper formate has commercial distributors with purities below 97%) the precursors used in this work had to be synthesized in a first step from other sources. As base material several different metal salts have been evaluated and the identified possibilities are presented in the first part of this section. The focus has been set on the commercial availability and applicability for a synthesis. The second part gives an introduction in the chosen synthesis routine applied in this thesis.

2.2.1 Base materials for the formate synthesis

When choosing the right base material for the formate synthesis several requirements had to be fulfilled. Firstly, the anion of the starting material either had to decompose completely or had to take part in an ion exchange reaction with formic acid. Secondly, a high initial purity was considered as important due to the fact that the precursor salts can be a source of unwanted metal impurities incorporated into the final solar cell. Pianezzi et al. have shown that several metal contaminations can have detrimental effects on the device performance [77]. The third requirement was again a reasonable price to keep the competitive advantages of the process compared to the standard vacuum techniques. Considering these limitations a variety of possible metal salts have been evaluated including acetates, alkoxides, amines, carbonates and nitrates. In the following section the properties of the mentioned metal salts are briefly discussed and their use as precursor salt is reviewed.

Metal acetates

Acetates are the salts of the acetic acid and are commercially available for copper and indium. Because the acetates are slightly less acidic than the formates an ion exchange of the anion in solution can be expected. However, the purification of the product mixture makes this synthesis complicated. In order to separate the metal formates the forming acetic acid has to be removed which can be problematic due to the similar boiling points of both acids. Experiments with indium acetate yielded mostly the pristine acetates.

Metal alkoxides

Metal alkoxides are a very convenient source to synthesize formates. The alkoxides are highly alkaline and readily take the associated base proton from the formic acid forming an alcohol. Due to the low boiling points of these alcohols a subsequent separation from the product salt by evaporation can be easily achieved. Regarding their availability, methoxides are only available for copper while ethoxides can be bought from all three metals. On the downside, alcoxides are rather expensive as well as water sensitive. Exposed to water containing air, the metal alkoxides readily hydrolyze.

Metal amides

An example for an amide is the commercially available but rather expensive Tris-(dimethylamido)-gallium. Dissolved in formic acid, solid dimethyl-ammonium-formate is forming with gallium formate as byproduct. Due to the resulting solid salt mixture a subsequent separation is necessary making this route complex and therefore uninteresting.

Metal carbonates

Carbonates are only available for copper as a base material in large quantities with a moderate purity and high amounts of trace elements. However, due to their basicity, carbonates are nevertheless very interesting. Mixed with formic acid the basic carbonate anion undergoes an acid-base reaction. The resulting carbonic acid is unstable and decomposes cleanly to gaseous CO_2 and H_2O. The water catalytically increases the reaction speed.

$$CO_3^{2-} + 2HCOOH \rightleftharpoons H_2CO_3 + 2HCOO^- \rightarrow 2HCOO^- + CO_2\uparrow + H_2O \qquad 2\text{-}1$$

The decomposition leads to a constant loss of carbonic acid and therefore shifts the acid-base reaction to the right. The resulting metal formates are therefore expected to be highly pure as has also been reported by Rosendband et al. [78]. They converted the carbonates by mixing them with formic acid followed by a stirring step at 80°C for 30 min. However, the absence of commercially available In- and Ga-carbonates is a considerable disadvantage of this route for the processing of the necessary salt mixtures.

Metal nitrates

In contrast to the carbonates, metal nitrates are available from copper, indium and gallium in purities as high as 99.999%. Additionally, the nitrates can also easily be prepared from the base metals and nitric acid. Thus, independently of the chemical suppliers, the expected price range of metal nitrates should be close to the pure metals.

Regarding the formate synthesis metal nitrates behave similar to carbonates in the presence of formic acid. Mixed with the acid they are decomposing to oxygen and water as well as nitrous fumes ranging from N_2 to N_2O_5 including NO, NO_2, N_2O and N_2O_4 [79]. Which compound actually forms depends among others on the salt, the temperature and the conditions.

From the presented options metal nitrates have been chosen due to the available purities, the price ranges as well as the easy formate synthesis and product purification routine. Thus, the reactions leading to the formate salts are discussed in detail in section 2.2.2.2.

2.2.2 Formate synthesis with metal nitrates

This section begins with an investigation of the metal nitrate composition with a focus on the amount of water of crystallization. Thereafter, the reaction paths are discussed and the applied synthesis procedure is explained.

2.2.2.1 Nitrate salt composition

To process CIGS solar cells the metal ratios have to be very precise in the range of Cu:In:Ga = 0.9:0.8:0.2. Thus, the exact composition of the available metal nitrates has to be determined in a very first step. Apart from the documented purity and the known quantity of trace elements, the amount of water of crystallization had to be measured regularly to assert the metal fraction. This can be achieved in several ways. The easiest possibility and mostly used in this thesis is to take a sample of the pristine nitrates with a known weight and decompose it in air at elevated temperatures. As product the respective most stable oxides are formed. It is important to note that the presence of hydroxides has to be excluded which requires sufficiently high temperature and heating times. The metal fraction in the resulting oxides is known and can be used to calculate the initial metal fraction in the nitrates. From this information the amount of water of crystallization can be determined. In order to confirm these measurements, a second method has been carried out. Copper nitrate, the salt with the most noble metal in the mixture, has been reduced to the pure metallic phase by a heat treatment at 500°C in a hydrogen containing environment (forming gas, 5%H_2, 95%N_2). This allows a direct measurement of the metal fraction.

Regarding the available metal nitrates, copper nitrate can be bought as trihydrate as well as x-hydrate with an unknown composition. Both salts have been used in this thesis and therefore the amount of water had to be estimated individually. Indium and gallium nitrate are only available as x-hydrate. An overview of the measured metal fractions in the respective nitrate salt and the calculated molar ratios of water are listed in Table 1.

Table 1: Metal fractions and the corresponding amount of water in the metal nitrates determined by oxidation in air (all metal salts) and by reduction in hydrogen (copper only).

Metal nitrate	Oxidation in air		Reduction in hydrogen	
	Metal fraction in % (calc.)	Molar amount of water (calc.)	Metal fraction in % (calc.)	Molar amount of water (calc.)
Cu nitrate trihydrate	25.8 (26.3)	3.3 (3)	25.6 (26.3)	3.3 (3)
Cu nitrate x-hydrate	23.6	4.5	23.5	4.5
In nitrate x-hydrate	29.1	5.1	-	-
Ga nitrate x-hydrate	16.1	10.0	-	-

As can be seen in Table 1, the amount of water in the copper nitrate trihydrate corresponds to the expected value of three water molecules per copper ion. The difference can be explained by uncertainties in the measurement. Compared to this the measured water in the copper nitrate x-hydrate is significantly higher. Experiments have also shown that in this compound the water fraction is dependent on the storage conditions. Days with high humidity eventually lead to the formation of copper nitrate hexahydrate which can be easily identified by its low melting point of 26.4°C (trihydrate: 114.5°C). Thus, a regular control of the composition is necessary. In contrast to copper nitrate, In and Ga nitrate both showed constant values of hydration water of 5 and 10, respectively.

2.2.2.2 Synthesis

For the synthesis an excess of formic acid has been added to the mixed metal nitrates and the suspension was stirred on a hotplate for several minutes at low temperatures. Under these conditions formic acid reduces the nitrate anions to gaseous products and the excess of formate ions leads to an ion exchange. The possible reaction paths are stated below:

$$\mathrm{HCOOH} + \mathrm{NO_3^-} \rightleftharpoons \mathrm{HCOO^-} + \mathrm{HNO_3} \tag*{2-2}$$

$$\mathrm{HCOOH} + 2\mathrm{HNO_3} \rightarrow 2\mathrm{H_2O} + 2\mathrm{NO_2}\uparrow + \mathrm{CO_2}\uparrow \tag*{2-3}$$

$$\mathrm{HCOOH} + \mathrm{NO_2} \rightarrow \mathrm{H_2O} + \mathrm{NO}\uparrow + \mathrm{CO_2}\uparrow \tag*{2-4}$$

$$4\mathrm{HCOOH} + 2\mathrm{NO_3^-} \rightarrow 2\mathrm{HCOO^-} + 3\mathrm{H_2O} + \mathrm{NO}\uparrow + \mathrm{NO_2}\uparrow + 2\mathrm{CO_2}\uparrow \tag*{2-5}$$

When mixed the formic acid and the nitrate ion first undergo an acid-base reaction with a proton transfer to the nitrate ion (2-2). It is important to note that the low basicity of nitric acid shifts the equilibrium of this reaction to the far left. However, the formed nitric acid gets further reduced by the excess formic acid to gaseous NO_2 (2-3) and in a second step to NO (2-4). The loss of these gaseous products is the reason why reaction (2-2) is shifted to the right. Simultaneously, the highly exothermic reactions quickly increase the temperature of the mixture. Both effects lead to a fast conversion. The gaseous products contain the mentioned nitrous fumes including NO_2 that can be clearly identified by its brown color. Thus, it is advisable to carry out this synthesis in a fume hood. For the three metal nitrates used in this thesis the overall reactions are shown below.

$$\mathrm{Cu(NO_3)_2 \cdot xH_2O} + 4\mathrm{HCOOH} \rightarrow \mathrm{Cu(HCOO)_2} + \mathrm{NO}\uparrow + \mathrm{NO_2}\uparrow + 2\mathrm{CO_2}\uparrow + \mathrm{(x+3)H_2O} \tag*{2-6}$$

$$2\mathrm{In(NO_3)_3 \cdot xH_2O} + 12\mathrm{HCOOH} \rightarrow 2\mathrm{In(HCOO)_3} + 3\mathrm{NO}\uparrow + 3\mathrm{NO_2}\uparrow + 6\mathrm{CO_2}\uparrow + \mathrm{(x+9)H_2O} \tag*{2-7}$$

$$2\mathrm{Ga(NO_3)_3 \cdot xH_2O} + 12\mathrm{HCOOH} \rightarrow 2\mathrm{Ga(HCOO)_3} + 3\mathrm{NO}\uparrow + 3\mathrm{NO_2}\uparrow + 6\mathrm{CO_2}\uparrow + \mathrm{(x+9)H_2O} \tag*{2-8}$$

The resulting formates have a poor solubility in the excess formic acid. To separate the residual formic acid and the residual water from the metal formates, the liquids have to be evaporated which can be carried out on a hotplate in air. Due to the relatively high boiling point of formic acid (101°C), a complete evaporation in reasonable times requires elevated temperatures. To exclude any unintentional formate decomposition during this drying step and reduce the evaporation time, the separation of the salt and the acid can also be achieved in a rotary evaporator. By slowly decreasing the pressure to 1 mbar, the temperature can be limited below 70°C leading to a reproducible and high purification.

2.2.3 Characterization and stability issues of metal formates

Controlling the synthesis regarding product quality and composition of the precursor salts plays a key role in terms of reproducibility. Therefore, a characterization of the precursor salts and an evaluation of the storage stability have been carried out. In the first part of this section, the newly synthesized metal formates are analyzed in terms of composition and purity. In the second part the influence of a storage in air on the salt properties are examined by X-ray diffraction and infra red spectroscopy.

With the determined metal fractions in the metal nitrates (see section 2.2.2) and the remaining weight of the metal formates after the synthesis, the final metal fraction in the product salts can be calculated. Table 2 shows the resulting values revealing a total metal fraction in the CIG mixture of 40.5%. The results are close to the expected values derived from mass balance considerations.

Table 2: Calculated and expected metal fractions of the purified formates salts as well as a CIG formate salt mixture with a composition of Cu:In:Ga = 0.9:0.8:0.2

Metal formate	Calculated metal fraction from experimental results in mass-%	Expected metal fraction in mass-%
Copper formate	41.0	41.4
Indium formate	44.8	45.9
Gallium Formate	28.8	28,8*
CIG mixture	40.5	40.4

*calculated with $Ga(HCOO)_3(CO_2)_{0.75}(H_2O)_{0.25}$

The metal formates synthesized in this thesis are crystalline powders. Thus, X-ray diffraction analyses can be used to identify the crystalline phases. Figure 6 shows the XRD pattern of the individual salts. Copper formate is known to crystallize in several modifications [80]. The applied synthesis routine yielded two modifications that could be easily distinguished by their color ranging from light to dark blue. Two different copper samples have been analyzed by XRD that could be identified as almost pure orthorhombic ($Cu(HCOO)_2$, JCPDS #00-032-0332) and monoclinic modifications ($Cu(HCOO)_2$, JCPDS #00-032-0331). The orthorhombic sample revealed small additional peaks that could not be assigned to any phase (e.g. at 37.3°). Indium formate shows the expected hexagonal structure ($In(HCOO)_3$, JCPDS #01-077-4470) and the pattern of gallium formate could be assigned to a cubic unit cell containing carbon dioxide and water ($Ga(HCOO)_3(CO_2)_{0.75}(H_2O)_{0.25}$, JCPDS #01-076-4359). Tian et al. explained the unusual presence of CO_2 in the crystal by caged molecules which are hydrogen bonded to the formic acid [81]. Additional crystalline phases have not been found.

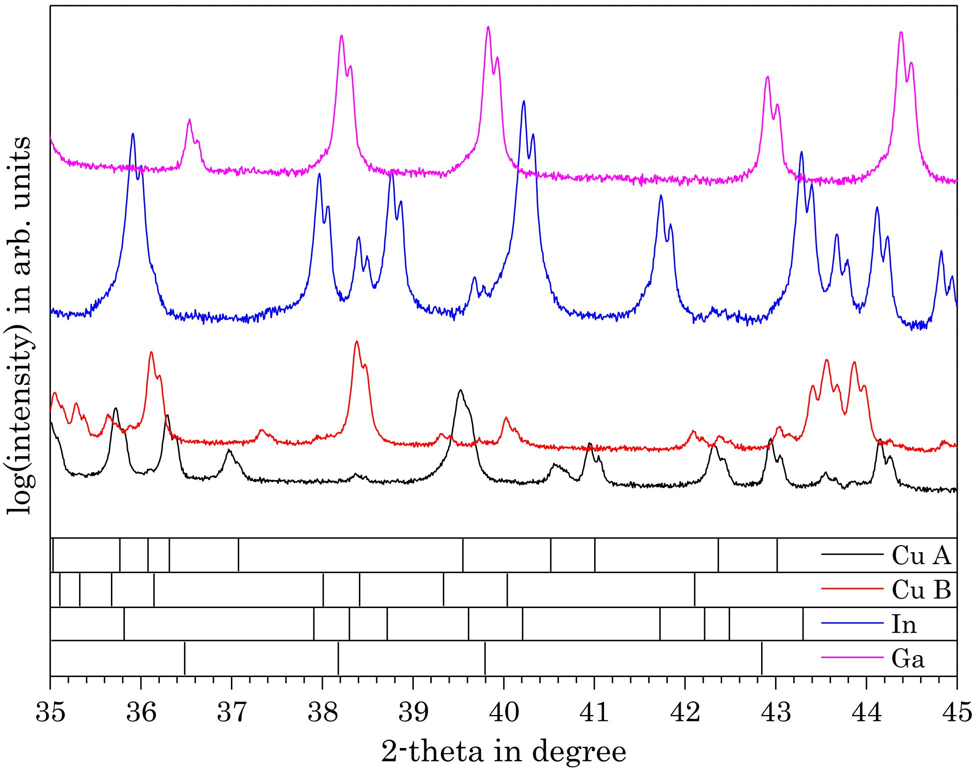

Figure 6: X-ray diffraction pattern of the three metal formates. Copper formate has been synthesized in two modifications, monoclinic (Cu A) and orthorhombic (Cu B). The lower part of the figure indicates reference data.

Regarding the salt stability, a decreasing solubility mainly of indium and gallium formate in the used solvents has been observed after storage in air. In order to investigate the degradation behavior all metal formates have been analyzed after one and three weeks air exposure compared to storage in nitrogen. The samples have been evaluated by XRD and Fourier transformed infrared spectroscopy (FTIR). Beginning with the former, Figure 7 shows the XRD pattern of the three metals with a focus on a small 2-theta area containing at least two peaks. In the case of copper formate only the monoclinic modification has been evaluated. Yet, the resulting XRD patterns reveal a partial phase transition to the orthorhombic modification after 3 weeks in air. The diffraction peaks of indium formate show a slightly decreased height after one week of air exposure which most likely is in the fault range of the measurement.

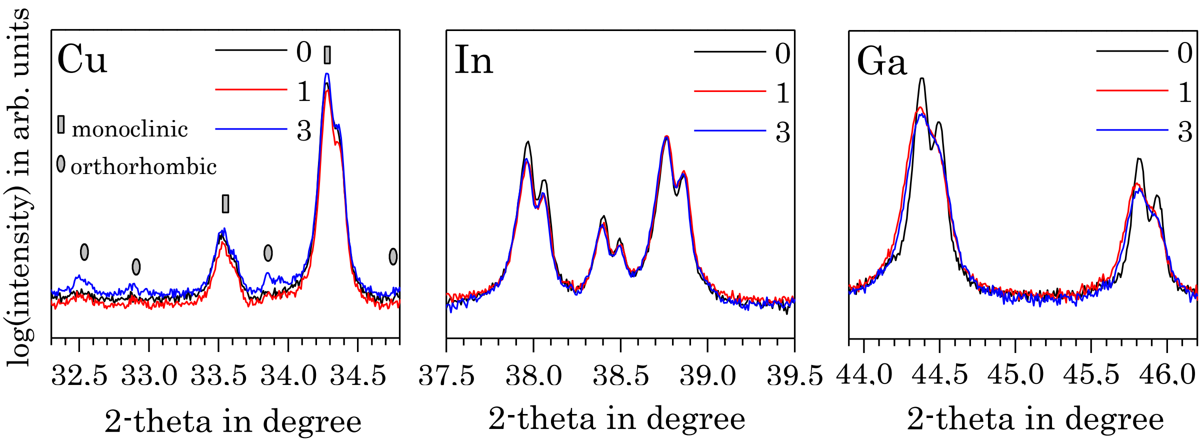

Figure 7: XRD pattern of copper, indium and gallium formate salts stored in nitrogen and exposed to air for 0, 1 and 3 weeks. The measurements have been carried out with the same machine setup.

Regarding gallium formate the changes in the XRD pattern can't be neglected. In this sample the proposed salt degradation leads a significant drop in signal intensity and a superposition of the two neighboring $K_{\alpha 1}$ and $K_{\alpha 2}$ peaks of the Cu X-ray source to a single maximum. In order to gain more information about the degradation mechanism, FTIR analyses have been carried out which can be seen in Figure 8. The overview graphs on the left show that the IR absorption of all samples occurs mostly between 2000 and 500 cm^{-1}. In this range are most of the absorption bands of the expected carboxylate ion with the exception of the C-H stretches weakly absorbing the infrared light around 2940 cm^{-1}. The detailed graphs on the right show that the formate anion can be observed in all three samples with the C=O and the C-O stretching vibrations clearly visible between 1550 and 1600 cm^{-1} and around 1350 cm^{-1}, respectively [82]. The related O-C=O bending of the carboxylate ions are visible in the range of 800 cm^{-1} [83]. A similar IR study has already been executed on copper formate yielding comparable results [84].

The analyzed monoclinic copper formate salt shows two additional peaks around 1730 cm^{-1} and 1330 cm^{-1} which could only be assigned to an ester group. Methyl formate for example absorbs IR radiation in these regions [85]. The discrepancy about the unknown origin of the methyl group is discussed later. In the case of copper formate the exposure to air does not change the pattern. Indium formate does not show any ester peaks in the sample stored exclusively in nitrogen and also not within one week of air exposure. After 3 weeks in air, however, the mentioned ester peaks are visible as well. Another small peak around 1650 cm^{-1} could not be identified.

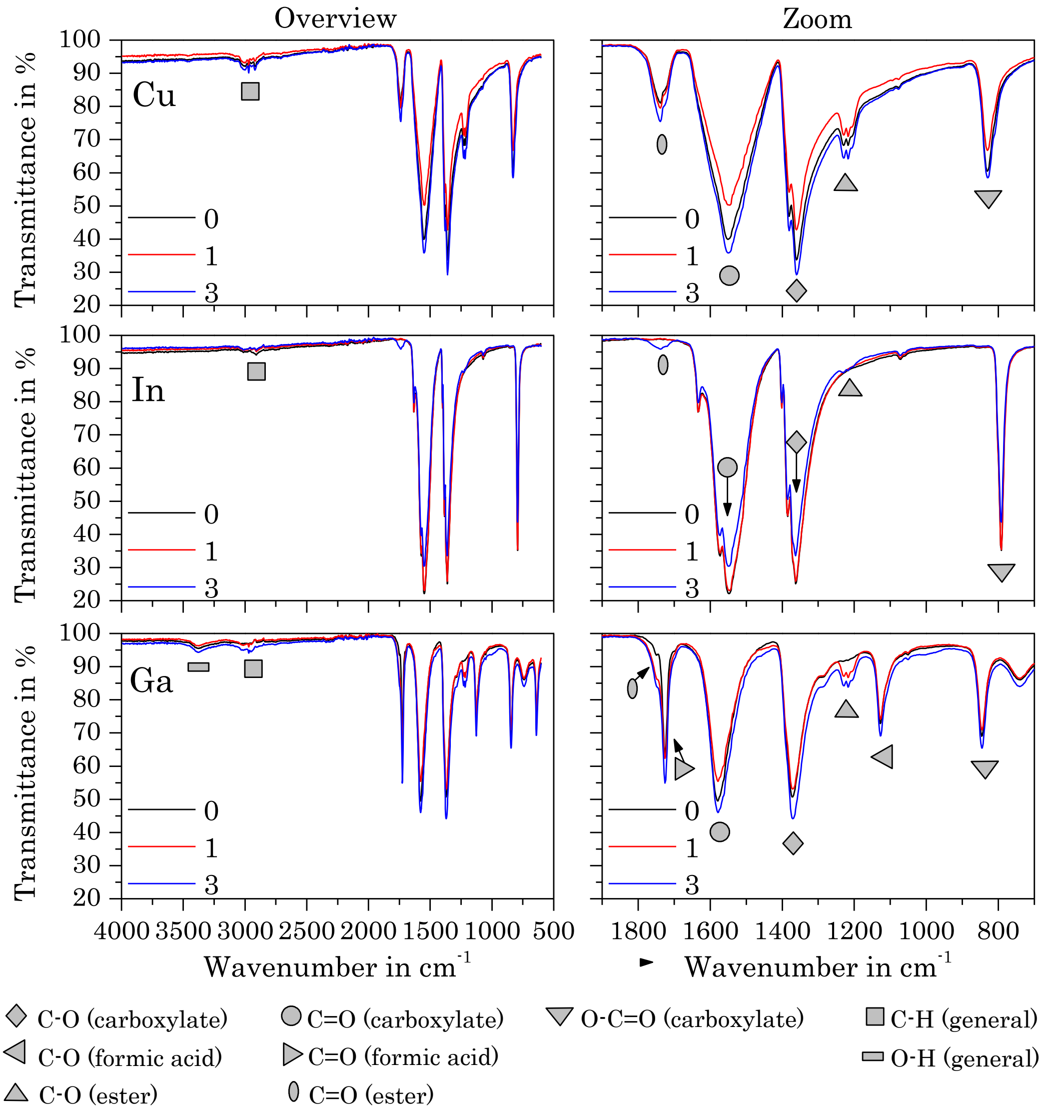

Figure 8: Fourier transformed infrared spectroscopy on metal formates stored in air for one and three weeks compared to a storage in nitrogen.

The IR results of gallium formate are different to the mentioned copper and indium salts showing several additional absorption bands. Around 3350 cm^{-1} a small peak can be observed indicating the presence of an O-H group which would be in agreement with the crystal structure measured by XRD that suggested incorporated water of crystallization [81]. However, the strong peaks around 1120 and 1730 cm^{-1} can be attributed to residual formic acid, most likely remaining from the synthesis routine due to an incomplete evaporation. The C-O and C=O vibrations of the acid molecule absorb the radiation in this region, respectively [86]. Thus, the -OH absorption around 3350 cm^{-1} could also be explained by the formic acid. The missing peak around 740 could not be assigned to any group. Similar to indium formate, gallium formate stored exclusively in nitrogen does not contain any measureable ester groups. Yet, the air exposure leads to the typical ester absorption bands already after one week.

The formation of the observed esters would require the presence of a molecule with a methyl group like an alcohol. Due to the absence of suchlike compounds during the synthesis one might speculate about a disproportionation reaction of formic acid or the formate ion to methanol. This reaction has been observed on formic acid for example in the presence of a catalyst [87], [88]. Due to the fact that the ester peaks don't occur in an inert atmosphere water or oxygen in the air might be necessary for the reaction. This is of course highly speculative. Yet, the formation of insoluble precipitates after the storage in air emphasizes the instability of the synthesized metal formate salts.

In summary, the characterization experiments reveal that copper formate does not show any air storage dependent changes in the XRD and IR results. The IR analysis of indium formate indicates the formation of a possible ester groups under air exposure. In gallium formate the same ester peaks can be observed with a significantly higher intensity and therefore quantity. Correspondingly, the measured XRD pattern shows broadened peaks indicating a decreased crystal coherence length. In combination with the experimental observation of a deteriorated solubility of the salts after air exposure these results clearly emphasize the necessity to keep the precursor salts under inert atmosphere.

2.3 Solvent characterization and ink processing

In this section the two liquids used in the presented process are characterized. Both are critical components and have been chosen with regard to their physical and chemical properties including the high temperature behavior, boiling point and viscosity. In the first section, the solvent is presented followed by the diluting agent. Finally, the ink formulation procedure is explained.

2.3.1 The solvent

1,1,3,3-tetramethylguanidine (TMG) has been chosen as solvent for this process. Guanidines have the basic structure $[(R_2N)_2C{=}NR]$ with a center consisting of a trigonal CN_3 unit. The sp_2 hybridization of this central carbon atom leads to a planar core [89]. In TMG four methyl groups are attached to the tertiary amine groups. The double bonded imine nitrogen is connected to a hydrogen atom (Figure 9).

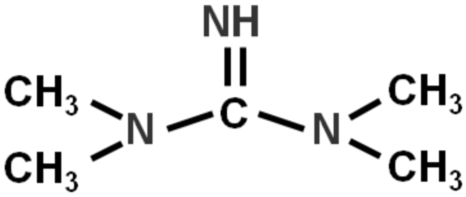

Figure 9: Chemical structure of 1,1,3,3-tetramethylguanidine.

Unlike similar nitrogen containing compounds such as urea or amidines/amides, the coordination chemistry of guanidines is limited to non-aqueous solutions. In water guanidines readily form the guanidinium cation due to their high basicity (pK_b=0.4). The reason for the high basicity can be explained by a mesomeric delocalization of the positive charge. The guanidinium cation itself is a bad complexation ion. This can be explained by the lowered energy of the π-system due to the missing lone electron pair [89]. Thus, to achieve soluble metal salt complexes the ink has to be water free.

The physical properties of the solvent are also important for the process. Density, vapor pressure and viscosity are examples that have an influence on the process results during the coating and drying steps. However, there are only a few publications on the pure compound [90]–[92] and the physical properties found for TMG are listed in the appendix B. The reported values for the vapor pressure show large deviations. Anderson et al. [91] noted a significant difference between their measurements and the values published by the American Cyanamid Company which can be found in most data sheets (e.g. [92]). For this reason, the vapor pressure values used in this thesis have been calculated from the heat of vaporization taken from [90] and the Clausius-Clapeyron relation.

In water free environments TMG readily dissolves the metal formates. Inks with metal concentrations of more than 15 mass-% could be produced. However, the viscosity significantly increases with the amount of salt. In order to investigate the qualitative influence of the dissolved salts on the viscosity, rheometric measurements on inks have been carried out under nitrogen. Yet, the solutions have been shown to be highly sensitive to oxygen and/or water in the air during the sample preparation, instantly leading to precipitates. An explanation could be the mentioned formation of the guanidinium cation with water resulting in the insoluble precipitates. Therefore the viscosity of the ink could not be measured accurately.

2.3.2 The diluting agent

Sufficiently concentrated solutions of metal formates dissolved in tetramethylguanidine are highly viscous. Yet, all coating processes have a specific viscosity range for inks to be processed which mostly is significantly lower [93]. Thus, an additional diluting agent is necessary to adjust the ink properties. Besides the mentioned viscosity requirements the surface tension is an important factor influencing the quality and homogeneity of the liquid film and the dried precursor layer. Regarding the chemical properties, the liquid also must not be oxidizing and have good solubility properties. While adjusting the viscosity is necessary for the coating method, changes in the surface tension can be disadvantageous for the drying step. Significant differences in this parameter between the used solvents can lead to the Marangoni effect which will be discussed in section 3.2.1. In order to minimize this effect, one option is to quickly evaporate the diluting agent. This can be achieved by choosing a compound with a high vapor pressure and correspondingly low boiling point. Table 3 lists the physical properties of suitable organic solvents.

The shown alcohols cover a large area of vapor pressure and viscosity. High values in the latter require larger solvent volumes to reduce the overall viscosity of the ink. Thus, the metal concentration decreases making the smaller alcohols more interesting. For this reason methanol has been chosen in this thesis, however, experiments have shown that n-propanol is also suitable for the processing of solar cell. From a production point of view, the non toxic ethanol might be a suitable compromise.

Table 3: Physical properties of selected organic solvents.

Compound		Boiling point at 1 atm in °C	Vapor pressure at 20°C in Pa	Viscosity at 20°C in mPas
Solvent	TMG	161	131 (calc.)	1.4 [91] 2 [92]
Diluting agent	Methanol	64.7	12900	0.6
	Ethanol	78.4	5800	1.1
	i-Propanol	82.6	4300	2.0
	n-Propanol	97	1990	1.9

2.3.3 Ink formulation

This section briefly explains the ink formulation. The prepared metal formate salt mixture (for the synthesis see section 2.2.2) with metal ratios of Cu/(In+Ga)=0.9 and Ga/(Ga+In)=0.2-0.25 is filled in a small vial with a stirring bar. The solvent TMG is added with a metal salt:solvent mass-ratio of 1:1.2. Subsequently the mixture is placed on a hot plate at 100°C and stirred for a few minutes. The salts slowly dissolve leading to a dark almost black solution. Longer stirring leads to a reduction of the Cu(II) ions to Cu(I) which can be easily observed by a color change of the ink from black over green to colorless (see also section 3.3.2). The reduction can be inhibited by adding the diluting agent methanol with a metal salt:methanol mass-ratio of 1:1.5-1.6. The ink color change from green to blue indicates a complexation of the Cu(II) ions with methanol. If additional sodium salts are required which are introduced in Chapter 5, premixed solutions consisting of methanol and the preferred sodium salt with a known composition are added. The amount of methanol in this solution substitutes the same amount of pure methanol. Finally, the additive 4-amino-1,2,4-triazole (4ATA) is added with a metal salt:4ATA mass-ratio of about 1:0.03. The function of this additive is discussed in detail in Chapter 3.

2.4 Summary of chapter 2

Chapter 2 evaluates the individual compounds that have been chosen for the described ink system. Copper, indium and gallium formate salts as metal source are used due to the high reduction potential of the formate anion and its clean decomposition behavior. The strong base tetramethylguanidine has been selected as solvent for its good complexation properties and its chemical structure consisting of individual carbon atoms separated by nitrogen atoms. This property is expected to inhibit the formation of carbon residues during the solvent decomposition. Methanol is added to the ink to decrease the viscosity and the surface tension of the solution which is necessary for the deposition of homogeneous liquid films.

The used metal formate salts have to be synthesized due to their poor availability at commercial suppliers. Thus, several source materials are evaluated regarding price, applicability and product purity. Metal nitrates are chosen due to the simple synthesis and purification. The thereby produced metal nitrates are characterized in terms of phase composition and air stability. XRD and IR analysis after air exposure revealed a degradation which is in agreement with the observed decreasing solubility.

Chapter 3

From the ink to a metallic layer

In this chapter, the individual steps necessary to produce a thin layer consisting of metallic Cu, In and Ga containing nanoparticles are presented. Beginning with the prepared ink, section 3.1 investigates the deposition of continuous and homogeneous liquid films on the preferred substrate. From these films the organic solvents have to be evaporated carefully in a subsequent drying step which is the topic of section 3.2. Due to the presence of a multi-component ink system consisting of the alcohol methanol and the strong base TMG, one focus is set on the changing fluid properties of the film during the consecutive solvent evaporation and their impact on the film homogeneity. The redox reactions of the formate salts occurring at elevated temperatures which transfer the dissolved metal ions to metallic nanoparticles are investigated in section 3.3 and 3.4. In section 3.5 an additive is introduced which is necessary to achieve a sufficiently dense and homogeneous precursor layer quality.

3.1 Deposition of uniform liquid films

In order to deposit homogeneous and flat liquid films on the substrate a suitable coating method is necessary. In the introduction, several lab scale coating techniques have been introduced and evaluated regarding their applicability. As a result blade coating has been selected as method of choice for this process for several reasons. The most important advantages are summarized below in random order.

- easy and fast liquid film deposition
- almost unlimited choice of substrate geometries
- high material utilization
- application of inks with a wide range of properties
- easy film thickness tailoring by adjusting the coating parameters

On a lab scale, however, blade coating also has two major disadvantages. Firstly, the film thickness is a function of the length meaning that for long substrate geometries a thickness gradient can develop. Secondly, predicting the final film thickness without a calibration based on empirical results is very complex and may require very elaborate computations. Both issues are briefly discussed in the next section. Regarding the latter a possible way to adjust the film height is addressed in an empirical study on the influence of the coating velocity.

3.1.1 Theory of blade coating

Blade coating is a self metered coating technique, meaning that the resulting film height cannot be preset and is dependent solely on the process parameters. The process parameters include the geometrical properties of the blade as well as the ink volume and device parameters like coating speed and base plate temperature. Apart from these, the fluid properties play a large role, especially the temperature dependent viscosity and surface tension of the processed ink. Due to the variety of parameters it is obvious that a prediction of the resulting layer properties, most importantly a calculation of the resulting film height, can get very complex [94], [95]. Therefore this section is intended to give a short overview on the most important parameter dependencies with a special focus on the reproducibility. For a detailed review of the blade coating process, the reader is referred to the literature [96], [97].

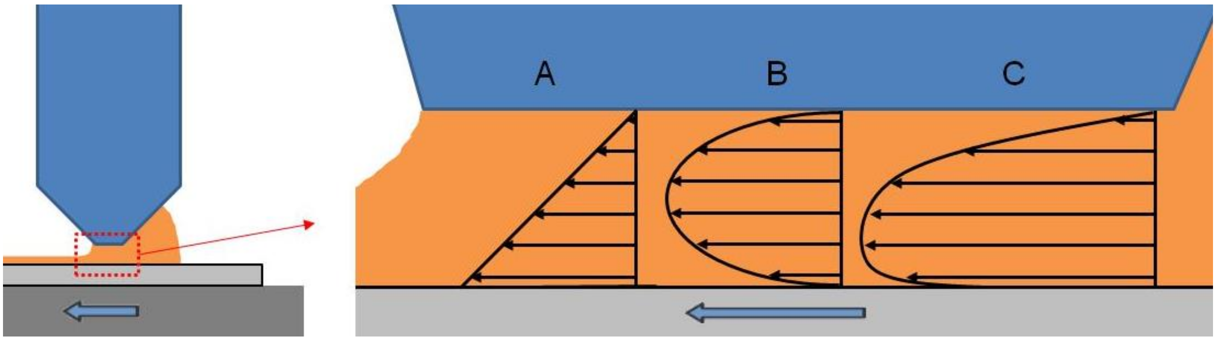

Figure 10: Schematic representation of the possible flow profiles in the blade gap in a static coordinate system around the blade. A: couette flow; B: channel flow; C: superposition of A and B.

An analytical investigation of the flow pattern in the blade gap reveals for laminar conditions a superposition of two flow profiles which are schematically shown in Figure 10 [98]. The volumetric flow of ink at the exit of the blade gap determines the amount of liquid deposited on the surface and is directly dependent on the velocity distribution in the blade gap. Profile A belongs to a shear-driven couette flow and has a simple triangular shape which is mostly dependent on the coating speed. The second profile B is more complex and represents a pressure-driven channel flow. Beside the pressure gradient which is a function of the amount of excess liquid in front of the blade and the coating speed, the velocity distribution in this profile is also dependent on the fluid parameters like the viscosity and the the surface tension of the ink. The share of each profile depends on the chosen process parameters and influences the thickness of the final layer. The effects of two selected parameters are discussed in the next section.

3.1.2 Influence of the blade coating parameters

In the previous section the two prevailing flow profiles in the blade gap have been introduced. In this section the influence of two parameters, the ink volume and the coating speed are discussed regarding their impact on the flow profiles and consequently the film thickness.

Ink volume

Beginning with the ink volume the presented lab scale coating process has been optimized to minimize the waste. Therefore, the total amount of ink in front of the blade has been adjusted to be sufficient for a full surface coverage without leaving high amounts of residues on the coating device. The thereby used low ink volumes result in a decreasing liquid reservoir in front of the blade during the film deposition leading to a proportionally decreasing pressure gradient in the blade gap. This issue has a significant impact on the shape of the developing flow profile. As has been discussed before, a decreasing pressure gradient eventually diminishes the share of the pressure-driven channel flow which necessarily leads to a decreasing film height during the deposition as a function of the coating path.

The effect can be visualized by measuring the thickness at several positions on dried precursor layers. Figure 11 shows the dry film thickness distribution of multiple metallic layers measured by profilometry. For this experiment several samples have been prepared by depositing a constant amount of ink on 8 cm long and 1.7 cm wide substrates followed by a drying and alloying step up to 200°C.

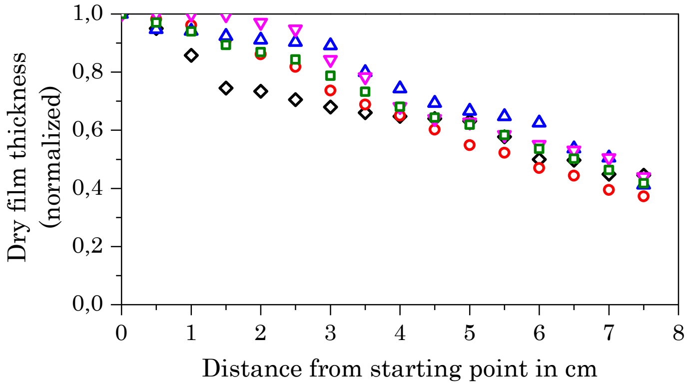

Figure 11: Film height deviation as a function of the distance from the starting point of the coating process. The values belong to four different samples processed up to 200°C with thicknesses around 500 to 1000 nm. The measurement has been done by profilometry.

The graph shows that the total film height decreases to roughly 50 % of its initial value within 7 cm of substrate length. This deviation seems very large especially regarding a future up scaling. Thus, at this point it has to be noted that this effect can easily be minimized by keeping the amount of ink in front of the gap nearly constant e.g. by using a large excess ink volume. However, for the current investigation the film height deviation offers the opportunity to evaluate the thickness dependent electrical properties of the final solar cells. With the used grid design 10 adjoined solar cells can be processed from one substrate after the selenization and the deposition of buffer and window layer. Due to the used blade coating deposition method, each of the cells has a different absorber layer thickness influencing the optoelectronic properties. In Figure 12 the normalized current densities of 9 substrates corresponding to 90 cells are depicted as a function of the cell position. The graph clearly shows a trend to lower j_{sc} values towards the end of the substrate. It also suggests that the highest values are achieved around the third cell.

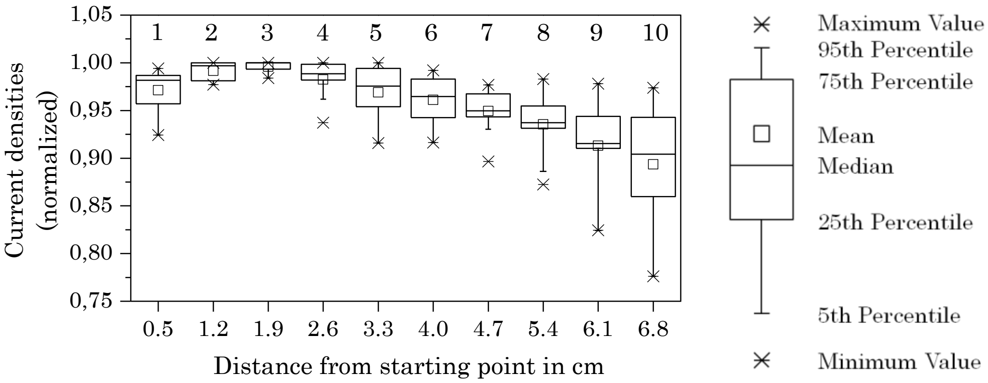

Figure 12: Current densities of 10 adjoined solar cells normalized to the highest value on 7 cm long substrates as a function of the cell position. Each data point is based on 9 cells. The illustration on the right explains how to read the box chart.

To explain the trend in the current densities, external quantum efficiency (EQE) measurements have been carried out over a full substrate length on every second cell. The results are shown in Figure 13. The graph confirms the presence of an identical ZnO window layer (A) and CdS buffer layer (B) on all cells over the substrate length. At short wavelength the collection is also similar (C). Photons with a wavelength above 800 nm, however, are collected differently in the cells. The graph suggests that the collection is best at the cell positions 1 and 3. Thereafter, the collection decreases significantly from cell 3 to cell 9 with a drop at cell position 9. Above 1100 nm the EQE of all samples decrease quickly to 0% at 1180 nm (D). This last trend can be explained by the used EQE setup which has been calibrated only with a silicon solar cell (see also Appendix D).

These results can be correlated with the short circuit current measured on the same cells which are shown on the right. After a maximum of around 38 mA/cm² at cell position 1-3, the values decrease almost linearly to 32 mA/cm² at cell position 9. Simultaneously, the open circuit voltage stays almost constant while the fill factor also decreases slightly (not shown). Considering the measured decrease in the layer thickness (Figure 11) the results indicate that the absorber layer above cell position 3 is too thin to achieve a similar collection. In thinner layers the absorption of photons with a long wavelength occurs closer to the back contact where the collection of generated charge carriers is less likely due to recombinations. Lundberg et al. did a similar investigation on co-evaporated CIGS solar cells with varying absorber layer thicknesses between 0.15 and 1.8 µm [99]. They observed a significant drop in efficiency which could also mostly be correlated with a decreasing short circuit current at a constant open circuit voltage.

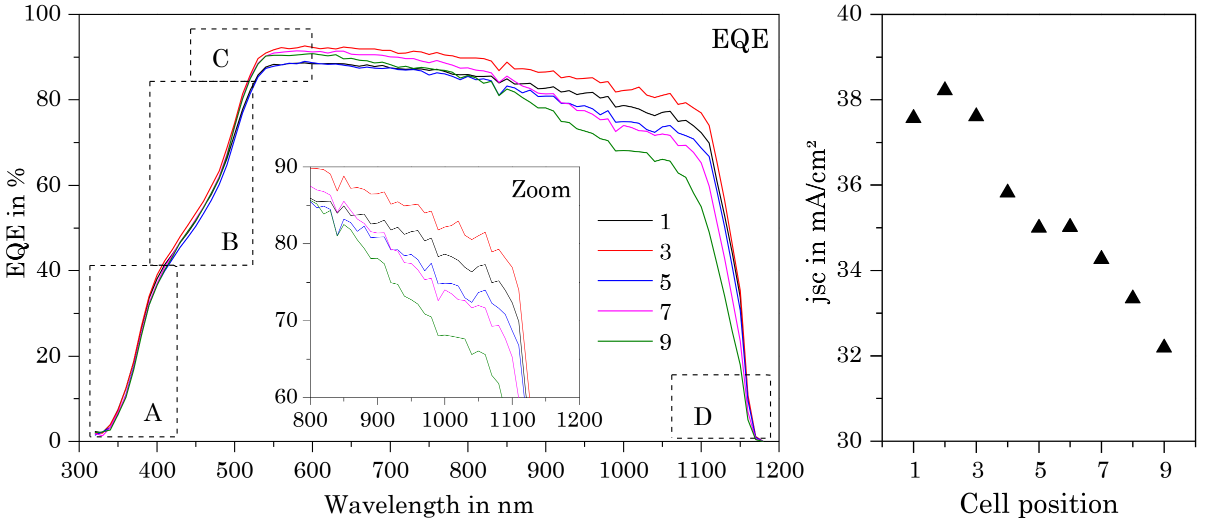

Figure 13: Left: EQE curves of five cells on a 7 cm long substrate at the positions 1, 3, 5, 7, and 9. Right: Corresponding short circuit currents at all cell positions measured with a solar simulator.

Coating speed

To calibrate the ink deposition and to simplify the adjustment of the resulting liquid film height, knowledge of the influence of the other coating parameter is necessary. In order to keep the deposition simple and to achieve a sufficient reproducibility most parameters including the salt concentration, the viscosity (mainly influenced by the methanol fraction), the temperature, and the blade gap height have been set as constant. Solely the coating velocity has been chosen to be variable. This parameter mostly determines the share of the shear-driven couette-flow in the blade gap which is less dependent on the ink-properties and therefore should have a reliable influence on the film height. Its influence has been investigated empirically with several process configurations. Figure 14 shows the measured dry film of layers deposited on glass followed by a tempering up to 200°C. The results can be fitted with an exponential function showing an average increase of about 13 % in film height for each 2.5 mm/s speed step.

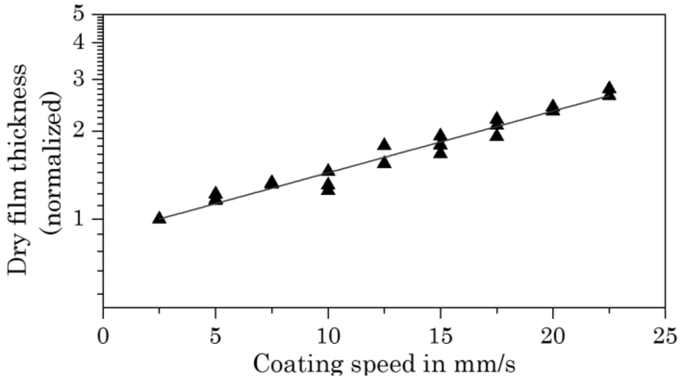

Figure 14: Precursor film height of several layers processed with different coating velocities. The values have been measured by profilometry and are plotted on a logarithmic scale. The results are normalized to the lowest thickness. In order to keep the results comparable the measurement position has been fixed to 1.5 cm after the starting point.

3.2 Solvent drying

Drying removes solvents by evaporation from a solid or mixture of liquids. Simultaneously, the drying process has to avoid any damage to the product which can be challenging especially regarding the drying of thin liquid film. This is further aggravated if the coated wet film consists of a multi component system where the individual compounds have deviating physical properties. In this case unwanted drying induced separation effects can have detrimental influences on the film homogeneity. Therefore this section focuses on the practical challenges in the drying of multi component inks. Derived from these findings, a new approach for the lab scale processing of homogeneous layers in the form of a combined coating/drying device is evaluated.

3.2.1 Drying induced film inhomogeneities

In section 3.1.2 the film thickness deviations over the substrate length induced by the blade coating process have been investigated. These deviations can get very large for long substrates in the range of 7-10 cm. However, due to the small scale of the individual solar cells (edge length is around 7 mm) each cell has an almost constant layer height. Apart from the blade coating induced thickness deviations, liquid deposited thin layers often show side effects like “fat edges” close to the substrate borders. These material agglomerations can form during the coating or afterwards during the drying [100]. In the presented process the mentioned “fat edges” also occur but only during the drying step. Due to their possible size in the range of several millimeters and the total substrate width used for the solar cells of around 16 mm, these material agglomerations can have a significant influence on the cells’ layer homogeneity. Therefore, this section investigates possible explanations for the formation of the “fat edges”.

In the present solution based approach drying is necessary to remove the solvent tetramethylguanidine (TMG) and the diluting agent methanol from the ink. Comparing the pure liquids, methanol has a very low boiling point of 65°C and therefore a high evaporation rate already at room temperature. TMG has a significantly higher boiling point of 160°C and is therefore expected to stay much longer in the ink. Thus, the evaporation of a mixture of both liquids can roughly be divided into two distinct steps. This section focuses on the mixture induced drying effects and thereby investigates the low temperature drying region where the ink still contains both liquids. In this region the properties of the ink are changing constantly due to the non simultaneous solvent evaporation. With a decreasing fraction of methanol in the ink, both the viscosity as well as the surface tension are increasing. This issue can have a severe influence on the homogeneity of the liquid layer and it is therefore crucial for the entire process [101].

Similar solution based approaches in the literature usually evaporate the solvents by simply placing the sample on a hot surface. If this procedure is transferred to the present process, a particular effect can be observed. The liquid layer containing both liquids is exposed to a convective gas flow ascending from the surface of the hot plate (T_{hp}), also denoted as free convection. In order to fill the empty space from the ascended gas, cold ambient air with $T_{sur} < T_{hp}$ is sucked in from the surrounding. The emerging flow field above the sample consists of parallel paths perpendicular to the hot plate edges [102]. Figure 15 shows a possible flow field around the sample.

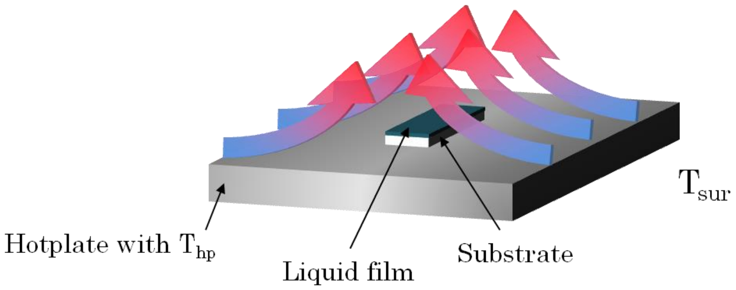

Figure 15: Simplified schematic representation of the gas flows around a substrate on a heated plate.

The convective gas flux from the surrounding has a negligible partial pressure of the solvents and arrives at the substrate from the sides where the film thickness is the lowest. Due to the differences in the flow conditions the mass transport of the solvent molecules from the film surface to the gas phase is anisotropic. This can be the reason for a faster solvent evaporation close to the edges leading to a depletion of the low-boiler methanol in these areas. Together with the slightly lower layer thickness at the edges, the faster methanol evaporation can lead locally to a significantly increased surface tension [103]. Surface tension gradients throughout the film surface can form which are inducing convective liquid fluxes in the film [104] and from the center of the film to the borders [101], [105]. This effect is known as the Marangoni effect which is a common problem in thin film drying [106], [107]. For small lab scale substrate dimensions, the thereby agglomerated ink at the borders can be detrimental due to the inhomogeneous thickness distribution which is discussed in the next section.

3.2.2 Influence on the solar cell quality

The dimensions of “fat edges” occurring during the drying can overlap with the solar cell area (Figure 16). Thus, the material agglomerations can also affect the opto-electronic properties of the final solar cell device. In order to show this issue light beam induced current (LBIC) measurements have been used. With this method the cell surface is scanned with a focused light beam and the respective current response is monitored giving a two-dimensional current distribution. The measurement has been carried out under a constant negative bias voltage of -300 mV. Figure 16 shows the current response map of a cell processed from a precursor layer with significant thickness deviations at the substrate borders. The color coded map in the lower part of the cell corresponding to the center of the substrate shows a rather homogeneous current distribution. Only small deviations can be observed at the bottom of the cell area. In contrast to this, the upper part close to the sample edges reveals large, stripe like areas with a significant drop in the current response (yellow/green color). The results can be explained by the high absorber layer thickness in this area which has been measured to be in the range of 4.5 µm. An absorber thickness that high can result in a decreased current collection due to recombination of the charge carriers.

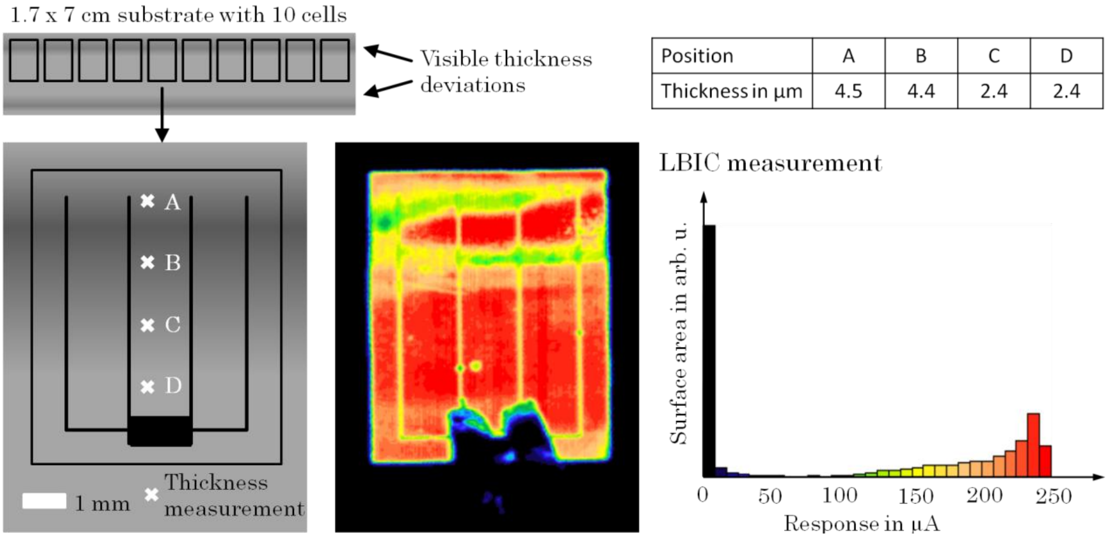

Position	A	B	C	D
Thickness in µm	4.5	4.4	2.4	2.4

Figure 16: LBIC measurement on a cell with drying induced thickness deviations in the absorber layer towards the substrate edges showing a high current loss in these regions. Left: schematic representation of the cell position on the substrate and the thickness measurement positions (profilometry). Right: Local current response map. A red laser was used with a wavelength of 658 nm

One possibility to improve the layer homogeneity is to decrease the ink volume by dividing the coating/drying process into multiple steps. However, this process fragmentation requires several more steps which are complicating the whole process. In order to improve the film properties without complicating the process (keeping only a one step film application), one option is to adjust the drying conditions which will be evaluated in the next section.

3.2.3 Controlled drying by forced convection

The key finding in the previous section is that the drying step has to be optimized regarding a quick and isotropic methanol removal from the binary solvent mixture to keep the uniformity of the film. This can be achieved by adjusting the drying which requires the control over two things, the methanol mass transport from the ink to the gas phase as well as the local mass transfer distribution over the film surface. Regarding the first, the solvent evaporation has been investigated in detail by estimating the diffusive fluxes of solvent molecules to the gas phase. The calculation is based on diffusion phenomena that can be described by Fick's law [108] where the diffusive flux is a function of a concentration gradient and a diffusion coefficient.

$$J = -D \frac{\partial c}{\partial x}$$

J	diffusion flux in mol/(m^2 s)
D	diffusion coefficient in m^2/s
c	concentration in mol/m^3
x	position in m

For the binary liquid mixtures of the components 1 (methanol) and 2 (TMG) with a steady state evaporation from the liquid/gas interface to the surrounding atmosphere and a diffusion path length (boundary layer) between position A at the liquid-gas interface and B in the surrounding equation (3-1) can be written as:

$$J_i = -\beta_i \, (c_{iA} - c_{iB}) \;\; with \;\; \beta_i = \frac{D_{igas}}{l_{AB}}$$

β_i	mass transfer coefficient of component i in m/s
D_{igas}	binary diffusion coefficient of component i in the gas phase in m^2/s
l_{AB}	diffusion path length in m

Assuming an ideal gas phase and a negligible concentration of the components 1 and 2 in the surrounding atmosphere ($c_{iB} = 0$) equation 3-2 can be written as:

$$J_i = -\frac{\beta_i}{R\,T}\, p_{iA}$$

p_{iA}	partial pressure of component i at position A in Pa
R	universal gas constant in J/(mol K)
T	absolute temperature in K

Raoult's law can be used to describe the partial pressure of the two solvents at the liquid gas interface (position A) as a function of the compounds' molar fraction in the liquid mixture. The film composition is assumed to be gradient free (completely intermixed) due to the small vertical dimensions.

$$p_{iA} = \gamma_i \, x_i \, p_{iA}^{*}(T)$$

γ_i	activity coefficient of component i in the mixture
x_i	molar fraction of component i in the liquid
$p_{iA}^{*}(T)$	vapor pressure of component i in Pa

Equation (3-5) can be obtained by extending equation (3-3) with the evaporation surface and by using equation (3-4).

$$J_i A = \dot{N}_i = -\frac{\beta_i}{R\,T}\,A\,\gamma_i\,x_i\,p_i^*(T)$$

$\dot{N}_\mathrm{i}$	absolute diffusion flux in mol/s
A	evaporation surface in m^2

Equation (3-5) shows that there are two parameters which can be modified to improve the diffusion flux, the temperature to increase the vapor pressure and the mass transfer coefficient. The temperature of the liquid can be easily adjusted by increasing the hot plate temperature. However, with this modification the solvent evaporation is still anisotropic and preferably takes place at the substrate edges (see above). The second parameter, the mass transfer coefficient is a function of the diffusion coefficient and the boundary layer. The latter is directly influenced by the drying conditions such as the flow configuration close to the film surface [108]. The drying conditions are incorporated in the dimensionless Sherwood number.

$$\beta_i = \frac{Sh\,D_{igas}}{L_c}$$

Sh	Sherwood number
L_c	characteristic length of the liquid surface in m

The binary diffusion coefficient D_{igas} of component i in the gas phase is a function of the pressure and the temperature and can be approximated using the Fuller equation [109].

$$D_{igas} = \frac{10^{-3}\ T^{1.75}\sqrt{\left(\frac{M_i + M_{gas}}{M_i\,M_{gas}}\right)}}{p\left(\sqrt[3]{\Sigma v_i} + \sqrt[3]{\Sigma v_{gas}}\right)^2}$$

D_{igas}	diffusion coefficient of component i in the gas medium in cm^2/s
M_i, M_{gas}	molar mass of component i and the surrounding gas in kg/kmol
v_i, v_{gas}	diffusion volume of component i and the surrounding gas
p	total pressure in bar

The diffusion volumes in equation (3-7) are tabulated for example in [110]. The Sherwood number can be calculated using an empirical correlation. In case of a film drying on a hotplate, the matching correlation is the Sherwood number for free convection Sh_{free} which is a function of the Rayleigh number Ra and Schmidt number Sc [110].

$$Sh_{free} = 0.766\ [Ra\ f(Sc)]^{1/5}$$

$$Ra = \frac{g}{T_M\ \nu_{gas}\ a_{gas}} (T_A - T_B)\ L_c^3$$

$$Sc = \frac{\nu_{gas}}{D_{igas}}$$

g	gravitational acceleration in m/s²
T_M	median temperature in K
ν_{gas}	kinematic viscosity of the gas in m²/s
a_{gas}	thermal diffusivity in m²/s

In order to adjust the mass transfer coefficient the free convection can be changed to a forced convective gas flow of inert gas, a procedure which is widely used in the industry. In terms of possible flow configurations, multiple setups are suitable ranging from impingement to cross flows. The main advantage of the forced gas flow is the controlled transfer of the preferred evaporation areas away from the edges to the center of the substrate. Therefore the evaporation rate as well as the isotropy of the evaporation can be adjusted. For simplicity reasons, the presented lab scale process has been optimized using a laminar transverse flow. The corresponding Sherwood number for this flow configuration can be calculated as a superposition of a laminar (Sh_{lam}) and a turbulent component (Sh_{turb}) [110].

$$Sh_{forced} = \sqrt{Sh_{lam}^2 + Sh_{turb}^2}$$

Both are a function of the Schmidt Sc and the Reynolds number Re.

$$Re = \frac{u_{gas}\ L_c}{\nu_{gas}}$$

u_{gas}	gas velocity in m/s

With equation (3-5) and the two different mass transfer coefficients calculated for free convection with equation (3-8) as well as forced convection with equation (3-11) the drying of a liquid film can be modeled. Regarding the surrounding atmosphere a glovebox filled with pure nitrogen has been assumed. The drying temperature T_A of the liquid has been set to 35°C and the temperature in the surrounding T_B to room temperature (22°C) for both calculations. In the case of the forced convection a nitrogen gas stream at room temperature and a velocity u_{gas} of 7.5 cm/s has been assumed. With these parameters the evaporation of TMG (2) having a high boiling point of 160°C can be neglected shifting the focus of the calculation to the methanol (1) evaporation. Nevertheless, to implement the presence of the strong base TMG into this model, which is forming a non-ideal solution with methanol, the composition dependent binary activity coefficient γ_1 of methanol in the mixture has been estimated using the group contribution method UNIFAC (Universal Functional-group Activity Coefficients). In this model the activity coefficient is derived from the enthalpy of mixing and calculated from the interactions between the individual chemical groups of TMG and methanol. In principle the UNIFAC model can be broken down in a combinatorial and a residual component $\gamma_1^{(c)}$ and $\gamma_1^{(r)}$, respectively. These components are dependent on the group surface area and volume as well as specific interaction parameters. More information about this model can be found elsewhere [110].

$$\gamma_1 = \ln \gamma_1^{(c)} + \ln \gamma_1^{(r)}$$

With the mentioned parameters, the time and composition dependent mass transport of methanol from the mixture to the gas phase has been calculated. Methanol mass transfer coefficients of 0.012 m/s and 0.006 m/s have been calculated for the forced and the free convection, respectively. Figure 17 shows the resulting mass loss as a function of the drying time.

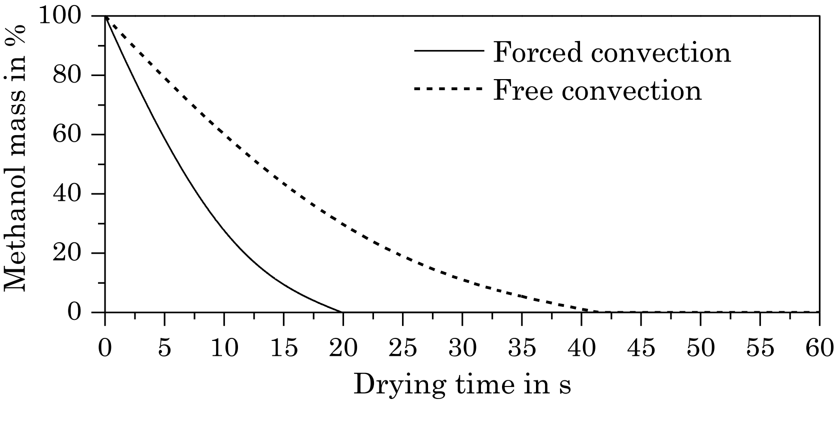

Figure 17: Mass loss curves for a liquid thin film of methanol in the presence of TMG dried at 35°C by free convection on a hot plate as well as by heating at 35°C in combination with a forced nitrogen gas flow with a gas velocity of 7.5 cm/s at ambient pressure.

Both curves suggest an almost linear mass loss in the beginning which is slowing down with a decreasing methanol fraction due to the increased influence of the solvent TMG. It can be seen that by applying the forced convection the time necessary to evaporate the alcohol decreases by a factor of two to 20 seconds. Thus, this calculation shows that drying under these conditions is significantly faster due to the improved mass transfer. However, this reduction in evaporation time is only an additional benefit. More importantly, the forced gas flow leads to a more homogeneous flow profile above the substrate supposedly shifting the mass transfer away from the edges to the center of the substrate [111], [112]. Drying by forced convection can be implemented into the process by using a flow channel. Figure 18 shows schematically the first prototype developed in this thesis. The channel consists of a long rectangular tube with a height to width ratio of 1.5:5. On the right side the cross section of the channel tapers off uniformly to a small mounted tube attached to a nitrogen source. The nitrogen gas entering the device is initially deflected by an impingement plate to improve the formation of a laminar flow at the final position of the substrate.

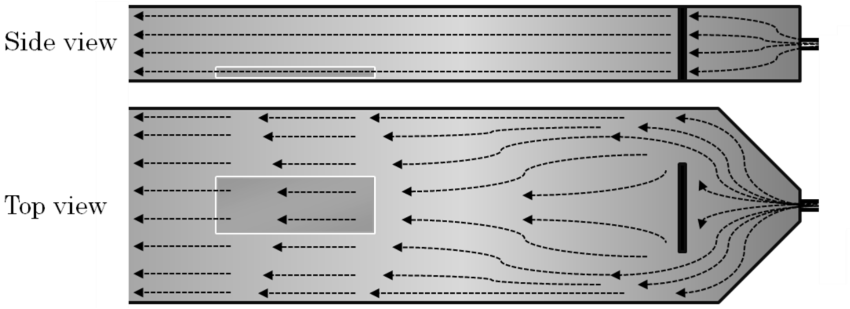

Figure 18: Cross section (side view and top view) of the drying channel. The final position of a coated substrate with dimensions of 3.6 x 10 cm is highlighted. The black rectangular opposite to the gas inlet shows the position of an impingement plate. Arrows indicate the estimated flow field inside of the drying channel.

In the presented design the device has one significant disadvantage. Due to its low boiling point methanol has a high evaporation rate already at room temperature. Thus, the time between the deposition of the liquid film and the transfer of the sample in the flow channel can be critical. For this reason, the initial drying channel has been revised to a combined coating/drying device. Figure 19 shows a schematic cross section of the device including the basic procedure for the film deposition and drying. In contrast to the first version, the sample is placed on a fixed base plate in front of the channel. The blade coater is positioned on top of the sample (A). After the addition of ink the nitrogen flow is started and the blade as well as the drying channel are moved with a constant speed over the substrate by a film applicator machine (B+C). Following the withdrawal of the blade, the outer part of the base plate is moved manually into the channel and the film is dried for several minutes (D). In order to improve the drying effect the base plate below the device is heated to a slightly elevated temperature of 35°C.

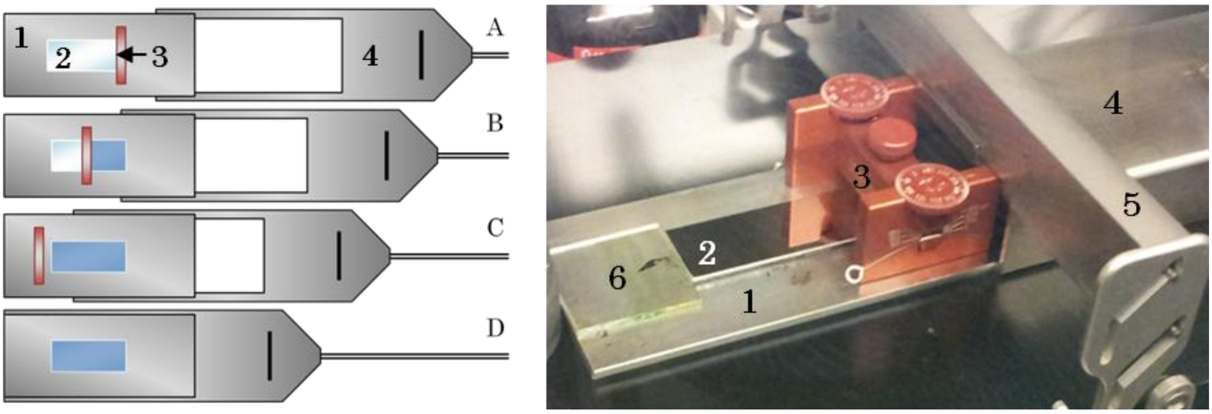

Figure 19: Left: Film deposition with the coating/drying device divided into four steps. A: Positioning of the Mo-coated substrate (2) and the blade (Zehntner ZUA 2000) (3) on a fixed metal plate (1) in front of the flow channel (4). A glass spacer (6) is used to fix the position of the substrate. The ink is added in the blade gap with an Eppendorf pipette. B+C: Moving of the blade and the channel over the substrate with an automatic film applicator (Zehntner ZAA 2300) (5). D: Final drying position. The liquid film stays inside of the channel under a forced gas stream for several minutes. Right: Photography of the setup in position A.

3.2.4 Improved layer quality

LBIC measurements have been used to visualize the improved homogeneity result achieved with the optimized drying conditions. Figure 20 shows the current response map of a cell processed from a precursor layer that has been dried in the flow channel. For this sample a substrate with double the width (3.3 cm times 7 cm) has been coated and dried which limits the drying inhomogeneities to one side after breaking the sample in half. The presented current response map shows a very homogeneous current distribution. The dark spot in the lower left corner can probably be explained by a microscopic particle contamination either from the ink or from the drying.

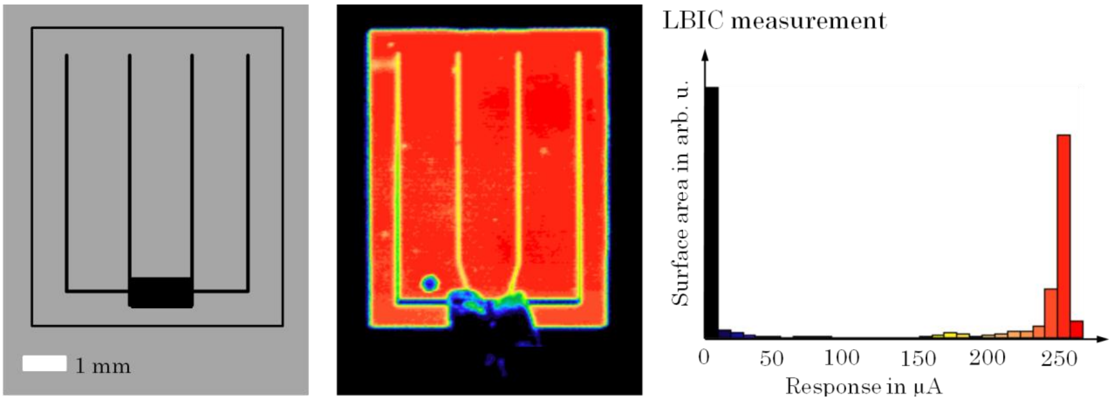

Figure 20: Potentiostatic LBIC measurement on a solar cell processed from a precursor layer dried in the flow channel with the following parameters. Drying time: 4 min, gas speed: 7.5 cm/s, hot plate temperature: 35°C, gas temperature: 22°C. For the LBIC a red laser has been used with a wavelength of 658 nm.

3.2.5 Summary of section 3.2

Solvent drying is one of the crucial steps in this process. Due to the deliberate simplification of the film processing to one single step, a thick liquid film has to be deposited and consequently a high amount of solvent has to be evaporated. The physical properties of the two individual liquids in the ink are highly diverging with regard to the surface tension and the vapor pressure. The latter leads to a stepwise evaporation while the former is responsible for a composition dependent surface tension. Due to an inhomogeneous evaporation by free convection (increased mass transfer at the substrate edges) these differences in the local surface tension can induce the so-called Marangoni effect. This effect describes the presence of inhomogeneous liquid mass transport fluxes in the film leading to non-uniformities in the material distribution. The resulting material agglomerations can be observed in the dried film by visible thickness deviations. In order to minimize this effect a drying channel has been introduced which can help to achieve isotropic methanol evaporation. This can be achieved already at low temperatures by using an additional forced nitrogen gas flow.

3.3 Electroless reduction of metal ions

In the previous section the challenges in the formation of homogeneous liquid films have been discussed. In this section the subsequent tempering step at higher temperatures is introduced comprising two simultaneously proceeding incidents. Number one is a second drying including the evaporation of the solvent TMG as well as the remaining residues of methanol. Number two is the reduction of the dissolved metal ions to metallic nanoparticles. The latter, the formation of elemental particles from the ink is one of the key processes of the presented approach. Therefore this section begins with an introduction in electroless plating. Following this, the redox reactions of the used metal salts which have already been introduced in section 3.3.2 are evaluated. Thereafter, the theoretical considerations are transferred to the present ink system. The solvent evaporation during the second drying is discussed in the context of the thermogravimetric experiments.

3.3.1 Introduction to electroless plating

Electroless plating (EP) usually describes the chemical deposition of a metal from an aqueous solution of a salt or complex where the metal is either solvated in the form of a single cation or in an anionic complex [113]. For this purpose a mechanism is needed where the metal ion is reduced from a higher oxidation state to its elemental form. The simplest form of EP is the metal displacement reaction. This reaction can be accomplished for example by immersing a solid metal with a low standard redox potential in a solution of a dissolved metal with a high standard redox potential. In this setup, the less noble metal is acting as the reducing agent and is getting oxidized and dissolved while the solvated more noble metal cations are getting reduced on the solid surface. In order to find out if a chemical reaction is running spontaneously the thermodynamic aspects of the involved chemical species have to be considered. In principle the main condition for any reaction to occur at constant temperature and pressure is that the Gibbs free energy of the reaction $\Delta_R G$ is negative.

$$\Delta_R G < 0$$

In the case of a redox reaction the overall mechanism can be divided into two individual processes, usually called the two half cell reactions. For a metal displacement reaction the individual paths are stated below.

Reduction* $M_1^+ + e^- \rightarrow M_1$ 3-15

Oxidation* $M_2 \rightarrow M_2^+ + e^-$ 3-16

Overall* $M_1^+ + M_2 \rightarrow M_1 + M_2^+$ 3-17

*With the standard oxidation potentials $E^0_{M1} > E^0_{M2}$ and $\Delta_R G < 0$

Both half cell reactions have a standard cell potential which can be measured against the standard hydrogen electrode. The sum of both cell potentials is written $E^{\ominus}$ and called standard potential.

$$E^{\ominus} = E^{\ominus}_{red}(M_1^+/M_1) - E^{\ominus}_{ox}(M_2^+/M_2)$$

The connection between the standard potential of a reaction and its Gibbs energy can be expressed as:

$$\Delta_R\, G^{\ominus} = -vFE^{\ominus}$$

v	number of electrons transferred within the half cell reactions
F	Faraday constant (96.48 kC/mol)

Thus, a requirement for a spontaneous redox reaction is a positive value for the standard potential which is the sum of both half cell potentials. A typical example for a metal displacement reaction is a Zn bar immersed in a solution containing copper ions. In this specific case the standard potential is +1.1 V under standard conditions meaning that the reaction should run spontaneously. For non standard conditions including different ion concentrations the cell potential can be calculated by using the Nernst equation. More information can be found elsewhere [114].

In the metal displacement reaction, the redox reaction occurs until the surface of the solid metal is completely covered with the reduced noble metal. This process is, of course, dependent on a suitable metal ion-substrate system and therefore limited to few examples. In order to deposit continuously on various substrates, a sustainable redox-reaction in the bulk solution is necessary. This means that the driving force for the reduction has to be provided by a dissolved chemical reducing agent. An example for a chemical system containing a reducing agent in the bulk is the Tollens' reagent. It is usually used to prove the presence of aldehyde groups that are acting as reducing agent. Silver ions having a high standard electrode potential are used as an oxidation agent in form of a diaminesilver(I) complex. The redox reactions occurring when mixing aldehydes with the Tollens' reagent and a source of hydroxide ions are listed below:

Reduction $2[Ag(NH_3)_2]^+ + 2e^- \rightarrow 2Ag + 4NH_3$ 3-20

Oxidation $RCHO + 3OH^-$ $\rightarrow RCOO^- + 2H_2O + 2e^-$ 3-21

Overall $2[Ag(NH_3)_2]^+ + 3[OH]^- + RCHO$ $\rightarrow 2Ag + 4NH_3 + 2H_2O + RCOO^-$ 3-22

The aldehydes are oxidized to carboxylic groups leading to a reduction of the silver complex. Thus, the evidence for the presence of the aldehyde group is the precipitation or EP of solid silver nanoparticles on the surface of the vessel (silver mirror).

3.3.2 Electroless plating of metal formates

In the previous section the Tollens' reaction has been presented as an example for an EP system with a reducing agent that is dissolved in the bulk. In this particular chemical system, the aldehyde group is getting oxidized in order to reduce silver ions. Regarding the redox-potential of the aldehydes, the formate anion shows similar reactivity. The oxidation of the formate ion can be written as following.

			Potential in V	
Formate	$HCOO^-$	$\rightarrow CO_2\uparrow + \frac{1}{2} H_2\uparrow + e^-$	-0.42 [115]	3-23

To process metallic Cu-In-Ga layers, the solvated silver-amino complex has to be substituted by the respective metal cations or cation complexes. The standard potentials of the three metal ions are stated below.

			Potential in V	
Copper	$Cu^{2+} + 2e^-$	$\rightarrow Cu$	+0.34	3-24
Indium	$In^{3+} + 3e^-$	$\rightarrow In$	-0.34	3-25
Gallium	$Ga^{3+} + 3e^-$	$\rightarrow Ga$	-0.55	3-26

By looking at the possible half cell reactions it can be easily concluded that the formate anion has a sufficiently high standard reduction potential to spontaneously reduce copper and indium ions. The potential of the gallium ions, however, is too low. It is important to note that this only applies for standard conditions and can't be transferred to the used ink system. The actual reactions in the ink are discussed below and in the next sections.

In contrast to the Tollens' reagent containing various compounds the proposed ink system can be simplified by choosing metal formate salts that already contain copper, indium and gallium. The reduction of copper from its formate salt has already been reported in the literature yielding elemental nanoparticles. Noteworthy, due to the composition of the metal formates containing both, reducing agent and the desired metal cation, a metallic copper formation can be achieved without any admixtures. Several groups reported metallic nanoparticles from the pure salt on a surface or in an aerosol [78], [116]. The redox reaction and therefore the metal cation reduction could be easily initiated by supplying energy in form of heat to achieve a sufficiently high reaction kinetic. However, to process homogeneous layers, the presence of an inert solvent as transfer agent is required to facilitate a uniform material deposition.

The general function of the solvents is to form a stable complex during the ink formulation and the liquid film deposition. It is also important that the solvent does not evaporate or decompose before the initiation of the redox reaction. Otherwise the precipitation of the dissolved salts during the solvent evaporation beginning at the solubility limit would consequently lead to a recrystallization and eventually to the formation of crystals on the surface. The presence of crystals and therefore unwanted material agglomerations would counter a uniform deposition of metal nanoparticles.

Concerning the solvent-salt interactions it is important that the complex itself is inert and does not change the reaction products. However, the presence of the solvent can still have a huge impact on the thermodynamic properties of the reaction and on the morphology of the reduced metal nanoparticles. Rosenband et al. investigated several solid and liquid additives mixed with copper formate salt and evaluated their influence on the morphology of the copper particles. By analyzing SEM images of the products they could show a huge influence on the particle size and the formation of agglomerates [78]. This issue will be evaluated for the current copper inks consisting of different solvent mixtures in section 3.4.3.1.

Reaction pathways

The reaction pathways depend on the individual metal ion and the respective standard electrode potential. Metals with a high potential are more likely to get reduced by the formate anion. However, it is hard to predict the exact reaction pathway in the presence of a distinct solvent. Therefore the following reaction paths are taken from the solid state reactions. Metal ions with a sufficiently high electrode standard potential most likely react as following [117]. An example for this pathway is copper formate.

Reduction $M^{x+} + xe^- \rightarrow M$ 3-27

Oxidation $xHCOO^- \rightarrow xCO_2\uparrow + x/2H_2\uparrow + xe^-$ 3-28

Overall $M^{x+} + xCOOH^- \rightarrow M + xCO_2\uparrow + x/2H_2\uparrow$ 3-29

In case of metals with a low standard electrode potential, the reduction potential of the formate ion can be insufficient. Here, the decomposition of the anion most likely leads to metal oxides. An example for this reaction pathway is zinc formate [117]. Zinc has a very low standard potential of -0.79 V.

Overall $Zn^{2+} + 2COOH^- \rightarrow ZnO + CO_2\uparrow + CO\uparrow + H_2\uparrow$ 3-30

The reaction pathways and products are highly dependent on the surrounding conditions and are prone to catalytic effects. For example at elevated temperatures the presence of oxygen will eventually lead to the formation of the most stable metal oxide for almost all metals. Additionally Mohamed et al. published a report on the decomposition (in this context also the redox-reaction) of copper formate salts in reductive, inert and oxidizing atmospheres [118]. They found an increased reactivity under reducing conditions as well as a decreased decomposition rate in the presence of oxygen.

The presented reaction pathways suggest a one step decomposition mechanism. However, also multistep reductions are possible which can be found for example in copper salts. Galwey et al. reported evidence for a intermediate Cu(I) formate in the solid state reaction [80]. Concerning its properties, Edwards et al. and Ogura et al. analyzed it to be volatile with a dimeric structure in the gas phase [119], [120]. This stepwise reduction is relatively common for copper(II) salts and also occurs in other compounds including copper(II) oxalate [121] or malonate [122]. In case of copper formate, the two distinct reduction steps leading to the pure metal can be written as following:

Reduction 1. step $Cu^{2+} + HCOO^- \rightarrow Cu^+ + CO_2\uparrow + 1/2H_2\uparrow$ 3-31

Reduction 2. step $Cu^+ + HCOO^- \rightarrow Cu + CO_2\uparrow + 1/2H_2\uparrow$ 3-32

The presence of two types of copper formate (Cu(I) and Cu(II)) is of great importance for the process developed in this thesis and will be further discussed in section 3.4.1 in the context of the thermogravimetric results and in section 3.5 due to the importance of Cu(II) ions for the layer stabilization.

3.4 Investigations on the metal ion reduction

In the previous section the theory of the metal ion reduction with formate ions has been introduced. The application of this theory on the presented process is the content of this section. In contrast to the section 3.2 evaluating the drying of methanol, the focus here is set on the temperature area between 100°C and 200°C. In this temperature range the kinetics of the discussed redox-reactions is sufficiently fast to proceed. The existence of the proposed reactions is supported by two independent analyses. Firstly, the signature of carbon dioxide as an indicator for the salt decomposition has been traced by thermogravimetric (TG) analyses in combination with a mass spectrometer (MS). With this measurement the temperature range of the proposed reactions can be localized. Secondly, these findings have been compared to the result of an in-situ X-ray diffraction (XRD) analysis on a heated liquid layer to prove the reduction of the metal ions and thus the formation of pure metals and metal alloys.

3.4.1 Thermogravimetric and mass-spectrometric analyses

TG-MS analyses have been carried out to measure the mass loss and the gaseous products during the heating of the pure metal formates as well as the dissolved salt inks. For these experiments small amounts of each sample have been heated from room temperature to 350°C in open containers in an oxygen-free environment. The focus of the analyses has been set on the formation of carbon dioxide due to its function as a tracer for the anion decomposition (see section 3.3.2). With this information the temperature range of each reaction has been estimated. In order to evaluate the influence of the solvents on the reactions, the first experiment has been carried out on a pure metal formate mixture. Following this, inks containing each metal salt separately as well as a stoichiometric mixture of all three salts have been analyzed. Thereafter, the ratio between the measured CO and CO_2 molecules is discussed in detail to extract information about the reaction product.

3.4.1.1 TG-MS of solid metal formate salts

To evaluate the TG-MS characteristics of the solid metal salts, a formate mixture with a molar metal ratio suitable for solar cells (Cu:In:Ga = 0.9:0.8:0.2) has been prepared and heated inside of the TG furnace with a constant heating ramp of 10 K/min to 600°C in inert atmosphere. The results in the temperature interval between room temperature and 325°C are shown in Figure 21.

Beside some instrument related fluctuations at low temperature that can be attributed to the low initial sample mass, the TG curve shows no mass loss up to a temperature of 180°C. Here, the anion decomposition begins which ends at around 280°C visible by the constant mass above this temperature. Within this temperature range the total mass decreases to 45 % of the initial value in two steps around 210°C and 270°C. In the first step, the total weight decreases by about 20 mass-%. This value corresponds to the weight of the decomposed copper formate anions suggesting that the second step can be exclusively attributed to indium and gallium formate. The weight of the salt residues above 280°C is in good agreement with the calculated mass fraction of the metals in the salt suggesting a full decomposition of the anions.

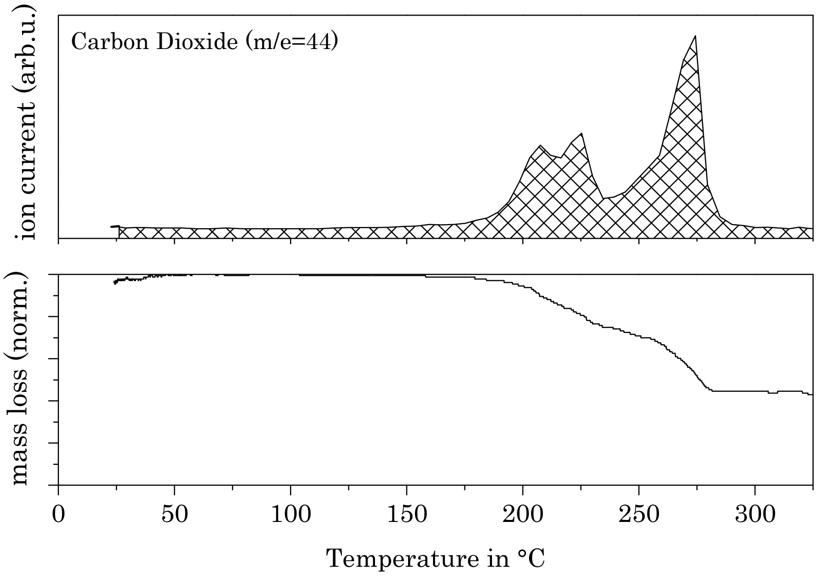

Figure 21: TG-MS graph of a stoichiometric mixture ($Cu_{0.9}In_{0.8}Ga_{0.2}$) of solid formate salts with 10 K/min. Top: Ion current with m/e=44 corresponding to CO_2. Bottom: Normalized mass loss.

The analyzed ion current with m/e=44 reveals two distinct areas with peak maxima of 205/225°C and 275°C. These areas coincide with the measured TG mass-loss steps that can therefore be explained by the decomposition of the formate ions to carbon dioxide as has been predicted in section 3.3.2. The presence of the steps as well as the separate peaks in the ion current can probably be correlated to the diverging behavior of the three different metal salts. In order to support this hypothesis, the results have been compared to TG investigations of copper formate previously published in the literature [78]. In this publication the thermal decomposition of the pure salt has been measured to occur between 180°C and 225°C which corresponds to the first step/peak area in the current analysis. They also confirmed the formation of residue free metallic copper nanoparticles.

An important observation in the present ion current graph is the split-peak shape of the first CO_2 peak area supposedly belonging to copper formate. The measured data suggests the existence of two overlapping peaks with similar heights and maxima of 205 and 225°C. As an explanation, the mentioned stepwise reduction of Cu(II) formate with a Cu(I) intermediate can be exerted [80]. The second peak is singular with a small shoulder at around 250°C suggesting an almost simultaneous reaction of indium and gallium formate in this temperature range.

3.4.1.2 TG-MS of dissolved metals (inks)

As discussed in section 3.4.1.1, the results of the solid state TG cannot directly be transferred to metal formates dissolved in a liquid compound as the solvent is expected to have an influence on the reaction pathways as well as the kinetics and therefore the temperature range of the decomposition. For this reason separate TG experiments with dissolved metal salts have been carried out. In order to approximate the final ink conditions, inks consisting of the typical compositions used for the solar cell processing have been evaluated. In contrast to the experiments on the solid metal salts and in addition to the dissolved CIG mixture, unary samples each containing only one of the metal salts have been prepared. The results are shown in Figure 22.

Due to the complex ink systems containing the salt, the solvent TMG, and the diluting agent methanol, two additional ion currents are plotted in Figure 22 with m/e=31 and m/e=71 that can be used to clearly identify the alcohol and the solvent, respectively. However, in the mixture the carbon dioxide signal (m/e=44) belongs to both, carbon dioxide and to the base tetramethylguanidine (probably in form of the molecule fragment $N(CH_3)_2$). Hence, the measured signal is a superposition of both compounds. The two signals can be separated with the help of the rather weak ion signal with m/e=12 corresponding to an ionized carbon atom. This ion can only be found in carbon dioxide. On the other side TMG can be easily identified by the signal with m/e=71. The initial molar ratios of the investigated inks are shown in Table 4. Due to different solubilities, the compositions are slightly diverging. Copper ions for example can be complexed by two TMG molecules while the indium and gallium salts need at least three to get dissolved.

Table 4: Composition of the investigated inks (molar ratios).

Ink	TMG:Metal-ions	TMG:Formate-ions	TMG:MeOH
Copper	1.9:1	0.89:1	1:1.24
Indium	3.4:1	1.05:1	1:1.19
Gallium	3.1:1	0.83:1	1:1.19
Cu0.9In0.8Ga0.2	2.5:1	0.87:1	1:1.25

In all experiments the methanol signal (m/e=31) can be measured up to high temperatures reaching 150°C. This is significantly different to the behavior that would be expected from the pure alcohol. Thus, additional forces are necessary to explain the delayed evaporation. This topic is further investigated in appendix A where a simple model is used to quantify this effect in the form of a vapor pressure reduction. It is important to note that the calculation of the solvent evaporation in section 3.2 is unaffected by this consideration as the amount of methanol that is highly bound in the ink is only a very small fraction of the total initial methanol mass.

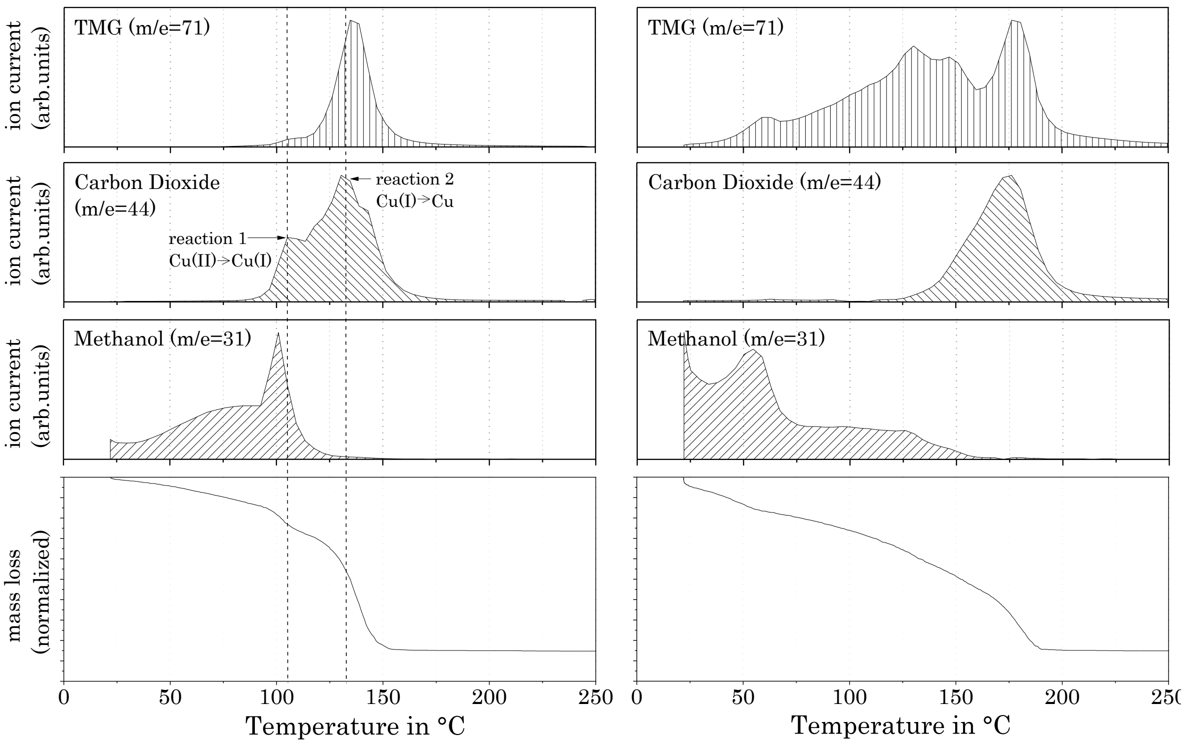

Copper

Indium

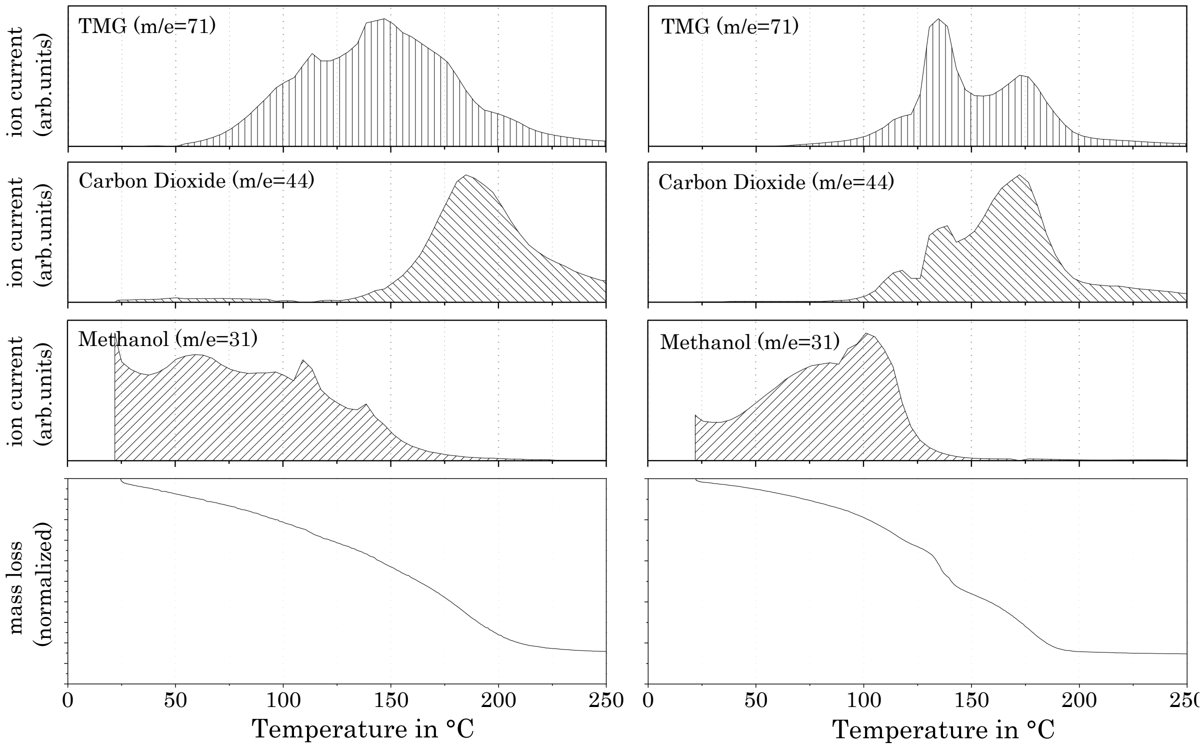

Gallium

Cu0.9In0.8Ga0.2

Figure 22: TG-MS of inks containing the formate salts of Cu, In, Ga and a CuInGa mixture measured with a heating rate of 10K/min in inert atmosphere. The bottom graph shows the TG mass loss while the three graphs above represent the measured ions currents of TMG (m/e=71), CO_2 (m/e=44) and methanol (m/e=31).

Copper ink

Beginning with the copper ink, the TG graph shows a slow mass loss in the temperature range between room temperature and 100°C followed by two steps with a residual mass of 14% at 250°C (Figure 22). The two steps can be divided into a first small mass loss of about 10 abs-% at 100°C and a significantly larger step of 55 abs-% around 130°C. The first step can be correlated with the abrupt evaporation of methanol in this temperature range visible by the ion current signal with m/e=31. It is obvious that this mass spectroscopic methanol peak coincides with the beginning of the CO_2 signal (m/e=44). The CO_2 peak can be measured up to 160°C reaching two maxima at 105 and at 130°C. The presence of two separate peaks can again be attributed to the mentioned stepwise copper ion reduction. Thus, a possible explanation for the abrupt methanol evaporation might be found in the different solvation energies of the alcohol to the two copper cations Cu(II) and Cu(I). Cu(II) has a much higher charge density than Cu(I). Thus, the fast evaporation of methanol molecules might occur due to the reduction of Cu(II) to Cu(I) and therefore the release of the bound methanol molecules.

The second step in the TG graph, can be assigned to the decomposition of the copper(I) formate TMG complex due to the simultaneously appearing signals of TMG and CO_2. It is important to note that pure TMG evaporates at lower temperatures. Therefore it can be concluded that the salt complex is decreasing the vapor pressure significantly similar to the effects found in the evaporation of methanol (see appendix A). With the arising salt decomposition the TMG molecules are released instantly from the complex explaining the occurrence of the sharp TMG peak in the ion currents.

In summary, the TG reveals that the reduction of copper ions to metallic nanoparticles occurs in the temperature range around 130°C. This observation coincides with the visible color change of the deposited film on the hot plate at the same temperature. Compared to the reaction in the solid state the decomposition of copper formate in the ink is shifted by almost 100°C to lower temperatures. Another obvious difference to the decomposition of the solid salts can be found in the height ratio between the two CO_2 peaks marking the two separate copper ion reduction steps. Instead of two similar peak heights the second one is significantly more pronounced. This can be explained by a previous partial reduction of Cu(II) to Cu(I) during the ink formulation and therefore less Cu(I) ions in the initial ink. The metal formate salt is dissolved in TMG at around 110°C which is in the same temperature range as the first copper reduction.

Indium ink

The mass fraction of indium formate in the final CuInGa formate salt mixture is around 50 %. Correspondingly, 55% of the formate anions belong to indium formate. Thus, during the reduction of the indium ions most of the carbon dioxide formation will take place. The results of the TG-MS measurement of an indium ink are shown in Figure 22. The TG graph clearly shows that the metal reduction occurs significantly later compared to the previously discussed sample containing the copper formate ink. The end of the reaction marked by the constant residual mass of 14.5 % is reached above 190°C. This value coincides with the initial amount of indium indicating a complete reduction.

A closer look at the measured ion currents reveals that the first evaporating methanol shows a significantly diverging behavior compared to the copper ink. Instead of an abrupt evaporation at around 100°C, methanol can be traced up to 160°C. Again the signal disappears with the arising CO_2 peak indicating the release of solvate-stabilized methanol molecules. However, the amount of methanol measured in this temperature range is significantly lower. The TMG signal begins at 50°C and reaches two maxima at around 130 and 175°C. Compared to this the CO_2 formation occurs only in a short temperature interval between 150 and 190°C coinciding with the second TMG peak. This can be explained by a decomposing salt-TMG complex releasing bound solvent molecules. However, in contrast to the copper ink, TMG can also be measured before the decomposition indicating a less pronounced binding of these solvent molecules. An integration of the areas below the two TMG peaks, the first between room temperature and 160°C and the second between 160°C and 200°C, results in a ratio of roughly 70% to 30%, respectively. By correlating this with the initial amount of TMG, the ratio between the TMG molecules and the dissolved indium ions at 175°C can be calculated. The result is 1:1 meaning that every indium ion stabilizes one TMG molecule. The other 70% of the TMG molecules evaporating at lower temperatures are less strongly bound in the ink.

Gallium ink

Gallium formate has the smallest share in the salt mixture with less than 8 mass-%. However, in contrast to the other metals the reduction of the ions is hindered due to the low standard electrode potential of gallium. This issue can be noticed in the TG graph in Figure 22 showing a residual mass fraction of 13.8% above 200°C. This value is significantly higher than the initial amount of metal in the ink which was around 9.6%. The deviation of 4% can be explained by the formation of Ga_2O_3. Further evidences for this assumption are presented below as well as in section 3.4.3.1.

The measured ion currents show almost constant methanol evaporation up to 125°C decreasing quickly with the beginning decomposition of the formate salts. Contrary to the other salt inks, TMG and CO_2 don't share a congruent peak. TMG evaporates in a broad region between 50 and 250°C with no significant maximum. The salt decomposition occurs around 180°C. From this information it can be concluded that the gallium formate most likely decomposes after precipitating from the ink.

Further indication for the formation of gallium oxide

In the paragraph describing the TG-MS of the pure copper solution the result could be correlated with the literature suggesting a full metal ion reduction. Regarding the indium and gallium salts, no literature on the respective formate decomposition has been found. The residual masses of the TG experiments, however, lead to the assumption that indium can be reduced while gallium formate is yielding Ga_2O_3. Further evidence for this hypothesis can be extracted from the gaseous products analyzed by the mass spectrometer. In section 3.3.2 the discussed reaction pathways suggest the formation of carbon monoxide in the case of metal oxides as reaction products. Due to the same mass to charge ratios of CO and N_2 (m/e=28) making a discrimination impossible, the presented TG-MS experiments have been carried out under helium. The measured relative ion currents for CO as well as CO_2 are depicted in Figure 23.

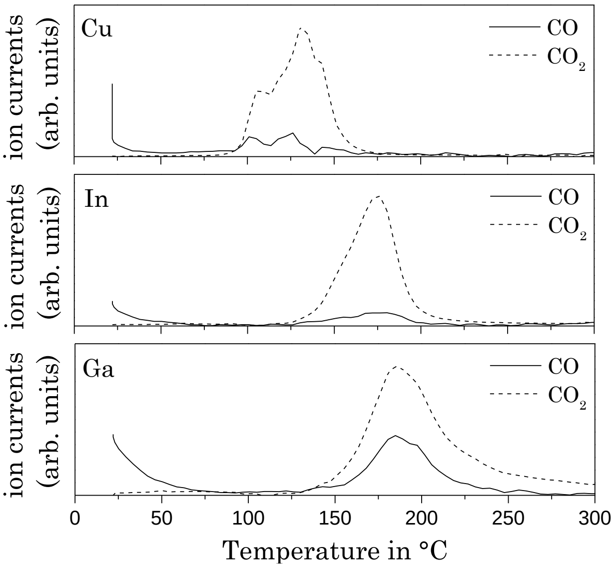

Figure 23: Mass spectrometric data for the Cu, In and Ga formate containing inks with a focus on the measured ions belonging to CO and CO_2 (m/e=28 and 44).

The measured ion currents of all three experiments start with a high initial value for ions with m/e=28 reaching zero at about 50 to 75°C. This can be explained by residual nitrogen molecules in the measurement tube due to the preparation procedure in air and are not a product of the ink heating. However, the ion currents above 100°C can be directly correlated to forming carbon oxide. By comparing the three graphs it is obvious that the peak intensity ratios I(CO_2):I(CO) are diverging. While copper and indium show small CO signals, the peak for the gallium ink is significantly more pronounced indicating a different anion decomposition behavior. Copper and indium formate mostly decompose to carbon dioxide while the heating of gallium formate yields a high amount of carbon monoxide. Therefore, the measurements suggest a reduction of the former and the formation of a metal oxide in the latter with a possible reaction path as following (see also section 3.3.2).

$$2Ga(HCO_2)_3 \rightarrow Ga_2O_3 + 3H_2\uparrow + 3CO\uparrow + 3\,CO_2\uparrow \qquad 3\text{-}33$$

Ternary CuInGa-ink suitable for solar cells

Figure 22 shows that the TG as well as the MS results of the CuInGa-ink represent a superposition of the discussed unary inks. The total mass decreases to 14% above 200°C in three distinct steps. The first step can be attributed to the methanol evaporation ending with a peak around 100°C. As has been discussed for the copper ink, this coincides with the arising CO_2 signal around 115°C indicating the reduction of Cu(II) to Cu(I). Beside this, the CO_2 signal has two more maxima at 135°C and 175°C increasing in height in the same order. The second maximum represents the copper reduction to the metallic state while the third, broad peak comprises the decomposition of both, indium and gallium formate. Due to the superposition of several peaks and the low amount of gallium salt no information about the decomposition product of the gallium salt can be derived from this graph. TMG molecules appear at the mass spectrometer above 100°C with two maxima around 135°C and 175°C simultaneously to the CO_2 peaks revealing the decomposition of the salt-TMG complexes. The differences in peak height can be correlated to the discussed metal ion to TMG ratios of 1:2 for copper ions and 1:1 for indium ions.

Table 5: Residual mass of analyzed inks compared to the expected value of the pristine concentration.

Ink	Measured mass at 600°C	Initial amount of dissolved metals
Copper	14.2%	14.0%
Indium	14.6%	14.6%
Gallium	13.8%	9.6%

3.4.2 In-situ and ex-situ XRD analyses

In the previous section TG-MS has been used to estimate the decomposition temperatures and to confirm the formation of carbon dioxide during the heating of the metal formate containing inks. In the introduction of the electroless plating, the formate decomposition always came along with the formation of CO_2 (oxidation of $HCOO^-$). However, the presence of carbon dioxide is not necessarily an indicator for a metal ion reduction. Depending on the standard electrode potential of the metal a reduction as well as the formation of oxides is possible. The TG analyses suggested the reduction of copper and indium to metallic particles. Gallium formate supposedly decomposes to gallium oxide based on the residual mass and the ratio between the measured gases CO_2 and CO. In order to prove the formation of metallic phases, an in-situ XRD analysis has been carried out. The results are discussed on the basis of the copper-indium phase diagram shown in Figure 24 reproduced from a publication by Bahari et al. [123].

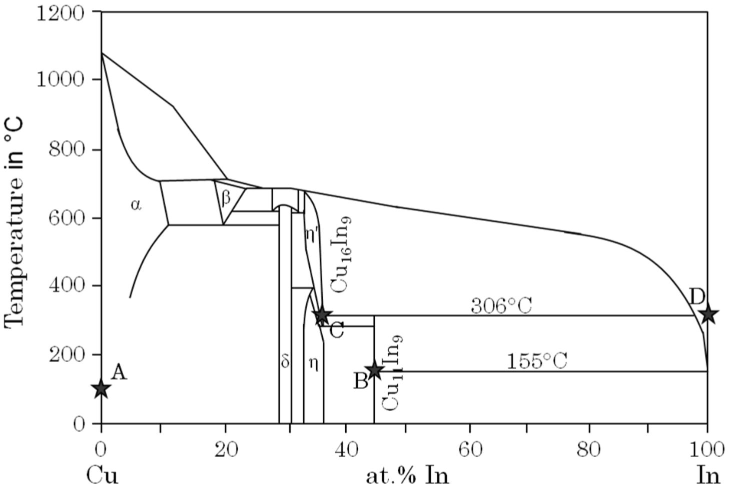

Figure 24: Copper-indium phase diagram reproduced from [123]. The stars A-D mark the most important phases occurring during the annealing which are explained in the text.

For the sample preparation a CuInGa containing ink has been coated on a Mo back contact in the glovebox. In order to stabilize the layer a small amount of an organic additive (introduced in section 3.5) has been added to the ink. Thereafter the layer has been dried at 100°C for several minutes to evaporate most of the methanol. This liquid film was then subsequently placed in the center of the XRD furnace followed by an evacuation of the chamber. After calibrating the diffractometer to the molybdenum peak (111 reflex, 2-theta=40.52°) the sample has been heated quickly to 100°C followed by a constant heating ramp of 5 K/min up to 325°C while taking 10 XRD scans per minute in Bragg-Brentano geometry. The resulting XRD patterns are shown in Figure 25 for 2-theta angles between 40 and 45° visualizing all important crystalline phase changes.

At 2-theta = 40.52° the Mo-(110) peak of the back contact is visible throughout the whole temperature range. At the beginning of the measurement no other crystalline phase could be observed up to 115°C. Shortly after a broad peak appears around 43.3° with a low intensity suggesting an initial reduction of the copper-ions to metallic copper particles (point A in Figure 24, JCPDS #04-0836). This observation corresponds to a visual change of the transparent film to a dark brownish color on the hotplate (Figure 25 top) and to a peak in the MS signal with m/e=44 (CO_2) plotted below the i-XRD.

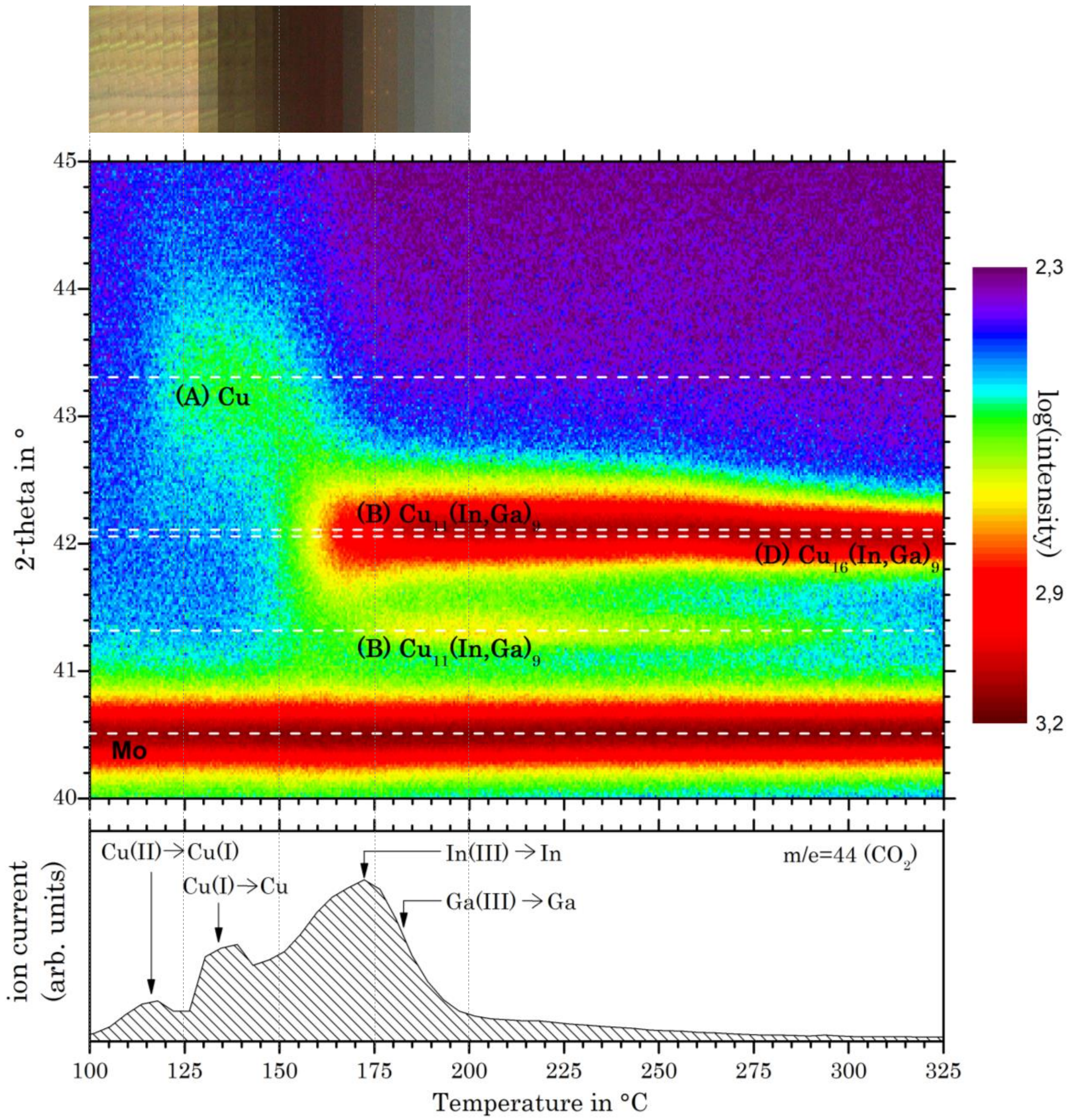

Figure 25: Top: Photographs (every 5 K) of a liquid layer deposited on glass heated from 100°C to 200°C on a hotplate with a heating ramp of 5 K/min. Center: In-situ XRD pattern of the drying of a ternary ink between 100 and 325°C. The color coded intensities are plotted

in a logarithmic scale. Bottom: MS data of a ternary ink heated up to 325°C. Plotted is the signal of ions with m/e=44 (CO_2).

The second peak in the CO_2 signal belongs to the formation of metallic Cu which occurs in the same temperature rage. The copper-(111) peak is broad indicating a short crystal coherence length due to an insufficient thermal energy for the crystallization and the small sizes of the emerging nanoparticles in the still existing organic matrix.

The MS data suggests the formation of metallic indium above 150°C with a CO_2 signal peak maximum at 175°C. However, the presence of pure crystalline indium could not be confirmed with the i-XRD. Instead, new peaks starting at 160°C (most prominent at 42.07° and 41.4°) signalize the formation of a $Cu_{11}In_9$ alloy (JCPDS #41-0883) corresponding to point B in Figure 24. This transition occurs close to the melting point of indium (157°C) and the decomposition temperature of the metastable $CuIn_2$ (153°C [124]) resulting in an increased mobility of the indium atoms. At the same time, the copper (111) peak disappears suggesting the crystalline parts of the final precursor layer consist of a copper indium alloy. A possible explanation for the direct conversion of indium to the CuIn-alloy could be a catalytically controlled indium reduction on the surface of the present copper nanoparticles.

The TG-MS measurement in section 3.4.1.2 carried out on pure Ga inks showed the decomposition of gallium formate above 170°C and the probable formation of the metal oxide Ga_2O_3. A crystalline gallium oxide reflex could not be found the i-XRD pattern. However, the absence of any crystalline phases containing Ga in this temperature range has also been reported in the literature [125]. A significant difference to the unary gallium ink is the presence of metallic copper above 130°C. In fact, by the time of the gallium formate decomposition, most of the copper ions have already been reduced. Thus, the gallium ions in the mixture can be reduced on the copper surface resulting in a copper gallium alloy (probably Cu_9Ga_4 [126]). The main advantage of this reaction pathway is the additional enthalpy of fusion. Li et al. measured this enthalpy for Ga in Cu at a mol fraction of about 30% Ga by differential scanning calometry. The result was around 10-12 kJ/mol_{Ga} [127]. Unfortunately it is hard to identify this Cu_9Ga_4 phase in the i-XRD graph due to the similar peak positions with the $Cu_{11}In_9$ phases. At higher temperatures Purwins et al. observed the incorporation and substitution of gallium atoms in copper-indium alloys and the formation of $Cu_{11}(In,Ga)_9$ [128]. Thus, the possible phase formation paths up to 300°C with the initial stoichiometry Cu0.9In0.8Ga0.2 can be written as following (based on [126]).

Up to 170°C $9Cu + 8In + 2Ga \rightarrow 0.4Cu_{11}In_9 + 0.5Cu_9Ga_4 + 4.4In$ 3-34

Up to 306°C $0.4Cu_{11}In_9 + 0.5Cu_9Ga_4 + 5.3In \rightarrow 0.82Cu_{11}(In,Ga)_9 + 2.6In$ 3-35

The i-XRD results show that the proposed $Cu_{11}(In,Ga)_9$ phase is present for more than 100 K with a decreasing peak width indicating an increasing crystal coherence length. Above 280°C, a phase transition can be observed visible by a peak shift of the strong $Cu_{11}(In,Ga)_9$ (511)/(313)/(202) reflex at 42.2° and the disappearing $Cu_{11}(In,Ga)_9$ (112) reflex at 41.4°. The transition results in a stable η-phase of $Cu_{16}(In,Ga)_9$ which has also been observed by Purwins [128] ($Cu_{16}In_9$ JCPDS #42-1475). This is in agreement with the phase diagram predicting a peritectic decomposition of $Cu_{11}In_9$ at 306°C (point C in Figure 24). The proposed decomposition reaction is shown below.

Above 306°C $0.82Cu_{11}(In,Ga)_9 + 2.6In \rightarrow 0.56Cu_{16}(In,Ga)_9 + 5In$ 3-36

The discrepancy in the temperatures being about 25 K lower in our experiment than expected by the phase diagram can be attributed to the measurement position of the thermocouple. Due to the heating mechanism by infra red irradiation, the temperature of the thin layer on the surface of the substrate is rising faster than the temperature measured in the oven wall.

To investigate further phase transitions in the ternary Cu-In-Ga layers above 325°C, wide-angle ex-situ XRD measurements of samples alloyed at 200–600°C have been performed. Therefore several layers have been deposited identically on glass followed by a heating up to 200°C. Thereafter the substrates have been alloyed for two additional minutes on a hotplate preheated with the intended different temperatures followed by a fast cool down. Figure 26 shows the diffraction pattern of the samples. As expected by the i-XRD analysis, the only crystalline phase present at 200°C is $Cu_{11}(In,Ga)_9$ decomposing at 300°C and above to $Cu_{16}(In,Ga)_9$. However, also small reflexes belonging to $Cu_{11}(In,Ga)_9$ are visible in the samples heated above 400°C probably due to an insufficiently fast cool down rate [129]. Furthermore, the XRD patterns indicate the presence of a crystalline indium phase above 300°C that can be observed by the indium reflex. This can be explained by an enrichment of copper in the metal alloy after the phase transition leading to a phase separation of liquid indium (point D in Figure 24). With higher temperatures this indium reflex increases due to a decreasing solubility of indium in the alloy (Figure 24). The formation of a separated indium phase is an important observation and its influence on the precursor layers is further discussed in section 3.5.3.

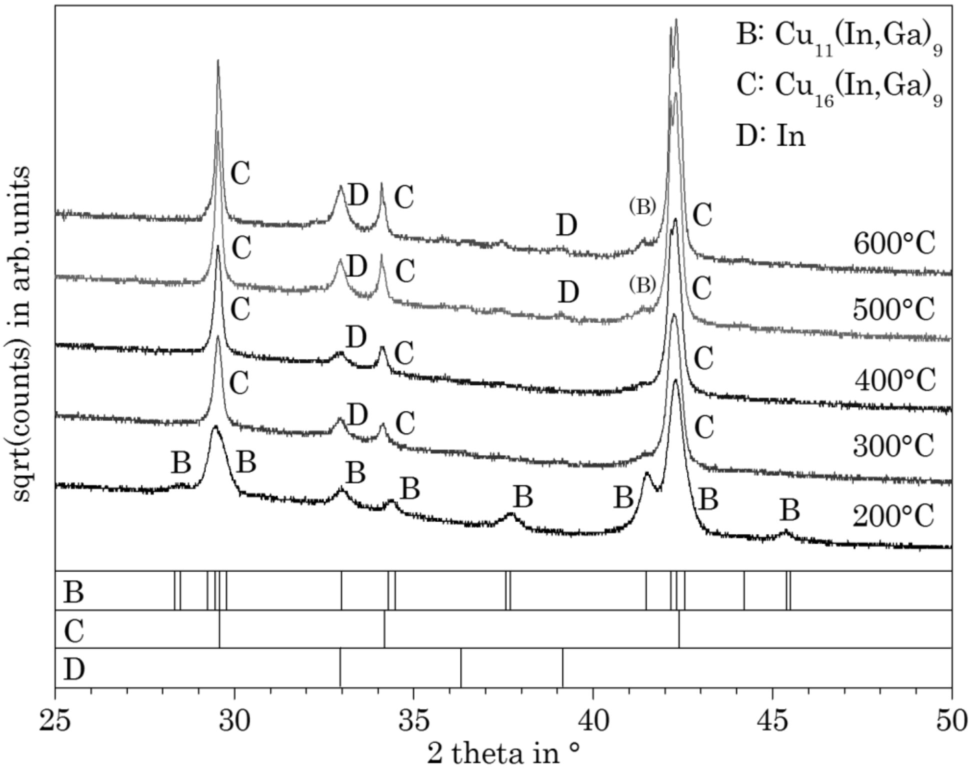

Figure 26: Ex-situ XRD of alloyed layers on glass tempered for two additional minutes at 200 to 600°C.

3.4.3 Characterization of processed layers

The TG-MS and the i-XRD measurements presented in the previous section proved that copper and indium formate can be reduced directly to their respective metals and that heating of a pure gallium formate containing ink likely resulted in gallium oxide. In this section the reaction products of the three different unary metal inks as well as a mixture suitable for solar cell processing are characterized in terms of morphology and composition. Therefore the inks have been processed to uniform liquid films and consequently heated to 200°C. As method of choice SEM has been chosen to evaluate the layers.

3.4.3.1 Unary inks

This section evaluates the morphology and composition of layers processed from inks containing only one of the respective metal formates. The results are discussed in detail due to their importance for the interpretation of the ternary layer which is the topic of the next section.

Copper layer

Metallic layers processed from copper salts have been investigated intensively in the literature due to their application as metallic thin film material for various fields including printed circuit boards or nonlinear optical devices. The advantages of copper as material are a low bulk resistivity and thermal stability [130], [131]. Layers of nanoparticles have been synthesized using various techniques and precursor chemicals [132]–[134]. Thermal decomposition is one of the most common methods. In this context, a detailed review on the thermal decomposition of ionic solids including organic acids has been published by Galwey et al. [117]. In their work the formation of elemental nanoparticles from solid copper formate is discussed. Suitable layers for the mentioned applications require small particles with a narrow mean diameter distribution that increase the chances of a sufficiently low porosity. Rosenband et al. published a report on nanoparticles made from copper formate [78]. They described the changes in the morphology and particle size distribution depending on the presence of several additives including solvents and dispersants. Liquid additives have been found to increase the particle size while the presence of salts like NaCl led to the smallest nanoparticles. It has to be noted that the mechanisms leading to these results are very complex. Several studies report Ostwald ripening as the dominant mechanism of growth while other results are significantly diverging [135]. Thus, the following experimental findings are discussed on a phenomenological basis.

In the case of copper the influence of two liquid additives has been evaluated and compared to a pure solution of copper formate in TMG (sample A). As first additive dimethylformamid (DMF) has been chosen for sample B due to its high boiling point of 153°C which is in the same temperature region as the solvent TMG (T_b=160°C). The solvent mass ratio has been set to 2:1 (TMG:DMF). Because of the high boiling point DMF is expected to be present during the particle formation which might have a strong effect on the resulting morphology. Methanol with a significantly lower boiling point of 56°C has been added to the pure TMG ink in the third sample C in the same mass ratio. As has been discussed in section 2.3.2, methanol has the advantage to decrease the film viscosity and the surface tension which can be beneficial for the deposition of uniform liquid layers. In order to make the results between the three experiments comparable, the drying temperature has been set to a high initial value above the reduction temperature of the copper ions (200°C). With these settings the copper reduction has been expected to occur with all solvents present. SEM images and AFM surface profiles of the resulting layers are shown in Figure 27.

The images on top depict top view SEM images in two magnifications. It is obvious that there are significant differences between the evaluated samples. Beginning with the pure TMG ink, the annealing leads to the smallest particles while the addition of DMF results in fewer but larger particles. The particle alignment is also different with rather loose particles in sample A, a chain-like structure in sample B and a flat and sintered looking structure in sample C. The separated particles in A compared to the aggregates in B and C might be an indication for a different nucleation mechanism and/or location. The 3D visualizations at the bottom depict the surface profiles measured by atomic force microscopy (AFM). Overall, the profiles confirm the already discussed observations for example the differences in the particle diameters. However, additional information about the film height distribution can be derived. While sample A and C have a similar roughness of ±350 nm, sample B appears to be significantly more porous with a total film height deviation of ±800 nm. This observation is in agreement with the SEM pictures clearly showing areas of the uncovered substrate as well as large particle agglomerations.

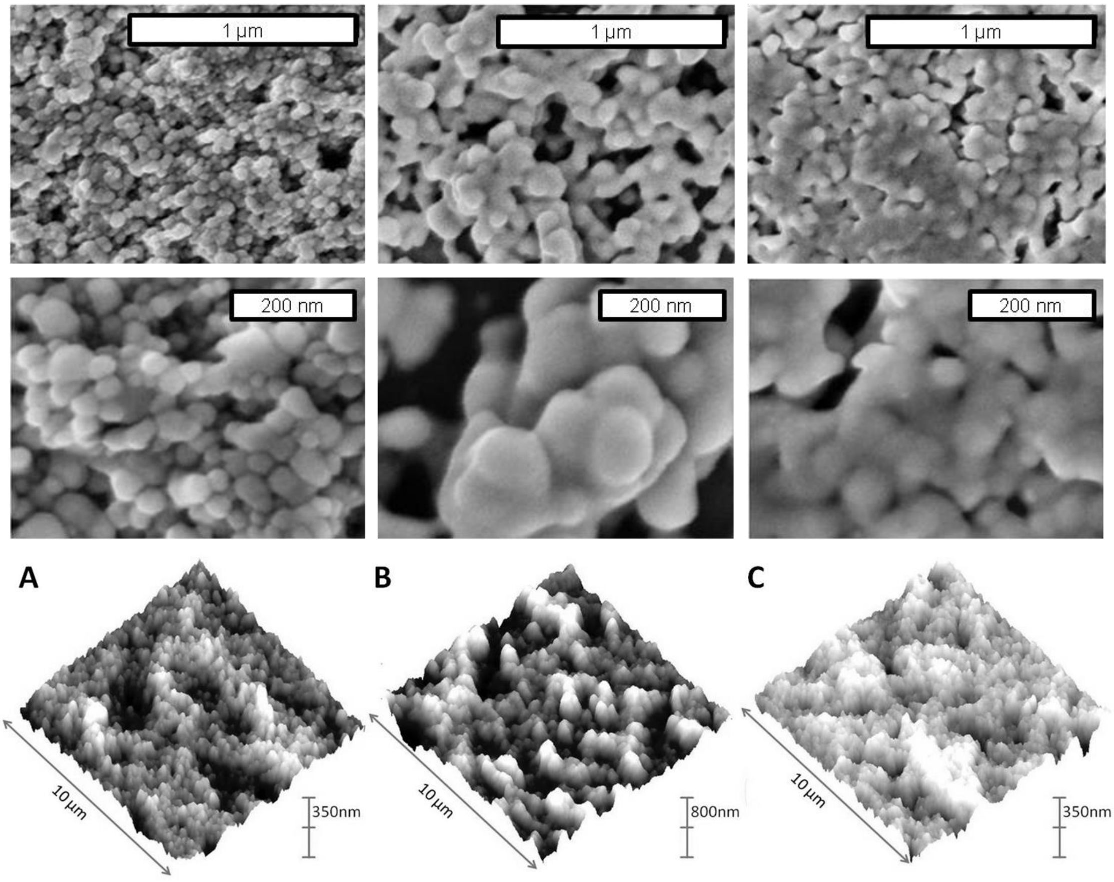

Figure 27: SEM top view and AFM surface profiles of copper nanoparticle layers processed with different solvent mixtures. A: Reference with pure TMG. B: Mixture of TMG and DMF. C: Mixture of TMG and methanol.

Additionally to the ink additives, the size and morphology of the nanoparticles is also dependent on the process temperature that directly influences the kinetics of the redox-reaction and therefore the prevailing nucleation mechanisms and the particle growth [135], [136]. Rosenband et al. measured an increase in particle size with higher temperatures independent of the used additives [78]. In this work copper formate inks with TMG as solvent have been processed at 150 and 200°C (below and above the boiling point of the solvent). The resulting SEM images are shown in Figure 28. In comparison to the already discussed sample processed at 200°C showing small nanoparticles with a narrow mean diameter distribution, the layer prepared at 150°C reveals significantly larger particles. The image also shows that the diameters are varying from below 50 nm to more than 400 nm. An explanation for the differences in the morphology might be the slowed down reaction kinetics at 150°C that might have led to less nucleation centers growing to larger particles and vice versa the formation of significantly more growth centers at 200°C.

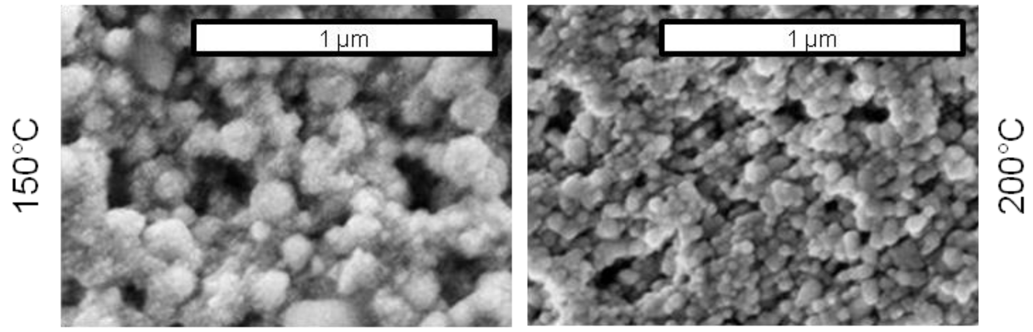

Figure 28: SEM images of copper layers processed from an ink with TMG on glass at 150 and 200°C. The right layer at 200°C corresponds to sample A in Figure 27.

Indium layer

In indium formate containing inks the anion decomposes at temperatures above 160°C. Deposited liquid thin films heated to 200°C result in highly transparent grey layers on the surface of the substrate. SEM analyses of these layers reveal the formation of separated spherical particles with a broad diameter distribution as can be seen in Figure 29. The image shows particles with diameters in the range of several 100 nm which are scattered over the substrate next to small nanoparticle agglomerations with a total size below 50 nm. Experiments with larger ink volumes and correspondingly a higher amount of metal as well as longer solvent evaporation times led to the formation of a single pearl with a diameter above 100 µm. These results can be explained by the low melting point of elemental indium which lies within the temperature range of the drying process ($T_{m,In}$=156°C).

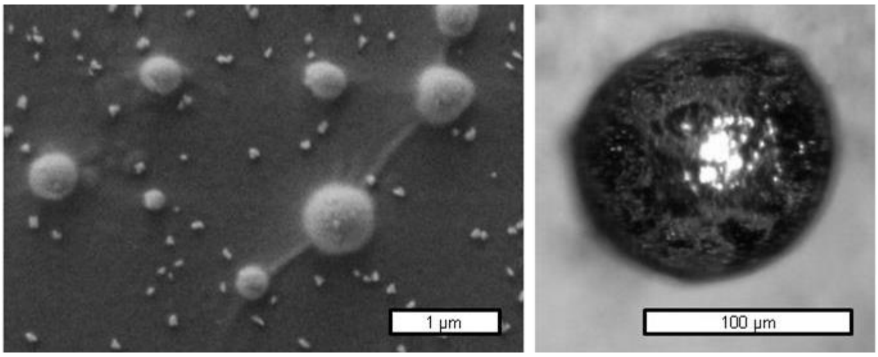

Figure 29: Left: SEM image of solidified elemental In-droplets on a glass substrate. Right: Microscopic picture of a single pearl resulting from the heating of high ink volumes.

In contrast to the independent formation of solid copper particles stacking up to a porous layer, the reduction of indium ions above 160°C instantly results in separated liquid droplets dispersed in the bulk of the evaporating wet film. These highly mobile droplets tend to minimize their surface energy by coalescing when brought in contact with nearby droplets. In sufficiently thin wet films, this phenomenon eventually ends when all accessible indium droplets in range have coalesced to separated pearls. Due to the high surface tension of liquid indium these pearls keep their spherical shape on the surface of the substrate even after the solvent evaporation. Larger volumes of ink and accordingly liquid metallic indium decrease the space between the individual droplets leading to the observed single pearl after the solidification.

Gallium layer

The thermogravimetric analysis of a pure gallium ink discussed in section 3.4.1.2 showed a significantly higher residual weight than expected by the initial metal mass and the formation of considerable amounts of carbon monoxide during the ink heating. Both points suggest the formation of gallium oxide. Another difference to the copper and indium containing inks is that the anion decomposition occurs mostly after the solvent evaporation and therefore does not take place in the liquid film. Hence, the salt most likely precipitates on the surface of the substrate prior to the decomposition. The result is a flat and solid glass-like structure at around 160°C that decays to small fragments above 180°C. The morphology of the resulting layers is shown in Figure 30.

The microscopic picture on the left shows large transparent fragments with dimensions of several millimeters. The SEM images on the right reveal the fine structure of a thinner layer consisting of cracked flakes with diameters of several 100 µm and an approximate thickness of around 1.5 µm.

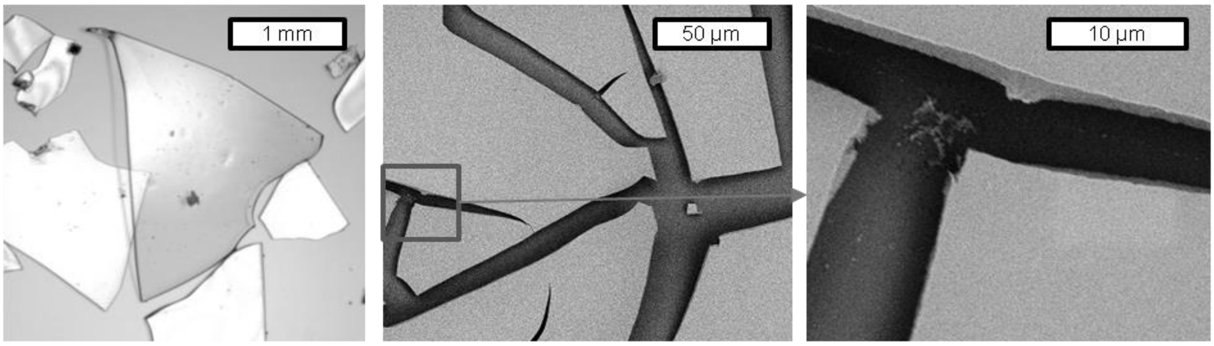

Figure 30: Morphology of layers processed from Ga-inks on glass. Left: Light microscopic image of large transparent flakes. Center and right: SEM top view images.

The composition of the flakes has been further characterized by Fourier transformed infra red analysis (FT-IR). The results are shown in Figure 31. The graph reveals a high transmission of IR radiation at wave numbers above 1000 cm^{-1} with negligible absorption bands in the range of 1500 cm^{-1} suggesting that the solvents have evaporated completely. At lower wave numbers a strong absorption band suggests the presence of an oxide. The gallium oxide thin films reported by Ortiz et al. have a similar IR spectrum [137]. Thus, the IR measurement further strengthens the hypothesis that the heating of gallium formate containing inks leads to a complete evaporation of the organic solvents and the formation of Ga_2O_3.

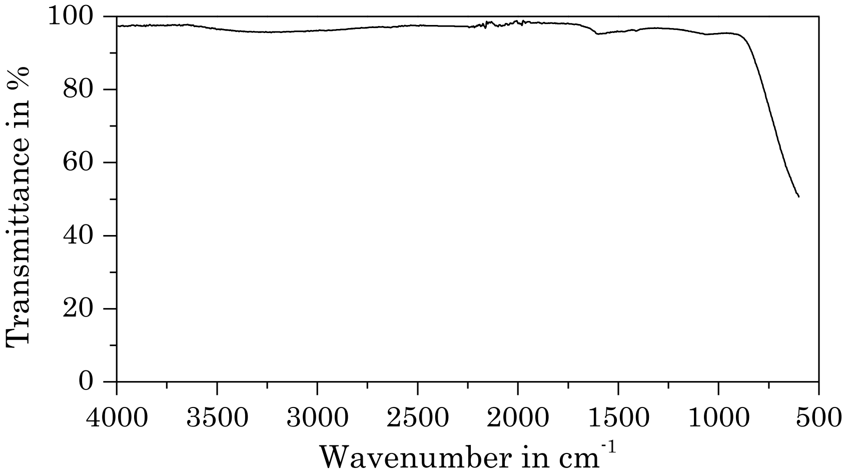

Figure 31: FT-IR spectra of a layer processed from a Ga-formate containing ink.

Summary of the unary inks

In this section the residues of a heating of unary inks has been investigated. Pure copper inks led to porous layers consisting of small metallic nanoparticles with diameters in the range of 50 nm. The morphology of these layers and also the individual particles has been shown to be highly dependent on additional solvents as well as the processing temperature. Indium ions could also be reduced to the metallic state. The individual liquid metal droplets emerging during the tempering coalesced due to the applied processing temperature above the melting point. The resulting large droplets eventually solidified to spherical particles after cooling. Gallium as the metal with the lowest standard electrode potential could not be reduced to its elemental form. Instead, a cracked layer consisting of gallium oxide flakes could be observed.

3.4.3.2 Ternary mixtures

The target morphology of ternary precursor layers consists of flat, crack free and dense structures with a sufficiently low porosity. This way a transformation to dense chalcopyrites can be expected. In section 3.4.3.1 the individual reaction products and layer morphologies of the three different unary metal inks have been investigated. Precursor layers made from inks containing the ternary salt mixture, however, look significantly different. In order to explain the following results two points are particularly important that deviate from the unary experiments.

Firstly, the interactions between the reduced metals have a huge influence on the morphology. The i-XRD measurements discussed in section 3.4.2 showed the consecutive metal ion reductions at different temperatures and the formation of alloys in agreement with the phase diagrams. Secondly, the previous section revealed that gallium ions can’t be reduced with formate ions to the metallic state. Instead, heating of pure gallium inks led to the formation of Ga_2O_3. In the ternary ink, however, no gallium oxide could be detected. A possible explanation is that gallium cations can get reduced in the presence of elemental copper which has a high Ga solubility (see also section 3.4.2).

Two different process conditions have been chosen for the layer processing. Within these experiments all parameters have been kept constant beside the annealing routine.

A: For experiment A, a low starting temperature around the reduction point of the copper ions (~130°C) has been chosen followed by a slow heating ramp up to 200°C with 10 K/min. With these parameters the individual metal ions are reduced consecutively. This experiment also allows a controlled evaporation of the solvents and a separated decomposition of the salt anions.

B: In experiment B the annealing has been carried out at a constantly high temperature above the decomposition point of all three metal salts (~200°C). Thus, the reactions of the three metal ions occur simultaneously. A disadvantage of this routine is the fast evaporation of the solvents leading to a significant gas evolution.

Also the instantaneous formation of large amounts of carbon dioxide might be critical for the layer integrity.

Because an in-situ investigation of the morphological changes is not possible with the available methods, the following discussion is based on the SEM images of the resulting precursor layers. Separate models explaining the experiments A and B have been developed which include a comparison to the investigated unary inks and the previously presented crystalline phase formations derived from the i-XRD measurements.

A: Consecutive ion reduction by slowly increasing temperature

Figure 32 shows the morphology of the processed precursor layer. Porous structures consisting of sponge-like agglomerations of nanoparticles can be seen with a total film height in the range of 5 µm. On top of this layer a thin dense skin is visible. In the bulk large spherical particles can be observed.

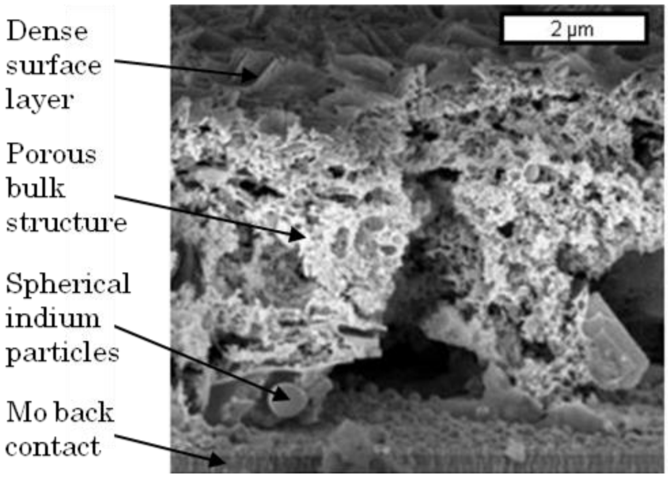

Figure 32: Experiment A. Cross sectional SEM image of a layer processed from a CuInGa ink by a slow consecutive reduction of the different metal ions.

The mechanism leading to the formation of these structures can be explained by a model illustrated schematically in Figure 33. Beginning with the temperature region around 130°C the previous TG results suggest a fast reduction of copper ions as well as a negligible slow reaction kinetic for indium and gallium formate. Due to the high wet film thickness in this temperature range consisting mostly of the solvent TMG (~25 µm), the particle formation probably occurs independently in the bulk liquid and at the interfaces. With the advancing copper ion reduction, a large fraction of the solvent is evaporating as has been shown by the TG-MS analysis of the ternary ink. Due to the thereby decreasing film height, the highly mobile nanoparticles are approaching each other. In pure copper inks, this would eventually lead to an accumulation of particles on the substrate resulting in a flat layer. In the ternary system, however, indium ions are getting reduced above 160°C in the still existing liquid film. The reduction most likely takes place on the surface of the already present copper nanoparticles leading to the observed $Cu_{11}In_9$ phase measured above 160°C. Yet, the alloy formation is slow [138] which is why the liquid indium shell has time to pin particles together that get in contact. Eventually this leads to interconnections over large areas which would explain the observed highly porous sponge like structures. At some point the copper rich $Cu_{11}(In,Ga)_9$ alloy is saturated and can't incorporate more group III elements. Due to the initial Cu/(Ga+In) ratio of 0.9, about 25% of the group III elements can't be incorporated. In agreement with the copper-indium phase diagram (Figure 24), this effect necessarily leads to the formation of a pure liquid indium phase forming highly mobile droplets.

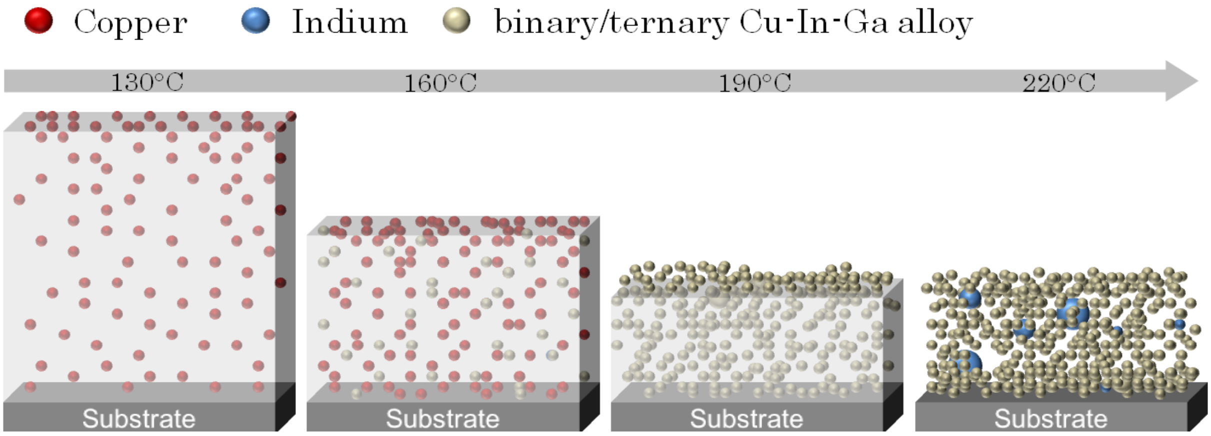

Figure 33: Schematic model of the metal layer formation at slow heating rates (experiment A). Subsequent formation of Cu starting around 130 and In/Ga above 160°C on the copper surface leading to a phase transition to CuInGa alloy particles. This results in a limited particle mobility and thus a porous structure. The formation of small indium droplets due to the saturation of the copper rich alloy occurs above 190°C.

B: Simultaneous reduction by isothermal heating

In experiment A the slow consecutive reduction of the three metals led to highly porous structures probably due to a pinning of the separately emerging alloy nanoparticles. The formation kinetics of the intermetallic $Cu_{11}(In,Ga)_9$ alloy is known to be diffusion controlled and rather slow [138]. Therefore an enhanced reaction speed should inhibit the pinning due to a faster particle formation and solvent evaporation. This hypothesis has been implemented into this experiment by an isothermal annealing of a ternary CIG containing liquid film at 200°C. The resulting layer is shown in Figure 34 revealing a completely different morphology. Under these conditions the surface of the substrate is only partially covered with sintered particle agglomerations. The size of the individual structures is in the range of 1-2 μm. Most of them are further interconnected to clusters.

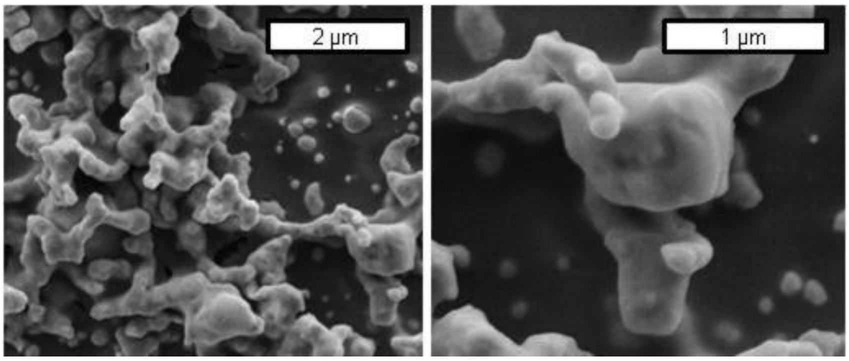

Figure 34: Experiment B. SEM top view images of a CIG layer processed by isothermal heating.

In Figure 35 a proposed model explaining the result of the isothermal tempering experiment is depicted. Due to the elevated hot plate temperature of 200°C the ink quickly reaches very high temperatures up to the boiling point of the solvent TMG around 160°C. Keeping in mind the high concentration of dissolved salts an additional significant boiling point elevation can be assumed. In any case, the reductions of Cu and In/Ga ions are initiated almost simultaneously in this temperature range. Thus, in contrast to the previous experiment the emerging liquid indium droplets don't have enough time to alloy with copper to the thermodynamically favorable $Cu_{11}(In,Ga)_9$ alloy. Instead the droplets coalesce to larger drops at the surface of the substrate. With advancing time the residual solvents evaporate resulting in a compaction of the metals which eventually form an alloy and solidify to the visible complex structures.

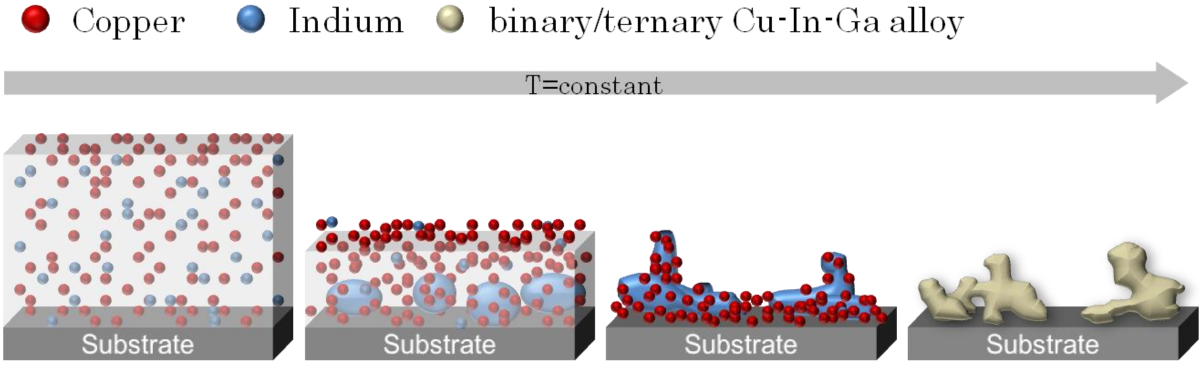

Figure 35: Schematic model of the film formation at a constant high temperature annealing (experiment B, T=200°C). The metals are reduced simultaneously forming small copper nanoparticles and liquid indium droplets that coalescent to larger drops. The drops are sinking to the surface of the substrate where they eventually alloy with copper and solidify to non homogeneous complex structures.

Summary of the ternary ink

In this section the particle and phase formation behavior of ternary CIG inks has been evaluated under two annealing conditions. In experiment A, the consecutive ion reduction has been investigated by a slow heating ramp. In contrast to this, experiment B focused on the simultaneous ion reduction by an isothermal annealing at 200°C. The former led to highly porous structures supposedly due to a pinning of the emerging copper particles in a $Cu_{11}(In,Ga)_9$ alloy. In B a highly mobile liquid indium phase is present in the ink which solidifies with copper on the surface in the same alloy as complex structures. Due to the high porosity of layer A and the incoherent metal layer in experiment B, both morphologies are inapplicable for solar cell devices.

3.5 Homogenization and densification of the layer

In the previous section 3.4 the metal formation as a result of the reduction of the metal ions has been presented. It could be shown that the tempering conditions have a huge impact on the layer morphology resulting either in porous layers or large separated structures. For an efficient energy conversion CIGS solar cells require dense and homogeneous pin-hole free layers of chalcopyrite crystals with a film thickness between 1 and 3 µm. These requirements can be transferred to the metallic precursor layer. In this context the observed morphologies of the experiments A and B discussed in section 3.4 are both unsuitable for a further solar cell processing. Therefore this section focuses on the homogenization and densification of the precursor layer. The proposed method is based on an additional additive that forms a stable organic matrix during the solvent evaporation and the metal ion reduction. In section 3.5.3 a model for the influence of this matrix on the precursor morphology is discussed. The results have been published in Thin Solid Films [74].

3.5.1 The organic matrix

Many metal salt based approaches published in the literature use an organic matrix to stabilize the intermediate layer after the solvent evaporation. In most cases a high molecular organic polymer is used, e.g. ethylcellulose [52], polyvenylacetate [53] or polymethyl methacrylate [54] which have poor decomposition properties (see section 1.3.2.2). In this section a new method is proposed based on an intermediately forming polymer consisting of copper formate and a low molecular additive which can complex and bridge between metal ions. Thus, the matrix consists of metal-additive chains connected by weak Cu-N bindings. These connections can be broken at elevated temperatures releasing the small additive molecules which have a good decomposition behavior compared to the organic polymer binders. The molecular structure of this polymer is investigated in detail beginning with the physical and chemical properties of the additive and its abilities to form complexes with transition metals. Finally, several new copper-additive complexes are described.

3.5.1.1 Triazoles

The used additive is a derivative of 1,2,4-triazole (TA). Because of the similar complexation behavior, this section begins with a short introduction to the TA chemistry. TAs are heterocycles consisting of three N atoms and two C atoms as can be seen in Figure 36.

Depending on the atom alignment, three tautomeric hydrogen positions are known. In the solid state the hydrogen is bound to N1 giving the molecule an asymmetric arrangement [139]. Unless stated otherwise all triazoles and triazole derivatives mentioned in the following sections refer to this isomeric core structure.

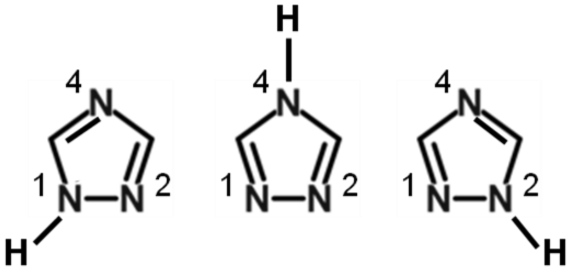

Figure 36: Chemical structure of the three tautomers of the 1,2,4-triazole molecule.

TAs are versatile ligands that can form complexes with several metal cations. They have been focus of intense research for many years due to similar metal complexes appearing in nature, e.g. in the form of metallo-proteins. Many TAs are also used in fungicides, herbicides, for the antibiotics syntheses or as Pt(II) complexes exhibiting anti tumor activity [140]. The coordination properties of triazoles can be attributed to the position of the donor atoms in the ring allowing a complexation of a single cation as well as a bridging between two or more ions. The vast majority of published metal-triazole structures are oligo- and polynuclear and only a few mononuclear compounds are known to date. The structure of the resulting complex depends mostly on the ligands and the metal. A comprehensive study of metal-triazole compounds can be found here [139].

The possible bridging modes of TA between two or more ions are shown in Figure 37. N2-N4 bridging usually leads to two-dimensional structures. More common and also mostly found in N4-substituted TAs are N1-N2 bridges. In this mode the distance between the metal ions gets down to about 400pm. Depending on the substituent at 3 and/or 5 the number of TAs bridging between two ions can be one, two or three. Example complex structures have been achieved with TA and Cu, Co, Mn, Zn or Fe thiocyanate, Mn sulfate and Cu or Fe chloride.

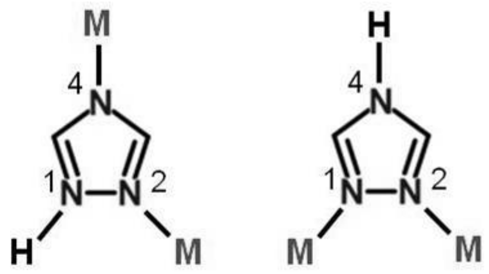

Figure 37: Coordination modes of 1,2,4-triazole for bridges between two metal ions [139].

3.5.1.2 4-amino-1,2,4-triazole

4-amino-1,2,4-triazole (4ATA) is a derivative of the 1,2,4-triazole and is used as additive in this process. The difference is the amino group at the N4 atom as can be seen in Figure 38. In this section the physical properties which are important for the ink process are discussed.

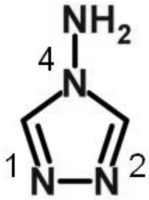

Figure 38: Chemical structure of the 4-amino-1,2,4-triazole molecule.

4ATA is a colorless and odorless compound that is solid at standard conditions having a melting point of 85°C. In order to evaluate the high temperature behavior of the pure compound TG-MS analyses have been carried out. Figure 39 shows the mass loss of pure 4ATA measured with a heating ramp of 10 K/min in N_2 atmosphere. The results indicate an evaporation/decomposition temperature around 250°C and a residual mass fraction of 2 % at 600°C. The simultaneously measured ion currents show a high number of molecule fragments with a pronounced peak at m/e=84 corresponding to the pristine molecule. The peak maximum is shifted to higher temperatures than expected by the TG mass loss due to the remote position of the mass spectrometer about 15 cm away from the sample.

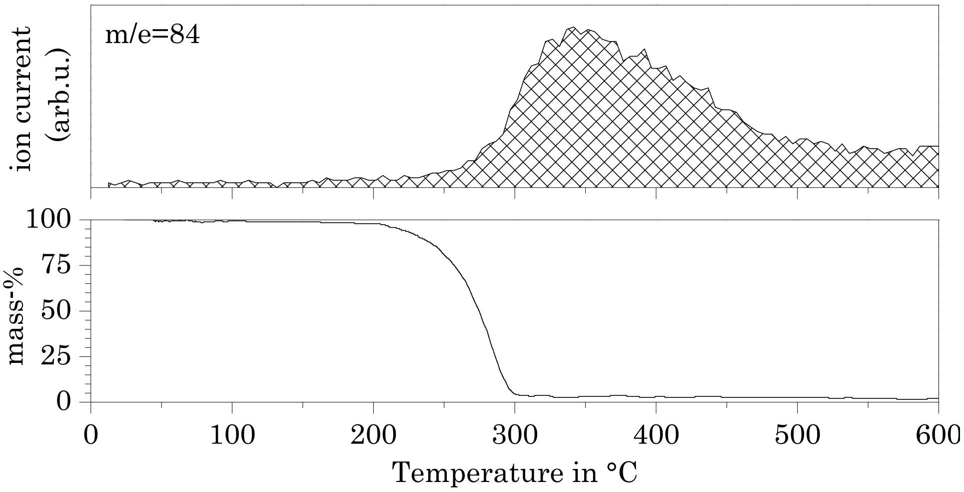

Figure 39: Bottom: TG mass loss of pure 4ATA at a heating ramp of 10 K/min in nitrogen. Top: corresponding ion current with m/e=84 (4ATA). Due to the high evaporation temperature and the local distance between the sample and the mass spectrometer the MS-peak is shifted to higher temperatures.

A Fourier transformed infra red analysis has been carried out on pure 4ATA and the decomposition residues of a 4ATA sample heated at 300°C under N_2 for several minutes. The results are depicted in Figure 40. The pure material shows various sharp absorption bands especially in the region below 1700 cm^{-1} due to the many possible vibration modes in the molecule. The two strong absorptions at 3250 and 3100 cm^{-1} belong to the amine N-H stretches, the absorption around 3030 cm^{-1} to the aromatic C-H stretches. The tempered sample has lost most of the sharp bands, especially the mentioned strong absorptions between 3000 and 3300 cm^{-1} which is in agreement with the publication by Li et al. proposing a degradation of 4ATA to a triazole ring based on their MS-results [141]. In the fingerprint area between 1750 and 1000 cm^{-1} one broad peak can be observed. This indicates the formation of various decomposition products without any long range order. The results are further discussed in section 3.5.2.1.

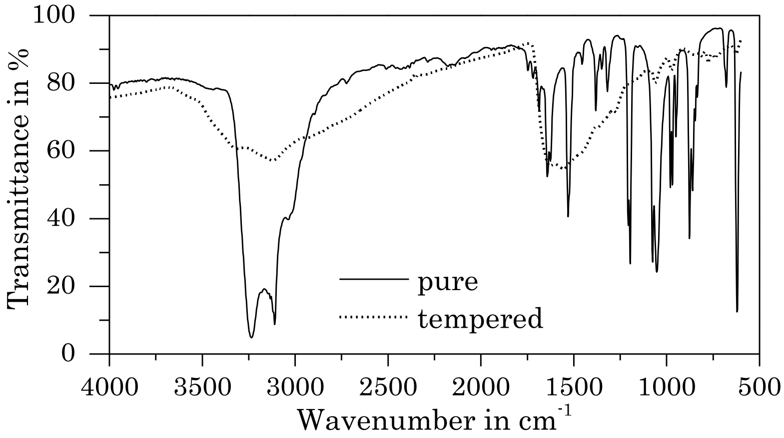

Figure 40: FTIR spectra of pure 4ATA (solid line) and a 4ATA sample tempered at 300°C for several minutes (dashed line). The result of the heated sample suggests a high degree of decomposition. The measurements have been carried out in transmission mode.

3.5.1.3 Transition metal complexes with 4ATA

The difference in terms of complexation behavior between 4ATA and the amino free core structure TA is the substitution of the H atom at N4 with an amino group. Therefore the complexing and especially bridging properties are limited to the N1-N2 positions. So far several structures have been published in the literature. The transition metal nitrates (of Fe, Co, Ni, Cu, Cd and Zn) for example have been reported to form similar structure with 4ATA with the composition $M(4ATA)_3(NO_3)_2 \cdot xH_2O$ (M=metal, x=0.5, 1, 1.5) [139]. For iron(II) the same structure could be synthesized with iodide and thiocyanate as anion [142].

A literature search for the metal formates with TA or the 4ATA used in this thesis revealed no published structures. From the three metals ions so far only copper 4ATA complexes have been published with different anions. Refat et al. could show with IR-spectroscopy that in adducts synthesized by a solid state route the Cu^{2+} ion of $CuCl_2$ is coordinating at the N1 atoms in the heterocycle [143]. A mixture of dissolved $CuCl_2$ with 4ATA (1:1) in H_2O and HCl yielded a polymeric chain which has also been found with TA [144], [145]. In this structure one single 4ATA molecule and two chlorine ions bridge between pairs of copper ions along polynuclear chains. The same structure has also been isolated from solutions containing $CuBr_2$ and TA.

3.5.1.4 $Cu(HCO_2)_2$-4ATA polymers

In the previous section the general complex formation abilities of 4ATA have been introduced and examples with transition metals have been discussed. In this context, the two polymers made with $CuCl_2$ and TA / 4ATA are of special interest due to the chemical similarities to the investigated ink system. Thus, several experiments have been carried out with copper formate to confirm the formation of similar polymers. As a result three new compounds have been synthesized, one at room temperature (sample A) and two between 50 and 100°C (sample B1 and B2). The synthesis procedure is described in appendix B.

Samples of A and B1 have been analyzed using single crystal XRD to determine the molecular structure. The measurements have been executed at the University of Tübingen and the original data are presented in appendix C. Figure 41 A shows the first compound which is forming at room temperature. The polymer consists of a Cu(II)-formate-Cu(II) backbone connected by the oxygen atoms of the formate anion. On the sides of this chain one formate and two 4ATA ligands are present at every copper cation. Therefore the molar ratio of Cu:4ATA in this molecule is 1:2. The Cu(II) ions are linked to 4ATA at the N1/N2 position.

The molecular structure of sample B1 shown in Figure 41 is significantly different. Again a polymeric chain has formed, however, the molecule alignment has changed and the backbone consists of a double bridge. The first bridge is represented by Cu(II)-4ATA-Cu(II) with a connection established through the N1-N2 atoms of 4ATA as has been expected for 4-substituted triazoles. The second bridge consists of Cu(II)-OH-Cu(II) and is therefore established via a hydroxide ion. The presence of the hydroxide ion can be explained by the synthesis routine which has been performed with water as solvent for the intermediate amorphous compound. The water molecules have probably been deprotonated by the basic formate ions. On the sides of this backbone each copper ion is additionally connected to a second formate ion. The molar ratio of Cu:4ATA in this structure is 1:1. These findings can't be transferred directly to the water free inks used for the solar cells. Thus, polymer B1 does not represent a possible candidate for the proposed mechanism. Nevertheless the measured structure gives valuable insights into how the polymer bridging with 4ATA can be established. A similar structure with a 3-5-substituted triazole has been published by Acevedo-Chavez et al. [146].

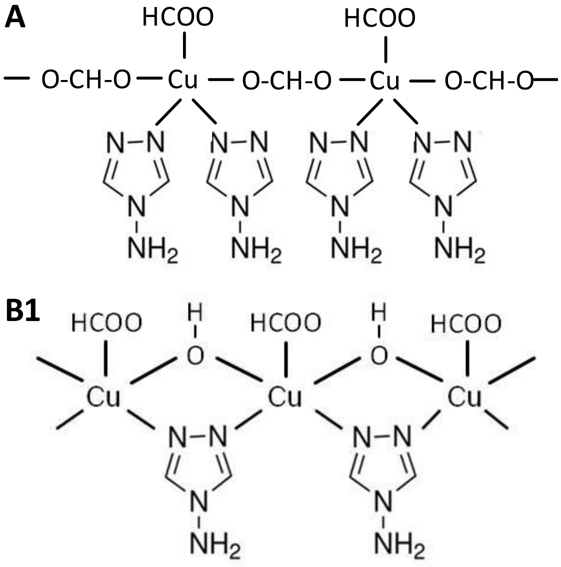

Figure 41: The molecular structures of two polymers identified by single crystal XRD. The samples have been synthesized with copper formate and 4ATA in methanol at room temperature (A) and around 50°C (B1). Additional water was present during the synthesis of B1.

As second characterization method the nitrogen mass fractions of several crystals made with the synthesis routines A and B have been measured by elemental analyses. The intermediate amorphous compound of experiment B yielded various intergrown crystals beside the well crystallized sample B1. The elemental analyses revealed that a second compound has been isolated (B2) having a different elemental composition. The measured amounts of nitrogen, which are characteristic for the amount of incorporated additive molecules, are shown in Table 6.

Table 6: Three molecular structures of polymers separated from copper formate 4ATA solutions and identified by single crystal XRD and elemental analyses.

Sample	Crystal color	Measured N-fraction	Corresponding molecular structure	Calculated N-fraction
A	blue	34.3 %	$[Cu(4ATA)_2(HCO_2)_2]_n$*	34.8 %
B1	blue	26.1 %	$[Cu(4ATA)(HCO_2)(OH)]_n$*	26.5 %
B2	blue	23.1 %	$[Cu(4ATA)(HCO_2)_2]_n$**	23.6 %

*based on single crystal XRD; **based on measured N-fraction and similar literature examples

In sample A the calculated nitrogen mass fraction of 34.3 % fits well to the measured values. From sample B several crystals have been analyzed with varying nitrogen fractions of 26.1 % and 23.1 %. The former corresponds to the discussed crystal structure where a hydroxide group bridges together with the 4ATA molecules due to the presence of water during the synthesis. The second nitrogen value of B2 can be explained by a water free structure with two formate ions at each copper ion. The proposed structure of B2 is shown in Figure 42.

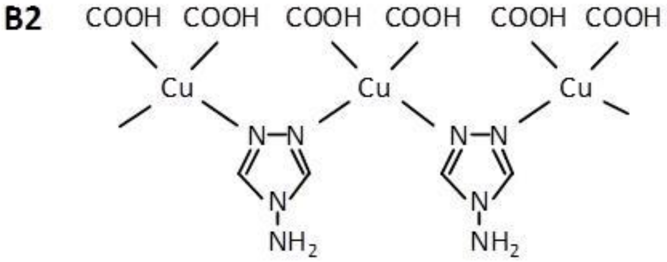

Figure 42: Proposed structure for polymer B2 based on the results of the elemental analysis.

Due to the fact that solar cells are processed at elevated temperatures from water free ink formulations, the proposed polymer B2 is probably the structure occurring during the ink processing. This is also in agreement with polymers synthesized from similar starting materials that have been published in the literature [144], [145].

3.5.2 Influence of the complex on the copper film processing

In section 3.5.1 the formation of polymeric structures with copper formate and 4ATA has been shown. In this section the influence of these compounds on the thermal behavior and the morphology of a pure copper ink are investigated. Thus, TG-MS analyses have been carried out on two copper formate solutions with and without 4ATA. The results are shown in Figure 43. It has to be noted that for clarity issues a higher concentration than normally used in the films has been chosen (used molar ratio of Cu:4ATA = 1:2, standard is 8:1). Beginning with the mass loss curves at the bottom, a comparison between the two inks reveals two distinct areas of interest. In zone A between 140 to 230°C the solution containing 4ATA shows a significantly slowed down mass loss. Because the initial mass fraction of 4ATA in the ink was about 6 mass-% and the measured decomposition temperature of 4ATA starts around 250°C, this observation can't be explained by the pure additive. Thus, the measured slow mass decrease has to be attributed to the presence of a polymer (probably B2) that has been shown to form at elevated temperatures below 100°C.

Further indications for this hypothesis are also given in section 3.5.2.1. Zone A ends around 230°C with a constant residual mass in the range of the additive free ink.

Regarding the solvent evaporation and the metal ion reduction, several differences in the ion currents measured by the MS can be observed. Beginning with carbon dioxide (m/e=44), the typical double peak of the two separated copper ion reductions is replaced by one single peak. This can be explained by the incorporation of the available Cu^{2+} ions in the polymer chain due to the high amount of additive. Therefore the first reduction step diminishes and the measured peak is shifted to higher temperatures corresponding to the reduction of Cu^{+} ions. Following this, the small shoulder between 150 and 200°C indicates the reduction of the missing Cu^{2+} ions from the decomposing polymer. Due to the missing free Cu^{2+} ions in the ink which probably stabilized methanol (m/e=31), the alcohol is less bound in the ink and evaporates significantly earlier (see appendix A and section 3.4.1.2). Most of the TMG (m/e=71) evaporation occurs in the same temperature range as without additive. However, low intensities of the corresponding ions can be measured up to 275°C suggesting that the diffusion of the solvent molecules from the 4ATA containing ink is hindered.

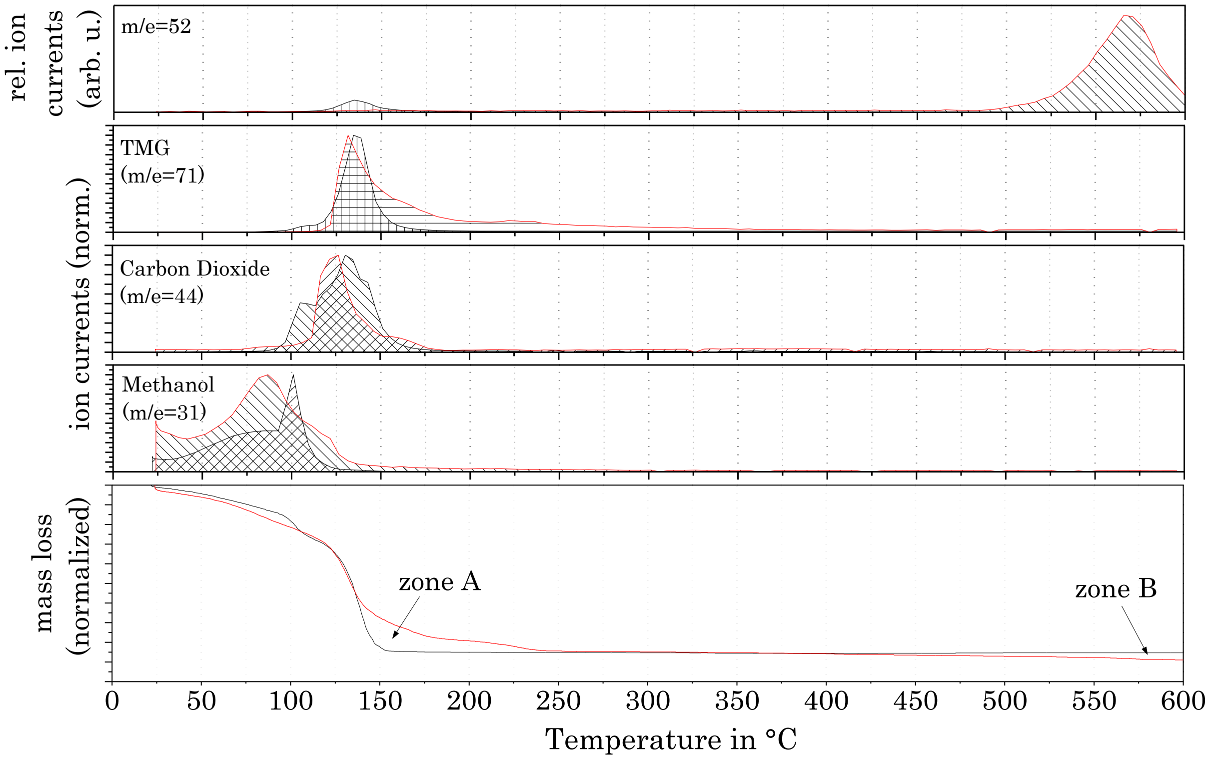

Figure 43: TG-MS of two copper inks with (red) and without 4ATA (black). Four ion currents with m/e = 31, 44, 71 and 52 are plotted against the temperature corresponding to methanol, carbon dioxide, TMG and an unknown compound, respectively.

Above 250°C the remaining mass of the additive containing ink stays constant up to 450…600°C where another decrease of about 3 absolute mass-% follows (zone B). The results of the simultaneously logged ion currents give an idea on what happens here. The topmost MS-graph in Figure 43 shows the measured ions with m/e=52. A peak can be observed at high temperatures above 500°C with a maximum around 575°C exclusively in the sample containing 4ATA. Together with the simultaneously measured ions with m/e=26 (not shown), a strong indication for the formation of C_2N_2 (cyanogen) is given. This molecule is known to be the decomposition product of nitrogen rich organics, e.g. the polymer C_nN_n (paracyanogen). In the present case the residues of the nitrogen rich copper-4ATA polymer probably have a similar polymeric structure. This hypothesis will be further discussed in the following sections.

The influence of the additive on the morphology of copper layers has been investigated by SEM analyses. Layers processed at 200°C from inks without additive (A) have been compared to inks containing 4ATA and solely Cu^+ ions (B) as well as inks with 4ATA and both Cu^{2+} and Cu^+ ions (C). In order to achieve the Cu^{2+} ion free ink, the solution has been stirred above 100°C for several minutes until the blue color disappeared completely. The SEM images of the resulting layers are depicted in Figure 44.

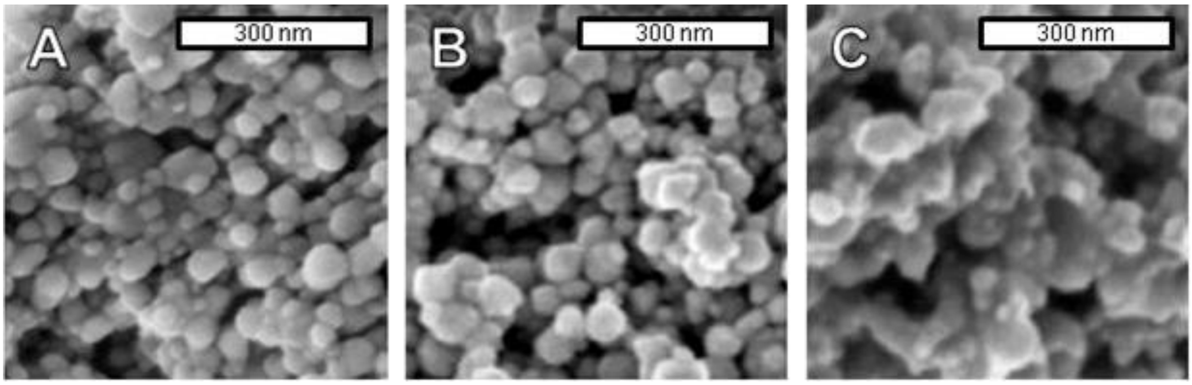

Figure 44: SEM images of layers processed from inks containing A: Cu^{2+}/Cu^+ ions without additive; B: only Cu^+ ions with additive; C: Cu^{2+}/Cu^+ ions with additive.

Sample A and B show comparable morphologies with a dense layer consisting of spherical nanoparticles. Thus, it can be concluded that 4ATA in combination with Cu^+ ions has no visible effect on the layers. This can be explained by the complexation properties of 4ATA. The presented polymers consist of Cu^{2+} ion chains interlinked by the additive molecules. Cu^+ ions most likely do not form these complexes. The influence of the polynucelar compound on the morphology can be seen in the SEM images of layers processed from an ink containing 4ATA and Cu^{2+} ions. Here, the individual particles are smaller and mostly grown together.

3.5.2.1 Organic residues in the precursor layer

In section 3.5.1.2 the physical properties of 4ATA have been discussed. Due to the late decomposition of the pure compound above 250°C the material properties of this additive are challenging for a residue free processing of solar cells. This can be confirmed by TG analysis of 4ATA dissolved in a copper ink which revealed a decomposition of an unknown nitrogen rich compound above 450°C to cyanogen. In order to estimate the amount of organics in the layer as a function of the temperature, elemental analysis on precursor layers have been carried out. For these experiments several layers have been processed identically up to 200°C. Contrary to the TG experiment, a low Cu:4ATA ratio of 8:1 has been used which has been shown to be sufficient for the processing of dense CIG layers. Subsequently, the as prepared samples have been tempered for additional two minutes at different temperatures. The short time interval of the tempering has been chosen to make the results comparable.

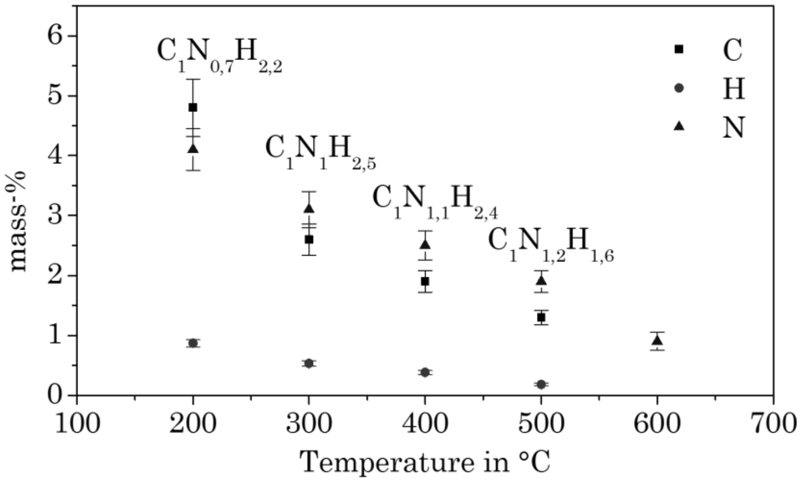

Figure 45: Mass fractions of the elements C, H and N of layers processed up to 200°C followed by a short tempering at 200…600°C for two additional minutes.

Figure 45 shows the resulting amounts of C, N and H each measured at 200, 300, 400 and 500°C as well as the amount of N at 600°C. The graph reveals an almost linear decrease of all elements with a significant drop in carbon between 200 and 300°C. The molecular ratio at 200°C can be explained by residues of the proposed polymer B2 consisting of copper formate and 4ATA (C:N:H=1:1:1.5) and remaining solvent molecules of TMG (C:N:H=1:0.6:2.6). This is consistent with the TG analysis presented in the previous section showing a delayed TMG evaporation up to 275°C. At 300°C the amount of carbon has decreased disproportionately to nitrogen resulting in a C:N ratio of 1:1. In agreement with the TG result this can be explained by the evaporation of the remaining carbon rich TMG. The chemical nature of the residual organics is unknown. However, the high temperatures above the decomposition point of pure 4ATA suggest the formation of various decomposition products similar to the residues found by IR for pure 4ATA. With increasing temperatures the amount of carbon and hydrogen are further decreasing resulting in a slightly nitrogen rich residue. In order to be stable at temperatures this high, the residual compounds might be of polymeric nature. The enrichment of nitrogen is a difference to the known carbon residues in the precursor layers of similar approaches discussed in section 1.3.2.2.

To investigate the chemical nature of the remaining organics IR analyses have been carried out on a copper layer made from an ink containing a high amount of 4ATA (Cu:4ATA = 1:2). In order to minimize the IR signals of residual solvents TMG or methanol the layer has been heated to 300°C. The resulting graphs are compared to the previously discussed transmission IR spectrum of pure 4ATA tempered at the same temperature (section 3.5.1.2). The results are depicted in Figure 46. In transmission mode (dashed lines) the mostly inorganic metallic layer shows a low transmission at longer wave numbers. In the fingerprint region below 1700 cm^{-1} the previously found absorption bands of tempered 4ATA are visible probably due to the high amount of additive. A significant difference between the two samples which could be confirmed at several measurement positions on the copper layer are the absorption bands between 2160 and 2110 cm^{-1} which are missing in the pure 4ata sample. They could be further enhanced by measuring the IR spectra on the same sample in attenuated total reflection (ATR) mode (blue solid line). These absorption bands correspond to vibrations found in various carbon and nitrogen containing multiple bonds, for example aliphatic isonitriles (-C-N≡C-, 2175-2130 cm^{-1} [147]), alkynes (e.g. terminal C≡C, 2140-2100 cm^{-1}), azides (terminal $-N_3$, 2160-2120 cm^{-1}) or -N=C=N- groups (2155-2130 cm^{-1}).

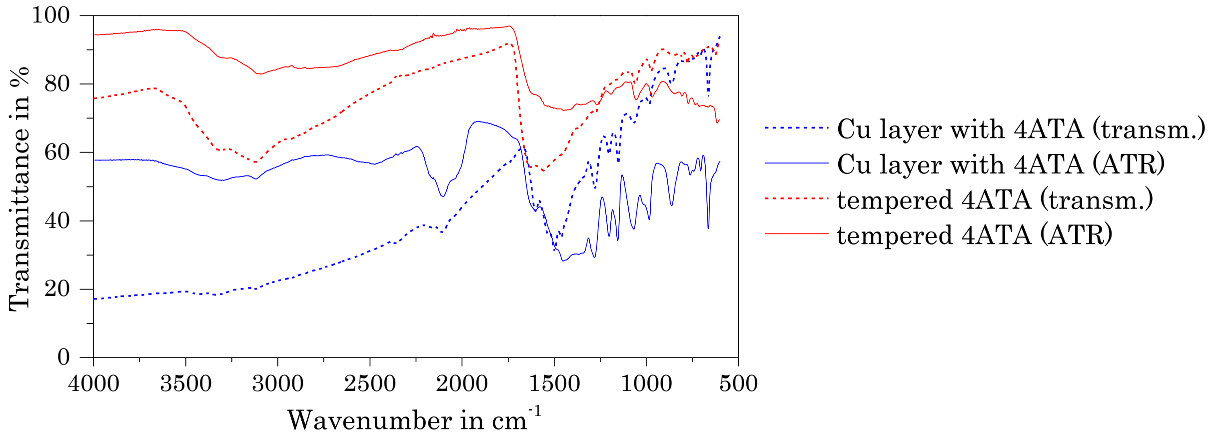

Figure 46: IR spectra taken from a copper layer produced with an ink containing 4ATA (blue). The results are compared to tempered 4ATA (red). Two measurement modes have been applied: transmission-IR (dashed lines) and ATR-IR (solid lines).

These IR analyses do not allow an exact identification of the present chemical groups in the residues of the sample made from the 4ATA containing copper ink. However, the possible carbon and nitrogen containing multiple bonds are a strong indication for the formation of the proposed temperature stable polymeric C-N structure which would explain the observed cyanogen molecules as decomposition product above 500°C.

3.5.3 Model for the film stabilization of ternary layers

In the last sections the molecular structures of the proposed copper polymers, their high temperature behavior and the organic residues in the precursor after a heat treatment have been investigated. With these information and additional SEM images a model has been developed to explain the formation of the dense metallic precursor layers in presence of the polymer.

As could be shown in section 3.5.1.4 copper-additive polymers are forming in the ink below 100°C. The presence of these compounds during the heating of the deposited liquid film above 100°C changes the properties of the precursor layer significantly compared to the additive free samples. With a decreasing amount of the solvents TMG and methanol the polymers precipitate and form a highly viscous matrix. Eventually, this matrix solidifies above 150°C to a stable film. By adding high amounts of 4ATA to the ink this solid metal-organic layer can be visualized by SEM imaging. Figure 47 shows a cross sectional SEM image of a precursor processed with a Cu:4ATA ratio of 1:2 tempered up to 180°C. A homogeneous and flat structure can be observed containing separated nanoparticles with diameters below 20 nm. The morphology of this film is highly different to the previously described layers.

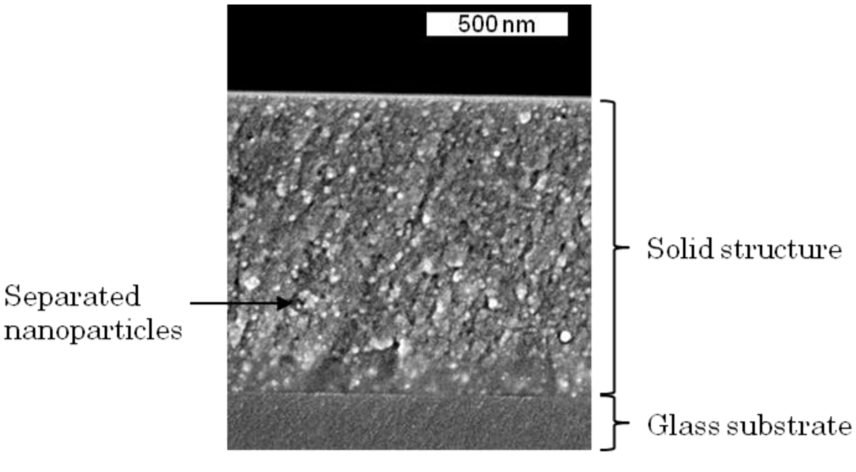

Figure 47: Cross sectional SEM image of a layer containing CuInGa and 4ATA (Cu:4ATA=1:2) tempered up to 180°C. The solid structure consists mostly of the 4ATA polymer and small nanoparticles.

Based on these results a model for the formation of homogeneous films with 4ATA has been proposed which is depicted in Figure 48. Beginning with the layer tempering at around 130°C the precipitating polymers form a highly viscous film eventually resulting in a solid matrix. Thus, the reduction of copper ions initiated in this temperature region occurs inside of this immobile environment. With increasing temperature the film height decreases due to the evaporation of large fractions of the solvent TMG (see TG, section 3.4.1.2) and a partial decomposition of the copper polymer. Consequently the separated copper particles are approaching. Simultaneously, above 160°C the indium cations are getting reduced most likely close to or on top of the copper nanoparticles resulting in the formation of Cu-In alloy particles. The same considerations apply for the gallium ions above 170°C. In contrast to the discussed additive free inks, this alloying does not necessarily result in the formation of clusters and finally the observed porous structures due to the local separation of the individual particles by the polymer matrix. Instead, with decreasing film height the converging particles agglomerate to dense layers.

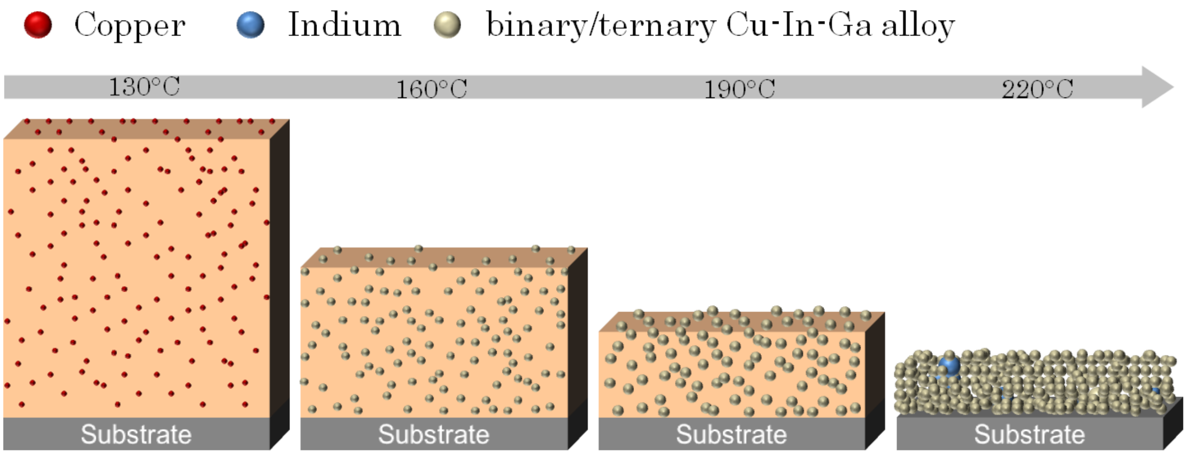

Figure 48: Proposed model of the metal film formation with 4ATA: Cu^{2+} polymerizes with 4ATA in the solution below 100°C. This polymer slowly solidifies during the solvent evaporation leaving an organic matrix. At 130°C the copper ions get reduced forming nanoparticles, followed by In^{3+} and Ga^{3+} at T>170°C. The film thickness is decreasing due to sintering effects, solvent evaporation and partial polymer decomposition. Above 250°C most of the organic matrix has decomposed leaving a stable metal film.

3.5.4 Layer characterization

In the previous section a model has been introduced describing the formation of dense flat layers. The final morphologies of layers processed with 4ATA at 200°C are depicted in Figure 49 in three magnifications showing a dense film with a flat surface over large areas. The molar copper:4ATA ratio necessary to achieve this degree of homogeneity is about 8:1.

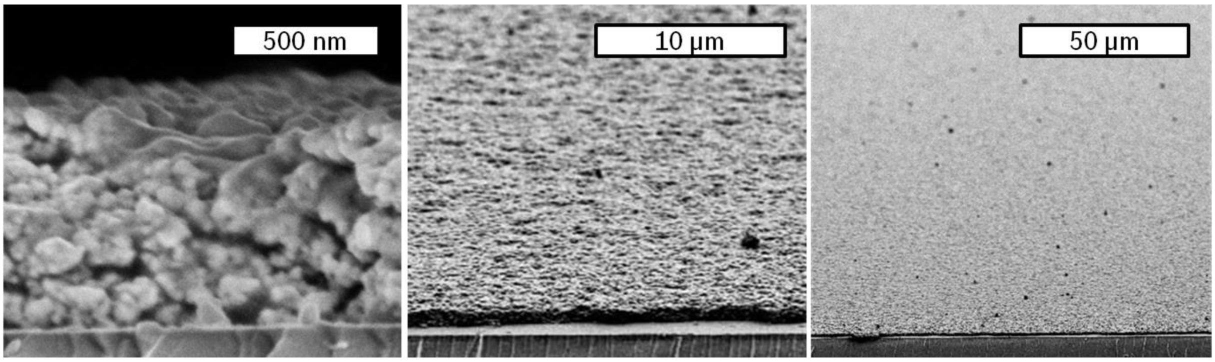

Figure 49: SEM images of CIG layers processes on glass at temperatures up to 200°C. Left: cross section. Middle and right: tilted view (10°).

The vertical element distribution in a layer tempered up to 200°C has been measured by secondary ion mass spectrometry (SIMS). The results are shown in Figure 50. Flat signals of the metals as well as carbon and nitrogen can be observed over the whole film thickness. The rising Mo signal indicates the end of the precursor layer and the beginning of the back contact. The results are in agreement with the layer formation model which proposes a separated and independent metal particle formation over the film height.

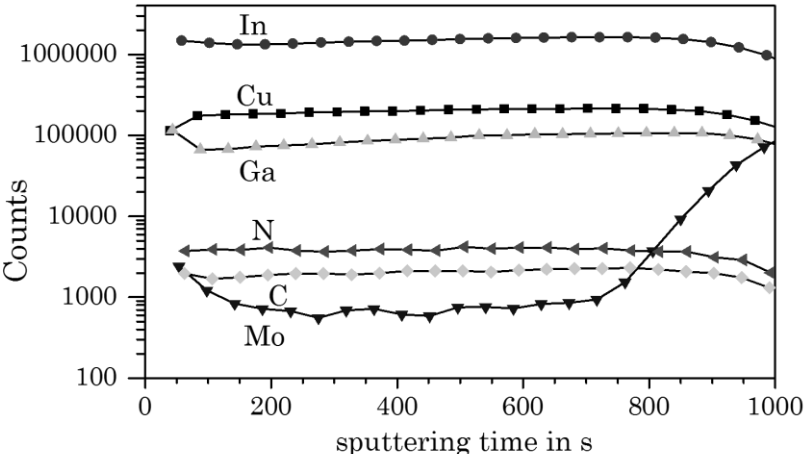

Figure 50: SIMS depth profile showing the vertical element distribution of a precursor layer processed with temperatures up to 200°C.

Similar to the additive free experiments the elemental indium is only partially incorporated in the copper rich alloy while the rest is most likely homogeneously distributed as small indium droplets. At temperatures around 200°C the layer mostly consists of $Cu_{11}(In,Ga)_9$. Thus, the total amount of phase separated indium is low and the individual particles are widely distributed throughout the layer with a limited mobility. However, above 300°C the peritectic phase decomposition to $Cu_{16}(In,Ga)_9$ decreases the amount of incorporated group III elements and therefore an increase in the separated indium phase is expected. Together with the higher mobility at this temperature the individual droplets tend to coalesce forming larger drops due to the thermodynamically driven efforts to decrease the surface energy. Because of the limited space inside of the porous layer, the larger drops are escaping the film at the surface where they agglomerate similar to the droplets found in the experiments with the pure indium inks (see section 3.4.3.1). Thus, large spherical particles can be observed after cool down. Figure 51 shows examples for this effect found on layers tempered at 350°C for 10 minutes. The indium particle diameters in both experiments exceed 1 µm. These findings strongly suggest that low temperatures during the metal precursor processing have to be favored to ensure a homogeneous element distribution.

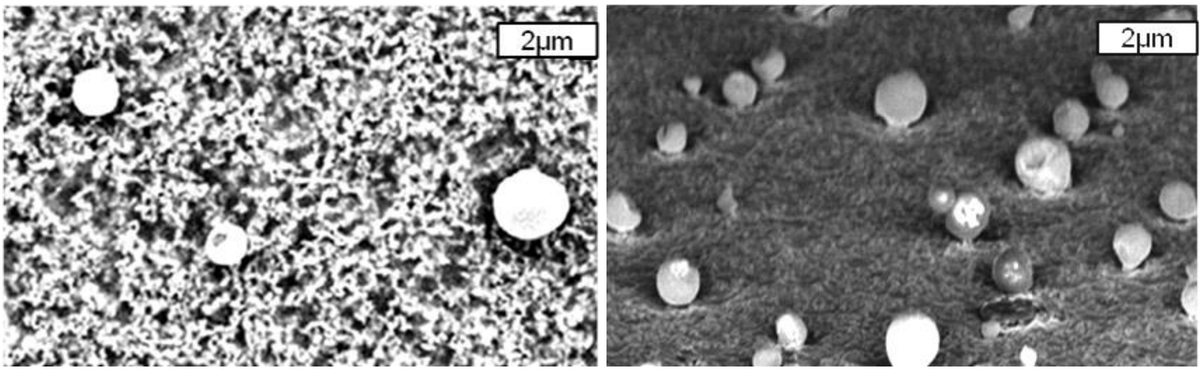

Figure 51: Top view (left) and tilted view (15°, right) SEM images of layers tempered above 300°C for several minutes showing large separated indium peals.

3.5.5 Summary of section 3.5

In this section the influence of 4ATA as additive is investigated. Its purpose is to support the morphological integrity of solution processed Cu-In-Ga layers at temperatures above 160°C. The stabilization effect is explained by the formation of a polynuclear compound consisting of Cu^{2+} cations, formate anions and 4ATA molecules during the ink preparation at temperatures below 100°C. This polymer solidifies prior to the metal ion reduction. Thus, an organic matrix is present surrounding the metal salt TMG complexes. During the reduction step between 120 and 200°C, separated Cu and binary/ternary Cu-In-Ga alloy nanoparticles emerge in this simultaneously decomposing polymer layer. At 200°C most of the organic matrix has decomposed which could be confirmed by elemental analysis revealing a homogeneous and dense layer of metallic nanoparticles. The remaining organic residues above 200°C are nitrogen rich and the absolute amount decreases with higher temperatures. Layers tempered above 300°C for several minutes showed significant indium segregation resulting in large bubbles on the surface. This has to be avoided by keeping the alloying temperature low.

Chapter 4

From the metallic layer to a semiconductor

For a working solar cell device, the metallic precursor layer described in chapter 3 has to be transformed into a semiconductor suitable as absorber layer. This can be achieved by a reaction of the metals and metal alloys with selenium and/or sulfur to polycrystalline chalcopyrites. The chalcogens are usually incorporated by a high temperature diffusion process which is the topic of this chapter. In this work selenium has been exclusively used as chalcogen source, therefore, the annealing step is mostly denoted as selenization. The chapter begins with an in-situ XRD analysis showing the most important phase changes during the selenization of a chemically deposited precursor layer. Thereafter, the focus is set on the lab scale process technology. Section 4.2 introduces the developed tube furnace including a characterization of the temperature profile inside of the tube. In the following section 4.3 the selenium evaporation inside of this tube furnace is modeled and the importance of an exact timing during the annealing run is explained. The resulting chalcopyrite absorber layers are characterized in chapter 5.

4.1 In-situ investigation of the selenization

Similar to section 3.4.2 where the precursor layer formation during the tempering has been monitored by an in-situ XRD measurement, this section evaluates the selenization of this chemically deposited precursor to a chalcopyrite layer. Therefore, a metallic precursor with the composition Cu:In:Ga = 0.9:0.8:0.2 has been positioned in the center of the in-situ XRD furnace. As chalcogen source, elemental selenium has been used which was placed in an open graphite container above the sample. Finally, the whole system has been heated up to 600°C within 4 minutes and kept at this temperature for an annealing time of 6 minutes. During the whole process XRD scans have been taken with a frequency of 60 scans/min. The measured patterns are depicted in Figure 52.

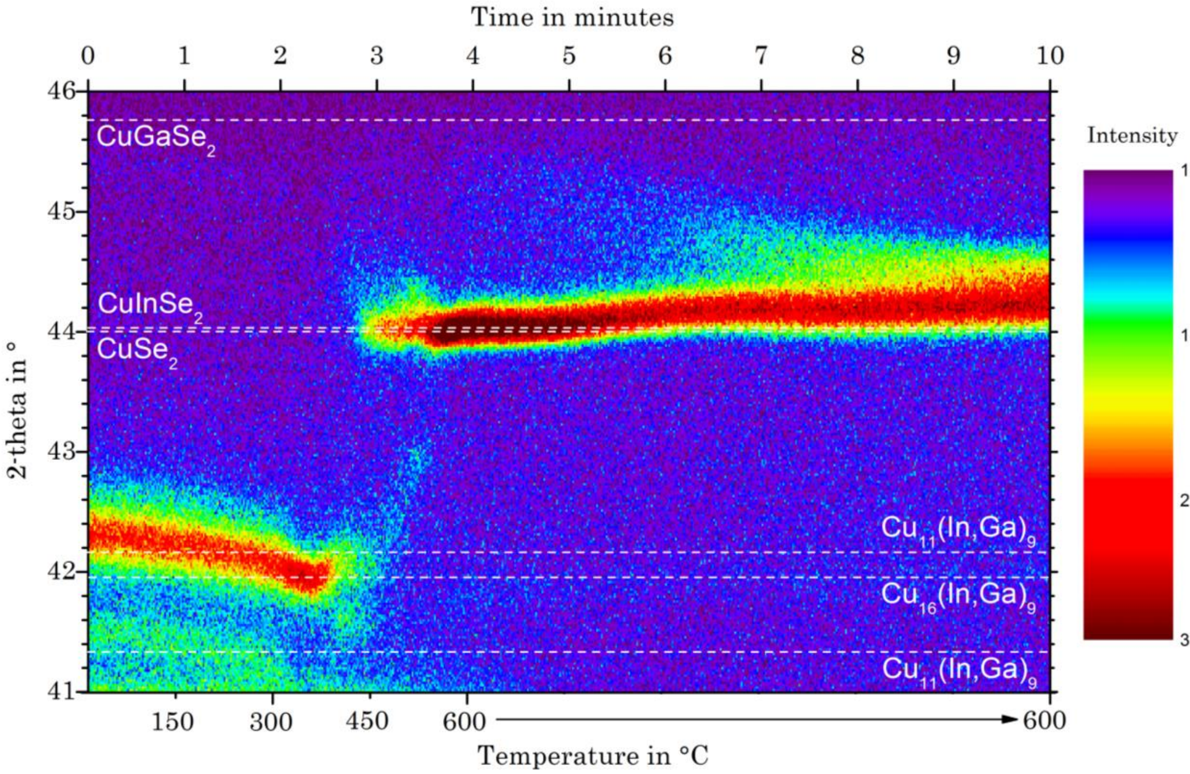

Figure 52: In-situ-XRD pattern of a typical selenization run. The precursor layer processed on a Mo coated glass substrate has been tempered up to 200°C. At room temperature the sample consists mostly of $Cu_{11}(In,Ga)_9$. Above 300°C a phase transition to $Cu_{16}(In,Ga)_9$ can be seen. Copper selenides and $CuInSe_2$ chalcopyrites appear above 450°C. Gallium is incorporated slowly at 600°C.

The used precursor layer has been previously prepared at temperatures up to 200°C. Thus, only the expected $Cu_{11}(In,Ga)_9$ phase is present at room temperature. Above 300°C a phase transition to $Cu_{16}(In,Ga)_9$ is visible. Because of the slow transport of evaporated selenium to the metal surface the first selenide reflex of $CuSe_2$ appears not until temperatures of around 450°C. At this temperature the $Cu_{16}(In,Ga)_9$ phase decomposes and a new peak appears that can be assigned to copper selenides. The remaining copper poor alloy probably forms a $Cu_9(Ga,In)_4$ phase (JCPDS 71–0458) which can be observed with low peak intensities around 43° 2-theta. Above 500°C the formation of a chalcopyrite phase is visible which can be identified as $CuInSe_2$ (JCPDS-40-1487) by its (204/220) reflex around 44° 2-theta. The kinetics of the formation of the ternary $CuGaSe_2$ (JSCPD-35-1100) is significantly slower and no pure CGS peak is visible [148]. Gallium is gradually incorporated into the $CuInSe_2$ crystals via the ternary CGS phase which can be observed by a weak peak around 45°-46° 2-theta shifting to lower angles. The first formation of the quaternary $Cu(In,Ga)Se_2$ (JCPDS 35-1102) can be clearly seen at around 6 minutes process time by a peak shift of the CIS peak to higher angles. The reason for this can be found in the smaller chalcopyrite lattice constant due to the smaller atom size of gallium [149].

4.2 Selenization process

In the in-situ XRD oven the selenium is evaporated from a solid source and diffuses from its position above the sample to the precursor. For the absorber layer manufacturing a similar process has been developed based on a tube furnace. For this process the samples as well as the selenium source are placed inside of a quartz glass tube on a hard carbon sample holder as can be seen in Figure 53. The whole system is open and operated at ambient pressure conditions with a nitrogen gas inlet on the left side and an outlet on the right. Thus, the selenium is positioned in front of the sample in the flow direction. As chalcogen source elemental selenium powder has been chosen.

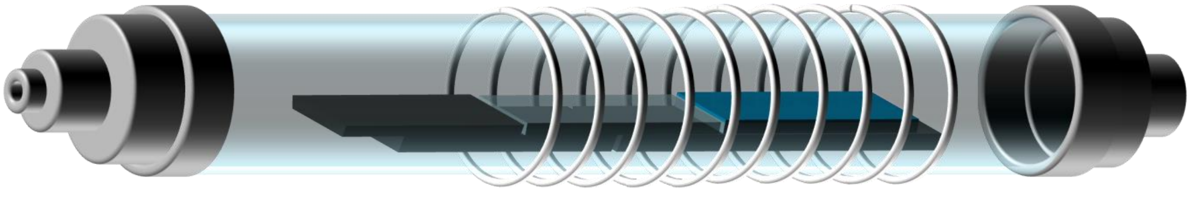

Figure 53: Graphical visualization of the selenization oven with the precursor layer shown in blue placed on the right. The inlet for the inert gas is positioned on the left. The rings symbolize the attached heating cords.

In contrast to the i-XRD oven, the selenium vapor flux to the samples in this setup is controlled by a nitrogen gas flow with a purity of 99.9999%. The volume flow can be adjusted by a mass flow controller within a range of 0 to 500 standard cubic centimeters (sccm) corresponding to a maximum gas velocity of 3.5 cm/s. In order to remove oxygen contaminations from the tube atmosphere, the tube is flushed with 500 sccm nitrogen for several minutes prior to each experiment. To limit a possible air indiffusion during the annealing, a back pressure of about 15 mbar has been applied by attaching a wash bottle to the gas outlet filled with 15 cm of water. Regarding the heating, good initial results have been achieved with one heating zone ranging from the selenium source to the end of the precursor [73]. However, to gain a better control over the temperature distribution a two heating zone concept has been developed. In this setup the oven is divided into two separately controlled zones. Figure 54 depicts a schematic illustration of the furnace. In order to minimize the heat transfer between the two zones through the highly heat conductive carbon, the sample holder has been divided into two pieces. For the sake of simplicity the basic temperature control is established by thermocouples placed on the inner wall of the glass tube.

Due to a direct connection between the temperature at the selenium source and the vapor pressure of the elemental selenium, this setup gives valuable information on the evaporation properties. Furthermore the known nitrogen volume flow allows a calculation of the selenium partial pressure at the precursor layer position. This topic is discussed in detail in section 4.3.

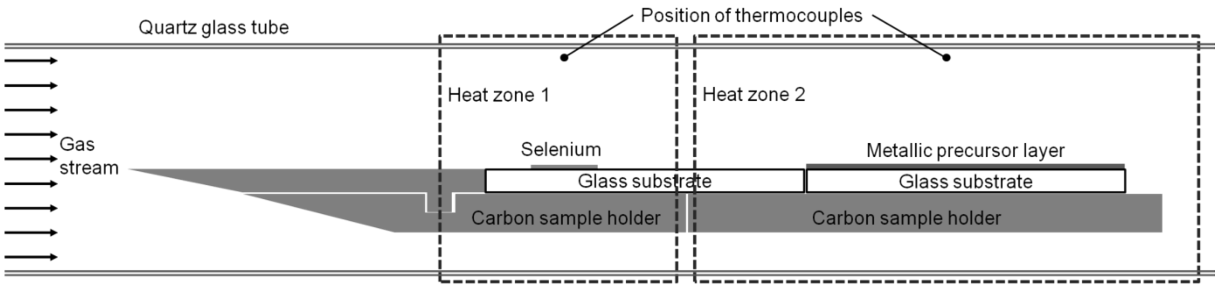

Figure 54: Schematic representation of the tube furnace used in this thesis. The metallic precursor layer and the selenium source are placed on a carbon holder inside of the tube. Two separately controlled electrical heating cords are attached on the outside.

4.2.1 Furnace characterization

Knowing the temperature profile inside of the tube oven can be beneficial to interpret and optimize annealing results. Therefore, the selenization furnace has been characterized with several thermocouples during a typical annealing run. Additional thermocouples to the ones shown in Figure 54 have been placed inside of holes drilled 5 mm into the carbon holder and the glass substrate. Due to the thin dimensions of the glass substrate, the inner temperature of the glass substrate corresponds to the temperature of the precursor layer on the surface of the sample and therefore resembles very accurately to the precursor temperature.

For a typical selenization routine the furnace is quickly heated to 600°C and kept at this temperature for 7 minutes. The measured annealing time begins when the target temperature has been reached. After the 7 minutes the heating is turned off and the upper part of the heat insulation is removed to increase the cool down rate.

Figure 55 shows the measured temperatures over the processing time. With the current setup a maximum heating rate of 220 K/min can be achieved. The temperature at the inside of the glass tube reaches 600°C after 4 minutes followed by small overshooting up to 614°C which can be observed at around 5 minutes processing time. The temperature of the glass substrate and the carbon holder follow with a significant deviation of up to 100 K and reach 600°C after 5 minutes. In contrast to the glass wall, the overshooting does not occur. The temperature decrease after unplugging the power supply and removing the heat insulation can be approximated by a power function with a steep slope in the beginning. As expected the glass tube exposed to the ambient surrounding cools down faster than the glass substrate and the carbon.

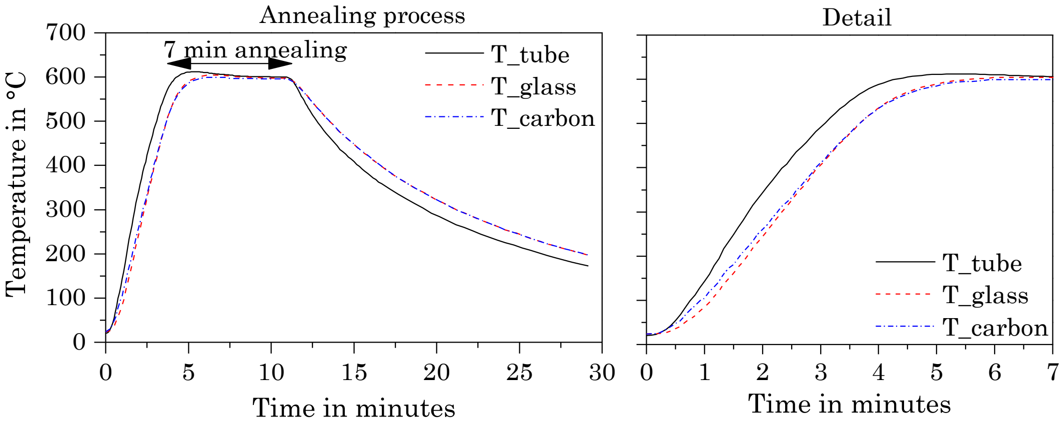

Figure 55: Temperature trends measured during a typical annealing process at three different positions in the furnace. T_tube describes the temperature at the tube wall and T_glass/T_carbon inside of the glass substrate as well as the carbon holder, respectively.

4.3 Selenium evaporation

The evaporation rate of selenium is directly dependent on the temperature. By using the temperature profile measured in the previous section, the evaporation rate during the annealing process can be estimated by a mass transfer model which is introduced in section 4.3.1. With the help of the known volume flow of nitrogen this evaporation rate can subsequently be translated into a partial pressure. Thus, the sections 4.3.2 and 4.3.3 evaluate the influences of two process parameters on the selenium partial pressure. Finally, section 4.3.4 describes the importance of the process timing with regard to the selenium partial pressure at the precursor position. With these results a process optimization is proposed.

4.3.1 Modeling of the selenium partial pressure

Selenium is a solid that exists in several allotropic modifications. It melts at 221°C and boils above 685°C and evaporates in several polynuclear species consisting of two to eight atoms [150]. The actual composition of the vapor is mostly dependent on the temperature. With increasing temperature the fraction of the short molecules increases. In the temperature range of the annealing around 600°C the evaporation products can be approximated as Se_5 chains [151].

The evaporation of selenium has been calculated similar to methanol presented in section 3.2.3. The schematic model used for this calculation is shown in Figure 56. The shape of the liquid elemental selenium is assumed to be a flat elliptical cylinder which coincides to the observed appearance of the solid powder after melting. As initial weight, a typically used mass of 120 mg has been chosen. With this mass, the density of liquid selenium, and an approximate diameter of 1 cm, the initial height has been estimated to be around 200 µm. For the calculation this cylinder is on a heated surface in an open system. The evaporation is enhanced by a laminar gas stream of nitrogen from the left side. As simplification the Se_5 molecules are assumed to behave like an ideal gas justified by the ambient pressure conditions and the low partial pressures.

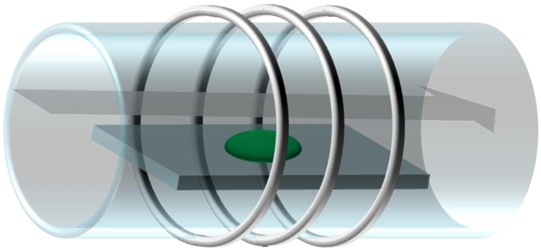

Figure 56: Schematic model used for the calculation of the selenium evaporation in an open system. Liquid selenium in the shape of an elliptical cylinder is positioned on a flat surface. Heating is applied through the substrate and the system is overflown with a cold nitrogen gas stream.

With these boundary conditions and the assumption of an open system in the two directions of the tube the diffusion flux of selenium from the liquid gas interface A to the center of the tube B can be estimated similar to the solvent evaporation discussed in chapter 3. For simplicity reasons Se_5 molecules are abbreviated as Se. One difference to the previous calculation is the not negligible selenium partial pressure in the tube (B).

$$\dot{N}_{Se} = -\frac{\beta}{R\,T}\,A\,(p^*_{SeA}(T_{Se}) - p_{SeB})$$

$\dot{N}_{\mathrm{Se}}$	absolute diffusion flux of selenium in mol/s
β	mass transfer coefficient in m/s
R	universal gas constant in J/(mol K)
T	absolute temperature in K
A	surface of selenium in m²
$p^*_{SeA}(T_{Se})$	vapor pressure of selenium in Pa
p_{SeB}	partial pressure of selenium in the tube in Pa

The value of p^*_{Se} as a function of the temperature has been taken from [152]. For the selenium temperature the profile measured inside of the glass substrate (see section 4.2.1) has been used with a target temperature of 600°C. Due to the slow gas flow and the small tube diameter, the partial pressure of Se $p_{Se,\infty}$ above the liquid has been assumed to be the saturation pressure of selenium at the N_2 gas temperature. The nitrogen gas stream enters the tube at room temperature. Further inside the tube at the selenium source position this temperature has been measured to be about 80% of the substrate temperature in degree Celsius. The surface A of the liquid selenium decreases during the annealing due to the mass loss. In order to include this in the equation a constant height to width ratio has been assumed. The mass transport coefficient β has been approximated by a Sherwood correlation for a laminar overflown plate [110] which has already been introduced in section 3.2.3.

$$\beta = \frac{Sh \cdot D_{SeN_2}}{L_c}$$

Sh	Sherwood number
D_{SeN_2}	diffusion coefficient of selenium in nitrogen in m²/s
L_c	characteristic length of the selenium surface in m

The Sherwood correlation is a function of T_{Se} as well as the temperature of the gas stream T_{N_2} which affects the viscosity μ_{N_2} and density ρ_{N_2} of the nitrogen. Thus, it is worth mentioning that the Sherwood number Sh is a function of various parameters.

$$Sh = f(T_{Se},\, T_{N_2},\, \rho_{N_2}(T_{N_2}),\, \mu_{N_2}(T_{N_2})\,, u_{N_2})$$

The gas velocity u_{N_2} has been assumed to be constant around 3.5 mm/s corresponding to 50 sccm, a typical volume flow used for the selenizations. The binary diffusion coefficient D_{SeN_2} for selenium in nitrogen has been calculated following the kinetic gas theory.

$$D_{SeN_2} = \frac{1}{3} \bar{u}_{Se}\, \lambda_{Se}$$

$$\bar{u}_{Se} = \sqrt{\frac{8\, R\, T_{Se}}{\pi\, M_{Se}}}$$

$$\lambda_{Se} = \frac{k_B\, T_{Se}}{\sqrt{2}\, \sigma\, p}$$

$\bar{u}_{Se}$	mean velocity of Se_5 molecules in m/s
M_{Se}	molar mass of the Se_5 molecules in kmol/kg
λ_{Se}	mean free path of Se_5 molecules in m
σ	collision area

Figure 57 left shows the resulting mass loss of selenium over the time during the annealing process. The curve indicates a measurable Se evaporation at temperatures above 450°C due to the slowly rising vapor pressure of elemental selenium. However, once the temperature has reached 550°C the mass loss slope highly increases and the selenium evaporates within 6 minutes. This period coincides with the time the liquid selenium can be observed in the furnace. As mentioned before, the thereby calculated evaporation rate can be combined with the known volume flow of nitrogen to a local selenium partial pressure and the determined values are depicted on the right in Figure 57. The graph shows that the Se partial pressure reaches 1 mbar at around 450°C and increases to a peak pressure of around 100 mbar at 600°C source temperature and 5 minutes process time.

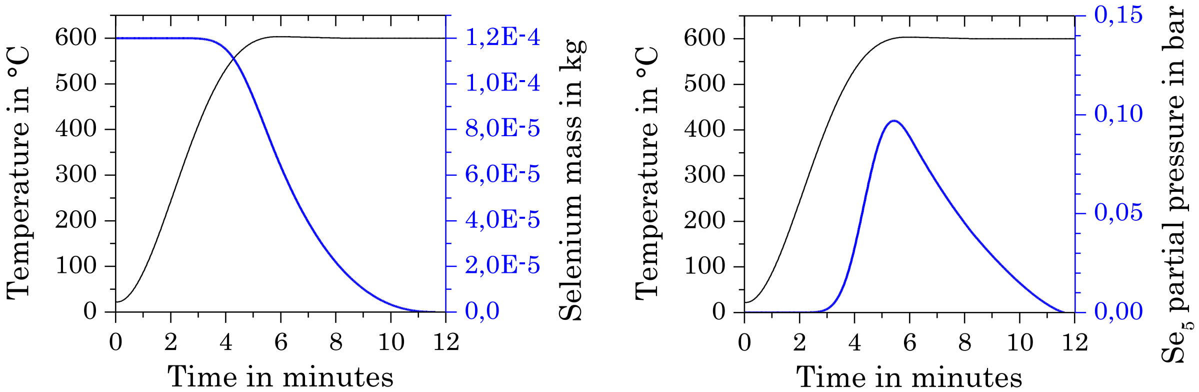

Figure 57: Selenium mass loss (left) and local selenium partial pressure (right) each compared to the glass substrate temperature as a function of the process time.

The peak shape trend can be explained by the limited amount of selenium and the diminishing evaporation surface. After the peak pressure the decreasing surface lowers the evaporation rate and the calculated partial pressure decreases quickly.

In summary both graphs clearly show that the selenium is evaporating quickly under the chosen conditions. At 600°C the initial amount of selenium evaporates within 6 to 7 minutes with an end marked by a remaining partial pressure of below 1 mbar. Transferred to the typically applied 7 min long annealing process and the following cool down phase this suggests that the selenized layer is most of the time in an atmosphere containing a high amount of chalcogen. This is important as Liao et al. could show that low selenium partial pressures can be detrimental for the chalcopyrite properties leading to segregations and defects [153]. Scragg et al. observed that annealing without selenium can also lead to a selenium loss in the layer [49]. Thus, a sufficiently high vapor pressure over the process time has to be guaranteed. Regarding this issue, the furnace setup has two parameters to adjust the evaporation conditions for longer annealing routines which are the selenium source temperature as well as the gas flow velocity. The influences of both parameters are calculated and discussed separately in the following sections.

4.3.2 Influence of the selenium source temperature

The selenium source temperature directly influences the vapor pressure as well as the diffusion coefficient and therefore the evaporation rate. Thus, lowering the source temperature is an easy way to slow down the selenium evaporation. For the calculation three temperatures between 500 and 600°C have been chosen keeping all other parameters constant. Figure 58 depicts the resulting mass losses as well as the trends in the vapor pressure.

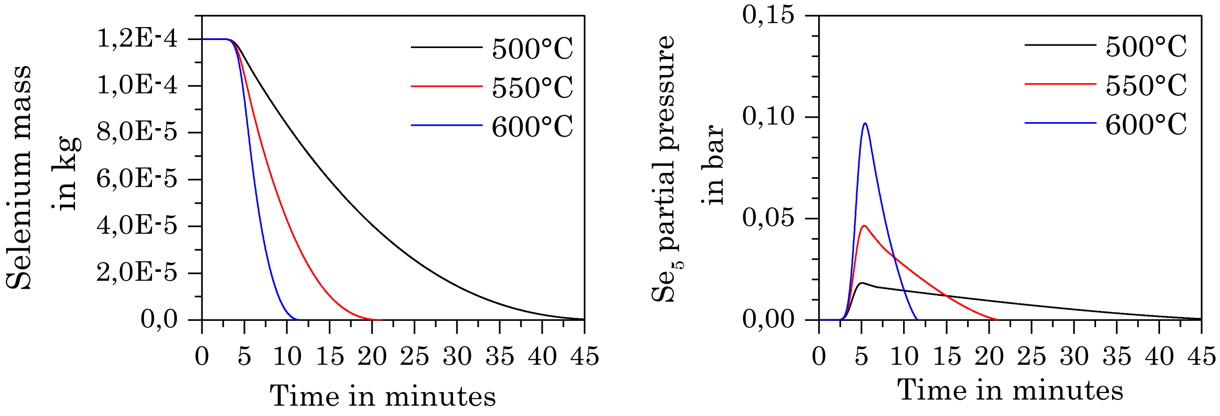

Figure 58: The graph on the left shows the mass losses of selenium and the graph on the right the corresponding partial pressure, both as a function of the process time.

The graphs clearly show the strong influence of the temperature. Compared to 600°C, a decrease of 50°C leads to a doubling in the evaporation time (beginning at around 3 minutes process time). This is achieved by a slowed down evaporation which can be visualized by the peak height and trend of the selenium partial pressure. Under these conditions the maximum partial pressure is 55 mbar slowly decreasing down to 1 mbar at 20 minutes process time. The same considerations apply for the calculated curves at 500°C. Here, the partial pressure already decreases after reaching 20 mbar and the Se_5 molecules are present in the furnace with more than 1 mbar for more than 35 minutes at 600°C. Thus, a lower source temperature can increase the time selenium is present in the gas phase, however, it also decreases the vapor pressure.

4.3.3 Influence of the gas velocity

The velocity of the gas flow (equivalent to the volume flow) affects two things, the mass transport coefficient and the time the evaporated selenium vapor stays above the source equivalent to the selenium partial pressure. The former is only marginally influenced due to the slow gas velocities applied. The latter, however, is highly affected. In order to find a suitable velocity range one has to consider a gas flow free experiment. Without the additional forced flow, the movement of the evaporating Se molecules would be controlled solely by the gas diffusion of the molecules which have no preferential orientation. Inside of the furnace this would eventually lead to a selenium transport in the two open tube directions. For this reason a minimum gas flow is necessary to control the diffusion path towards the sample. Experiments have shown that a condensation of selenium at the tube wall left of the selenium source occurs at gas velocities below 20 sccm. Thus, 25 sccm has been set as minimum speed. In Figure 59 the calculated trends in vapor pressure for three different gas velocities for a constant maximum temperature of 550°C are presented. The graph on the left shows the mentioned constant evaporation rates leading to congruent mass loss curves. On the right the partial pressures are depicted. In this graph a clear trend can be observed revealing a factor between the curves dependent on the gas velocities. With the lowest volume flow of 25 sccm corresponding to a gas speed of 1.8 mm/s the nitrogen atmosphere above the evaporation source is more concentrated with selenium resulting in a significantly increased partial pressure of up to 95 mbar which is similar to the value achieved with a source temperature of 600°C and a volume flow of 50 sccm (3.5 mm/s). For the fast gas velocity of 100 sccm (7 mm/s) the opposite happens due to a more diluted selenium containing nitrogen gas phase and therefore a decreased maximum partial pressure of 20 mbar.

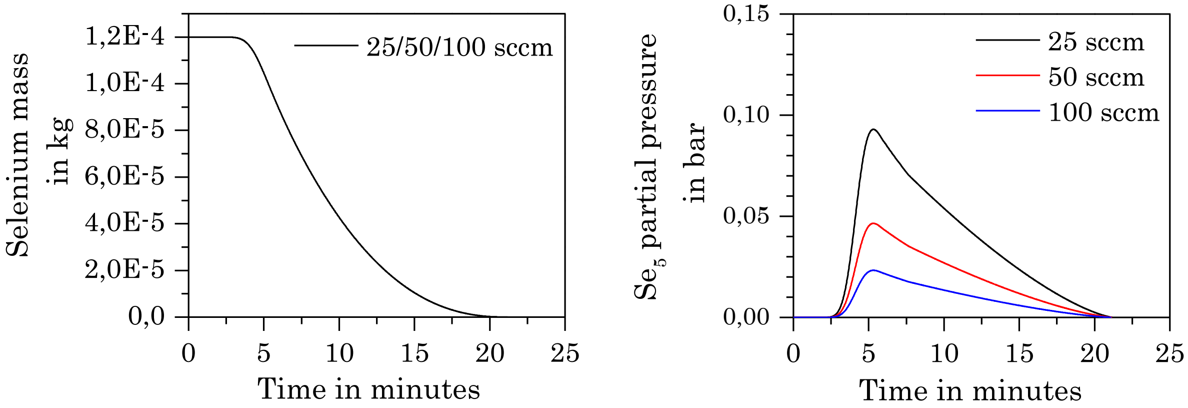

Figure 59: Influence of the gas velocity on the selenium evaporation as a function of the process time for a maximum temperature of 550°C. Left: Mass loss of selenium. Right: Partial pressure.

Thus, for longer annealing times a decreased source temperature in combination with a lower gas velocity can be applied to achieve similar vapor pressure conditions.

4.3.4 Importance of timing during the selenization

In section 4.3 the evaporation at the selenium source has been modeled. Regarding the properties of the selenium vapor arriving at the precursor position the geometry of the tube has to be considered. As mentioned in section 4.2, the selenium source and the precursor layer in the furnace are about 10 cm apart. With a nitrogen volume flow of 50 sccm the selenium vapor takes about 25 seconds to travel this difference (in the case of a pure convective flow). Assuming a simultaneous heat up of both heating zones with the same temperature profile, the precursor temperature increases by up to 90 K within this time period at a heating rate of 220 K/min (see section 4.2.1). In other words, by the time the selenium vapor arrives at the precursor the layer is up to 90 K hotter.

This furnace related issue has to be taken into account when designing the selenization procedure because the timing of the selenium arriving at the heated chemical deposited precursor is of great importance. The easiest way to show this is by comparing the j-V curves of solar cells processed with different heater timings presented in Figure 60. The delay time refers to the difference between the starting time of the selenium source heater and the precursor heater. 0 seconds means the instantaneous start of both heaters, 45 sec seconds means that the precursor heater is started 45 seconds before the selenium heater.

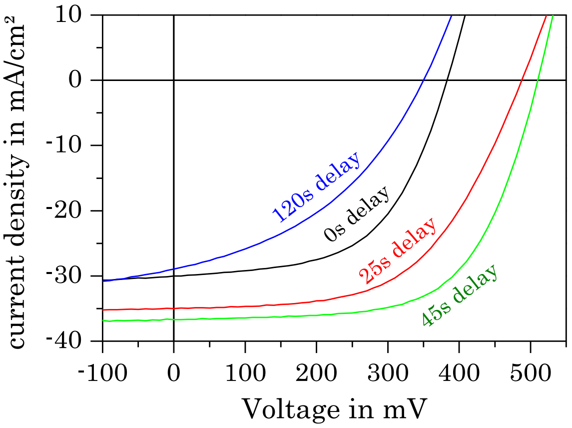

--	0 s	25 s	45 s	120 s
Effic.total in %	6,4	9,5	11,8	4,1
Voc in mV	383	488	510	350
Fill factor in %	55,2	55,6	63,1	40,7
jsc in mA/cm²	30,9	35	36,7	29
Total area in cm²	0,5	0,5	0,5	0,5

Figure 60: J-V curves of two solar cells processed with different delay times between the start of the selenium and the precursor heating. The flow rate and temperature have been set constant to 50 sccm and 600°C, respectively. For this graph a cell in the center of each particular sample substrate has been chosen.

The graph clearly shows the large differences between the samples. The absorber layers processed with the 25 and 45 seconds delay time reach significantly higher values in all optoelectronic properties. Between the two, the longer delay seems to be beneficial especially regarding an improvement in the fill factor. The reason for this can presumably be found in the time dependent selenium distribution inside of the tube furnace. Figure 61 shows in black the temperature profile of the precursor layer which is heated to 600°C.

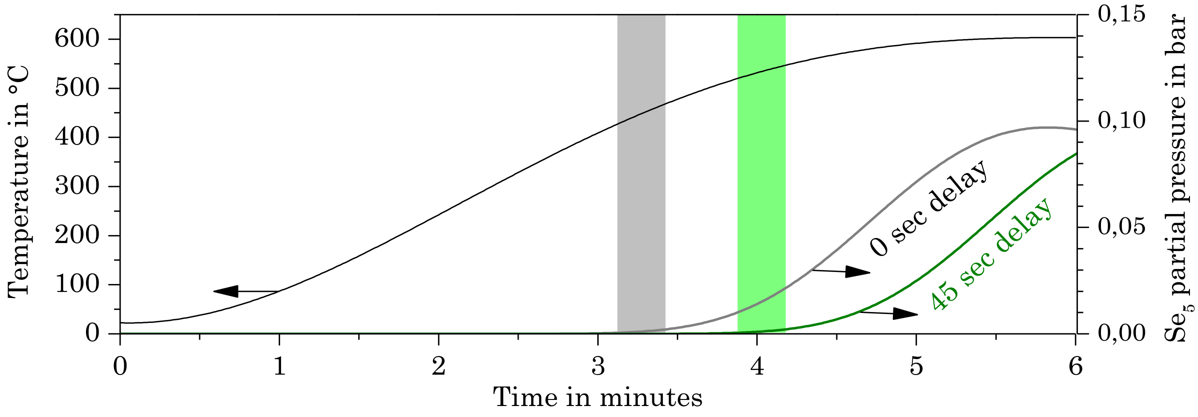

Figure 61: Precursor temperature and the selenium partial pressure at the substrate position as a function of the process time. The differences between the partial pressures are due to a delayed heating of the selenium source by 45 seconds.

The grey curve belongs to the selenium partial pressure of the incoming nitrogen flow arriving at the precursor position in the case of an instantaneous heating of both zones (0 s). Included in this calculation are the 25 seconds necessary for the transfer of the selenium vapor from the source to the precursor (at 50 sccm). The light grey area marks the time when the selenium arrives at the precursor layer with more than 1 mbar of partial pressure. This area intersects with the temperature profile of the precursor at about 440°C. The green curve belongs to the selenium vapor pressure in case of a selenium source heating which is delayed by 45 seconds. In this case the precursor has already reached 540°C by the time the partial pressure is at 1 mbar.

To explain the solar cell parameters, the properties of the additive might have to be considered. In section 3.5.2.1 it has been shown that small amounts of the 4ATA polymer residues are stable up to a temperature of 500°C. Above, the final decomposition could be observed by the measured ion currents of cyanogen (C_2N_2, m/e=26 and 52). Thus, the delayed arrival of the selenium vapor might be necessary due to the high temperature behavior of the additive residues. Without the delay time, selenium vapor with a partial pressure above 1 mbar arrives at the precursor layer significantly below 500°C. The in-situ XRD measurement in section 4.1 showed the instantaneous conversion of the metals to metal selenides in this temperature region. The occurring phase transitions can lead to a volume expansion and a layer densification which supposedly hinders the residue decomposition. Therefore, the proposed explanation for the beneficial effect of the delay time is based on a decomposition of the polymer residues before the arrival of the selenium vapor.

The longest delay time of 120 seconds shows the worst optoelectronic properties with a fill factor of around 40. With this parameters, the precursor layer is kept at temperatures above 500°C for several minutes without selenium. This time is probably critical due to a high sensitivity of the metals to traces of oxygen and possible phase segregations (e.g. of indium) in the film which has been shown in section 3.5.4.

4.4 Summary of chapter 4

Chapter 4 covered the last process step in the manufacturing of CIGS absorber layers from the chemical precursors, the selenization. In the first part the used tube furnace has been described and characterized in terms of the temperature profile. The targeted substrate temperature of 600°C can be reached in this furnace within 4 minutes. With these information and a model for the selenium evaporation, the mass loss of the selenium source as well as the partial pressure of Se_5 molecules in the tube furnace have been calculated. It could be shown that a typical initial selenium amount of 120 mg evaporates at 600°C within 6 to 7 minutes which coincides to the experimentally observed times. At this temperature a maximum selenium partial pressure of 100 mbar is reached. The calculated time frame is close to the chosen annealing time of the precursor layers. Thus, the selenization procedure has been optimized by adjusting the model using the available process parameters. With a decreased temperature, the retention time of the selenium source could be increased significantly. The thereby lowered partial pressure can be adjusted by changing the volume flow of nitrogen gas. In the last part of the chapter, the importance of the timing regarding the arrival of the selenium vapor at the precursor layer has been discussed. The quality of the processed solar cells from the chemical deposited precursor layers has been shown to be highly dependent on a delayed arrival of selenium. The introduced hypothesis explaining this issue is based on the necessary decomposition of the remaining additive polymer residues before the arrival of selenium vapor leading to the formation of dense metal selenides.

Chapter 5

The influence of sodium salts

In this chapter the processed absorber layers are further characterized. In this context the influence of sodium salts dissolved in the ink is investigated with a focus on the chalcopyrite layer and the solar cell properties. In the first part of the chapter the motivation for the sodium experiments is given by a short literature review. Thereafter, several experiments are discussed that aim to estimate the differences between two sodium incorporation approaches. In detail, sodium free samples are compared to a diffusion of sodium from the glass substrate as well as the sodium addition to the ink in the form of three different salts. Regarding the characterization the differences in the layer morphology and phase composition as well as the optoelectronic properties of the final solar cell devices are evaluated. Unless stated otherwise, the measured energy conversion efficiency values discussed in this thesis are referring to the total area efficiency. The results presented in this chapter have been published in Progress in Photovoltaics [75].

5.1 Motivation and literature review

In this section the general role of sodium in CIGS is introduced explaining the most important effects on the layer as well as the optoelectronic properties. Thereafter, the typically applied physical incorporation techniques as well as new chemical approaches are introduced.

5.1.1 Role of sodium

In 1993, the beneficial influence of sodium has been discovered by accident when soda lime glass had been used instead of the preferred alkaline free borosilicate glass [154]. However, it took some time to attribute the positive effects correctly to the presence of Na. Intense research led to a significant efficiency gain within a few years, showing the importance of this topic for CIGS solar cells. Yet, there are still many unanswered questions and the complete role of Na is far from understood. In this section, an introduction into the role of sodium is given. For further information the reader is referred for example to the thesis of Rudmann [155]. After describing the effects an overview is given on the state-of-the art physical incorporation techniques as well as first published chemical approaches.

In general, sodium doping has been reported to lead to changes among others in the absorber layer morphology, the grain orientation, the number and type of defect, the charge carrier density, the conductivity and the optoelectronic properties of the final device. Beginning with the morphology, several groups observed an influence of sodium on the grain size. However, there is still a controversy going on about this topic. While some groups noticed an increase [156], others did not observe any differences [157]. Some studies even reported a decreasing grain size, when sodium was present during the grain growth [158]. Yet, it is also believed that the grain size does not play a critical role in terms of the cell efficiency [159]. Regarding the grain orientation, Na is observed to enhance the (112) texture [160], [161].

Due to its low solubility in CIGS, sodium is usually found at the grain boundaries where it is believed to passivate defects [158], [162], [163]. Erslev et al. also found a passivation of defect states near the CdS/CIGS interface [164]. Additionally, they observed an increase in the free carrier and deep acceptor densities when exposed to white light. A dramatically increased hole concentration has also be found by other groups [165]. This effect usually comes with a decrease in resistivity by several orders of magnitudes [166]. The improvement in the optoelectronic properties is mostly based on better values for the V_{oc} and the fill factor. This has been proposed to originate from the mentioned increased density in the effective acceptors [167]. Apart from that, sodium is also believed to influence the absorption of selenium during the annealing. Braunger et al. proposed a model based on the formation of sodium polyselenides on the surface acting as a selenium reservoir [168].

5.1.2 Incorporation techniques

This section gives a brief overview on typical incorporation techniques. It is divided into two parts, the physical and the chemical methods. Physical incorporations have an advantage that can be quantified by the significantly higher number of research publications in this field. Therefore, the first part gives a short introduction in physical sodium incorporation strategies. The reported chemical sodium incorporation techniques are presented in the second part.

5.1.2.1 Sodium incorporation by physical deposition methods

Sodium can be incorporated in various ways and also at different times during the layer processing. Figure 62 shows the possible strategies used in the two stage process. The probably simplest and most convenient way to incorporate sodium is by diffusion from a Na containing substrate like soda lime glass (A). An important disadvantage of this method is the badly adjustable amount of incorporated sodium depending on various factors. This can be problematic as both insufficient as well as excessive supplies of Na can lead to deteriorated cell results [157]. Several groups reported the ideal amount of sodium to be between 0.1…0.5% of the CIGS atoms [169]–[171]. One approach to solve this issue has been proposed by Sakurai et al. who used a preheating step of the SLG/Mo substrate to adjust the amount of sodium in the CIGS layer [172].

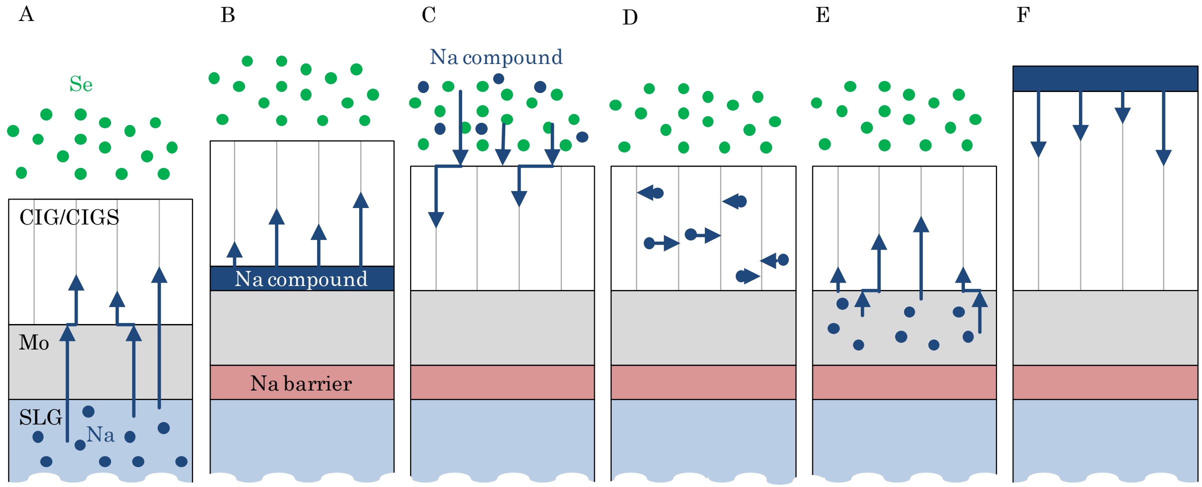

Figure 62: Sodium incorporation strategies in the two stage process. A) Diffusion from Na-containing substrate. B) Sodium containing layer on top of the BC. C) Use of Na containing gas phase species during selenization. D) Use of sodium doped metal sputter targets. E) Incorporation from MoNa back contact. F) Post deposition of a Na compound on top of the CIGS layer. Image has been reproduced and extended from [155].

All other methods B-F usually rely on an additional sodium source which is thought to be superior to method A [173]. In order to show the full potential of these approaches, a diffusion blocking layer is necessary to exclude any sodium diffusion from the substrate. This blocking layer can consist for example of Al_2O_3 or Si_3N_4 [174]. In method B a sodium containing layer is deposited between the molybdenum back contact and the precursor. This way a precise amount of Na can be supplied [175]. As Na source compound several materials are applicable. High quality devices could be produced among others with Na_2S [176], Na_2Se [165] and NaF, however, the air stable and less hygroscopic NaF is usually favored [175]. The fluorine anion also has been shown to leave no residues in the bulk [177]. Method C describes a gas phase incorporation. Wieting et al. reported the transfer of Na into the precursor layer via a gaseous Na_2Se_x species [178]. They observed this effect during their selenization run of numerous samples with the sodium coming from an adjacent soda lime glass. The methods D and E are based on modified sputter targets. For D a doped Cu-Ga target is proposed produced from a mixed powder composed of NaF and Cu-Ga [179]. E uses a sodium doped Mo sputter target (also called "MoNa") with an adjusted composition [180]. However, in this approach the back contact/absorber interface can suffer from adhesion problems. F is the only post selenization treatment. Here, the Na compound is deposited similar to B on the final chalcopyrite layer. Rudmann et al. investigated the influence of a NaF post treatment on co-evaporated absorber layers [155]. They noticed that this method is mainly successful in the case of low temperature annealed absorbers. At standard temperatures, method B showed better results.

5.1.2.2 Sodium incorporation by chemical deposition methods

In contrast to the physical incorporation methods, the number of publications dealing with a chemical sodium deposition is smaller. Sutter-Fella et al. showed with their solution processed kesterites which behave similar to the chalcopyrites a significant improvement of the optoelectronic parameters when adding sodium [181]. The novelty about this result was that they achieved comparable results from a physically evaporated NaF film as well as a spin coated NaCl solution both deposited on top of the precursor layer prior to the annealing [182]. Another wet chemical approach in the chalcopyrite system has been introduced by Guo et al., who dipped their precursor layer consisting of ink deposited sulfide nanocrystals in an aqueous 1 molar NaCl solution for 10 min [183]. This led to a significantly improved crystal coherence length and solar cell parameters. However, adjusting the incorporated amount of sodium with both methods is complicated and dependent on several factors such as the precursor morphology (e.g. porosity) as well as the film thickness and the dipping/spin coating time. Thus, the reliability is poor. Very recently, at the same time as the presented work Werner et al. reported a different approach. They added the sodium source (NaCl) directly to the ink of their chemically deposited kesterite layers [184], [185]. Contrary to the usually observed sodium effects these solar cell devices showed a better carrier collection and therefore j_{sc} values. V_{oc} and FF remained similar.

5.2 Sodium diffusion vs. additional Na salts

This section is based on a manuscript to be submitted. The first question to answer is the principal influence of additional sodium salts on solution processed CIGS absorber layers. Therefore, this section comprises an evaluation of three experiments where all process parameters have been kept constant beside the sodium incorporation method. CIG precursor layers have been prepared from inks containing the metal salts with a Cu:In:Ga ratio of 0.9:0.8:02. The layers have been tempered up to 200°C and subsequently selenized at 600°C for 7 minutes with a delay time of 45 seconds. The differences in the experimental conditions are listed in Table 7. As baseline, a precursor layer without additional sodium has been processed on a molybdenum back contact without barrier. In this sample, a sodium diffusion from the soda lime glass (SLG) during the selenization is expected. In order to estimate the influence of the diffusion, a similar precursor layer has also been prepared on a back contact with a diffusion barrier where no sodium incorporation is expected. Both samples are finally compared to a precursor layer processed from an ink containing NaCl. The amount of added salt has been chosen to be 2.5 mol-% of copper (corresponding to about 0.55 mol % of CIGS atoms) and kept constant in all further experiments. This value is at the upper level of the reported optimum.

Table 7: Experimental conditions for the evaluation of different sodium incorporation techniques.

Series	Diffusion barrier	Additional Na salt	Expected Na incorporation pathway
1	yes	no	-
2	no	no	Diffusion from SLG
3	yes	2.5 % NaCl	Na salt in precursor

The chalcopyrite layers of the sample series 1-3 have been further processed to solar cell devices and the current-voltage properties are shown in Figure 63 (all without antireflective coating). From these graphs several trends can be derived. Compared to the sodium free device, both sample series with sodium have significantly higher values in V_{oc} and FF. This is in agreement with the reported influence of Na. However, the specific values are varying significantly depending on the diffusion pathway. Concerning the V_{oc}, Na incorporated by diffusion from the SLG leads to an increase of about 50 mV while the presence of NaCl salt enhances the voltage by up to 150 mV. A similar but less pronounced trend can be observed in the graph showing the fill factors. In agreement with the literature, the average values of the short circuit current (j_{sc}) are almost constant for all samples in the range of 36-38 mA/cm² with a larger spread found in the sodium-free samples. The overall trends are reflected in the efficiency values with the Na from SLG sample having an average increase of 30 rel.-% and the NaCl enhancing the average efficiency by more than 70 rel.-%. One possible reason for the lower efficiency of the sodium diffusion sample compared to the NaCl sample is that there was insufficient time during the selenization for Na to diffuse from the glass substrate into the chalcopyrite layer. This result suggests that doping the precursor ink directly with Na salts might allow significantly shorter annealing times, thus reducing the energy consumption during annealing.

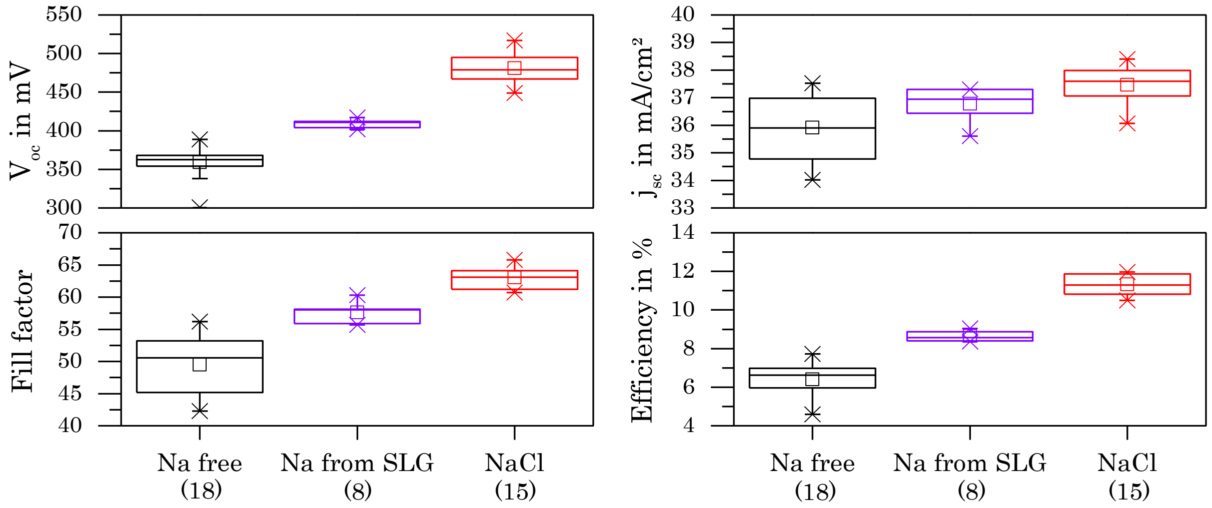

Figure 63: Optoelectronic properties of three samples without any sodium, sodium diffusion from the glass and a sodium incorporation via dissolved NaCl. The numbers in brackets correspond to the number of measured cells (published in [75]).

It can be concluded that the addition of NaCl to the ink is a practical way to incorporate sodium. The lower opto-electronic values achieved by diffusion from the SLG substrate suggest that the chosen annealing conditions are not optimal for this incorporation pathway presumably resulting in an insufficient sodium supply.

In further experiments the relative concentration of NaCl in the precursor ink was varied between 1 and 5 at.-% (of Cu content). The resulting precursors were selenized and completed into devices in an identical fashion, and their jV characteristics were determined. Both lower and higher NaCl concentrations resulted in lower device efficiencies. Thus, the Na concentration of 2.5 at-% has been kept constant in the next part of the study. Here, the sodium salt has been varied to determine whether the salt anion has an effect on the absorber characteristics and the device properties.

5.3 Salt variations

In the previous section a proof of concept for soluble sodium salts added to the ink has been presented. It could be shown that the precursor containing NaCl has highly improved solar cell parameters compared to the Na diffusion from the SLG. Yet, there are literature reports suggesting that the presence of chloride anions might have negative effects on the final solar cell. Tanaka et al. found that Cl^- ions can act as donor in chalcopyrite layers resulting in a n-type conductivity [60]. Thus, the following sections are dealing with the differences between NaCl and two halogen free Na salts, $NaHCO_2$ and NaSCN. Regarding the precursor processing the same parameters and CIG salt composition have been used as in section 5.2.

5.3.1 Choice of sodium salts

To be a candidate as sodium source in this chemical approach, the Na salts have to be soluble either in methanol or in TMG, preferably in both. NaCl is not soluble in TMG but can be dissolved to some extent in methanol. At high salt concentration (>5 mol-% of Cu) this issue can lead to a precipitation of large NaCl crystals on the substrate during the methanol evaporation. Yet, in experiments carried out with a salt concentration of 2.5 % NaCl did not show any crystal precipitates. Regarding sodium salt alternatives, NaF the preferred material used in physical deposition methods is not soluble in either solvent. Thus, other salts had to be considered that have not yet been evaluated in the literature. From the various options, soluble salts with anions having an expected good decomposition behavior have been preferred. As a result sodium formate ($NaHCO_2$) and sodium thiocyanate (NaSCN) have been chosen, both of which are highly soluble in the two solvents. Contrary to the thermally stable NaCl these compounds are decomposing both above 300°C [186], [187]. In summary in this section three sodium salts and the sodium free samples are evaluated in detail (Table 8).

Table 8: Sample nomenclature depending on the chosen sodium salts with a concentration of 2.5% compared to a sodium free precursor layer.

Series	Additional Na salt	Na concentration in mol-% of Cu	Diffusion barrier
1	*no*	-	*yes*
3	NaCl (chloride)	2.5	yes
4	$NaHCO_2$ (formate)	2.5	yes
5	NaSCN (thiocyanate)	2.5	yes

5.3.2 Characterization of the absorber layers

The processed layers have been characterized by several analytical methods. Figure 64 illustrates the measurement positions of the individual techniques including SIMS, SEM and grazing incidence X-ray diffraction (GIXRD) on a typical substrate. The image also includes the opto electronic analysis (j-V), the photoluminescence maps (PL) and the EQE measurement on the final solar cells, which are the topic of the next section. It is important to emphasize that the results are not fully comparable due to the different measurement positions and areas. While SIMS only measures on a small spot, the range of the GIXRD covers a very large area with several cells. This is particularly important for the investigated samples due to the observed thickness deviation over the substrate length (see also section 3.1.2). This issue will be further discussed below.

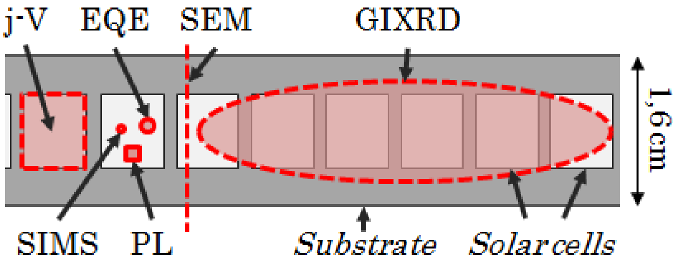

Figure 64: Illustration showing a typical substrate with several consecutive solar cells. The applied analysis techniques and their respective measurement range are highlighted.

For the cross sectional SEM imaging the samples have been broken at the dashed lign shown in Figure 64. The results are shown in Figure 65. Significant differences can be observed in grain size and structure. Helpful tools to interpret the morphologies are grazing incidence X-ray diffraction (GIXRD) where the penetration depth of the x-rays is dependent on the incidence angles as well as SIMS depth profiling (only measured on the samples with sodium salts). The former can be used to illustrate vertical crystallographic phase gradients in the chalcopyrite layer. The presented measurements have been carried out at Bosch CIS tech in Brandenburg. Figure 66 shows the results measured on the samples 1, 3, 4 and 5. The latter yields the qualitative gallium distribution over the film height. The SIMS results are depicted in Figure 67.

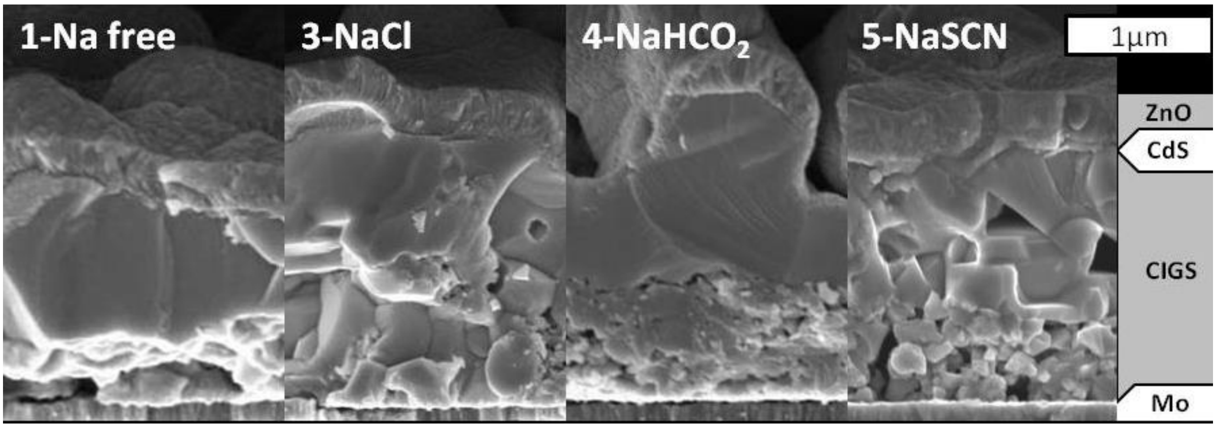

Figure 65: Cross sectional SEM images of solar cells with CdS buffer and ZnO window layer. The absorber layers have been processed from precursors containing no sodium (1), NaCl (3), $NaHCO_2$ (4) and NaSCN (5) (published in [75]).

The SEM image of sample 1 without any sodium source shows a two layer structure with a fine grained bottom layer and large crystals on top. With the results of the GIXRD analysis a Ga free CIS top layer (112 peak of $CuInSe_2$ is at 26.67° 2-theta [188]) and a Ga rich CIGS bottom layer can be clearly identified. This phase separation with a Ga accumulation at the back contact is widely found in the literature especially in the two stage precursor annealing processes [189]. The reason for this can be found in the different formation kinetics of the ternary CIS and CGS chalcopyrites from the metal alloys with selenium [188]. CIS forms first and the remaining gallium alloys are accumulating at the back contact. Thus, if the annealing time is too short the missing interdiffusion leads to the separated phases. Compared to this, sample 3 prepared with 2.5% NaCl looks more homogeneous with larger crystals near the back contact. The GIXRD graph explains this by a Ga interdiffusion up to the surface with a 2 theta peak shift of around 0.1° at an x-ray incidence angle of 0.4°. The interdiffusion is also the reason for the less pronounced Ga back accumulation resulting in a better vertical gallium distribution. The SIMS results, however, indicate only a very low gallium diffusion up to the surface with the rest accumulating at the back contact. In order to explain this the measurement positions have to be taken into account. While the SIMS measurement has been carried out at the front of the sample (in the direction of the previous ink deposition), the GIXRD covers most of the back. Here, the lower film thickness might have led to an improved gallium interdiffusion which would explain the slightly diverging results.

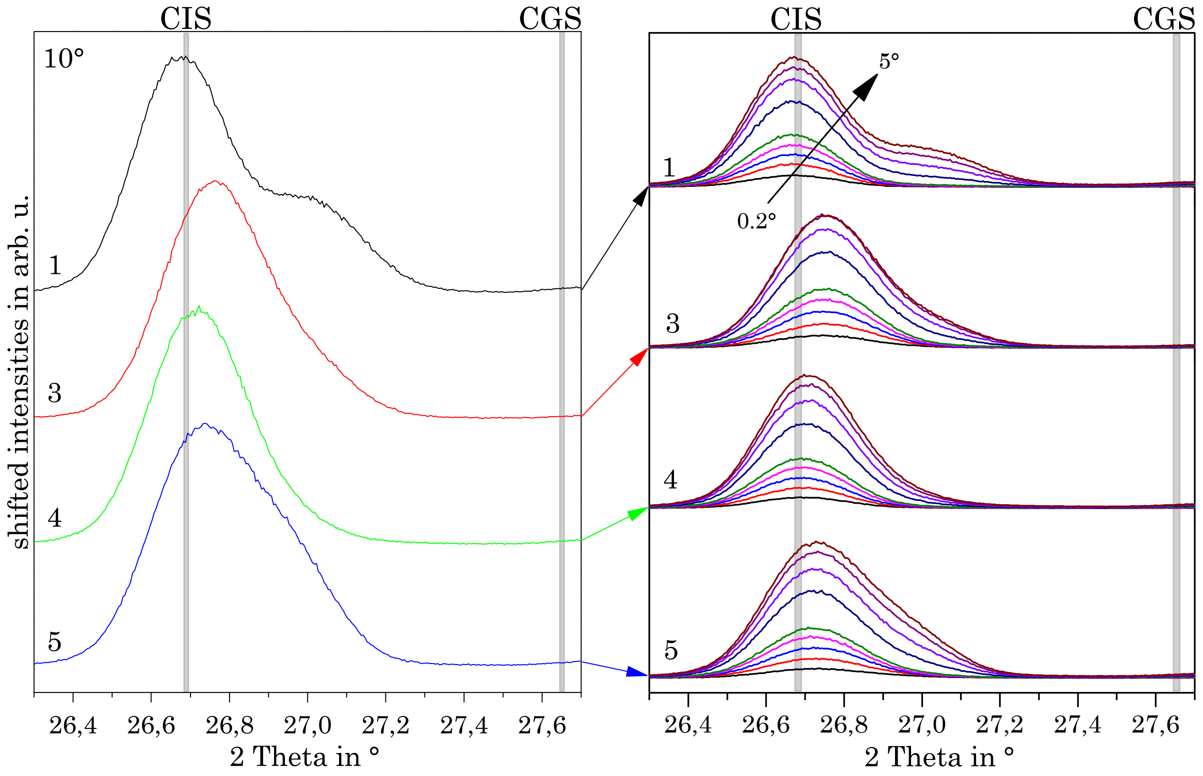

Figure 66: X-ray diffraction analyses of samples 1 (Na free), 3 (NaCl), 4 ($NaHCO_2$) and 5 (NaSCN). Left: total phase composition measured at an incidence angle of 10°. Right: GIXRD results measured at incidence angles of 0.2°, 0.4°, 0.6°, 1°, 2°, 3°, 4° and 5° (published in [75]).

The SEM image of sample 4 containing 2.5 % Na formate shows a deviating morphology with the absorber consisting again of two layers. Beside a high surface roughness, a layer of big grains on top of small nanoparticles surrounding smaller crystals is visible. The GIXRD pattern at 0.4° incidence angle suggests a Ga-poor CIGS phase near the surface due to a very small peak shift. At higher angles the peak shifts slightly further indicating an agglomeration of Ga near the back contact. The total amount of incorporated Ga has been calculated to Ga/(Ga+In) or Ga/III=0.11 by integrating the Ga fractions from the GIXRD results. For these calculations a model developed by Kötschau et al. has been used [190]. At this point it is important to note that the integrated Ga amounts in the chalcopyrite phase of the samples 1, 3 and 5 have been calculated to the initial value (Ga/III=0.2) suggesting a complete gallium incorporation. Thus, this result indicates that in sample 4 about half of the gallium has not been incorporated into the chalcopyrite. This can clearly be seen by looking at the 112 peak which is near to the pure CIS position while no large shoulder is observed at higher angles.

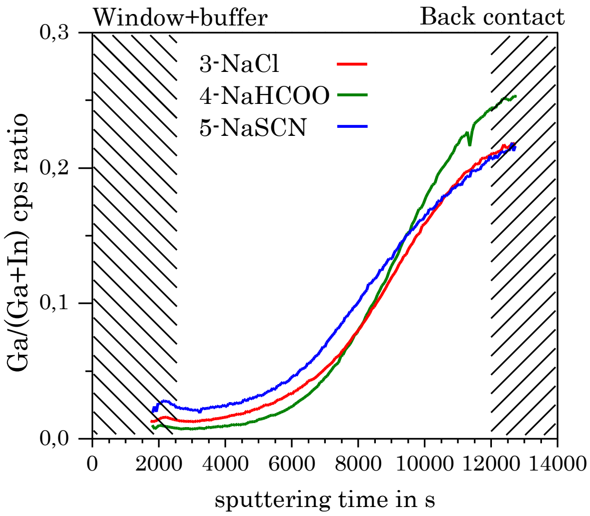

Figure 67: Ion count ratio of Ga over (Ga+In) over the layer height measured by SIMS (published in [75]).

An explanation can be found in the high temperature behavior of alkaline formates. In contrast for example to the Cu formate, Na formate has been reported to decomposes in inert atmosphere above 300°C to the corresponding oxalate reacting further to the chemically stable carbonate and oxide [20]. A thermodynamic evaluation indicaties that Na_2O has the ability to partially oxidize the metallic gallium in the precursor layer to gallium oxide. For indium and copper this is highly unlikely [191]. The formed Ga_2O_3 is not further available for the selenization to chalcopyrites since the oxide is significantly more stable than the selenide. Dirnstorfer et al. reported similar results. They annealed their CIGSe precursor in air and observed a gallium loss in the chalcopyrite phase due to the formation of Ga_2O_3 [192]. Additional high resolution XRD measurements did not show a crystalline gallium oxide phase in sample 4 to support this hypothesis which can be explained by the expected small size of the oxide particles being X-ray amorphous (not shown). The SIMS measurements, however, can be used to prove the presence of an increased amount of oxygen near the back contact. Figure 68 shows the oxygen over zink count ratio over the layer thickness. The graph clearly shows a constant O:Zn ratio over the window, buffer and most of the absorber layer. This can be explained by the constant composition of the window layer which should be the only oxygen source. At sputtering times above 8000 s the ratios increase in all samples. Yet, in comparison the sample made with NaHCOO shows by far the largest increase in accordance with the likely formation of Ga_2O_3.

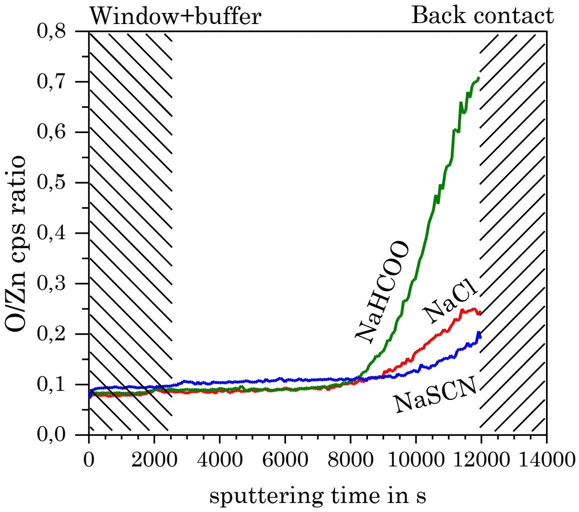

Figure 68: SIMS depth profiles showing the ion count ratios of oxygen over zink in the samples with NaHCOO(3), NaCl(4) and NaSCN(5) (published in [75]).

The GIXRD pattern of sample 5 prepared with 2.5 % NaSCN shows again a significant Ga incorporation near the absorber surface. However, the thiocyanate anion seems to lead to a slightly different vertical Ga gradient visible at higher incidence angles equivalent to deeper film levels. Above incidence angles of 1° the 112 peak of the absorber processed from the NaSCN containing precursor broadens significantly to the right due to a superposition of two peaks indicating a second gallium rich phase. This observation is in agreement with the SEM images showing a decreasing grain size towards the back contact which is typical for a gallium accumulation. The gallium profile measured by SIMS again confirms the gallium back contact accumulation. Yet, in comparison to the samples with NaHCOO and NaCl here the highest amount of surface gallium has been measured.

In summary, these results suggest that the addition of sodium salts improves the gallium interdiffusion. This is contradictory for example to a report by Rodriguez-Alvarez et al. who found a lowering of the gallium diffusivity in the presence of sodium [193]. However, one of the main differences in their process apart from the precursor deposition method is the sodium supply. In their work sodium is incorporated by diffusion from the SLG substrate, a method where the diffusion rate and therefore incorporation is temperature and time dependent. The present results based on an initial uniform sodium distribution in the precursor layer suggest an improved gallium interdiffusion independent on the sodium salt source.

Regarding the impurities carbon and nitrogen, the SIMS depth profiling measures identically low counts for both elements in the final chalcopyrite layer as can be seen in Figure 69. This is in agreement with the results of an elemental analysis revealing low carbon and nitrogen residues within the detection limit (0.07 ± 0.05 and 0.15 ± 0.1 mass-%, respectively). Sample 5 processed with NaSCN has also been analyzed regarding the incorporation of additional S atoms. Yet, a comparison of the SIMS results with the other two samples did not show any notable differences (not shown).

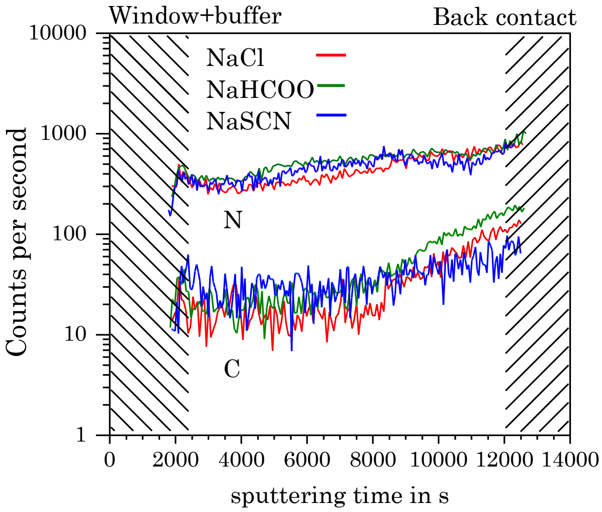

Figure 69: SIMS depth profiles with the ion counts of the impurities carbon and nitrogen in the samples with NaHCOO(3), NaCl(4) and NaSCN(5) (published in [75]).

The sodium distribution has also been measured by SIMS and is depicted in Figure 70. The y-scale shows the Na cps ratio to the selenium signal where Se has been used as reference. In the literature it is well known that in CIGS sodium is mostly found at the grain boundaries [162]. This means that a smaller grain size implying a larger grain boundary area consequently result in a greater possible sodium concentration. The graph shows a high Na/Se signal close to the buffer interface for the NaSCN sample and close to the back contact for all samples. This is consistent with the smaller grains seen in the cross sectional SEM images presented in Figure 65. A comparison of the Na signal with the Ga/III distribution in Figure 67 reveals that the Na distribution seems to be proportional to Ga/III ratio. This stands except for the back contact of the NaHCOO sample where only a very low Na concentration has been measured. The difference might be explained by the discussed formation of Ga_2O_3 in this sample which could have resulted in metallic Na as byproduct. This elemental sodium could then have evaporated [194] or formed volatile Na_2Se_x species during the selenization leading to the overall lower Na concentration in the NaHCOO sample shown by the SIMS measurement.

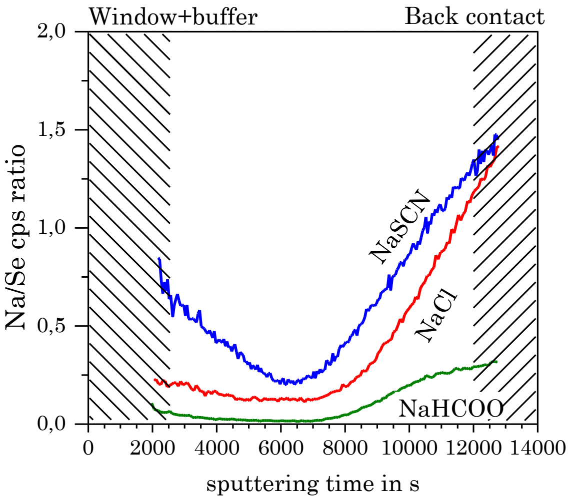

Figure 70: SIMS depth profiles showing the ion count ratios of sodium over selenium in the samples with NaHCOO(3), NaCl(4) and NaSCN(5) (published in [75]).

5.3.3 Characterization of the solar cells

In this section the final solar cell devices are evaluated in terms of external quantum efficiency (EQE) as well as current-voltage (j-V) properties. Figure 71 (left) shows the current collection of solar cells taken from the samples with NaHCOO(3), NaCl(4) and NaSCN(5). All samples discussed have again been processed without anti reflective coating (ARC). It can be seen that the photon generated carrier collection in all samples shows a squared behavior with a deviations in the long wavelength region. Only marginal differences can be observed in the area between 300 and 500 nm where the parasitic effects of the supplemental functional layers CdS and ZnO are visible, absorbing all (up to 360 nm, mostly absorption of the window layer) and more than half (up to 450 nm, absorption of the buffer layer) of the incoming radiation. This indicates that the buffer and window layers are identical in all samples. Between 500 nm and 1100 nm most of the photon harvesting takes place. All measured cells show the best carrier collection for photons with wavelengths between 550 and 900 nm resulting in a good broad middle band response of around 90%. In the long wavelength region above 1000 nm the current collection of sample made with NaSCN is significantly lower compared to the other two.

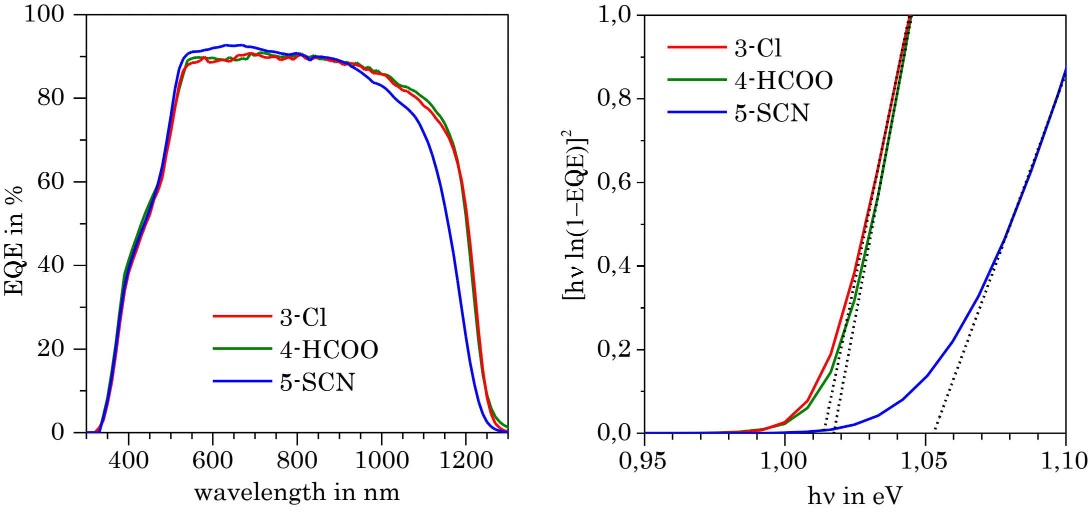

Figure 71: Left: EQE of the samples 3, 4 and 5. Right: Estimation methodology for the band gap from a linear fit and an extrapolation of the plot [hν ln(1-EQE)]^2 over (hν) (published in [75]).

The band gaps of the three samples have been estimated by plotting the relation [hν ln(1-EQE)]^2 over (hν) and using a linear fit, a method which has been proposed by Zoppi et al. [195], [196] (Figure 71 right). The samples 3 and 4 have a band gap between 1.01 and 1.02 eV indicating a gallium free CIS layer at the top [10]. Sample 5 has a slightly higher band gap of 1.05 eV. The results can be correlated with the previously discussed SIMS results measured at the same position showing a very low amount of surface gallium in the samples 3 and 4 as well as an improved Ga interdiffusion in sample 5 [197].

Micron resolved photoluminescence maps have been prepared from the samples containg NaCL and NaSCN showing the peak position. The graphs indicate a constant lateral band gap for the NaCl sample while the absorber layer in the NaSCN containing sample shows significant deviations. An explanation might be that the latter consists of two separate phases possibly as a result of an inhomogeneous sodium salt and consequently sulfur distribution during the film drying. The presence of two different band gaps in the NaSCN sample does also explain the shallower slope of the EQE edge at lower wavelengths compared to the steeper slope of the NaCl sample.

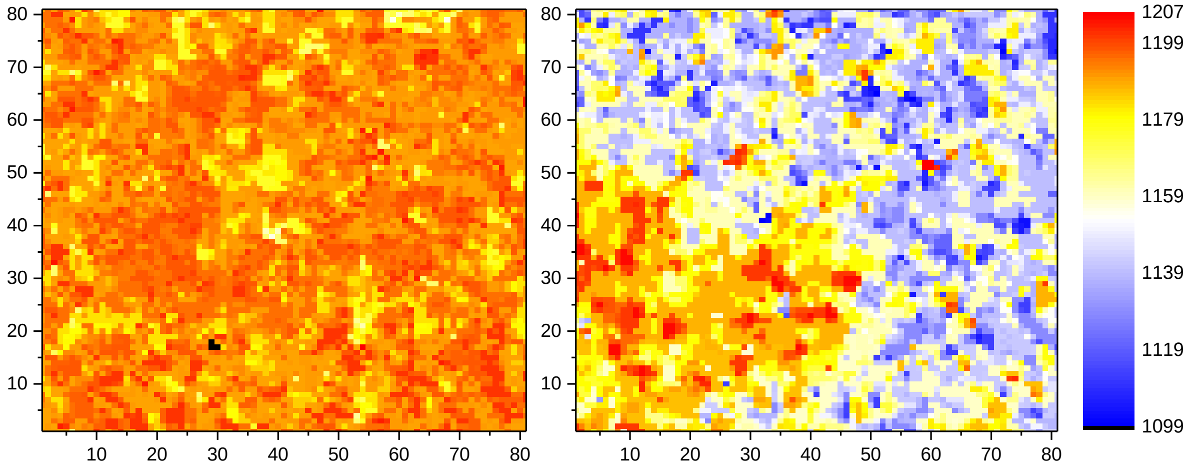

Figure 72: Wavelength-PL maps showing the intensity maxima in a 80x80µm² area measured on the samples containing NaCl(3, left) and NaSCN(5, right) (published in [75]).

The optoelectronic properties of the solar cells are depicted in Figure 73. In general, the measured values for all samples are very similar. Consequently, high efficiencies above 11% can be achieved with all three Na salts. Values above 12% have been achieved only with NaCl and NaSCN. The best V_{oc} values are found for the samples made with NaSCN which can be correlated to the discussed higher band gap as a result of the improved gallium interdiffusion. High j_{sc} values can be seen for the sample made with NaHCOO most likely due to the observed gallium depletion.

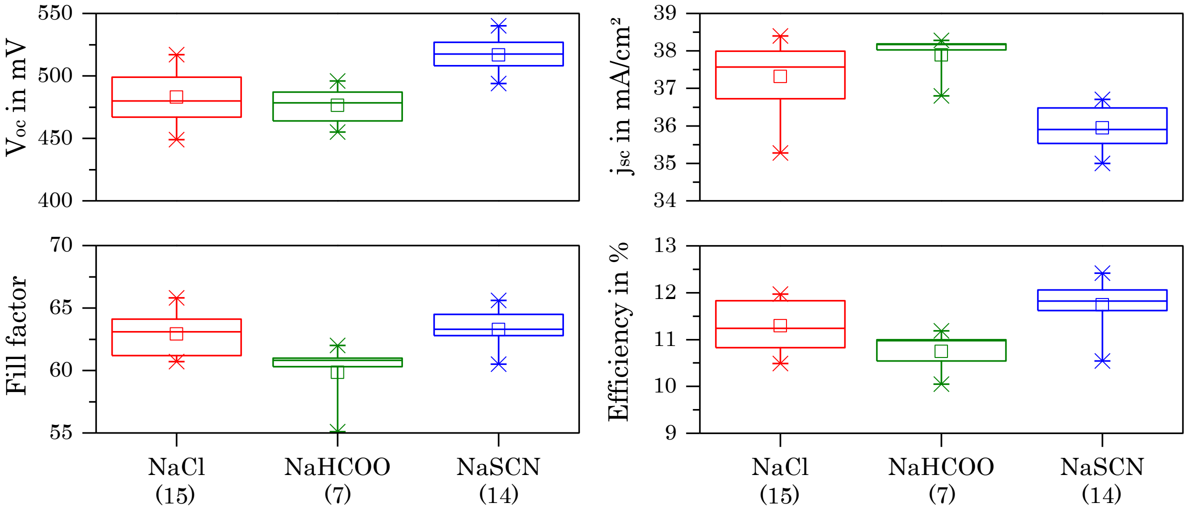

Figure 73: Current-voltage properties of solar cells processed with the different sodium salts NaCl, $NaHCO_2$ and NaSCN. The numbers in brackets correspond to the number of measured cells (published in [75]).

5.4 Optimization of the selenization

In the chapters 2 and 3 a lot of effort has been invested into the precursor layer optimization. Chapter 4 evaluated the process step selenization with the lab scale tube furnace and revealed a high dependency of the cell device performance depending on the parameter delay time. This gives an idea how delicate this process step is. In this section the selenization routine is further evaluated by applying the same annealing procedure on sputtered precursor layers. Based on these results an optimization is proposed.

5.4.1 Comparison to sputtered precursor layers

In order to estimate the quality of the selenization process the same annealing routine has been carried out on a sputtered metal precursor layer. This layer has been deposited on the back contact by sputtering from alternating CuGa and In targets. For more information about the precursor the reader is referred to a publication by Probst et al. [198]. In this publication they showed that modules with efficiencies of up to 15.1% can be fabricated from this type of precursor. At this point it has to be noted that these values have been achieved with a surface near incorporation of sulfur. The incorporation mechanism for sodium is also different as the industrially optimized precursors usually have a separate sodium source [199]. Nevertheless, the lab scale selenization process used in this thesis with the gas phase chalcogen transport is similar to the one described in the publication. They also transfer evaporated selenium to the heated metal layers via the gas phase. Thus, a characterization of cells made from a sputtered precursor layer that has been selenized in the tube furnace can give valuable information about the quality of the annealing routine.

The achieved current-voltage properties of the best cell denoted as “Sput” are shown in Figure 74. In order to compare the results to the solution based samples the champion cells (in terms of efficiency) from the experiments 1, 3, 4 and 5 are added to the graph. It can be clearly seen that the sputtered sample reaches similar values in all optoelectronic properties. Assuming an optimized sodium supply in the vacuum deposited sample, this result suggests that one of the bottle necks of the presented chemical approach regarding an efficiency improvement is the selenization procedure. This hypothesis is further investigated in the next section.

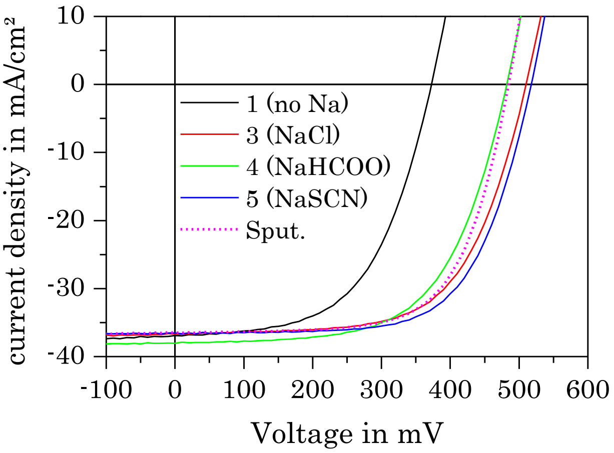

Figure 74: J-V curves of solar cells processed from the chemically processed precursor layers compared to a sputtered precursor annealed using the same routine.

5.4.2 Adjustment of the annealing time

In the previous section a possibly high optimization potential has been identified in the selenization step. With the chosen parameters, similar device results have been achieved from sputtered as well as chemically deposited precursors. One of the main differences to other approaches regarding the process parameters is the annealing time. In contrast to the 7 minutes applied in the lab scale tube furnace industrially processed absorbers are usually annealed for longer than one hour. Thus, two experiments have been carried out to investigate the influence of an increased annealing time.

Chemically deposited precursor layers with 2.5% NaCl have been chosen for these experiments due to the absence of sulfur atoms in the sodium salt to exclude any possible sulfur related effects. Two identical precursor layers have been prepared which have been tempered up to 200°C using standard parameters. These samples have subsequently been selenized in the tube furnace for 7 and 20 minutes. Figure 75 (top left) shows the j-V curves of the two champion cells selected from the respective substrates. The graph indicates that the 7 min sample reaches a total an efficiency of 11.8 % whereas the sample annealed for 20 min is significantly better with 13.3 % (13.8% active area efficiency). This is the highest reported efficiency for solution processed CIGS solar cells without sulfur. The differences can be attributed to an increase in fill factor and a higher open circuit voltage while the j_{sc} value decreases slightly. An explanation for this can be found in the EQE, XRD and PL results shown in the same figure. The current collection as well as the absorber band gap both derived from EQE measurements are shown in Figure 75 (top right). It can be seen that the 7 minute sample has a good collection with a band gap of around 1.02 eV similar to the identically processed sample 3 discussed in the previous sections also containing 2.5% NaCl. In the 20 minute sample, however, the band gap increases to 1.05 eV. The reason for this is most likely the better gallium interdiffusion which could be measured using X-ray diffraction (Figure 75 bottom left). The 7 minute annealing leads to two separate chalcopyrite phases with a gallium segregation while the longer annealing time homogenizes the gallium distribution. The trend in the band gap increase is also visible in the PL graph (Figure 75 bottom right). Detrimentally, the EQE suggests that the longer annealing reduces the carrier collection length resulting in the measured lower j_{sc} value. This result shows that the selenization still has a high optimization potential.

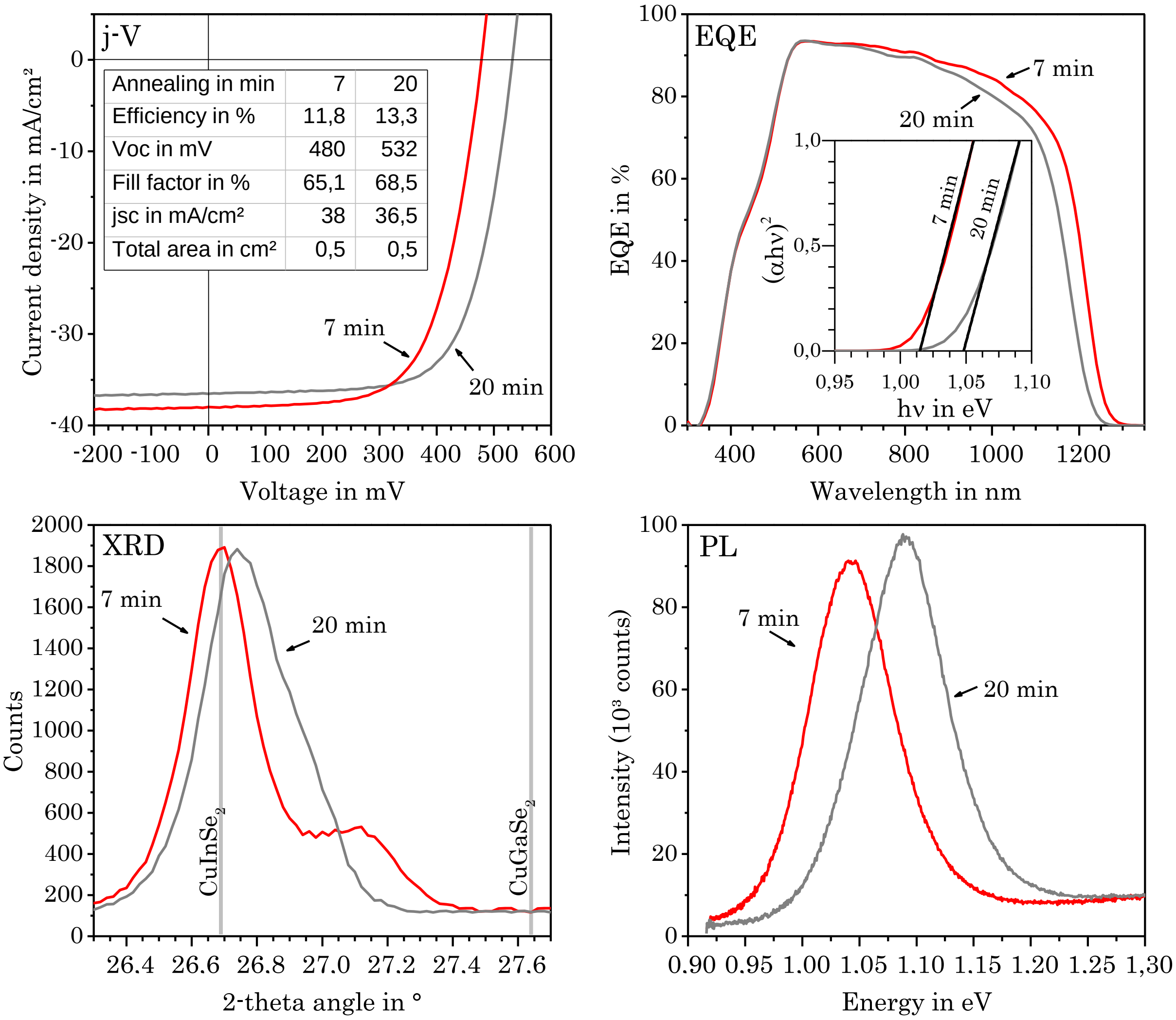

Annealing in min	7	20
Efficiency in %	11,8	13,3
Voc in mV	480	532
Fill factor in %	65,1	68,5
jsc in mA/cm²	38	36,5
Total area in cm²	0,5	0,5

Figure 75: Top left: J-V curves and solar cell parameters of precursor layers containing 2.5% NaCl annealed in selenium for two different times. Top right: EQE curves including the band gap estimation with α=ln(1-EQE). Bottom left: XRD data. Bottom right: PL graphs (published in [75]).

5.5 Summary of chapter 5

In this chapter the solar cells are characterized and the influence of additional sodium sources is evaluated. In the first part a sodium incorporation by diffusion from the soda lime glass substrate is compared to a precursor layer containing NaCl added to the ink and a sodium free sample. Annealed with the same parameters, the finished cells reveal large differences. Both sodium incorporation strategies reach higher values in open circuit voltage and fill factor than the sodium free sample. However, the cells made from the NaCl containing precursor yield significantly better values in all optoelectronic properties. These results indicate that the sodium salt addition to the ink is a useful technique to supply the alkali metal which outperforms the diffusion from the soda lime glass under the chosen selenization conditions.

In the second part of the chapter three different sodium salts (NaCl, $NaHCO_2$, NaSCN) and a sodium free sample are compared and are further characterized regarding the absorber layer morphology, the vertical element distribution and phase composition as well as the external quantum efficiency and the optoelectronic parameters. One particular finding are significant differences in the gallium interdiffusion. The results vary from a complete gallium back contact accumulation for the sodium free sample to a measureable diffusion of gallium up to the surface in the samples containing NaCl and NaSCN. $NaHCO_2$ in the precursor presumably leads to an oxidation of a significant gallium fraction resulting in gallium poor chalcopyrite crystals after the selenization. The differences in the EQE measurement are rather small revealing low semiconductor band gaps for the samples made with NaCl and $NaHCO_2$ and a slightly higher value for the sample with NaSCN. The optoelectronic properties of the sodium containing samples are very similar with slightly lower voltages in the $NaHCO_2$ containing device probably due the least gallium incorporation. The highest voltages have been measured on the sample containing NaSCN having also the best gallium gradient. Regarding the cell efficiency values between 11 and 12% have been achieved with all three salts.

In the last part of the chapter the chemically porcessed solar cells are compared to an industrially optimized sputtered precursor layer selenized the lab scale tube furnace using the same parameters. The device results are in the range of the cells processed from chemically deposited precursors. This finding strongly suggests a process limitation in the annealing procedure. Following this hypothesis, additional experiments carried out with an increased annealing time resulted in reproducible efficiencies above 13%.

Summary and outlook

In this work vacuum free processed Cu(In,Ga)Se_2 absorber layers for solar cells have been fabricated which show, despite the low maturity of the process, strikingly promising optoelectronic properties. By developing a new ink system based on cheap, reasonable toxic and non explosive chemicals the substantial drawbacks of the current efficiency record holder of the non-vacuum based processes represented by the hydrazine approach could be overcome. Therefore a key message of this thesis is that the solution based CIGS deposition with this approach can be highly competitive to the industrially preferred vacuum deposition processes. Further indications for this claim and also future challenges are presented in the outlook.

The ink used in this work is based on metal formates dissolved in a mixture of a good sequestering agent in the form of a strong base, an alcohol necessary to adjust the coating properties and an additive used to improve the final metal layer morphology. The metal ions in the ink system are highly concentrated making a one step ink deposition possible. Homogeneous liquid films have been fabricated with a blade coating technique followed by a solvent drying under a flowing nitrogen gas stream. The high reduction potential of the formate anion allows a metal ion reduction in a subsequent tempering step between 130 and 200°C. A new additive ensures a flat and dense layer morphology. The effect is based on the formation of intermediate polymers consisting of the additive as well as Cu(II) and formate ions. These polynuclear compounds lead to a stable metal-organic matrix during the metal ion reduction. At elevated temperatures the matrix decomposes cleanly revealing dense layers of metallic nanoparticles.

Chalcopyrites have been produced by exposing the metal layers to selenium vapor in a tube furnace at temperatures around 600°C. The quality of the absorber has been shown to highly depend on the state of the precursor layer by the time the chalcogen vapor arrives. Good solar cells have been produced by heating the precursor above 500°C before the arrival of the reactive selenium gas. Based on a modeled selenium evaporation the reason for this effect is proposed to be the necessary decomposition of small organic residues above 450°C.

In the presented process sodium can be easily incorporated by dissolving appropriate amounts of soluble sodium salts in the ink. The thereby achieved homogeneous sodium distribution in the precursor layer leads to an instantaneous sodium supply during the selenization which drastically improved the solar cell parameters compared to a typical sodium diffusion from the glass substrate. Additionally, significant differences in the gallium distribution as well as the layer morphology have been found within three investigated sodium salts. Despite the differences, solar cells with efficiencies of 11 to 12% could be produced with all three salts.

In order to evaluate the quality of the applied annealing routine, an industrially optimized sputtered precursor layer has been selenized in the same tube furnace. The thereby achieved cell results are in the same range as the chemically processed samples and are therefore significantly below their potential reported in the literature. An investigation of the influence of an increased annealing time from 7 to 20 min revealed a high improvement in fill factor and open circuit voltage. Thus, efficiencies of 13.3% (13.8% active area efficiency) could be achieved which is the highest reported value for solution processed CIGS solar cells without sulfur.

Outlook

The results presented in this thesis indicate a high optimization potential in several process steps. Thus, various recommendations for future work can be derived particularly in view of a scale up. Beginning with the ink chemistry, to further improve the applicability of the ink in a future industrial process the toxic solvent methanol can be easily substituted by the nonhazardous ethanol. The simple incorporation of sodium demonstrated with various salts dissolved in the ink leaves room for further investigations for example regarding other alkali dopants like potassium or additional metalloid salts (antimony). The influence of the salt anions is also far from understood.

Regarding the processing the lab scale ink deposition by bade coating chosen for this work already is compatible to a one step roll-to-roll processing. Yet, a further scale up most likely requires an investigation of the applicability of the ink in industrially well known coating techniques like slot die coating. In this case the solvent evaporation so far only optimized for the lab scale makes more sophisticated drying concepts necessary.

The selenization procedure has been shown to be a bottle neck regarding a process optimization towards a better absorber quality and higher cell efficiencies. In order to further improve the process a better understanding of the interactions between the decomposing organic residues and the arriving reactive selenium molecules has to be developed. Also other furnace concepts might have to be considered especially regarding a scale up. In order to increase the cell voltage an additional surface near incorporation of sulfur might have to be considered which can be easily achieved over the gas phase. The already good current collection can be further improved by depositing an antireflective layer on top of the final solar cell.

Appendix

A. Effects of intermolecular interactions on the methanol evaporation

In section 3.2 the evaporation of methanol is investigated which mostly occurs at low temperatures. The TG-MS results in section 3.4.1, however, suggest that a small part of the methanol (about a fifth) stays relatively long in the ink mixture and evaporates at significantly higher temperatures. The reason for this can most likely be found in several non ideal intermolecular interactions between the two liquids and also between methanol and the solvated metal salt ions. This section tries to evaluate these non idealities and to give a quantitative description in the form of a vapor pressure reduction.

Indications and explanations for the delayed methanol evaporation

The TG-MS measurements in section 3.4.1 can be used to trace the methanol evaporation between room temperature and 120°C. The ion currents measured by the mass spectrometer can directly be correlated to the evaporation rates of the solvent. Without exceptions, all analyzed inks (single and ternary) reveal significantly lower values than expected by pure methanol. This observation cannot solely be explained by the previously calculated non idealities between the two solvents based on the UNIFAC model used in section 3.2.3 [110]. Additional effects have to be considered.

One comprises the ternary (TMG)-(methanol)-(formate anion) interactions. Nelson et al. investigated the effect of methanol on dissolved copper(II) acetate salt at elevated temperatures [200]. They observed the formation of copper(II) methoxide and methyl acetate. They strongly suggest that the acetate ion is responsible for the methanol deprotonation. However, since the acetate ion is a much weaker base with a pK_b value of 9.25 than the methanolate ion (pK_b=-2), this indicates a relatively high enthalpy of the formation of the copper-methoxy complex. In the CuInGa ink, additional TMG is present and the acetates are substituted by formates which have a similar basicity (pK_b=10.25). TMG is a significantly stronger base having a pK_b value of 0.4, a value which is higher than found in typical amines due to a mesomeric cation stabilization [198] (see also section 2.3.1).

Gusakova et al. measured a value for the equilibrium constant K of the reaction of the formation of a molecular complex formed between TMG and methanol in the inert, nonpolar solvent CCl_4 (25 l/mol at 25°C) [201]. It is important to note that this value is highly dependent on the used solvent. Yet, a transfer of this K value to a typically used ink mixture with a molar ratio of TMG:methanol of 1:4.8, would lead to a complex formation affecting almost all TMG molecules. If a similar behavior can be assumed in the presented process, the resulting hydrogen bonding between the alcohol group and the imino nitrogen could be used as an explanation for the highly reduced vapor pressure.

Further indications for this hypothesis can be extracted from the TG-MS measurements of the individual inks. Table 9 shows that the methanol:TMG ratios in the ink after the TG-MS sample preparation in air is constant around 1:1.2 which is significantly lower than in the pristine inks where it was around 1:5. This can be explained by the fast evaporation of the low boiler methanol at room temperature during the sample preparation. The remaining methanol molecules in the ink have to be stabilized for example by the effect discussed above which would explain the molar ratio of around 1:1.

Table 9: Calculated amount of MeOH in the pristine ink and after the TG preparation

Sample	Molar ratios TMG:MeOH	
	Pristine ink	After TG preparation
Cu-ink	1:5.4	1:(1.24 ± 0.1)
In-ink	1:4.9	1:(1.19 ± 0.1)
Ga-ink	1:4.9	1:(1.19 ± 0.1)
CIG-ink	1:4.5	1:(1.25 ± 0.1)

A second effect might be attributed to the (methanol)-(salt ion) interactions. It is well known that methanol molecules can solvate several transition metal ions. Inada et al. determined the solvation structures of methanol in combination with Cu(II) and Ga(III) ions by X-ray absorption fine structure spectroscopy [203]. Both metal ions have been found to coordinate octahedraly. The presence of a methanol solvation shell surrounding the Cu(II) ions in our ink system might also be the reason for the observed color change from the greenish Cu(II) TMG ink to the typical blue color of Cu(II) ions after adding the alcohol. Also the evaporation rate of methanol increases significantly after the reduction of the Cu(II) ions to Cu(I) probably because the solvation of Cu(I) is less stable.

Quantitative description

A quantitative description of the mentioned effects on the ink behavior can be derived from the TG mass loss curve. The evaporation rate of methanol as a function of the temperature can be extracted by tracing the mass spectroscopic (MS) signals. As long as there is only one ion current present with m/e=31 the measured mass loss can be attributed exclusively to the alcohol. Figure 76 shows the TG mass loss of a typical CIG ink with a heating ramp of 10 K/min. As can be seen from the MS-data below 80°C only methanol is evaporating. Above TMG (m/e=71) can also be measured in the gas phase.

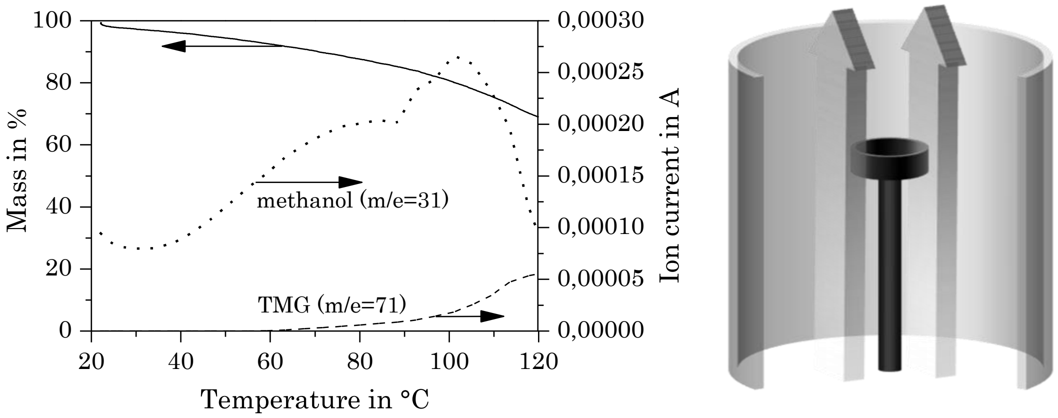

Figure 76: Left: TG mass loss + MS data of a CIG containing ink with the ion currents of methanol and TMG. The exclusive methanol evaporation occurs up to 80°C. Right: Illustration of the inside of the TG-MS with the sample holder placed in the center of a heated tube.

From the measured mass loss in the temperature range between 20 and 80°C, the molar flux of methanol can be extracted as a function of the temperature. With these values the theoretical partial pressure of methanol is accessible using the already introduced formula (3-5). In (5-1) γ_1'describes a theoretical activity coefficient containing all the non-idealities originating from the other ink ingredients.

$$\dot{N}_1 = -\frac{\beta_i}{R\,T}\,A\,\gamma_1'\,x_1\,p_1^*(T)$$

The missing variable, the mass transfer coefficient β, is dependent on the nitrogen gas flow configuration, the device geometry inside of the TG machine as well as the diffusion coefficient of methanol in nitrogen. The latter is again accessible with a group contribution method (Fuller equation [109]). Regarding the other two, Figure 76 (right) shows schematically the cross section of the TG device with the sample holder positioned in the center of a tube that has a forced nitrogen gas flow entering from the bottom. Due to the gas supply coming from beneath the sample, a simple approximation of beta using a tabulated Sherwood correlation is not possible for this setup. Thus, the mass transfer coefficient had to be estimated by a second TG experiment with pure TMG using identical parameters. The resulting TG curve is shown in Figure 77. Due to the known vapor pressure of the pure solvent, beta can be calculated as a function of the temperature showing an almost linear behavior in the specified temperature range. With this beta and the known ratio of the diffusion coefficients of TMG and methanol, a material-independent mass transfer coefficient for this TG setup has been generated. Having all variables in the equation (5-1), the theoretical vapor pressure $p^*_{1,th}(T)$ can be calculated.

$$p^*_{1,th}(T) = (\gamma'_1 p^*_1(T)) = -\frac{\dot{N}_1\, R\, T}{x_i\, \beta\, A}$$

Figure 77 shows the trend of $p^*_{1,th}(T)$ in the specified temperature range in comparison to the vapor pressure of the pure methanol. The difference between both curves increases from a factor of 6 to more than 12 with higher temperatures. An extrapolation of this theoretical curve leads to a boiling point elevation of +80 K.

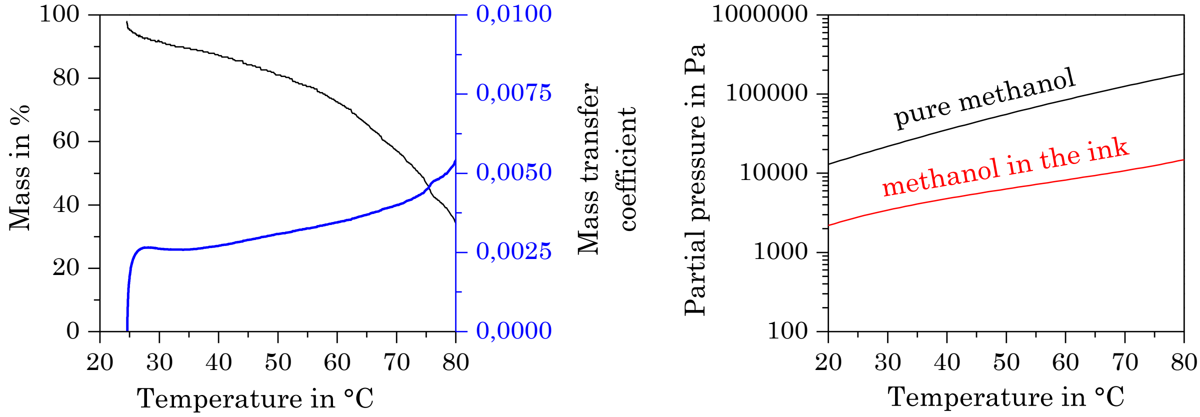

Figure 77: Left: mass loss and calculated mass transfer coefficient of pure TMG heated with 10K/min. Right: Partial pressures of methanol as a function of the temperature. Black: Pure methanol (Antoine-eq.); Red: Calculated partial pressure from the methanol mass loss in the ink.

In summary the discussed non-idealities in the ink mixture can be expressed as a vapor pressure lowering. Methanol molecules are probabaly highly bound to the present metal salt ions as well as the solvent TMG and are therefore showing a lowered readiness to leave the ink. A calculation of this vapor pressure lowering using the evaporation data from TG-MS experiments reveals a theoretical value which is around one order of magnitude below the vapor pressure of the pure liquid.

B. Crystal syntheses

The syntheses have been performed in inks consisting of copper formate and 4ATA dissolved in methanol and stirred at room temperature (A) and above 50°C (B). Single crystals from sample A could be separated by filtering the mixture followed by a slow evaporation of the alcohol.

The second reaction B executed at elevated temperatures has been observed by a color change of the solution from blue to green. Single crystals could be separated with the following procedure. At first the solution has been filtered followed by a fast evaporation of the methanol resulting in a green amorphous compound covered with blue copper formate crystals. The separation of the two materials has been performed manually. The separated pure green compound was then dissolved in a small amount of deionized water leading to an almost saturated solution. In order to grow crystals from this solution, a very slow indiffusion of isopropanol has been executed taking place in a time period of several months. The used diffusion methodology is schematically shown in Figure 78. The aqueous solution has been placed in an open vial and topped with a large amount of insoluble octanol. Two separated liquid phases formed and the vial was placed in a second closed vial filled with a small amount of isopropanol. Due to the insolubility of the product in octanol and isopropanol and the full miscibility of water and isopropanol, the slow indiffusion of isopropanol through the octanol layer into the solution led to a slow precipitation of blue crystals.

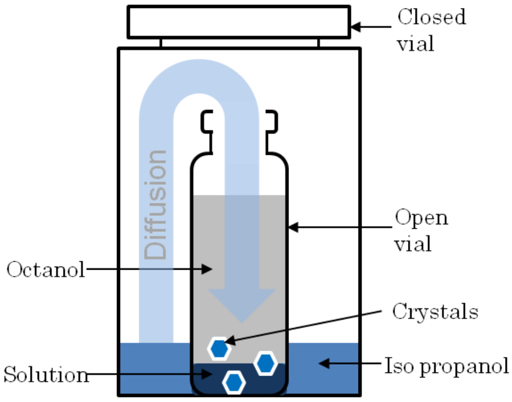

Figure 78: Crystallization methodology for polymer B: Slow indiffusion of isopropanol through an octanol barrier leading to a controlled precipitation of crystals from the aqueous ink.

C. Crystal structures

Two new materials have been synthesized during this work. The crystallographic structures are attached in the following.

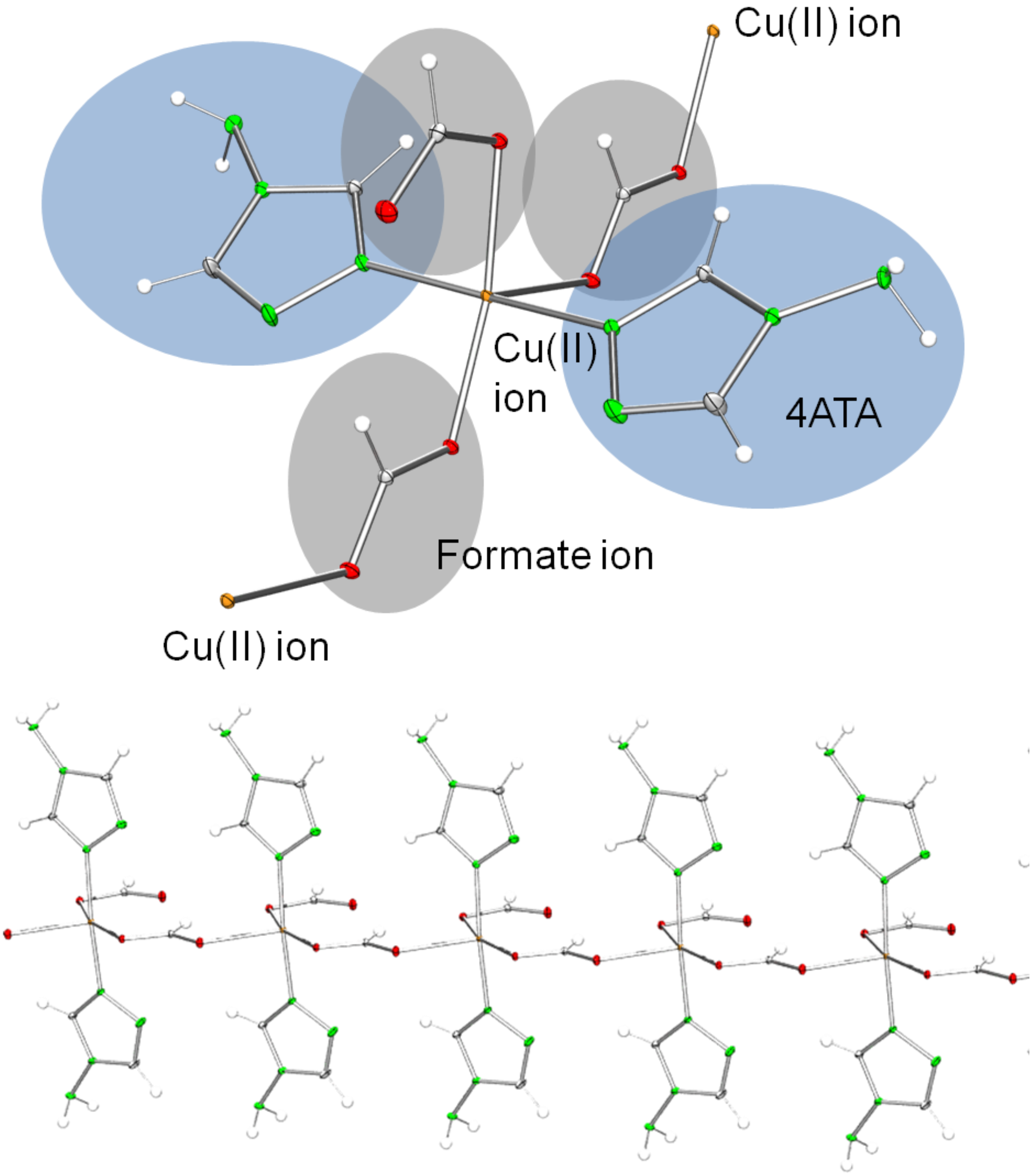

Figure 79: Crystal structure of polymer A. Top: basic unit cell. Bottom: Chain structure.

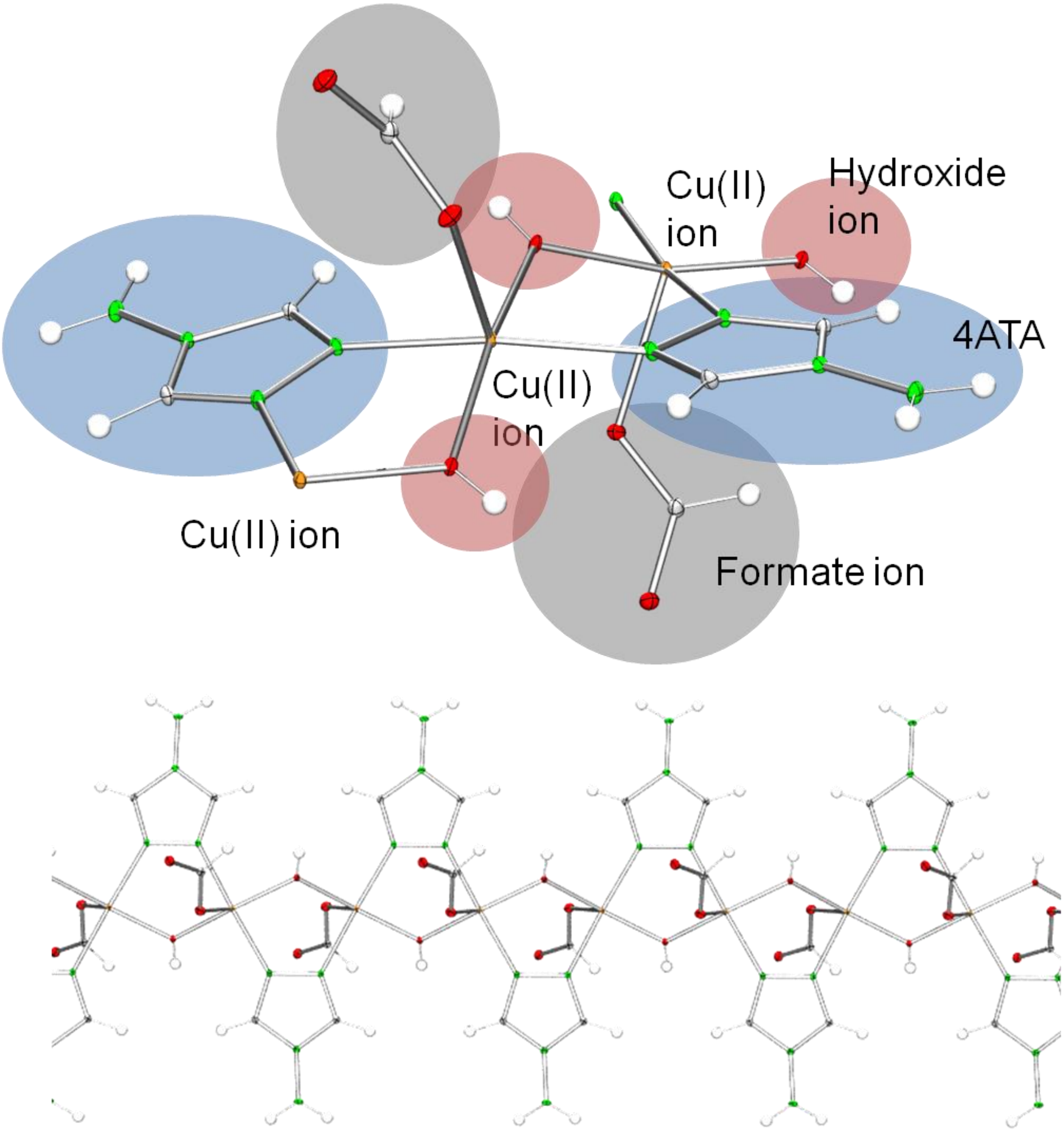

Figure 80: Crystal structure of polymer B1. Top: basic unit cell. Bottom: Chain structure.

D. Characterization methods

This section gives a brief introduction into the characterization techniques that have been used in this work.

Elemental analytics (EA)

Two element analytic techniques have been used in this thesis to measure the mass fractions of carbon, nitrogen, hydrogen and oxygen. They are based on different measurement methods which are sensitive to different atom sets.

To quantify the amount of nitrogen and oxygen, an inert gas fusion infrared and thermal conductivity detection has been applied. This method is based on the decomposition of the oxygen and nitrogen containing materials in an ultraclean carbon holder at temperatures above 2000°C in a helium atmosphere. Under these conditions the oxygen is reacting to carbon monoxide which is transported by a helium stream to a chamber filled with heated copper oxide where it is transformed to carbon dioxide. The amount of CO_2 is subsequently quantified by an infrared analysis. The nitrogen containing compounds in the sample are reduced at the carbon holder to N_2 which is also transported away with the helium stream. After the CO_2 detection the remaining nitrogen is separated by removing the CO_2 in special absorbers. Eventually, the amount of nitrogen is quantified in a thermal conductivity cell. The whole procedure is carried out automatically by a Leco TC600.

The mass fractions of the elements H, C and N have been quantified by a vario MICRO cube (Elementar). Here, the samples are heated in a furnace to temperatures up to 1200°C. Contrary to the previous method this combustion takes place in an oxygen containing environment which makes a detection of the incorporated amount of oxygen impossible. The gases from the combustion are subsequently transported to a heated copper matrix where they are reduced to N_2, CO_2, H_2O and SO_2. The gas mixture is then split in the individual components by three consecutive adsorption columns. These columns are filled with highly selective adsorbents. Nitrogen is not adsorbed and the N_2 molecules are transported directly to the adjacent conductivity detector where its amount is quantified. When the N_2 signal vanishes the three columns are heated successively and the individual signals are monitored. In the used adsorbents CO_2 is released at 60°C, H_2O at 100°C and finally SO_2 at 200°C. A low error within this method is ensured by a calibration of the machine with several calibration compounds having a known composition prior to every analysis.

External quantum efficiency (EQE)

External quantum efficiency measures the spectrally resolved current density of solar cells. In other words the obtained data gives the ratio between the charge carriers collected by the solar cell and the incident number of photons arriving at the cell. In order to be collected, the photons have to be absorbed in the cell generating an electron hole pair. These charge carriers have to be separated and have to travel to the electrodes without recombining. A chopped white light source is used to generate the photons which go through a monochromator to adjust the output to a specific wavelength.

The EQE spectra presented in this work have been measured by two different setups which have been calibrated with different solar cells. Setup 1 is calibrated by a silicon solar cell provided by the Fraunhofer ISE. Due to the silicon band gap of around 1.1 eV the measurement range of this setup is limited to wavelengths below 1200 nm. The second setup 2 is calibrated by two solar cells made of silicon and an InGaAs alloy, respectively. In contrast to setup 1, the lower band gap of the InGaAs cell allows a measurement over the full range including the long wavelength region. The graphs in Figure 81 show the differences in the output of the two EQE setups. For these graphs two CIGS solar cells have been analyzed at the same position on both EQE devices.

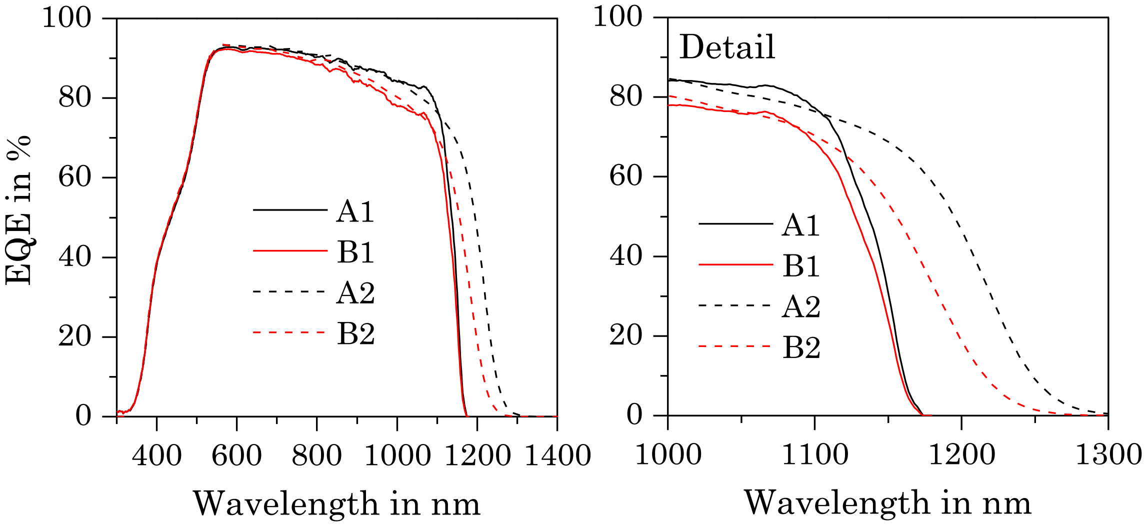

Figure 81: EQE curves of two CIGS solar cells (A and B) with different band gaps measured with the two EQE setups (1 and 2).

It can be seen that the graphs measured with the two different devices are almost identical for wavelengths below 1100 nm. Above, the setup calibrated with the silicon cell cuts off all information. Setup two shows here a carrier collection for photons with wavelengths of up to 1300 nm indicating a band gap below 1.1 eV. Thus, only these results can be used to estimate the band gap of the solar cell.

Fourier transformed infrared spectroscopy (FT-IR)

This technique measures the absorption of infrared light by chemical groups in a sample. The absorbed wavelengths are resonant frequencies matching a specific vibration mode in a chemical structure. The resulting IR spectra which is usually calculated by Fourier transformation can be used to identify the prevailing groups. In this thesis infrared spectroscopy has been carried out in two modes, transmission and attenuated total reflection which are briefly introduced below.

Transmission IR

Transmission IR is the most used IR setup. Here, infrared light directly shines through the sample and the not absorbed passing light is recorded and calculated to the typically found IR spectra. The transmission IR measurements for this thesis have been performed on an Equinox-55-2 (Bruker).

Attenuated total reflection IR (ATR)

ATR uses evanescent waves occurring at total internal reflections to measure the absorption. For this measurement the sample is placed on a crystalline compound consisting for example of germanium, zinc selenide or a diamond. The infrared light passes the crystal and is reflected at the internal surface in contact with the sample. At the reflection point evanescent waves are forming penetrating the sample placed on the crystal surface. Wavelengths that initiate vibration modes in the sample molecules are weakened. Finally, the beam exits the crystal and is collected by a detector. Due to the low penetration depth ATR-IR measurements have advantages with highly absorbing materials. The attenuated total reflection IR measurements discussed in this work have been carried out on a Lumos-1 (Bruker) with a diamond crystal in single reflection mode.

Light beam induced current (LBIC)

Light beam induced current is a technique that measures the global response of a solar cell to a focused light beam. Thus, by scanning the surface a two dimensional map of the cell can be generated. The method can be used to identify defects or film inhomogeneities as well as to measure the active area. In this work an advanced LBIC measurement technique has been used called CELLO [204]. The analyses have been performed under constant voltage without any bias illumination using a red laser (628 nm).

Scanning electron microscopy (SEM)

Scanning electron microscopy is a method to produce high resolution images of a sample. The measured signal is the result of the detected interaction between an electron beam and the surface near atoms of the sample. The electron beam is usually emitted by a field emission gun. This beam then scans the surface in a raster over a rectangular area. At contact of this primary electron beam with the sample several interactions are possible. High energy electrons are scattered elastically while secondary electrons are the result of an inelastic scattering. These electrons are emitted together with an electromagnetic radiation. All of these interactions can be detected and transferred to an image by synchronizing each pixel with the position of the beam and its intensity. In this work a SEM 1530 (Zeiss) has been used with an excitation voltage between 3 and 5 keV.

Secondary ion mass spectrometer (SIMS)

The secondary ion mass spectrometer is a surface sensitive technique to analyze the elemental, isotopic or molecular composition. Primary ions (e.g. Ar^+) accelerated from an ion gun and subsequently focused on the sample surface ejecting the secondary ions. These secondary ions are collected by a mass spectrometer. The ratio between mass and charge is used to identify the specific elements. The secondary ion mass spectrometry measurements presented in this work have been performed at the Luxembourg Institute for Science and Technology using a CAMECA SC Ultra instrument.

Thermogravimetric analysis and mass spectrometry (TG, MS)

Thermogravimetry is a powerful tool to characterize the temperature dependent behavior of materials. In principal every TG setup consists of a highly sensitive balance inside of a furnace. The samples are placed in an inert sample holder (usually aluminum oxide) on the balance and the TG system is heated with a programmed temperature profile. Depending on the sample a specific weight loss as a function of the temperature can be monitored.

In combination with a mass spectrometer, extensive information about the leaving chemical species can be generated. In the used setup the MS is positioned directly on top of the TG system at the gas outlet. Therefore the measurement signals of both machines arrive simultaneously which is important for the data analysis. In the MS, the incoming molecules are ionized by bombarding them with electrons. Due to this harsh treatment a fragmentation of the molecules is possible. The resulting ions are eventually separated according to their mass to charge ratio (m/e). A detector measures the ion current of the specific ions which can be translated into molecules by comparing the results with literature spectra.

The setup used in this thesis was a STA-MS-Skimmer-Kopplungssystem STA 409CD-QMS422 (Netzsch Gerätebau GmbH). In this thesis linear heating ramps have been applied and the measurements have been carried out under the inert atmosphere of pure nitrogen or argon.

X-ray diffraction (XRD)

X-ray diffraction is a method to analyze the composition of crystalline materials. The samples are placed within an X-ray beam having a wavelength in the range of the crystal lattice distances. The X-rays are scattered elastically on the crystal planes and the diffracted beam shows interference effects. Constructive interference can be achieved under the following conditions:

$$2d_{hkl}sin\theta_B = n_i\lambda$$

This equation is called the Bragg equation with the interplanar spacing d_{hkl} where hkl are the Miller indices. θ_B is the Bragg angle between the incoming beam and the sample and λ the wavelength of the X-rays. Usually the measurement of the scattered X-rays is done by a detector positioned at the focal point of the incident and diffracted beams. Therefore this setup is also called θ -2θ or Bragg Brentano geometry and the resulting patterns are shown in 2θ angles. The used diffractometer is a Bruker D8Advance DaVinci-Cu with a Cu-Kα X-ray source and an analyzed surface area of about 6 x 20 mm.

Grazing incidence XRD

Grazing incidence XRD describes a special geometry for XRD measurements where only the detector position is changed. Contrary to the θ -2θ setup, very small incidence angles (typically below 3°) are used. Thus, the information depth is decreased proportional to the angle allowing a highly improved background (e.g. substrate) to film ratio predestining this method for thin film technologies. By changing the incidence angle, vertical gradients in the crystalline phases can be distinguished.

The GIXRD measurements have been carried out at Bosch solar CIS tech in Brandenburg an der Havel using Cu-Kα radiation.

In-situ-XRD

In-situ XRD is an extended version of a θ -2θ XRD setup where a fast detector and a furnace allow the investigation of the crystallographic phase formations during the heating as a function of the substrate temperature. A schematic illustration of the used i-XRD oven is shown in Figure 82.

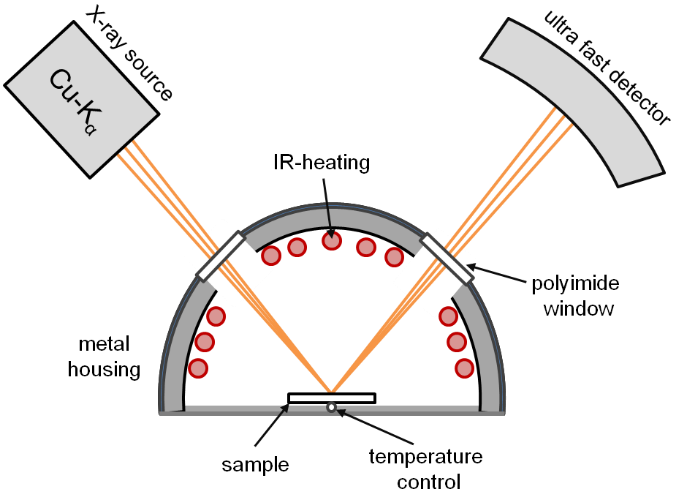

Figure 82: Schematic representation of the i-XRD setup.

In the used setup X-rays are emitted from a Cu-Kα source and focused on the sample surface inside of a gas tight oven chamber. The diffracted waves are analyzed by a fast detector attached on the opposite side of the XRD furnace. The heating is achieved by infrared illumination.

Single crystal X-ray diffraction

Single crystal XRD is technique to identify and visualize complex crystalline materials consisting of atoms or molecules. For this method the sample has to show a high degree of homogeneity (preferably the materials are single crystalline) in order to get information about the crystal system, space group, atom locations as well as bond types/locations/angles. The crystal is positioned on a fine tip where it is in the focus of a strong X-ray beam. The measured interference pattern taken at different orientations reveal a two dimensional image showing an electron density map. With additional information about the prevailing elements, this image can be translated into a three dimensional atomic/molecular model by Fourier transformation. The single crystal XRD measurements presented in this thesis have been carried out at the University of Tübingen with a Bruker APEX DUO using a Mo Kα X-ray source with a wavelength of 0.71Å.

E. Material properties of tetramethylguanidine

In Table 10 the physical properties of the main solvent tetramethylguanidine are summarized.

Table 10: Physical properties of 1,1,2,2-tetramethylguanidine.

	Value	Reference
Enthalpy of formation (l)	7.7 ± 2.8 kJ	[90]
Enthalpy of formation (g)	58.4 ± 4.0 kJ/mol (meas.)	[90]
	57.7 ± 4.0 kJ/mol (calc.)	[90]
Enthalpy of vaporization	46.89 kJ/mol	[91]
	50.0 ± 1.2 kJ/mol	[90]
Vapor pressure (25°C)	26 Pa	[92]
	131 Pa	calculated
	~260 Pa	[91]
Vapor pressure (65°C)	260 Pa	[92]
	1907 Pa	calculated
Freezing point	-78°C	[91]
Boiling point	159.5°C	[91]
	160-162°C	[92]
Viscosity (25°C)	1.4 mPas	[91]
	2.0 mPas	[92]
Viscosity (-25°C)	5.5 mPas	measured
Density (25°C)	0.9136 g/cm³	[91]
	0.91249 g/cm³	[90]

Bibliography

[1] C. E. Fritts, “On a New Form of Selenium Photocell,” *Am. J. Sci.*, vol. 26, p. 465, 1883.

[2] D. Chapin, C. S. Fuller, and G. Pearson, “Solar battery,” *J. Franklin Inst.*, vol. 258, no. 1, pp. 78–79, Jul. 1954.

[3] F. J. Morin and J. P. Maita, “Electrical Properties of Silicon Containing Arsenic and Boron,” *Phys. Rev.*, vol. 96, no. 1, pp. 28–35, Oct. 1954.

[4] J. Czochralski, “Ein neues Verfahren zur Messung der Kristallisationsgeschwindigkeit von Metallen,” *Zeitschrift für Phys. Chemie*, vol. 92, pp. 219–221, 1918.

[5] H. Hahn, G. Frank, W. Klinger, A.-D. Meyer, and G. Störger, “Über einige ternäre Chalkogenide mit Chalcopyritestruktur,” *Zeitschrift für Anorg. Chemie*, vol. 271, no. 153, p. 170, 1953.

[6] S. Wagner, J. L. Shay, P. Migliorato, and H. M. Kasper, “CuInSe2/CdS heterojunction photovoltaic detectors,” *Appl. Phys. Lett.*, vol. 25, no. 8, 1974.

[7] R. A. Mickelsen and W. S. Chen, “High photocurrent polycrystalline thin- film CdS/CuInSe2 solar cells,” *Appl. Phys. Lett.*, vol. 36, no. 5, 1980.

[8] ZSW, “New best mark in thin-film solar performance with 21.7 percent efficiency,” 2014. [Online]. Available: http://www.zsw-bw.de/en/support/press-releases/press-detail/zsw-brings-world-record-back-to-stuttgart.html. [Accessed: 29-Sep-2014].

[9] B. Panda, “Structural an electronic properties of chalcopyrite semiconductors,” National Institute Of Technology, 2012.

[10] S. Chichibu, T. Mizutani, K. Murakami, T. Shioda, T. Kurafuji, H. Nakanishi, S. Niki, P. J. Fons, and A. Yamada, “Band gap energies of bulk, thin-film, and epitaxial layers of CuInSe2 and CuGaSe2,” *J. Appl. Phys.*, vol. 83, no. 7, 1998.

[11] “Copper gallium sulfide (CuGaS2) band structure, energy gaps,” in *Ternary Compounds, Organic Semiconductors SE - 74*, vol. 41E, 2000, pp. 1–14.

[12] J. H. Werner, R. Brendel, and H. Queisser, “Radiative efficiency limit of terrestrial solar cells with internal carrier multiplication,” *Appl. Phys. Lett.*, vol. 67, no. 7, 1995.

[13] W. Shockley and H. J. Queisser, “Detailed Balance Limit of Efficiency of p- n Junction Solar Cells,” *J. Appl. Phys.*, vol. 32, no. 3, 1961.

[14] R. Scheer and H.-W. Schock, *Chalcogenide Photovoltaics*. 2011.

[15] W. Shockley, “The Theory of p-n Junctions in Semiconductors and p-n Junction Transistors,” *Bell Syst. Tech. J.*, vol. 28, no. 3, pp. 435–489, Jul. 1949.

[16] G. H. Shih, S. Maximenko, J. Frantz, J. Myers, R. Bekele, J. Mittereder, J. S. Sanghera, V. Q. Nguyen, D. Scheiman, R. Hoheisel, and R. Walters, “Optimization of electrical

performance of Cu(In,Ga)Se2 thin film solar cells sputtered from quaternary targets," *Photovoltaic Specialist Conference (PVSC), 2014 IEEE 40th*. pp. 1704–1706, 2014.

[17] H. K. Song, J. K. Jeong, H. J. Kim, S. K. Kim, and K. H. Yoon, "Fabrication of CuIn1-xGaxSe2 thin film solar cells by sputtering and selenization process," *Thin Solid Films*, vol. 435, no. 1–2, pp. 186–192, 2003.

[18] C.-Y. Su, W.-H. Ho, H.-C. Lin, C.-Y. Nieh, and S.-C. Liang, "The effects of the morphology on the CIGS thin films prepared by CuInGa single precursor," *Sol. Energy Mater. Sol. Cells*, vol. 95, no. 1, pp. 261–263, 2011.

[19] A. M. Gabor, J. R. Tuttle, D. S. Albin, M. A. Contreras, R. Noufi, and A. M. Hermann, "High- efficiency CuInxGa1−xSe2 solar cells made from (Inx,Ga1−x)2Se3 precursor films," *Appl. Phys. Lett.*, vol. 65, no. 2, 1994.

[20] "Solar Frontier Sets Thin-Film PV World Record with 20.9% CIS Cell." [Online]. Available: http://www.solar-frontier.com/eng/news/2014/C031367.html. [Accessed: 20-Dec-2014].

[21] T. Todorov and D. B. Mitzi, "Direct Liquid Coating of Chalcopyrite Light-Absorbing Layers for Photovoltaic Devices," *Eur. J. Inorg. Chem.*, vol. 2010, no. 1, pp. 17–28, 2010.

[22] C. E. U, C. Fredric, K. Pauls, and J. Serra, "Thin-film CIS alloy PV materials fabricated using non-vacuum , particles-based techniques," *Thin Solid Films*, vol. 387, no. 1–2, pp. 18–22, 2001.

[23] C. J. Stolle, T. B. Harvey, and B. a Korgel, "Nanocrystal photovoltaics: a review of recent progress," *Curr. Opin. Chem. Eng.*, vol. 2, no. 2, pp. 160–167, May 2013.

[24] C. J. Hibberd, E. Chassaing, W. Liu, D. B. Mitzi, D. Lincot, and A. N. Tiwari, "Non-vacuum methods for formation of Cu(In,Ga)(Se,S)2 thin film photovoltaic absorbers," *Prog. Photovoltaics Res. Appl.*, vol. 18, no. 6, pp. 434–452, 2010.

[25] V. a. Akhavan, B. W. Goodfellow, M. G. Panthani, C. Steinhagen, T. B. Harvey, C. J. Stolle, and B. a. Korgel, "Colloidal CIGS and CZTS nanocrystals: A precursor route to printed photovoltaics," *J. Solid State Chem.*, vol. 189, pp. 2–12, May 2012.

[26] Q. Guo, G. M. Ford, H. W. Hillhouse, and R. Agrawal, "A generalized and robust method for efficient thin film photovoltaic devices from multinary sulfide nanocrystal inks," *2011 37th IEEE Photovolt. Spec. Conf.*, pp. 003522–003526, Jun. 2011.

[27] S. Ahn, K. Kim, and K. Yoon, "Cu(In,Ga)Se2 thin film solar cells from nanoparticle precursors," *Curr. Appl. Phys.*, vol. 8, no. 6, pp. 766–769, Oct. 2008.

[28] G. Chen, L. Wang, X. Sheng, H. Liu, X. Pi, and D. Yang, "Chemical synthesis of Cu(In) metal inks to prepare CuInS2 thin films and solar cells," *J. Alloys Compd.*, vol. 507, no. 1, pp. 317–321, Sep. 2010.

[29] D. L. Schulz, C. J. Curtis, R. A. Flitton, H. Wiesner, J. Keane, R. J. Matson, M. Kim, P. A. Parilla, R. Noufi, and D. S. Ginley, "Cu-In-Ga-Se Nanoparticle Colloids as Spray Deposition Precursors for Cu(In,Ga)Se2 Solar Cell Materials," *J. Electron. Mater.*, vol. 27, no. 5, pp. 433–437, 1998.

[30] C. Kind, C. Feldmann, A. Quintilla, and E. Ahlswede, "Citrate-Capped Cu 11 In 9 Nanoparticles and Its Use for Thin-Film Manufacturing of CIS Solar Cells," *Chem. Mater.*, vol. 23, no. 23, pp. 5269–5274, 2011.

[31] H. Liu, Z. Jin, W. Wang, Y. Wang, and H. Du, “Well-dispersed, size-tunable chalcopyrite CuInSe2 nanocrystals and its ink-coated thin films by polyhydric solution chemical process,” *Mater. Lett.*, vol. 81, pp. 173–176, Aug. 2012.

[32] H. Liu, Z. Jin, J. Wang, J. Ao, and G. Li, “Well-dispersed CuInSe2 nanoplates and nanoplates-ink-coated thin films for photovoltaic application by a triethylene glycol based solution process,” *Mater. Lett.*, vol. 94, pp. 1–4, Mar. 2013.

[33] S. H. Mousavi, T. S. Müller, and P. W. de Oliveira, “Synthesis of colloidal nanoscaled copper-indium-gallium-selenide (CIGS) particles for photovoltaic applications.,” *J. Colloid Interface Sci.*, vol. 382, no. 1, pp. 48–52, Sep. 2012.

[34] V. R. Reddy, J. Wu, and M. O. Manasreh, “Colloidal Cu(InxGa1−x)Se2 nanocrystals for all-inorganic nano-heterojunction solar cells,” *Mater. Lett.*, vol. 92, pp. 296–299, Feb. 2013.

[35] G. Norsworthy, C. R. Leidholm, a. Halani, V. K. Kapur, R. Roe, B. M. Basol, and R. Matson, “CIS film growth by metallic ink coating and selenization,” *Sol. Energy Mater. Sol. Cells*, vol. 60, no. 2, pp. 127–134, 2000.

[36] B. Vidhya, S. Velumani, and R. Asomoza, “Effect of milling time and heat treatment on the composition of CuIn0.75Ga0.25Se2 nanoparticle precursors and films,” *J. Nanoparticle Res.*, vol. 13, no. 7, pp. 3033–3042, Mar. 2011.

[37] S. Mehdaoui, N. Benslim, M. Benabdeslem, O. Aissaoui, L. Bechiri, and X. Portier, “Investigation of Copper-Chalcopyrite Thin Films from Nanoparticle Powder,” *Energy Procedia*, vol. 10, pp. 94–100, 2011.

[38] V. K. Kapur, A. Bansal, P. Le, and O. I. Asensio, “Non-vacuum processing of Cu(In 1-y,Ga x)Se2 solar cells on rigid and flexible substrates using nanoparticle precursor inks,” *Thin Solid Films*, vol. 432, no. 03, pp. 53–57, 2003.

[39] Y.-M. Choi, Y.-I. Lee, B.-S. Kim, and Y.-H. Choa, “Oxide nanoparticle-based fabrication and optical properties of Cu(In1−xGax)S2 absorber layer for solar cells,” *Thin Solid Films*, vol. 546, pp. 312–316, Nov. 2013.

[40] M. Kaelin, H. Zogg, A. N. Tiwari, O. Wilhelm, S. E. Pratsinis, T. Meyer, and A. Meyer, “Electrosprayed and selenized Cu/In metal particle films,” *Thin Solid Films*, vol. 457, no. 2, pp. 391–396, 2004.

[41] A. N. Goldstein, C. M. Echer, and A. P. Alivisatos, “Melting in semiconductor nanocrystals.,” *Science*, vol. 256, no. 5062, pp. 1425–7, Jun. 1992.

[42] Q. Guo, G. M. Ford, H. W. Hillhouse, and R. Agrawal, “Sulfide Nanocrystal Inks for Dense Cu (In1-x,Ga x)(S1-ySe y)2 Absorber Films and Their Photovoltaic Performance,” *Nano Lett.*, vol. 9, no. 8, pp. 17–22, 2009.

[43] M. Casteleyn, M. Burgelman, B. Depuydt, A. Niemegeers, and I. Clemminck, “Growth studies of $CuInSe_2$ using Cu-Se fluxes,” *Photovoltaic Energy Conversion, 1994., Conference Record of the Twenty Fourth. IEEE Photovoltaic Specialists Conference - 1994, 1994 IEEE First World Conference on*, vol. 1. pp. 230–233 vol.1, 1994.

[44] M. Kaelin, D. Rudmann, F. Kurdesau, T. Meyer, H. Zogg, and a. N. Tiwari, “CIS and CIGS layers from selenized nanoparticle precursors,” *Thin Solid Films*, vol. 431–432, pp. 58–62, May 2003.

[45] B. M. Basol, V. K. Kapur, G. Norsworthy, A. Halani, C. R. Leidholm, and R. Roe, “Efficient CuInSe2 Solar Cells Fabricated by a Novel Ink Coating Approach,” *Electrochem. Solid-State Lett.* , vol. 1 , no. 6 , pp. 252–254, Dec. 1998.

[46] B. M. Başol, “Low cost techniques for the preparation of Cu(In,Ga)(Se,S)2 absorber layers,” *Thin Solid Films*, vol. 362, pp. 514–519, 2000.

[47] T. Arita, N. Suyama, Y. Kita, S. Kitamura, T. Hibino, H. Takada, K. Omura, N. Ueno, and M. Murozono, “CuInSe$_2$ films prepared by screen-printing and sintering method,” *Photovoltaic Specialists Conference, 1988., Conference Record of the Twentieth IEEE.* pp. 1650–1655 vol.2, 1988.

[48] A. R. Uhl, M. Koller, A. S. Wallerand, C. M. Fella, L. Kranz, H. Hagendorfer, Y. E. Romanyuk, A. N. Tiwari, S. Yoon, A. Weidenkaff, T. M. Friedlmeier, E. Ahlswede, D. Vangenechten, and F. Stassin, “Cu (In , Ga) Se 2 absorbers from stacked nanoparticle precursor layers,” *Thin Solid Films*, vol. 535, pp. 138–142, 2013.

[49] J. J. Scragg, P. J. Dale, D. Colombara, and L. M. Peter, “Thermodynamic Aspects of the Synthesis of Thin-Film Materials for Solar Cells,” *ChemPhysChem*, vol. 13, no. 12, pp. 3035–3046, 2012.

[50] S. Ahn, C. Kim, J. Yun, J. Lee, and K. Yoon, “Effects of heat treatments on the properties of Cu(In,Ga)Se2 nanoparticles,” *Sol. Energy Mater. Sol. Cells*, vol. 91, no. 19, pp. 1836–1841, 2007.

[51] E. Ahmed, A. Zegadi, A. E. Hill, R. D. Pilkington, R. D. Tomlinson, A. A. Dost, W. Ahmed, S. Leppävuori, J. Levoska, and O. Kusmartseva, “The influence of annealing processes on the structural, compositional and electro-optical properties of CuIn0.75Ga0.25Se2 thin films,” *J. Mater. Sci. Mater. Electron.*, vol. 7, no. 3, pp. 213–219, 1996.

[52] M. Kaelin, D. Rudmann, and a. N. Tiwari, “Low cost processing of CIGS thin film solar cells,” *Sol. Energy*, vol. 77, no. 6, pp. 749–756, Dec. 2004.

[53] S. J. Park, J. W. Cho, J. K. Lee, K. Shin, J. Kim, and B. K. Min, “Solution processed high band-gap CuInGaS 2 thin film for solar cell applications,” *Prog. Photovoltaics Res. Appl.*, vol. 22, no. 1, pp. 122–128, 2013.

[54] A. R. Uhl, Y. E. Romanyuk, and A. N. Tiwari, “Thin film Cu (In , Ga) Se 2 solar cells processed from solution pastes with polymethyl methacrylate binder,” *Thin Solid Films*, vol. 519, no. 21, pp. 7259–7263, 2011.

[55] D. Lee, Y. Choi, and K. Yong, “Morphology and crystal phase evolution of doctor-blade coated CuInSe2 thin films,” *J. Cryst. Growth*, vol. 312, no. 24, pp. 3665–3669, Dec. 2010.

[56] E. Lee, S. J. Park, J. W. Cho, J. Gwak, M.-K. Oh, and B. K. Min, “Nearly carbon-free printable CIGS thin films for solar cell applications,” *Sol. Energy Mater. Sol. Cells*, vol. 95, no. 10, pp. 2928–2932, Oct. 2011.

[57] W. Wang, Y.-W. Su, and C. Chang, “Inkjet printed chalcopyrite CuInxGa1−xSe2 thin film solar cells,” *Sol. Energy Mater. Sol. Cells*, vol. 95, no. 9, pp. 2616–2620, Sep. 2011.

[58] W. Wang, S.-Y. Han, S.-J. Sung, D.-H. Kim, and C.-H. Chang, “8.01% CuInGaSe2 solar cells fabricated by air-stable low-cost inks.,” *Phys. Chem. Chem. Phys.*, vol. 14, no. 31, pp. 11154–9, Aug. 2012.

[59] M. Park, S. Ahn, J. H. Yun, J. Gwak, A. Cho, S. Ahn, K. Shin, D. Nam, H. Cheong, and K. Yoon, “Characteristics of Cu(In,Ga)Se2 (CIGS) thin films deposited by a direct solution coating process,” *J. Alloys Compd.*, vol. 513, pp. 68–74, Feb. 2012.

[60] T. Tanaka, T. Yamaguchi, T. Ohshima, H. Itoh, a Wakahara, and a Yoshida, “Effect of Cl ion implantation on electrical properties of CuInSe thin films,” *Sol. Energy Mater. Sol. Cells*, vol. 75, no. 1–2, pp. 109–113, Jan. 2003.

[61] G. Wang, S. Wang, Y. Cui, and D. Pan, “A novel and versatile strategy to prepare metal-organic molecular precursor solutions and its application in Cu(In,Ga)(S,Se) 2 solar cells,” *Chem. Mater.*, vol. 24, no. 20, pp. 3993–3997, 2012.

[62] W. Zhao, Y. Cui, and D. Pan, “Air-Stable, Low-Toxicity Precursors for CuIn(SeS) 2 Solar Cells with 10.1 % Efficiency,” *Energy Technol.*, vol. 1, no. 2–3, pp. 131–134, Mar. 2013.

[63] T. K. Todorov, O. Gunawan, T. Gokmen, and D. B. Mitzi, “Solution-processed Cu(In,Ga)(S,Se)2 absorber yielding a 15.2% efficient solar cell,” *Prog. Photovoltaics Res. Appl.*, vol. 21, no. 1, pp. 82–87, 2013.

[64] W. Liu, D. B. Mitzi, M. Yuan, A. J. Kellock, S. J. Chey, and O. Gunawan, “12% Efficiency CuIn(Se,S) 2 Photovoltaic Device Prepared Using a Hydrazine Solution Process †,” *Chem. Mater.*, vol. 22, no. 3, pp. 1010–1014, Feb. 2010.

[65] F. C. Krebs, “Fabrication and processing of polymer solar cells: A review of printing and coating techniques,” *Sol. Energy Mater. Sol. Cells*, vol. 93, no. 4, pp. 394–412, Apr. 2009.

[66] S. Abermann, “Non-vacuum processed next generation thin film photovoltaics: Towards marketable efficiency and production of CZTS based solar cells,” *Sol. Energy*, vol. 94, pp. 37–70, Aug. 2013.

[67] I.-K. Ding, “Pore Filling and Light Trapping in Solid-state Dye-sensitized Solar Cells,” Stanford University, 2011.

[68] K. Norrman, A. Ghanbari-Siahkali, and N. B. Larsen, “Studies of spin-coated polymer films,” *Annu. Reports Sect. “C” (Physical Chem.*, vol. 101, no. 0, pp. 174–201, 2005.

[69] J. Linden, C. Thanner, B. Schaaf, S. Wolff, B. Lägel, and E. Oesterschulze, “Spray coating of PMMA for pattern transfer via electron beam lithography on surfaces with high topography,” *Microelectron. Eng.*, vol. 88, no. 8, p. 2030, 2011.

[70] N. P. P. and J. N. B. and P. M. Sarro, “Spray coating of photoresist for pattern transfer on high topography surfaces,” *J. Micromechanics Microengineering*, vol. 15, no. 4, p. 691, 2005.

[71] L. Wengeler, M. Schmitt, K. Peters, P. Scharfer, and W. Schabel, “Comparison of large scale coating techniques for organic and hybrid films in polymer based solar cells,” *Chem. Eng. Process. Process Intensif.*, vol. 68, no. 0, pp. 38–44, Jun. 2013.

[72] S. Shirakata, T. Terasako, and T. Kariya, “Properties of CuIn(SxSe1−x)2 polycrystalline thin films prepared by chemical spray pyrolysis,” *J. Phys. Chem. Solids*, vol. 66, no. 11, pp. 1970–1973, Nov. 2005.

[73] U. Berner and M. Widenmeyer, “Solution-based processing of Cu(In,Ga)Se2 absorber layers for 11 % efficiency solar cells via a metallic intermediate,” *Prog. Photovoltaics Res. Appl.*, vol. 23, no. 10, pp. 1260–1266, 2015.

[74] U. Berner, M. Widenmeyer, P. Engler, and P. J. Dale, “4-Amino-1,2,4-triazole: Playing a key role in the chemical deposition of Cu–In–Ga metal layers for photovoltaic applications,” *Thin Solid Films*, vol. 582, pp. 39–42, May 2015.

[75] U. Berner, D. Colombara, J. De Wild, E. V. C. Robert, M. Schütze, F. Hergert, N. Valle, M. Widenmeyer, and P. J. Dale, “13.3% efficient solution deposited Cu(In,Ga)Se2 solar cells processed with different sodium salt sources,” *Prog. Photovoltaics Res. Appl.*, vol. DOI: 10.10, 2015.

[76] T. K. Todorov, O. Gunawan, T. Gokmen, and D. B. Mitzi, “Solution-processed Cu(In,Ga)(S,Se)2 absorber yielding a 15.2% efficient solar cell,” *Prog. Photovoltaics Res. Appl.*, vol. 21, no. 1, pp. 82–87, 2013.

[77] F. Pianezzi, S. Nishiwaki, L. Kranz, C. M. Sutter-Fella, P. Reinhard, B. Bissig, H. Hagendorfer, S. Buecheler, and A. N. Tiwari, “Influence of Ni and Cr impurities on the electronic properties of Cu(In,Ga)Se2 thin film solar cells,” *Prog. Photovoltaics Res. Appl.*, vol. 23, no. 7, pp. 892–900, Apr. 2015.

[78] V. Rosenband and a. Gany, “Preparation of nickel and copper submicrometer particles by pyrolysis of their formates,” *J. Mater. Process. Technol.*, vol. 153–154, pp. 1058–1061, Nov. 2004.

[79] K. H. Stern, “High Temperature Properties and Decomposition of Inorganic Salts: Part 3. Nitrates and Nitrites,” *J. Phys. Chem. Ref. Data*, vol. 1, no. 3, pp. 747–772, 1972.

[80] A. K. Galwey, D. Jamieson, and M. E. Brown, “Thermal decomposition of three crystalline modifications of anhydrous copper(II) formate,” *J. Phys. Chem.*, vol. 78, no. 26, pp. 2664–2670, Dec. 1974.

[81] Y.-Q. Tian, Y.-M. Zhao, H.-J. Xu, and C.-Y. Chi, “CO2 Template Synthesis of Metal Formates with a ReO3 Net,” *Inorg. Chem.*, vol. 46, no. 5, pp. 1612–1616, Jan. 2007.

[82] D. Forney, M. E. Jacox, and W. E. Thompson, “Infrared spectra of trans-HOCO, HCOOH+, and HCO2− trapped in solid neon,” *J. Chem. Phys.*, vol. 119, no. 20, 2003.

[83] K. Ito and J. Bernstein, “The vibrational spectra of the formate, acetate, and oxalate ions,” *Can. J. Chem.*, vol. 34, pp. 170–178, 1956.

[84] N. Narsimlu and G. S. Sastry, “Optical properties of anhydrous copper(II) formate single crystal,” *Solid State Commun.*, vol. 100, no. 10, pp. 687–689, 1996.

[85] NIST Chemistry WebBook, “NIST Standard Reference Database 69.” .

[86] S. Lopes, A. V Domanskaya, R. Fausto, and M. Räsänen, “Formic and acetic acids in a nitrogen matrix : Enhanced stability of the higher-energy conformer,” *J. Chem. Phys.*, vol. 133, pp. 1–8, 2010.

[87] A. J. M. Miller, D. M. Heinekey, J. M. Mayer, and K. I. Goldberg, “Catalytic Disproportionation of Formic Acid to Generate Methanol,” *Angew. Chemie Int. Ed.*, vol. 52, no. 14, pp. 3981–3984, 2013.

[88] S. Savourey, G. Lefèvre, J.-C. Berthet, P. Thuéry, C. Genre, and T. Cantat, “Efficient Disproportionation of Formic Acid to Methanol Using Molecular Ruthenium Catalysts,” *Angew. Chemie Int. Ed.*, vol. 53, no. 39, pp. 10466–10470, 2014.

[89] P. J. Bailey and S. Pace, "The coordination chemistry of guanidines and guanidinates," *Coord. Chem. Rev.*, vol. 214, no. 1, pp. 91–141, Apr. 2001.

[90] J. Vitorino, F. Agapito, M. F. M. Piedade, C. E. S. Bernardes, H. P. Diogo, J. P. Leal, and M. E. Minas da Piedade, "Thermochemistry of 1,1,3,3-tetramethylguanidine and 1,1,3,3-tetramethylguanidinium nitrate," *J. Chem. Thermodyn.*, pp. 1–11, Jan. 2014.

[91] M. L. Anderson and R. N. Hammer, "Properties of 1,1,3,3=Tetramethylguanidine as a Nonaqueous Solvent," *J. Chem. Eng. Data*, vol. 12, no. 3, pp. 442–447, 1967.

[92] A. Organics, "Safety data sheet," no. 3, pp. 1–8, 2012.

[93] P. M. Schweizer and S. F. Kistler, *Liquid Film Coating*. 1997, p. 783.

[94] F. Davard and D. Dupuis, "Flow visualisation experiments in a blade coating process," *J. Nonnewton. Fluid Mech.*, vol. 93, no. 1, pp. 17–28, Sep. 2000.

[95] R. E. Khayat and N. Ashrafi, "A boundary-element analysis for transient viscoelastic blade coating flow," *Eng. Anal. Bound. Elem.*, vol. 24, no. 5, pp. 363–375, May 2000.

[96] F. R. Pranckh and L. E. Scriven, "Elastohydrodynamics of blade coating," *AIChE J.*, vol. 36, no. 4, pp. 587–597, 1990.

[97] P. M. Schweizer and S. F. Kistler, *Liquid Film Coating*. Springer, 1997, p. 783.

[98] C. K. Aidun, "An Overview of Blade Coating Systems," 1993.

[99] O. Lundberg, M. Bodegård, J. Malmström, and L. Stolt, "Influence of the Cu(In,Ga)Se2 thickness and Ga grading on solar cell performance," *Prog. Photovoltaics Res. Appl.*, vol. 11, no. 2, pp. 77–88, 2003.

[100] E. B. Gutoff and E. D. Cohen, *Coating and Drying Defects: Troubleshooting Operating Problems*. 2006, p. 400.

[101] R. R. E. Ley, "Role of Surface Tension Gradients in Correcting Coating Defects in Corners," *J. Colloid Interface Sci.*, vol. 75, no. 179, pp. 66–75, 1996.

[102] R. B. Husar and E. M. Sparrow, "Patterns of free convection flow adjacent to horizontal heated surfaces," *Int. J. Heat Mass Transf.*, vol. 11, no. 7, pp. 1206–1208, Jul. 1968.

[103] T. Okuzono, M. Kobayashi, and M. Doi, "Final shape of a drying thin film," *Phys. Rev. E*, vol. 80, no. 2, p. 21603, Aug. 2009.

[104] I. D. Borcia, R. Borcia, and M. Bestehorn, "Long wave instabilities in binary mixture thin liquid films," *J. Optoelectron. Adv. Mater.*, vol. 8, no. 3, pp. 1033–1036, 2006.

[105] H. Kagami, "Impact of the Marangoni effect on thin film thickness profile after drying of polymer solution coated on a flat substrate," in *JPS Conf. Proc.*, 2014, vol. 015087, pp. 1–5.

[106] D. P. Birnie, "A Model for Drying Control Cosolvent Selection for Spin-Coating Uniformity: The Thin Film Limit," *Langmuir*, vol. 29, no. 29, pp. 9072–9078, 2013.

[107] J. Zhang, R. P. Behringer, and A. Oron, "Marangoni convection in binary mixtures," *Phys. Rev. E*, vol. 76, no. 1, p. 16306, Jul. 2007.

[108] H. D. Baehr and K. Stephan, *Heat and Mass Transfer*. 2011.

[109] E. N. Fuller, P. D. Schettler, and J. C. Giddings, “New method for prediction of binary gas-phase diffusion coefficients,” *Ind. Eng. Chem.*, vol. 58, no. 5, pp. 18–27, 1966.

[110] P. Stephan, *VDI Wärmeatlas*. 2006, p. 1760.

[111] J. Krenn, S. Baesch, B. Schmidt-Hansberg, M. Baunach, P. Scharfer, and W. Schabel, “Numerical investigation of the local mass transfer on flat plates in laminar flow,” *Chem. Eng. Process. Process Intensif.*, vol. 50, no. 5–6, pp. 503–508, May 2011.

[112] B. Schmidt-Hansberg, M. Baunach, J. Krenn, S. Walheim, U. Lemmer, P. Scharfer, and W. Schabel, “Spatially resolved drying kinetics of multi-component solution cast films for organic electronics,” *Chem. Eng. Process. Process Intensif.*, vol. 50, no. 5–6, pp. 509–515, May 2011.

[113] G. O. Mallory and J. B. Hajdu, *Electroless Plating: Fundamentals and Applications*. 1990, p. 541.

[114] P. W. Atkins, D. F. Overton, J. P. Rourke, M. T. Weller, and F. A. Armstrong, *Inorganic Chemistry*. 2010, p. 813.

[115] U. Ruschic, U. Muller, P. Willnow, and T. Hopner, “CO2 Reduction to Formate by NADH Catalysed by Formate Dehydrogenase from Pseudomonas oxalaticus,” *Eur. J. Biochem.*, vol. 70, no. 2, pp. 325–330, 1976.

[116] N. M. Khokhlacheva, V. N. Paderno, M. E. Shilovskaya, and M. A. Tolstaya, “Properties of fine metal powders produced by the formate pyrolysis method,” *Sov. Powder Metall. Met. Ceram.*, vol. 19, no. 3, pp. 145–149, 1980.

[117] A. K. Galwey and M. E. Brown, “Thermal decomposition of metal salts of organic acids,” in *Thermal decomposition of ionic solids*, Elsevier, 1999, pp. 441–492.

[118] M. A. Mohamed, A. K. Galwey, and S. A. Halawy, “Kinetic and thermodynamic studies of the nonisothermal decomposition of anhydrous copper(II) formate in different gas atmospheres,” *Thermochim. Acta*, vol. 411, pp. 13–20, 2004.

[119] T. Ogura and Q. Fernando, “Mass spectrometry and structures of copper(I) carboxylates in the vapor phase,” *Inorg. Chem.*, vol. 12, no. 11, pp. 2611–2615, Nov. 1973.

[120] D. A. Edwards and R. Richards, “Copper(I) carboxylates: preparations and infrared and mass spectral features,” *J. Chem. Soc. Dalt. Trans.*, no. 22, pp. 2463–2468, 1973.

[121] M. A. Mohamed and A. K. Galwey, “A kinetic and mechanistic study of the thermal decomposition of copper(II) oxalate,” *Thermochim. Acta*, vol. 217, no. 0, pp. 263–276, Apr. 1993.

[122] N. J. Carr, A. K. Galwey, and M. A. Mohamed, “A mechanistic investigation of the reaction between copper(II) malonate and copper(II) bromide,” *Thermochim. Acta*, vol. 102, no. 0, pp. 323–334, Jun. 1986.

[123] Z. Bahari, E. Dichi, B. Legendre, and J. Dugué, “The equilibrium phase diagram of the copper–indium system: a new investigation,” *Thermochim. Acta*, vol. 401, no. 2, pp. 131–138, 2003.

[124] W. Keppner, T. Klas, W. Körner, R. Wesche, and G. Schatz, “Compound Formation at Cu-In Thin-Film Interfaces Detected by Perturbed y-y Angular Correlations,” *Phys. Rev. Lett.*, vol. 54, no. 21, pp. 2371–2374, May 1985.

[125] W. K. Kim, E. A. Payzant, S. S. Li, O. D. Crisalle, and T. J. Anderson, “In-situ observation of selenization of Cu-Ga-In metallic precursors,” in *Conference Record of the 2006 IEEE 4th World Conference on Photovoltaic Energy Conversion*, 2006, pp. 453–456.

[126] P. Berwian, “Experimentelle Untersuchung und Modellierung Halbleiter-Dünnschichten für die Solarzellenherstellung,” 2005.

[127] J.-B. Li, L. N. Ji, J. K. Liang, Y. Zhang, J. Luo, C. R. Li, and G. H. Rao, “A thermodynamic assessment of the copper–gallium system,” *Calphad*, vol. 32, no. 2, pp. 447–453, Jun. 2008.

[128] M. Purwins, M. Schmid, P. Berwian, G. Müller, S. Jost, F. Hergert, and R. Hock, “Phase separation in Cu(In,Ga)Se2 absorbers - kinetics of the selenization of gallium containing metal alloys,” *Proc. 21st EU-PVSEC*, pp. 2002–2005, 2006.

[129] N. Orbey, R. Birkmire, T. W. F. Russell, and G. Jones, “Copper-Indium Alloy Transformations,” *J. Phase Equilibria*, vol. 21, no. 6, pp. 509–513, 2000.

[130] J. Rickerby and J. H. G. Steinke, “Current Trends in Patterning with Copper,” *Chem. Rev.*, vol. 102, no. 5, pp. 1525–1550, Apr. 2002.

[131] P. Zhu, Y. Masuda, and K. Koumoto, “Seedless micropatterning of copper by electroless deposition on self-assembled monolayers,” *J. Mater. Chem.*, vol. 14, pp. 976–981, 2004.

[132] M. Salavati-Niasari, F. Davar, and N. Mir, “Synthesis and characterization of metallic copper nanoparticles via thermal decomposition,” *Polyhedron*, vol. 27, no. 17, pp. 3514–3518, Nov. 2008.

[133] D. Deng, Y. Jin, Y. Cheng, T. Qi, and F. Xiao, “Copper Nanoparticles: Aqueous Phase Synthesis and Conductive Films Fabrication at Low Sintering Temperature,” *ACS Appl. Mater. Interfaces*, vol. 5, no. 9, pp. 3839–3846, Apr. 2013.

[134] Y. Lee, J.-R. Choi, K. J. Lee, N. E. Stott, and D. Kim, “Large-scale synthesis of copper nanoparticles by chemically controlled reduction for applications of inkjet-printed electronics.,” *Nanotechnology*, vol. 19, no. 41, p. 415604, Oct. 2008.

[135] C. N. R. Rao, A. Müller, and A. K. Cheetham, *Nanomaterials Chemistry: Recent Developments and New Directions*. 2007, p. 420.

[136] M. B. Mohamed, Z. L. Wang, and M. A. El-Sayed, “Temperature-Dependent Size-Controlled Nucleation and Growth of Gold Nanoclusters,” *J. Phys. Chem.*, vol. 109, pp. 10255–10259, 1999.

[137] A. Ortiz, J. C. Alonso, E. Andrade, and C. Urbiola, “Structural and Optical Characteristics of Gallium Oxide Thin Films Deposited by Ultrasonic Spray Pyrolysis,” *J. Electrochem. Soc.*, vol. 148, no. 2, p. F26, 2001.

[138] A. Paretta and A. Rubino, “Kinetics of intermetallic transformation in sputtered Cu-In alloys studied by electrical resistance measurements,” *Solid State Commun.*, vol. 96, no. 10, pp. 767–770, 1995.

[139] J. G. Haasnoot, “Mononuclear, oligonuclear and polynuclear metal coordination compounds with 1,2,4-triazole derivatives as ligands,” *Coord. Chem. Rev.*, vol. 200–202, pp. 131–185, May 2000.

[140] S. Komeda, S. Bombard, S. Perrier, and J. Reedijk, “Kinetic study of azole-bridged dinuclear platinum(II) complexes reacting with a hairpin-stabilized double-stranded oligonucleotide,” *J. Inorg. Biochem.*, vol. 96, pp. 357–366, 2003.

[141] J. Li and T. A. Litzinger, “Thermal decomposition of 4-amino-1,2,4-triazolium nitrate under infrared laser heating,” *Thermochim. Acta*, vol. 454, no. 2, pp. 116–127, Mar. 2007.

[142] L. G. Lavrenova, N. G. Yudina, V. N. Ikorskii, V. A. Varnek, I. M. Oglezneva, and S. V Larionov, “Spin-crossover and thermochromism in complexes of iron(II) iodide and thiocyanate with 4-amino-1,2,4-triazole,” *Polyhedron*, vol. 14, no. 10, pp. 1333–1337, May 1995.

[143] M. Refat and F. De, “Synthesis, characterization and thermogravimetric study of Cu(II) adducts with 3- and 4-amino-1,2,4-triazole, 2-mercaptothiazoline and 2-mercaptopyridine,” *J. Serbian Chem. Soc.*, vol. 71, no. 12, pp. 1289–1300, 2006.

[144] G. V Romanenko, Z. A. Savelieva, N. V Podberezskaya, and S. V Larionov, “Structure of the Cu(II) chloride complex with 4-amino-1,2,3-triazole Cu(C2H4N4)Cl2,” *J. Struct. Chem.*, vol. 38, no. 1, pp. 207–212, 1997.

[145] J. a. J. Jarvis, “The crystal structure of a complex of cupric chloride and 1:2:4-triazole,” *Acta Crystallogr.*, vol. 15, no. 10, pp. 964–966, Oct. 1962.

[146] R. Acevedo-cha, E. Costas, and R. Escudero, “Antiferromagnetic Coupling in the Cyclic Octanuclear Compound [Cu(II)(-3,5-dimethylpyrazolate)(-OH)] and Its Analogue [Cu(II)(-pyrazolate)(-OH)],” *J. Solid State Chem.*, vol. 32, no. 132, pp. 24–32, 1997.

[147] G. Socrates, *Infrared and Raman Characteristic Group Frequencies: Tables and Charts*. 2001, p. 249.

[148] M. Purwins, “Phasenbildung und Reaktionskinetik bei der Herstellung des Chalkopyrit-Solarzellenmaterials Cu(In,Ga)(Se,S)2,” 2010.

[149] W. N. Shafarman, R. Klenk, and B. E. McCandless, “Device and material characterization of Cu(InGa)Se2 solar cells with increasing band gap,” *J. Appl. Phys.*, vol. 79, no. 9, 1996.

[150] M. Bouroushian, *Electrochemistry of Metal Chalcogenides*. 2010, p. 357.

[151] L. Kaupmees, M. Altosaar, O. Volobujeva, T. Raadik, M. Grossberg, M. Danilson, E. Mellikov, and P. Barvinschi, “Isothermal and Two-Temperature Zone Selenization of Mo Layers,” *Adv. Mater. Sci. Eng.*, vol. 2012, 2012.

[152] L. S. Brooks, “The Vapor Pressures of Tellurium and Selenium,” *J. Am. Chem. Soc.*, vol. 74, no. 1, pp. 227–229, 1952.

[153] C. Liao, J.-F. Han, T. Jiang, H.-M. Xie, F. Jiao, and K. Zhao, “Effect of Se Vapor Concentration on CIGS Film Preparation,” *Acta Physico-Chimica Sin.*, vol. 27, no. 2, pp. 432–436, 2011.

[154] L. Stolt, J. Hedström, J. Kessler, M. Ruckh, K. Velthaus, and H. Schock, "ZnO/CdS/CuInSe2 thinfilm solar cells with improved performance," *Appl. Phys. Lett.*, vol. 62, no. 6, 1993.

[155] D. Rudmann, "Effects of sodium on growth and properties of Cu(In,Ga)Se2," ETH Zürich, 2004.

[156] V. Probst, J. Rimmasch, W. Riedl, W. Stetter, J. Holz, H. Harms, F. Karg, and H. W. Schock, "The impact of controlled sodium incorporation on rapid thermal processed Cu (InGa) Se 2-thin films and devices," in *Conference Record of the Twenty Fourth. IEEE Photovoltaic Specialists Conference-1994*, 1994, vol. 1, pp. 144–147.

[157] A. Rockett, J. S. Britt, T. Gillespie, C. Marshall, M. M. Al Jassim, and F. Hasoon, "Na in selenized Cu(In,Ga)Se2 on Na-containing and Na-free glasses: distribution, grain structure, and device performances," *Thin Solid Films*, vol. 372, no. 1–2, pp. 212–217, 2000.

[158] D. Rudmann, a. F. da Cunha, M. Kaelin, F. Kurdesau, H. Zogg, a. N. Tiwari, and G. Bilger, "Efficiency enhancement of Cu(In,Ga)Se2 solar cells due to post-deposition Na incorporation," *Appl. Phys. Lett.*, vol. 84, no. 7, p. 1129, 2004.

[159] W. N. Shafarman and J. Zhu, "Effect of substrate temperature and depostion profile on evaporated Cu(InGa)Se2 films and devices," *Thin Solid Films*, vol. 361–362, no. 0, pp. 473–477, 2000.

[160] M. Bodeg Ård, K. Granath, and L. Stolt, "Growth of Cu(In,Ga)Se2 thin films by coevaporation using alkaline precursors," *Thin Solid Films*, vol. 361–362, no. 0, pp. 9–16, Feb. 2000.

[161] M. Lammer, U. Klemm, and M. Powalla, "Sodium co-evaporation for low temperature Cu(In,Ga)Se2 deposition," *Thin Solid Films*, vol. 387, no. 1–2, pp. 33–36, 2001.

[162] D. W. Niles, M. Al-Jassim, and K. Ramanathan, "Direct observation of Na and O impurities at grain surfaces of CuInSe2 thin films," *J. Vac. Sci. Technol. A*, vol. 17, no. 1, pp. 291–296, 1999.

[163] O. Cojocaru-Miredin, P.-P. Choi, D. Abou-ras, S. S. Schmidt, R. Caballero, and D. Raabe, "Characterization of Grain Boundaries in Cu(In,Ga)Se2 Films Using Atom-Probe Tomography," *IEEE J. PHOTOVOLTAICS*, vol. 1, no. 2, pp. 207–212, 2011.

[164] P. T. Erslev, J. W. Lee, W. N. Shafarman, and J. D. Cohen, "The influence of Na on metastable defect kinetics in {CIGS} materials," *Thin Solid Films*, vol. 517, no. 7, pp. 2277–2281, 2009.

[165] T. Nakada, D. Iga, H. Ohbo, and A. Kunioka, "Effects of sodium on Cu(In, Ga)Se2-based thin films and solar cells," *Japanese J. Appl. Physics, Part 1 Regul. Pap. Short Notes Rev. Pap.*, vol. 36, no. 2, pp. 732–737, 1997.

[166] S. Ishizuka, A. Yamada, K. Matsubara, P. Fons, K. Sakurai, and S. Niki, "Alkali incorporation control in Cu(In,Ga)Se2 thin films using silicate thin layers and applications in enhancing flexible solar cell efficiency," *Appl. Phys. Lett.*, vol. 93, no. 12, p. -, 2008.

[167] M. Ruckh, D. Schmid, M. Kaiser, R. Schäffler, T. Walter, and H. W. Schock, "Influence of substrates on the electrical properties of Cu(In,Ga)Se2 thin films," *Sol. Energy Mater. Sol. Cells*, vol. 41–42, no. 0, pp. 335–343, 1996.

[168] D. Braunger, D. Hariskos, G. Bilger, U. Rau, and H. W. Schock, “Influence of sodium on the growth of polycrystalline Cu(In,Ga)Se2 thin films,” *Thin Solid Films*, vol. 361–362, no. 21, pp. 161–166, Feb. 2000.

[169] D. Rudmann, G. Bilger, M. Kaelin, F.-J. Haug, H. Zogg, and A. N. Tiwari, “Effects of NaF coevaporation on structural properties of Cu(In,Ga)Se2 thin films,” *Thin Solid Films*, vol. 431–432, no. 1, pp. 37–40, May 2003.

[170] R. Caballero, C. A. Kaufmann, T. Eisenbarth, A. Grimm, I. Lauermann, T. Unold, R. Klenk, and H. W. Schock, “Influence of Na on Cu(In,Ga)Se2 solar cells grown on polyimide substrates at low temperature: Impact on the Cu(In,Ga)Se2/Mo interface,” *Appl. Phys. Lett.*, vol. 96, no. 9, 2010.

[171] J. E. Granata, J. R. Sites, S. Asher, and R. J. Matson, “Quantitative incorporation of sodium in CuInSe2 and Cu(In,Ga)Se2 photovoltaic devices,” in *Conference Record of the Twenty Sixth IEEE Photovoltaic Specialists Conference*, 1997, pp. 387–390.

[172] K. Sakurai, A. Yamada, P. Fons, K. Matsubara, T. Kojima, S. Niki, T. Baba, N. Tsuchimochi, Y. Kimura, and H. Nakanishi, “Adjusting the sodium diffusion into CuInGaSe2 absorbers by preheating of Mo/SLG substrates,” *J. Phys. Chem. Solids*, vol. 64, no. 9–10, pp. 1877–1880, Sep. 2003.

[173] B. M. Keyes, F. Hasoon, P. Dippo, A. Balcioglu, and F. Abulfotuh, “Influence of Na on the Electro- Optical Properties of Cu(In,Ga)Se2,” in *26th IEEE Photovoltaic Specialists Conference*, 1997, no. September.

[174] A. Romeo, M. Terheggen, D. Abou-Ras, D. L. Bätzner, F.-J. Haug, M. Kälin, D. Rudmann, and a. N. Tiwari, “Development of thin-film Cu(In,Ga)Se2 and CdTe solar cells,” *Prog. Photovoltaics Res. Appl.*, vol. 12, no. 23, pp. 93–111, Mar. 2004.

[175] K. Granath, M. Bodegård, and L. Stolt, “The effect of NaF on Cu(In,Ga)Se2 thin film solar cells,” *Sol. Energy Mater. Sol. Cells*, vol. 60, no. 3, pp. 279–293, Jan. 2000.

[176] Y. M. Shin, D. H. Shin, J. H. Kim, and B. T. Ahn, “Effect of Na doping using Na2S on the structure and photovoltaic properties of CIGS solar cells,” *Curr. Appl. Phys.*, vol. 11, no. 1, Supplement, pp. S59–S64, Jan. 2011.

[177] K. Granath, L. Stolt, and M. B. A, “Growth of Cu(In,Ga)Se 2 thin films by coevaporation using alkaline precursors,” *Thin Solid Films*, vol. 361–362, pp. 9–16, 2000.

[178] R. Wieting, R. Gay, H. Nguyen, J. Palm, C. Rischmiller, A. Seapan, D. Tamant, and D. Willett, “CIS thin film manufacturing at Shell Solar: practical techniques in volume manufacturing,” *Photovoltaic Specialists Conference, 2005. Conference Record of the Thirty-first IEEE.* pp. 177–182, 2005.

[179] S. Zhang, Y. Shirai, and 白井孝典, “Sputtering target and process for production thereof,” EP2402482A1, 12-May-2011.

[180] L. M. Mansfield, I. L. Repins, S. Glynn, M. D. Carducci, D. M. Honecker, J. W. Pankow, M. R. Young, C. DeHart, R. Sundaramoorthy, C. L. Beall, and B. To, “Sodium-doped molybdenum targets for controllable sodium incorporation in CIGS solar cells,” *Photovoltaic Specialists Conference (PVSC), 2011 37th IEEE.* pp. 3636–3641, 2011.

[181] C. M. Sutter-Fella, J. A. Stu, H. Hagendorfer, F. La Mattina, L. Kranz, S. Nishiwaki, A. R. Uhl, Y. E. Romanyuk, and A. N. Tiwari, “Sodium Assisted Sintering of Chalcogenides and

Its Application to Solution Processed Cu 2 ZnSn(S,Se) 4 Thin Film Solar Cells," *Chem. Mater.*, vol. 26, no. 3, pp. 1420–1425, 2014.

[182] C. M. Sutter-Fella, "Solution-processed kesterite absorbers for thin film solar cells," 2014.

[183] Q. Guo, G. M. Ford, R. Agrawal, and H. W. Hillhouse, "Ink formulation and low-temperature incorporation of sodium to yield 12 % efficient Cu(In,Ga)(S,Se)2 solar cells from sulfide nanocrystal inks," *Prog. Photovoltaics Res. Appl.*, vol. 21, no. 1, pp. 64–71, 2012.

[184] M. Werner, C. M. Sutter-Fella, H. Hagendorfer, Y. E. Romanyuk, and a. N. Tiwari, "Cu2ZnSn(S,Se)4 solar cell absorbers processed from Na-containing solutions in DMSO," *Phys. Status Solidi*, vol. 2, pp. 116–120, Sep. 2014.

[185] M. Werner, C. M. Sutter-Fella, Y. E. Romanyuk, and A. N. Tiwari, "8.3% efficient Cu2ZnSn(S,Se)4 solar cells processed from sodium-containing solution precursors in a closed reactor," *Thin Solid Films*, vol. available , 2014.

[186] T. Meisel, Z. Halmos, K. Seybold, and E. Pungor, "The thermal decomposition of alkali metal formates," *J. Therm. Anal.*, vol. 7, no. 1, pp. 73–80, 1975.

[187] E. Skiba, J. Krystek, and B. Ptaszyn, "Thermal decomposition of alkali metal, copper(I) and silver(I) thiocyanates," *Thermochim. Acta*, vol. 319, pp. 75–85, 1998.

[188] G. M. Hanket, W. N. Shafarman, B. E. Mccandless, R. W. Birkmire, and I. I. Experimental, "Incongruent reaction of Cu-(InGa) intermetallic precursors in H2Se and H2S," *J. Appl. Phys.*, vol. 102, no. 7, pp. 1–10, 2007.

[189] B. M. Başol, V. K. Kapur, A. Halani, C. R. Leidholm, J. Sharp, J. R. Sites, A. Swartzlander, R. Matson, and H. Ullal, "Cu (In,Ga)Se2 thin films and solar cells prepared by selenization of metallic precursors," *J. Vac. Sci. Technol. A Vacuum, Surfaces Film.*, vol. 14, no. 4, pp. 2251–2256, 1996.

[190] I. M. Kötschau and H. W. Schock, "Compositional depth profiling of polycrystalline thin films by grazing-incidence X-ray diffraction," *J. Appl. Crystallogr.*, vol. 39, no. 5, pp. 683–696, 2006.

[191] J. F. Guillemoles, "Stability of Cu(In,Ga)Se2 solar cells: a thermodynamic approach," *Thin Solid Films*, vol. 361–362, pp. 338–345, Feb. 2000.

[192] I. Dirnstorfer, W. Burkhardt, W. Kriegseis, I. Österreicher, H. Alves, D. M. Hofmann, O. Ka, A. Polity, B. K. Meyer, and D. Braunger, "Annealing studies on CuIn(Ga)Se2: the influence of gallium," *Thin Solid Films*, vol. 361–362, pp. 400–405, Feb. 2000.

[193] H. Rodriguez-Alvarez, R. Mainz, R. Caballero, D. Abou-Ras, M. Klaus, S. Gledhill, A. Weber, C. A. Kaufmann, and H.-W. Schock, "Real-time study of Ga diffusion processes during the formation of Cu(In,Ga)Se2: The role of Cu and Na content," *Sol. Energy Mater. Sol. Cells*, vol. 116, no. 0, pp. 102–109, 2013.

[194] P. M. P. Salomé, H. Rodriguez-Alvarez, and S. Sadewasser, "Incorporation of alkali metals in chalcogenide solar cells," *Sol. Energy Mater. Sol. Cells*, vol. 143, pp. 9–20, Dec. 2015.

[195] G. Zoppi, I. Forbes, R. W. Miles, P. J. Dale, J. J. Scragg, and L. M. Peter, "Cu2ZnSnSe4 thin film solar cells produced by selenisation of magnetron sputtered precursors," *Prog. Photovoltaics Res. Appl.*, vol. 17, no. 5, pp. 315–319, Aug. 2009.

[196] S. Ahn, S. Jung, J. Gwak, A. Cho, K. Shin, K. Yoon, D. Park, H. Cheong, and J. H. Yun, "Determination of band gap energy (Eg]) of Cu2ZnSnSe4 thin films: On the discrepancies of reported band gap values," *Appl. Phys. Lett.*, vol. 97, no. 2, p. 021905, 2010.

[197] S.-H. Wei, S. B. Zhang, and A. Zunger, "Effects of Ga addition to CuInSe2 on its electronic, structural, and defect properties," *Applied Physics Letters*, vol. 72, no. 24. pp. 3199–3201, 1998.

[198] V. Probst, I. Koetschau, E. Novak, A. Jasenek, H. Eschrich, F. Hergert, T. Hahn, J. Feichtinger, M. Maier, B. Walther, and V. Nadenau, "A New Mass Production Technology for High-Efficiency Thin-Film CIS-Absorber Formation," *IEEE J. PHOTOVOLTAICS*, vol. 4, no. 2, pp. 687–692, 2014.

[199] F. Karg, "High Efficiency CIGS Solar Modules," *Energy Procedia*, vol. 15, no. 2011, pp. 275–282, 2012.

[200] K. J. Nelson, I. A. Guzei, G. S. Lund, and R. W. Mcgaff, "Copper (II) methoxide : direct sol v entothermal synthesis and X-ray crystal structure," vol. 21, pp. 2017–2020, 2002.

[201] G. V. Gusakova, G. S. Denisov, and A. L. Smolyanskii, "Proton acceptor power of 1,1,3,3-tetramethylguanidine: hydrogen bonding and protonation in inert solvents," *Zhurnal Obs. Khimii*, vol. 59, no. 10, pp. 2099–2103, 1990.

[202] T. Rodima, I. Kaljurand, A. Pihl, V. Mäemets, I. Leito, and I. A. Koppel, "Acid−Base Equilibria in Nonpolar Media. 2.1 Self-Consistent Basicity Scale in THF Solution Ranging from 2-Methoxypyridine to EtP1(pyrr) Phosphazene," *J. Org. Chem.*, vol. 67, no. 6, pp. 1873–1881, Feb. 2002.

[203] Y. Inada, H. Hayashi, K. Sugimoto, and S. Funahashi, "Solvation Structures of Manganese(II), Iron(II), Cobalt(II), Nickel(II), Copper(II), Zinc(II), and Gallium(III) Ions in Methanol, Ethanol, Dimethyl Sulfoxide, and Trimethyl Phosphate As Studied by EXAFS and Electronic Spectroscopies," *J. Phys. Chem. A*, vol. 103, no. 10, pp. 1401–1406, Feb. 1999.

[204] J. Carstensen, G. Popkirov, J. Bahr, and H. F, "CELLO : an advanced LBIC measurement technique for solar cell local characterization," vol. 76, pp. 599–611, 2003.

Nomenclature

Abbreviations

4ATA	4-Amino-1,2,4-Triazole
ARC	Anti reflective coating
ATR	Attenuated total reflection
BC	Back contact
BLC	Blade coating
BSF	Back surface field
CBD	Chemical bath deposition
CIGS	$Cu(In,Ga)(S,Se)_2$
DLC	Direct liquid coating
DMF	Dimethylformamide
EA	Elemental analysis
EP	Electroless plating
EQE	External quantum efficiency
MeOH	Methanol
EtOH	Ethanol
FF	Fill factor
GB	Grain boundary
GIXRD	Grazing incidence X-ray diffraction
i-XRD	in situ X-ray diffraction
i-ZnO	Intrinsic ZnO
(FT)-IR	(Fourier transformed) infrared spectroscopy
JCPDS	Joint Committee on Powder Diffraction Standards
LBIC	Light beam induced current
MS	Mass spectrometry
ODC	Ordered defect compound
PL	Photoluminescence
QNR	Quasi neutral region
SC	Spray coating
SCR	Space charge region
SDC	Slot die coating
SEM	Scanning electron microscopy
SIMS	Secondary ion mass spectrometry
SLG	Soda lime glass (float glass)
SPC	Spin coating
TA	Triazole
TCO	Transparent conductive oxide
TMG	Tetramethylguanidine
TG	Thermogravimetry
UNIFAC	Universal Functional-group Activity Coefficients

Symbols and dimensionless numbers

A	surface area in m²	M_i	molar mass of component i in kg/kmol
a	thermal diffusivity in m²/s	$\dot{N}_i$	absolute diffusion flux in mol/s
c	speed of light (in a vacuum) in m/s	p	total pressure
D	diffusion coefficient in m²/s	p_{iA}	partial pressure of component i at position A in Pa
$E^{\ominus}$	standard electrode potential in V	$p_{iA}^{*}(T)$	vapor pressure of component i in Pa
E_c	conduction band energy in eV	q	elementary charge (1.60×10^{-19} C)
E_F	Fermi level energy in eV	R	universal gas constant in J/(mol K)
E_G	band gap energy in eV	Ra	Rayleigh number
E_V	valence band energy in eV	Re	Reynolds number
E_{photon}	energy of a photon in eV	Sc	Schmidt number
f	frequency in 1/s	Sh	Sherwood number
F	Faraday constant (96.48 kC/mol)	Sh_{forced}	Sherwood number for forced convection
g	gravitational acceleration in m/s²	Sh_{free}	Sherwood number for free convection
h	Planck constant (4.14×10^{-15} eVs)	Sh_{lam}	laminar Sherwood number
j	current density in mA/cm²	Sh_{turb}	turbulent Sherwood number
j_0	reverse saturation current in mA/cm²	T	absolute temperature in K
j_{dark}	dark current in mA/cm²	T_M	median temperature in K
j_{max}	current density at maximum power in mA/cm²	u	velocity in m/s
j_{ph}	photo current in mA/cm²	$\bar{u}_i$	mean velocity of molecule i in m/s

j_{sc}	short circuit current in mA/cm²
J	diffusion flux in mol/m²s
k_B	Boltzmann constant (1.38×10^{-23} m² kg/s²K¹)
K	equilibrium constant
l_{AB}	diffusion path length in m from position A to B
L_c	characteristic length of the liquid surface in m
v	number of electrons transferred within the half cell reactions
V	voltage in V
V_{oc}	open circuit voltage in V
V_{max}	voltage at maximum power in V
x_i	molar fraction of component i in the liquid

β_i	mass transfer coefficient of component i in m/s
γ_i	activity coefficient of component i in the mixture
η	energy conversion efficiency
λ	wavelength in m
λ_i	mean free path of molecule i in m
ν_{gas}	kinematic viscosity of the gas in m²/s
σ	collision area
v_i	diffusion volume of component i

Acknowledgments

I am greatly indebted to many persons without whose assistance this work would not have been possible. My particular thanks go to:

My supervisor at BOSCH Dr. Markus Widenmeyer for his dedication, support and his always open ears for my various questions during the three years at the central research.

My academic supervisor at the University of Luxembourg Dr. Phillip Dale for accepting me as a Ph.D. student. Under his excellent guidance as well as through the many helpful discussions and advices this work highly improved.

Prof. Dr. Zeger Hens and Dr. Diego Colombara for agreeing to be part of my CET committee as well as Prof. Dr. Jan Lagerwall for participating in the defense jury.

All the colleagues at the department for applied chemistry especially Dr. Petra Neff and Dr. Carsten Herweg for giving me the chance to focus on my Ph.D.

My colleagues at BOSCH CIS Tech in Brandenburg for their support, especially Dr. Frank Hergert for the many fruitful discussions on the field of X-ray diffraction and Martin Schütze for helping me with the GIXRD measurements and the selenium evaporation modeling.

The „CIGS team“ consisting of the Ph.D. students Björn Müller, Christian Hönes and Rou Hua Chua for the various CIGS meetings leading to many interesting discussions.

My project leaders Dr. Siegmund Zweigart and Dr. Jochen Feichtinger for the continuous support allowing me to work highly independent as well as my colleague Veronika Haug for her help regarding the i-XRD measurements.

The people at the analytics department for the countless measurements and discussions.

My fellow Ph.D. colleagues at Bosch, namely Martin Schreivogel, Michael Butzin, Corinna Vonau and Daniel Maier for the plentiful non work related activities during the three years.

My family for the continuous support during my studies.

And finally Vera for everything she has given to me.

Publications

Journal publications

U. Berner and M. Widenmeyer, “*Solution-based processing of $Cu(In,Ga)Se_2$ absorber layers for 11% efficiency solar cells via a metallic intermediate*,” Progress in Photovoltaics: Research and Application, vol. 23, pp. 1260–1266, 2015

U. Berner, M. Widenmeyer, P. Engler, and P. J. Dale, “*4-Amino-1,2,4-triazole: Playing a key role in the chemical deposition of Cu–In–Ga metal layers for photovoltaic applications*,” Thin Solid Films, vol. 582, pp. 39–42, 2015

U. Berner, D. Colombara, J. de Wild, E. V.C. Robert, M. Schütze, F. Hergert, M. Widenmeyer, N. Valle, and P. J. Dale, “*13.3% efficient solution deposited $Cu(In,Ga)Se_2$ solar cells processed with different sodium salt sources*,” Progress in Photovoltaics: Research and Application, doi: 10.1002/pip.2721, 2015

S. Tombolato, U. Berner, D. Colombara, D. Chrastina, M. Widenmeyer, S. O. Binetti, and P. J. Dale, “*$Cu_2ZnSnSe_4$ device obtained by formate chemistry for metallic precursor layer fabrication*,” Solar Energy, vol. 116, pp. 287-292, 2015

Conference publications (* presenter)

U. Berner* and M. Widenmeyer, “*A New Solution Based Route to 11%-Efficiency Cu(In,Ga)Se2 Solar Cells*”, talk, EU-PVSEC 2013, Paris

U. Berner*, M. Widenmeyer, P. Engler, and P. J. Dale, “*4-Amino-1,2,4-triazole: Playing a key role in the chemical deposition of Cu–In–Ga metal layers for photovoltaic applications*,” poster, EMRS 2014, Lille

U. Berner, D. Colombara, T. Bertram, N. Valle, P. J. Dale*, “*On the Role of Vapour Phase Alkali Species for Efficient Cu(In,Ga)Se2 Solar Cells*”, talk, EU-PVSEC 2015, Hamburg

Patents

M. Widenmeyer and U. Berner, „*Beschichtungslösung und Verfahren zur nass-chemischen Abscheidung von Metall- und/oder Metallnitridschichten.*“ R. 348972

M. Widenmeyer and U. Berner, “*Metallschicht sowie Verfahren und Beschichtungs-flüssigkeit für ihre Herstellung.* ” R. 357333